University of Rhode Island

DigitalCommons@URI

2017

High Strain Rate Deformation Mechanisms of Body Centered Cubic Material Subjected to Impact Loading

William Visser

University of Rhode Island, visserw@egr.uri.edu

HIGH STRAIN RATE DEFORMATION MECHANISMS OF

BODY CENTERED CUBIC MATERIAL

SUBJECTED TO IMPACT LOADING

BY

WILLIAM VISSER

DISSERTATION SUBMITTED IN PARTIAL FULFILLMENT OF THE
REQUIREMENTS FOR THE DEGREE OF
DOCTOR OF PHILOSOPHY
IN
MECHANICAL, INDUSTRIAL, AND SYSTEMS ENGINEERING

UNIVERSITY OF RHODE ISLAND

2017

DOCTOR OF PHILOSOPHY DISSERTATION

OF

WILLIAM VISSER

APPROVED:

Dissertation Committee:

Major Professor: Hamouda Ghonem

Carl-Ernst Rousseau

Otto Gregory

David Taggart

Nasser H. Zawia
DEAN OF THE GRADUATE SCHOOL

UNIVERSITY OF RHODE ISLAND

2017

ABSTRACT

Low carbon steel is the most common grade of structural steel used; it has carbon content of 0.05% to 0.25% and very low content of alloying elements. It is produced in great quantities and provides material properties that are acceptable for many engineering applications, particularly in the construction industry in which low carbon steel is widely used as the strengthening phase in civil structures. The overall goal of this dissertation was to investigate the deformation response of A572 grade 50 steel when subjected to impact loading. This steel has a 0.23% by weight carbon content and has less than 2% additional alloying elements. The deformation mechanisms of this steel under shock loading conditions include both dislocation motion and twin formation. The goal of this work was achieved by performing experimental, analytical and numerical research in three integrated tasks. The first is to determine the relationship between the evolution of deformation twins and the impact pressure. Secondly, a stress criterion for twin nucleation during high strain rate loading was developed which can account for the strain history or initial dislocation density. Lastly, a method was applied for separating the effects of dislocations and twins generated by shock loading in order to determine their role in controlling the flow stress of the material. In this regard, the contents of this work have been categorically organized.

First, the active mechanisms in body centered cubic (BCC) low carbon steel during shock loading have been determined as being a composed of the competing mechanisms of dislocations and deformation twins. This has been determined through a series of shock loading tests of the as-received steel. The shock loading tests were done by plate

impact experiments at several impact pressures ranging from 2GPa up to 13GPa using a single stage light gas gun. A relationship between twin volume fraction and impact pressure was determined and an analytical model was utilized to simulate the shock loading and twin evolution for these loading conditions.

The second part of this research ties into the modeling efforts. Within the model for predicting twin volume fraction is a twin growth equation and a constant describing the stress at which the twin nucleation will occur. By using a constant value for the twin nucleation stress modeling efforts fail to accurately predict the growth and final twin volume fraction. A second shock loading experimental study combined with high strain rate compression tests using a split Hopkinson pressure bar were completed to determine a twin nucleation stress equation as a function of dislocation density. Steel specimens were subjected to cold rolling to 3% strain and subsequently impacted using the gas gun at different pressures. The increase in dislocation density due to pre-straining substantially increased the twin nucleation stress indicating that twin nucleation stress in dependent upon prior strain history. This has been explained in terms of the velocity and generation rates of both perfect and partial dislocations. An explicit form of the critical twin nucleation stress was developed and parameters were determined through plate impact tests and low temperature (77K) SHPB compression tests.

The final component in studying deformation twin mechanisms in BCC steel extends the research to the post-impact mechanical properties and how the twin volume fraction affects the dynamic flow stress. Compression tests between 293K and 923K at an average strain rate of 4700 s^{-1} were completed on the as-received and 3% pre-strained steels in both the initial condition and after being impacted at pressures of 6GPa and

11GPa. Results of the experimental testing were used in a thermal activation model in order to distinguish separate components in the microstructure contributing to the enhanced flow stress caused by the shock loading. It has been shown that the dislocations generated from shock loading are equivalent to those produced under lower rate straining and the addition of deformation twins in the microstructure contribute to the athermal stress by adding to the long range barriers.

ACKNOWLEDGEMENTS

First, Dr. Hamouda Ghonem, I would like to acknowledge you for your continuous support throughout my entire graduate carrier. Without your persistent nature and dedication to me and my research, I would never have achieved such a well-rounded understanding and passion of the subject. I am especially grateful for your patients and ability to put up with my stubbornness when it comes to experimental work. Over the years of work together I can honestly say that you are a great mentor and an even better friend.

Secondly, I would like to thank my family, especially my parents John and Nancy Visser. They have supported me throughout my academic endeavors beyond what I could ever expect or repay. Their never-ending love truly showed through their patients and understanding. Without such love and support I could never have come this far in life, let alone in my academic career.

I would like to extend my gratitude to Jinesh Dahal, Rick Jones, Kimberly Maciejewski, Justin Spirdione, Dan Spader, Yaofeng Sun and any other one of my colleagues that has come and gone in the Mechanics of Materials Research Lab over the years and spent countless hours to help me so much.

Thank you to Professors David Taggart, Otto Gregory and Wayne Lee for serving as my committee members. A special thanks to Professor Carl-Ernst Rousseau for both serving on my committee and for the incredible support you provided me during my early academic career. A special thanks to your student and my friend Dr. Gifford Plume III

for the help and technical discussions we had regarding shock loading physics and experiments.

Thank you to the technical staff at URI. In particular Joe Gomez, Jim Byrnes, Rob D'Ambrosca for all their guidance and help with my research equipment. A special thanks to Joe who taught me invaluable information in the machine shop which I will carry with me the rest of my life with my new found passion of machining.

Finally, I would like to thank my girlfriend, Victoria Venturini. We have been through this process at URI together for many years. She has always supported me in what I do, and even when I didn't believe in myself, she provided the encouragement to keep driving. For that, Victoria, I love you.

PREFACE

This dissertation is prepared in manuscript format.

Chapter 1 is an introduction into the subject for the reader to familiarize themselves with basic concepts of mechanical testing and the crystallography and deformation of metals. This is presented so that an understanding of the terms and concepts used throughout the dissertation can be fully understood.

Chapter 2 outlines the design and development of a single stage light gas gun built in the Mechanics of Materials Research Lab. The contents of this chapter include the motivation for the development and a brief description of gas guns in research. The full design of the main gas gun components and the diagnostic system used is outlined in detail

Chapter 3 is a manuscript published in the journal of Materials Science and Engineering: A 528.27 (2011): 7875-7866. The work in this chapter was done to determine the effects of impact loading on the microstructure and mechanical properties of A572 grade 50 low carbon steel. Plate impact tests were conducted using a single stage gas gun for shock loading specimens. In plane stress was measured and correlated with the volume fraction of deformation twins. An analytical approach was utilized to mathematically simulate the microstructural variations based on the conservation of mass and momentum equations. Results were discussed in relation to quasi-static properties linked to the impact loading.

Chapter 4 is a manuscript published in the journal of Materials Science and Engineering: A 687 (2017): 28-38. In this chapter an extensive experimental investigation of deformation twin nucleation is conducted through shock loading and high strain rate compression tests at 77K and 293K. Specifically the experimental work was utilized in order to develop a critical twin nucleation stress which accounts for a materials strain history. This is developed in terms of the dislocation density evolution and describes the mechanisms controlling twin nucleation in body centered cubic steel. This concept is utilized in an analytical model for predicting the volume fraction of twins as function of impact pressure. The model predictions were enhanced through comparison to experimental findings by including a twin growth parameter which accounts for the activation of multiple twin systems.

Chapter 5 is a manuscript under review in the journal of Metallurgical and Materials Transactions A. This chapter outlines the effects of shock loading on the post-impact mechanical properties of low carbon steel. In this chapter a physics based dynamic flow stress model is presented. The model is derived based on the concept of dislocations and their interaction with thermal and athermal stress barriers which control the flow stress. The microstructure evolution as function of shock loading is studied in terms of the contribution to long range and short range stress barriers. An experimental study including high temperature compression testing was completed in order to separate the contributions due to inherent microstructure features and those induced by shock loading.

Chapter 6 presents major conclusions of the dissertation and future recommendations for continuing with this work.

The appendices include operating procedures for the light gas gun as well as all related mechanical drawings for the design. Also included in the appendices are the Matlab code for the analytical model used and data analysis for dynamic compression testing.

TABLE OF CONTENTS

LIST OF TABLES

LIST OF FIGURES

CHAPTER 1

INTRODUCTION

1.1.　　Statement of Problem

Impact loading is employed in many engineering applications including manufacturing processes such as forming, welding, and compaction of metal and ceramic powders. In addition to employed engineering techniques, catastrophic events such as explosions can result in high rate shock loading conditions. An important aspect in this type of loading is the associated high strain rate which dictates the microstructure evolution characteristics of the impacted material. Current efforts to simulate the high rate loading response of materials are carried out using various numerical and/or analytical models. These models are, in general, phenomenological in nature, yet can successfully predict the stress-strain response under a set of prescribed loading conditions and are capable of interpolating the outcomes. However, the absence of explicit microstructure parameters limits their extrapolation capability. Furthermore, deformation response of materials under impact loading has shown to be highly dependent on prior strain history. While successful in accounting for current loading and material conditions, the current models lack the ability to include prior strain history in their simulation platforms. Additionally, the majority of work done on impact loading focuses on the microstructure and corresponding mechanical response during impact loading; little information, however, is available on the influence of the resulting microstructure

on the post impact mechanical behavior, which is of particular importance for manufacturing and structural survivability. It is therefore of interest to identify the relationship between post impact microstructure and flow stress. In doing so, material selection and loading conditions can be tailored to achieve desirable properties of the final material state.

The goal of this research therefore is to establish a stress criterion for twin nucleation which accounts for both loading conditions and prior strain history. This criterion is an important component in numerical simulation models designed to predict impact related flow stress and strain history. This will be carried out by a combined experimental, numerical, and analytical study. The experimental work will consist of a series of impact tests on low carbon steel using a gas gun followed by microscopic observation to identify microstructure evolution. These specimens will subsequently be used to identify post impact stress-strain behavior through a series of compression tests using a split Hopkinson pressure bar. Results of this experimental work will be incorporated into a thermal activation model to identify flow stress in terms of its thermal and athermal components which are in turn, functions of material and loading conditions.

1.2.   **Justification**

Of all the metals which have been subject to dynamic testing, steel is one of the most common materials. Its versatility has allowed steel to be a widely studied and used metal in structural engineering. For this reason, research on all varieties of steel has been carried out. The high strain rate properties is important for manufacturing processes such

as explosive forming and cutting to end-use applications such as safety of structural members in civil structures. In order to effectively design for the applications, experimental testing of related materials is required over a broad spectrum of strain rates and temperatures in order to understand the evolution of microstructure features which can facilitate in the development of physically based constitutive models. Several techniques exist by which related experiments can be conducted for strain rates in the range of 10^1 s^{-1} up to 10^6 s^{-1} in laboratory settings [1] [2]. These tests include compression and tension tests using a drop weight, split Hopkinson pressure bar (SHPB), Taylor impacts, plate impacts using single or two stage gas guns, and small scale explosive loading of plates. Results from shock loading studies include developing a relationship between the shock loading pressure and the particle velocity within the material during shock loading and is one of the most valuable contributions that can be made to the community for shock load modeling efforts. This, more commonly expressed as pressure vs. specific volume, is commonly known as the Rankine-Hugoniot relationship, of which the Los Alamos National lab has provide extensive amounts of data for a variety of materials [3] for this very reason.

The most common outcome related to microstructural features induced by high strain rate loading in most materials, including body centered cubic, face centered cubic, and hexagonally closed packed crystal structures; deformation can occur by two processes, dislocation slip and/or mechanical twinning. Meyers [4] found that the twin volume fraction is a function of stress, and is independent of temperature and strain rate and will increase monotonically with increasing stress. Visser et al. [5] established a relation for the volume fraction of twins to the applied stress through a series of plate impacts in low

carbon steel. Shock loaded iron has been shown to exhibit significant twin formation in by De Resseguier and Hallouin [6] using high-power lasers pulses and Johnson and Rohde [7] proposed a constitutive twinning model to determine twin volume fraction. Within a number of these studies the modeling efforts utilize a stress based twin nucleation criterion which contributes the final twin volume fraction prediction. The slip-twinning transition has been explained through a mechanistic model proposed by Armstrong and Worthington [8] based upon the Swegle-Grady relationship, grain-size and temperature to predict the threshold stress for twinning. Meyers [9] [10] discusses the influence of strain rate, temperature, grain size, and stress state on twin initiation for FCC, BCC, and HCP materials and showed that twin nucleation is related to dislocation motion and presented a model in which dislocation pile-ups are considered a key aspect in nucleation. Karaman et al. [11] suggested that twinning occurs by pile ups of dislocations from which partial separation occurs.

The above studies indicate that the twin nucleation stress is dependent upon several intrinsic and extrinsic material properties; therefore, numerical modeling of twin nucleation and growth should also include these factors. Several authors have shown that pre-straining at room temperature is effective in suppressing deformation twin nucleation. Twins have been shown to be suppressed in low carbon steel and in iron when testing at liquid nitrogen temperatures after a prior pre-straining to levels as low as 1% [12-15]. Pre-straining as little as 2% has also been shown to be effective in inhibiting twin nucleation in iron and in molybdenum during shock loading at 9GPa [16] [17]. What is missing from these studies is an explicit form of the twin nucleation stress which accounts for the prior strain history. This nucleation criterion can be explained in terms

4

of the increase in dislocation density. By straining the material an increased distribution of dislocations is generated and the propensity to twin becomes lower as plastic deformation can be accommodated by slip [17]. Therefore, prior mobile dislocation density is indirectly proportional to the number of probable twin nucleation sites. This could indicate that the mobile dislocation density and the degree of uniformity have a direct correlation with the critical stress required to twin. The characteristics of the dislocations generation rate and velocity can therefore be directly implemented into a criterion governing twin nucleation.

The role of deformation twins on subsequent mechanical properties has been studied by several authors. Twins have been shown to contribute to fracture mechanisms [18,19] including influence in crack path direction during quasi-static loading [5], and a correlation between deformation twins and the mode of fracture has been established [20]. Meyers et al. [9,10] noted that twinning can have two significant effects upon the flow stress; the twins act as barriers effectively subdividing the grains, thereby increasing the work hardening rate, and also contribute to plastic deformation due to twinning shear. Murr et al. [21] explain that the twin nucleation stress is highly dependent upon stacking-fault energy. Their work examined twin formation during shock loading and post-shock mechanical response of Tantalum consisting of quasi-static and dynamic compression tests as well as microhardness measurements. They concluded that twins are responsible for additional hardening of the microstructure and developed parameters for the Johnson-Cook model to account for the shock loading. This approach, while valid, does not attempt to separate the contributions of the shock induced microstructural changes and is still phenomenological in nature.

The studies mentioned above point out to different contributions that twins have on the mechanical properties of metals during subsequent testing. Missing from these efforts is a systematic examination of the microstructural variables influencing the dynamic flow stress. Thus, as discussed in Chapter 5, a physically based thermal activation model is utilized by including shock induced microstructural effects and separating these features into athermal and thermal stress contributions. The flow stress during plastic deformation is described by dislocation motion and their resistance to barriers. This stress is split into parts according to the type of barriers; short range and long range. The thermal stress component consists of short range barriers which, in BCC metals, are controlled by the resistance of the actual lattice and point defects within and is affected by the strain rate and temperature [23]. The athermal stress component consists of long range barriers and is controlled by stress fields from microstructural features such as grain boundaries and secondary phases which thermal energy is not sufficient to aid in overcoming these obstacles [23,24]. The results of this model would, therefore, indicate to what extent each shock induced parameter has on the magnitude and hardening features of the flow stress in shock loaded materials.

1.3.   **Approach**

As previously discussed, the goal of this dissertation is to establish a dynamic deformation criterion for twin nucleation as a function of both loading conditions and prior strain history as well as determining the influence of deformation twins on the overall flow stress. This goal will be carried out through experimental, analytical, and

numerical studies. Mechanical properties and microstructure variation of impacted specimens will be characterized at various temperatures and strain rates using several experimental methods. These tests, which are discussed in the following section, are divided on the basis of the strain rate level into three regimes; low, intermediate, and high strain rate as shown in Figure 1-1. This figure shows a full range of achievable strain rates in the laboratory setting and the typical testing methods used.
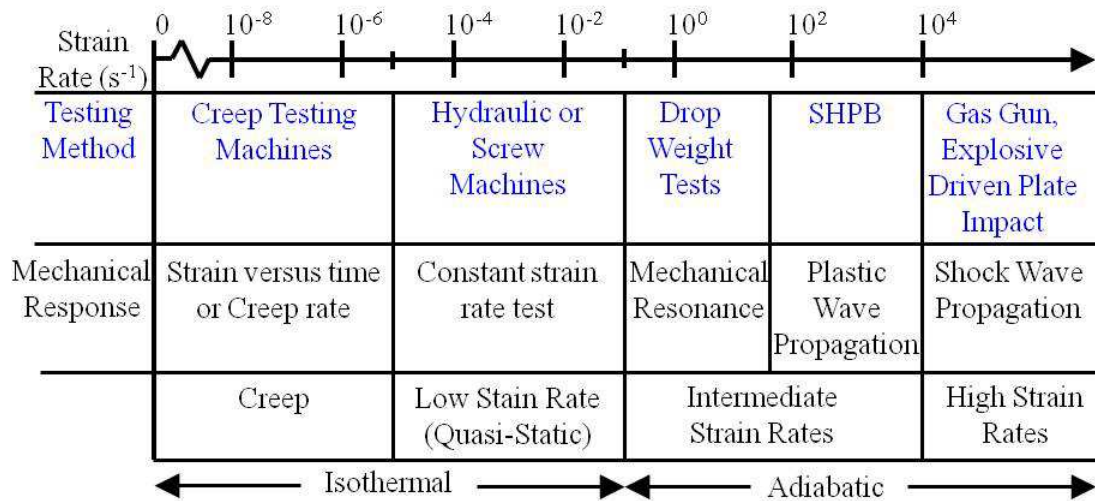
Figure 1-1: Strain rate regimes in mechanical testing of materials.

The low strain rate regime is the quasi-static strain rate range 10^{-5} to 10^{-2} s^{-1}. In the current work, quasi-static tension and compression tests were completed using MTS servo-hydraulic testing systems at room temperature. This strain rate level of testing is used to generate material properties as well as parameters required in the formulations of a constitutive model (Johnson-Cook model) used in this study to simulate the response of the material under different loading conditions. The intermediate testing regime is that which corresponds to the strain rate range 10^{2} to 10^{4} s^{-1}. Testing in this range was completed using a compression split Hopkinson pressure bar (SHPB) in the temperature

7

range 73 K to 923 K. The SHPB testing serves three objectives in this dissertation. The first objective is to determine constants for the Johnson-Cook model as functions of temperature and strain rate. The second objective is to determine the critical twin nucleation stress in the body centered cubic crystal structure of the low carbon steel under consideration. The third objective is to determine microstructural variables influencing the two components of the flow stress; athermal and thermal, in the as-received and pre-strained steel materials at various temperatures and strain rates. The third loading regime is the one corresponding to high strain rate which is achieved by the shock loading of both the as-received and cold rolled pre-strained steel specimens. These specimens are subsequently used to identify microstructure evolution as a result of impact loading through microscopy as well as to identify post impact stress-strain behavior through a series of intermediate strain rate compression tests. This level of high strain rate testing required the design and construction of a single stage light gas gun in the Mechanics of Materials Research Lab (MMRL) in order to shock load the specimens by means of planar plate impacts. The design and theory of light gas guns is discussed in detail in Chapter 2.

Results of the shock loading experiments will be investigated using analytical models coupled with finite element analysis. These models utilize material constitutive laws that require the knowledge of material parameters which, in turn, are determined using results from a set of tests performed at various temperatures within the low and intermediate strain rate regimes. These parameters are extended to shock load modeling by extrapolating their values to the high strain rate regime. Three models are examined in this dissertation; the empirically based Johnson-Cook (JC) model, the deformation twin

model, and the thermal activation flow stress model, which are briefly discussed here and are discussed in detail in Chapters 3, 4, and Chapter 5.

Several models for determining the flow stress under impact loading exist in literature; these include the Johnson-Cook (JC) model, Zerrilli-Armstrong (ZA) model, and Mechanical Threshold Stress (MTS) model. The JC model has been widely utilized in commercially available finite element programs, such as Abaqus, due to its simplicity and relative accuracy. As such, this model has been utilized in this work in a numerical procedure in order to provide initial impact particle velocity which is subsequently required in developing a model to determine deformation twin growth as a function of impact condition pressure. The JC model expresses the equivalent von Mises flow stress as a function of the equivalent plastic strain, ε, dimensionless plastic strain rate, $\dot{\varepsilon}^*$, and homologous temperature, T^*, as follows [25]:

$$\sigma = \underbrace{\left(A + B\varepsilon^n\right)}_{\text{Strain Hardening}} \underbrace{\left[1 + C\ln\dot{\varepsilon}^*\right]}_{\text{Strain Rate Effect}} \underbrace{\left[1 - T^{*m}\right]}_{\text{Temperature Effect}} \qquad (1.1)$$

where A, B, n, C, and m are empirical material constants to be experimentally determined. The expression in the first bracket represents the strain hardening effects, the second bracket represents the strain rate effects, and the third set of terms represents thermal effects. The dimensionless plastic strain rate is defined as

$$\dot{\varepsilon}^* = \dot{\varepsilon}/\dot{\varepsilon}_o \qquad (1.2)$$

in which $\dot{\varepsilon}$ is the imposed strain rate and $\dot{\varepsilon}_o$ is a reference strain rate at which parameters are determined. The homologous temperature is defined as:

$$T^* = \frac{T - T_r}{T_m - T_r} \tag{1.3}$$

where T is the imposed temperature, T_r is the reference temperature, and T_m is the melting temperature.

Determination of model constants requires a minimum of nine tests, at three different strain rates and three different temperatures. These were performed at the low and intermediate strain rate regimes. JC model constants are implemented into a numerical platform employing the commercial code Abaqus for plate impact simulations which are utilized for generating particle velocity profiles at the impact surface of the target specimen. These profiles are used as an input to a physics based twin model to predict the volume fraction of deformation twins during impact loads. This twin model is described by the laws of mass and momentum conservation, which are written as

$$\frac{\rho_0}{\rho^2} \frac{\partial \rho}{\partial t} + \frac{\partial u}{\partial X} = 0 \tag{1.4}$$

$$\rho_0 \frac{\partial u}{\partial t} + \frac{\partial \sigma}{\partial X} = 0 \tag{1.5}$$

where ρ_0 is initial density, ρ is an evolved density, and u is particle velocity during impact at time t at a distance of X from the impact surface. The initial particle velocity profile imposed at the front surface of the target specimen is a required input in order to explicitly solve Equations (4) and (5) through time and distance. Plate impacts of as-received and pre-strained steel specimens will be used to validate model predictions of

twin volume fraction. Full details of calculating twin volume fraction and determination of the critical deformation twin stress is provided in Chapter 4.

Finally, the effects of the shock loading on the residual flow stress of the material will be determined. Impact specimens will be prepared in the as-received condition and in different pre-strained states. Following plate impact tests, compression specimens will be machined from the impacted target specimens and post impact tests will be carried out on the specimens using a SHPB at several strain rates and temperatures. In this part of the study, the total flow stress is considered to be the sum of the thermal, σ_{th}, and the athermal $\sigma_{A,}$ stress components. The thermal component of stress is expressed as a function of both strain rate and temperature as follows:

$$\sigma_{TH} = \hat{\sigma}\left[1 - \left(\frac{kT}{G_0}\ln\frac{\dot{\varepsilon}}{\dot{\varepsilon}_r}\right)^{1/q}\right]^{1/p} \tag{1.6}$$

where $\hat{\sigma}$ is the mechanical threshold stress at 0K, k is Boltzmann's constant, T is current temperature, G_0 is the energy of the Peierl's barrier per atom, $\dot{\varepsilon}$ is the imposed strain rate, and $\dot{\varepsilon}_r$ is the reference strain rate. On the other hand, the athermal component of the flow stress can be described by a simple power law equation fit to experimental data as

$$\sigma_A = \sigma^*\varepsilon^n + \sigma_m \tag{1.7}$$

where ε is the strain, σ^* and n are the strain hardening sensitivity parameters, and σ_m is the stress component due to the current microstructure which can be measured as the yield stress at the critical temperature. An effort will be made to include the effects of prior impact, due to residual microstructure variation i.e. dislocation networks and

11

deformation twins, on the flow stress components. The model formulation and determination of constants will be shown in Chapter 5.

1.4.   **Mechanical Loading of Materials**

An experimental study has been carried out in order to determine the deformation response of low carbon steel at various temperatures and strain rates. This work has been completed using several experimental methods and apparatus. This section of the dissertation will focus on the testing methods and provide details of experimental procedures, specimen preparations, results and analysis, as well as detailed theoretical considerations. The performed tests are categorized in terms of the strain rate which is considered a significant factor in controlling the microstructural response of the material under study. The range of the strain rates is split into three regimes; low, intermediate, and high strain rate.

The low strain rate regime in this work is considered to be within the quasi-static range, between 10^{-5} to 10^{-2} s^{-1}, as this is the lowest strain rate used for characterizing the material studied. The quasi-static testing is used in the parametric study of constants for the JC model and for material parameters for finite element simulations.

The intermediate strain rate regime is in range of 10^{2} to 10^{4} s^{-1}, and was completed using a split Hopkinson pressure bar (SHPB) for compression tests at low and high temperatures. The SHPB compression tests are used for determining parameters for several models throughout this study.

The high strain rate regime is considered to be above strain rates of 10^4 s^{-1}. These tests are carried out using a single stage light gas gun for shock loading specimens, the design of which is detailed in Chapter 2. Foundations of the shock loading experiments will be discussed in section 1.2.2.2.

The details of these three testing regimes are discussed further in the following sections.

1.4.1.   **Quasi-Static Tension and Compression Testing (Low Strain Rate)**

Room temperature quasi-static tensile and compression tests were completed using a MTS electro-hydraulic testing machine, as shown in Figure 1-2. From these tests, Young's modulus, yield strength, and ultimate tensile strength are obtained. These parameters are valuable input parameters for FE analysis or numerical modeling. The stress strain curves obtained from as-received steel specimens also serve as a baseline for comparing stress-strain from the split Hopkinson pressure bar experiments.

Figure 1-2: MTS machine used for quasi-static tension and compression tests.

The quasi-static testing was done at room temperature on both the as-received steel and on post impacted samples. In order to obtain accurate results, specimen dimensions must meet ASTM standards when possible or otherwise be compared to other specimen geometries for validation. Figure 1-3 shows the tensile specimen dimensions for quasi-static testing.
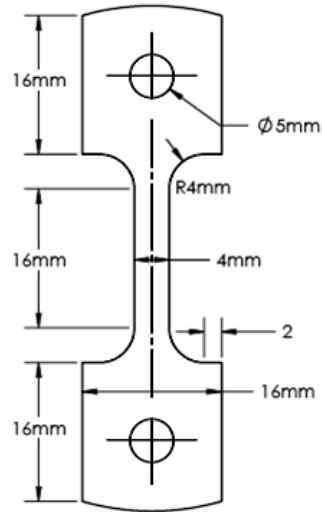
Figure 1-3: Specimens dimensions for monotonic quasi-static tensile testing. Thickness must be equal to or less than the gauge width of 4mm.

As shown in Figure 1-3, the gauge length of the specimen is 4x the width and the radius leading into the gauge section is at a radius equal to the width. The surfaces of the specimens were ground flat using conventional surface grinding methods to a final thickness of 4mm or less. The dimensions were chosen such that specimens could be extracted from discs which had previously been subjected to a shock load during plate impact experiments. A schematic of this is shown in Figure 1-4.
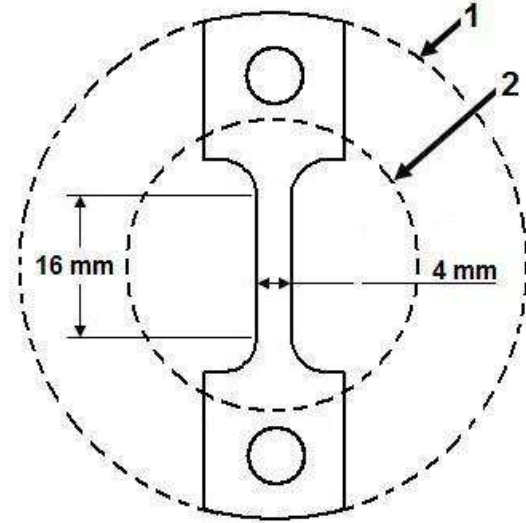
Figure 1-4: Tensile specimen extraction from plate impact disc (76.2mm diameter) after impact experiments. The gauge section is fully within the impacted region (44.5mm diameter).

The strain was measured using a MTS (model 632-13F-20) knife edge extensometer which has a gauge length of 10mm, as seen in Figure 1-5.

Figure 1-5: MTS model 632-13F-20 knife edge extensometer for quasi-static strain measurements in tension or compression.

The extensometer was attached to the gauge section of the specimen using spring clip attachments with half circles opposite the knife edge as shown in Figure 1-6. This extensometer can also be used for strain controlled actuation of the MTS machine. By doing so, the strain rate can be accurately set to the desired level which is retained throughout the entirety of the test. Strain rates for these tests were between 10^{-5} and 10^{-3} s^{-1}. Comparison of stress-strain curves between these two rates showed no appreciable difference; therefore for reducing test time, the higher rate of 10^{-3} s^{-1} was utilized.
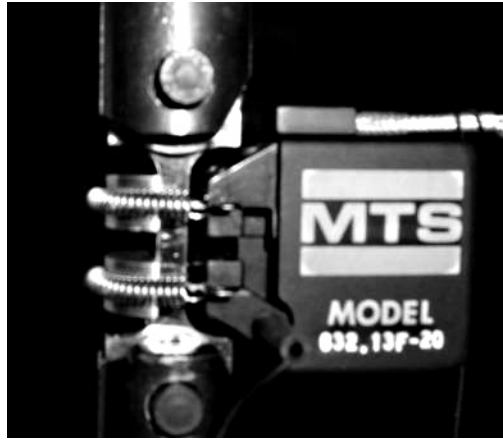
Figure 1-6: Tensile Specimen with knife edge extensometer attached for measuring strain

To check validity of the results, the stress-strain of the tensile specimens shown in Figure 1-3 were compared with stress-strain curves from circular cross section specimens with the gauge section dimension were 0.800in. in length and 0.250in. in diameter. A comparison of these curves is shown in Figure 1-7.
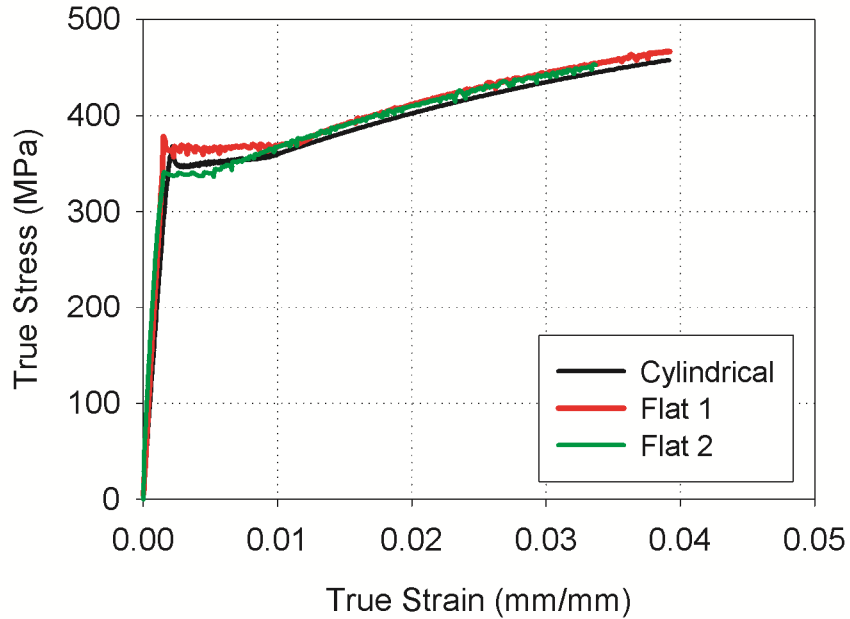
Figure 1-7: Comparison of stress-strain curves for validating results for tensile specimen dimensions. The cylindrical specimen had a gauge length and diameter of 0.800in and 0.250in, respectively. The flat specimens both had gauge length and width of 16mm and 4mm, respectively, with a thickness of just under 4mm.

As shown in Figure 1-7, two flat dog bone tensile specimens were compared with a cylindrical specimen. The yield point, elastic modulus, and hardening characteristics all coincide. Large variations in stress and strain data can occur when testing specimens that are dimensioned incorrectly and results must be checked before relying on the data for further use. As shown in Figure 1-8, four cylindrical compression specimens have been tested, each with different length to diameter ratios. In all tests, the surfaces of the specimens were surface ground flat to ensure parallelism between ends and to prevent bending. The surfaces of the specimen and grips were coated in graphite lubricant to reduce friction and barreling effects.
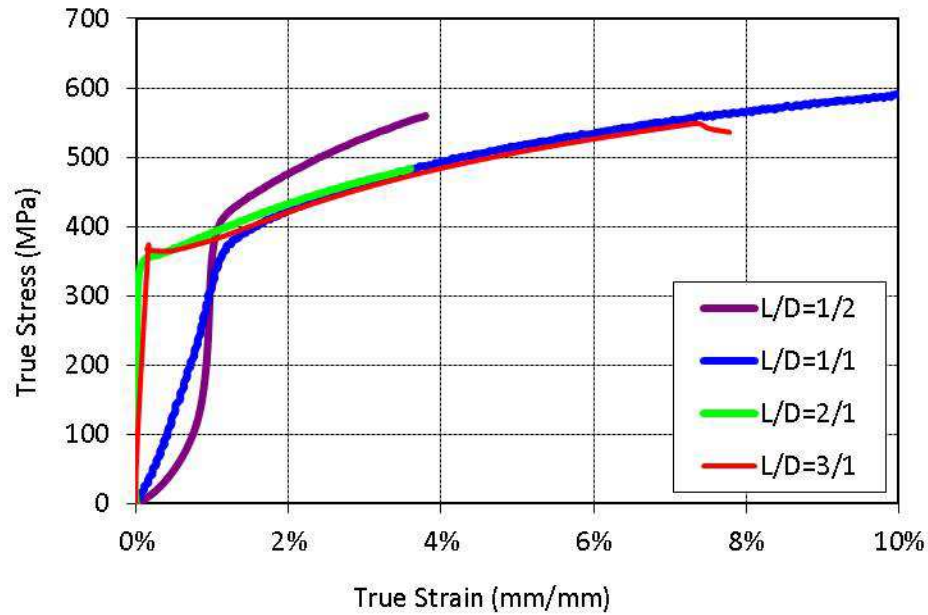
Figure 1-8: Compression tests of specimens with different length to diameter ratios.

As Figure 1-8 illustrates, the specimen length to diameter ratio significantly alters the elastic modulus of the material as well as the overall magnitude of the flow stress. Dimensional effects have been shown to influence the results in tensile tests by other authors as well [26]. The specimens with L/D ratios of 2:1 and 3:1 both have similar elastic modulus, yield strength, and hardening characteristics. The specimen with L/D ratio of 2:1 (green curve) was a specimen tested on an Instron screw driven machine while all others were tested on the MTS machine shown in Figure 1-2. This difference in the yielding behavior between the green and red curves is due to the Instron machine flexture and extracting the strain from the displacement output data of the load train as opposed to directly from a strain gauge or an extensometer attached to the specimen.

When running tension tests with an extensometer attached to the gauge section of the specimen, the machine can be controlled in strain control using the extensometer in a feedback loop or in displacement control using the MTS machines built in linear variable displacement transducer (LVDT). A comparison of the results from these tests is shown in Figure 1-9.
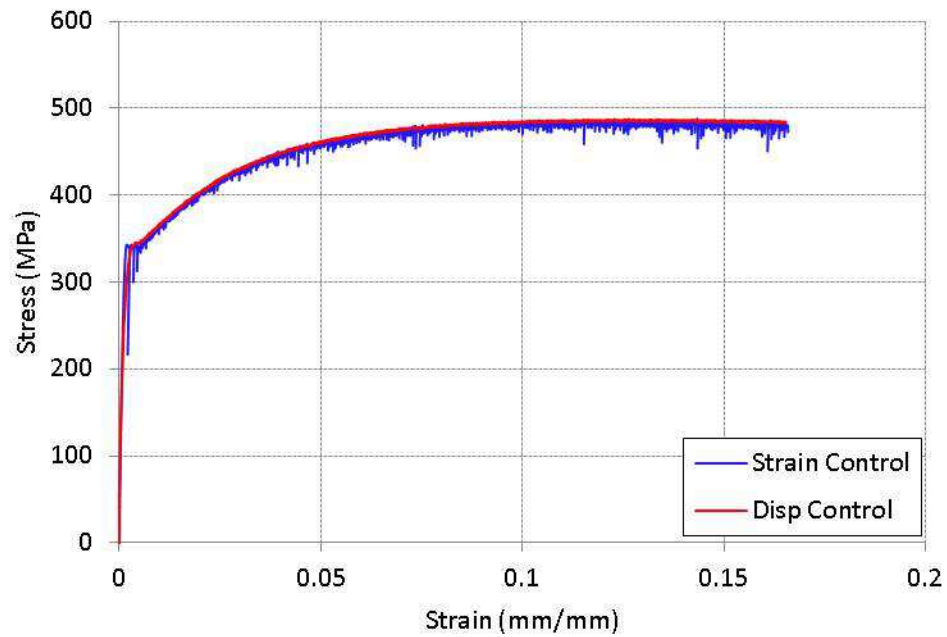
Figure 1-9: Comparison of tension tests run using strain control using the attached extensometer and displacement control using the machines built in LVDT.

As shown in the figure above, both tests provide accurate and comparable stress-strain curves of the steel. Strain control testing is advantageous in that the strain rate can be directly maintained during the entire experiment. Materials which are highly strain rate sensitive at low rates should be run in a strain controlled method. However, as shown in Figure 1-9 periodic load drops occur due to the sensitivity of the strain gauge and the

constant feedback to the LVDT to maintain that rate. The disadvantage of running in displacement control is that the strain rate will steadily increase during the duration of the experiment as the specimen is strained further. In Figure 1-9 the strain controlled specimen was maintained at a strain rate of 2E-5 s^{-1} throughout the entire test and the displacement controlled specimen had a strain rate ranging from 2E-5 s^{-1} up to 3E-5 s^{-1}. Within this strain rate range, this variation is not significant for this particular steel, however other materials with high strain rate sensitivity may be affected.

Direct comparisons can also be made between quasi-static compression and tension tests. Figure 1-10 shows the quasi-static stress-strain curves for a tension and compression test.
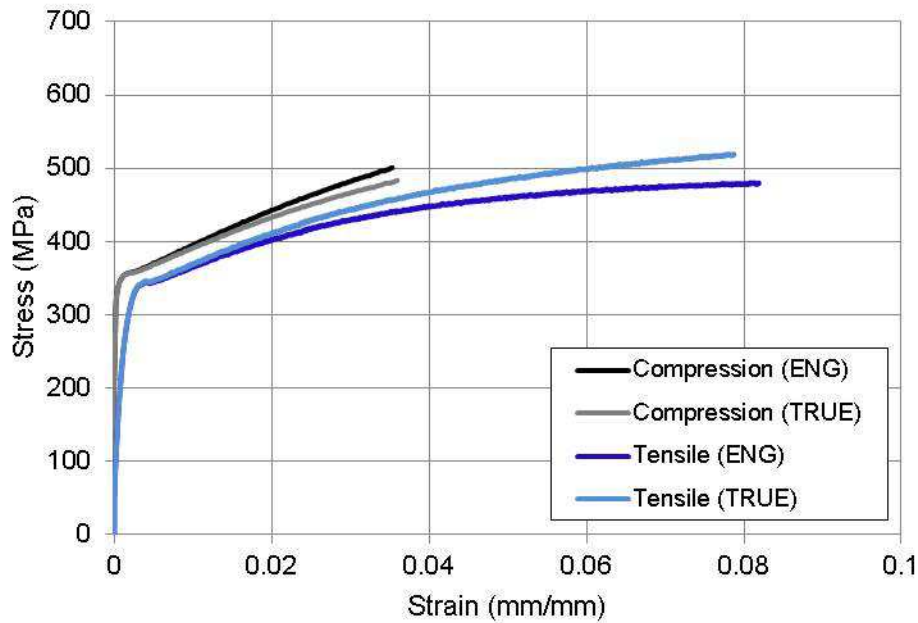
Figure 1-10: Comparison between quasi-static compression and tension stress strain curves in both engineering and true stress and strain.

The engineering stress and engineering strain are converted to true stress and true strain using the following equations

$$\varepsilon_{true} = \pm \ln\left(1 \pm \varepsilon_{eng}\right) \tag{1.8}$$

$$\sigma_{true} = \sigma_{eng}\left(1 \pm \varepsilon_{eng}\right) \tag{1.9}$$

where in tension the conversion utilizes the positive signs, and in compression the equations utilize the negative signs.

After conversion to true stress and true strain, the curves both exhibit similar hardening characteristics, despite the yield stress being slightly higher in the compression test. Results from the quasi-static testing are utilized in determining model parameters for constitutive modeling and material characterization in finite element simulation.

1.4.2.   **Dynamic Compression Testing (Intermediate Strain Rate)**

As defined previously, the intermediate strain rate range within this work will be between 10^2 and 10^4 s^{-1}. This range of strain rates can be achieved by utilizing a split Hopkinson pressure bar (SHPB). The SHPB has become widely accepted as being both accurate and repeatable and has become recognized as a standard piece of equipment in material testing laboratories. The earliest design iteration of the SHPB was made first by Bertram Hopkinson in 1913 [27]. Hopkinson presented a method by which the duration and pressure, therefore momentum, of an elastic pulse can be determined. His early design consisted of a long steel bar suspended horizontally by strings, with another short bar butted to the end. The wave in the long bar is produced by either a bullet or

detonation of gun-cotton. Upon detonation, an elastic wave travels through the long steel bar and passes into the short steel bar. The short bar is caught in a pendulum momentum trap. By varying the length of the short bar and measuring the pendulum movement, the maximum pressure and duration of the wave were deduced. This early design was revisited by Davies in 1948 [28] by adding condenser microphones to directly measure strain within the bars. In 1949 Kolsky [29] greatly improved upon the initial design by adding a second bar behind the specimen. The design improvements of Kolsky still exist in their basic form in modern SHPB apparatus with the exception of strain gauges and a light gas gun, which were first introduced by Krafft in 1954 [30]. Several modifications to the basic SHPB setup have been done since Krafft, including adaptation for tensile loading in 1968 [31], combined compression and torsion in 1973 [32], and for fracture dynamics in 1979 [33].

SHPB Design

A schematic of the SHPB apparatus showing its major components in shown in Figure 1-11. The striker, incident bar, and transmitted bar are all made of maraging 350 steel with a yield stress of 2GPa and a modulus of elasticity of 194GPa. The loading bars are 0.750 inches in diameter and have a length of 60 inches. It is important to maximize the length to diameter ratio of the loading bars in order to ensure that the axial stress distributes uniformly to ensure one dimensional wave propagation. The length to diameter ratio of the bars used in this work is 80, while some suggest that a minimum of 20 is required [34], the large ratio also prevents the incident pulse from overlapping.
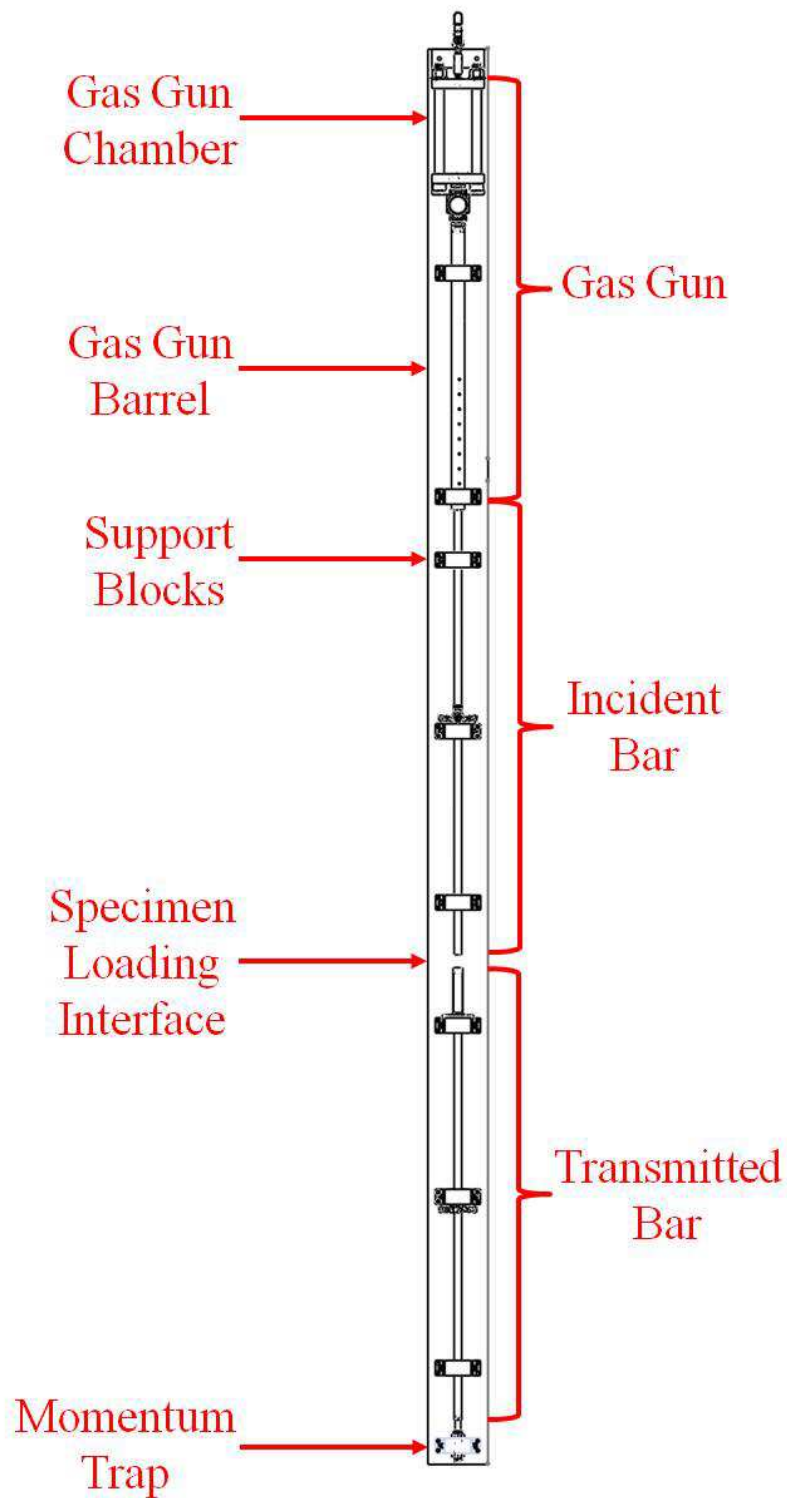
Figure 1-11: SHPB schematic showing major components of loading system: gas gun, incident and transmitted bars

The principle operation of a SHPB consists of elastic pulses in a set of loading bars which induce plastic deformation in the specimen. There are large amounts of literature describing in detail the SHPB design and theory [34-37].The SHPB consists of three main components; the gas gun, an incident bar and a transmitted bar, and additionally a data acquisition system. The gas gun is used to fire a striker bar at the incident bar, generating an incident compressive elastic strain pulse propagating towards the specimen. The magnitude of the pulse can be altered by changing the input pressure to the gas gun, thereby changing the striker velocity. The duration of the pulse can be altered by changing the length of the striker bar, which will also result in different levels of strain for a given strain rate. A graphical representation of the wave propagation during a SHPB compression test is shown in the time vs. distance diagram in Figure 1-12.
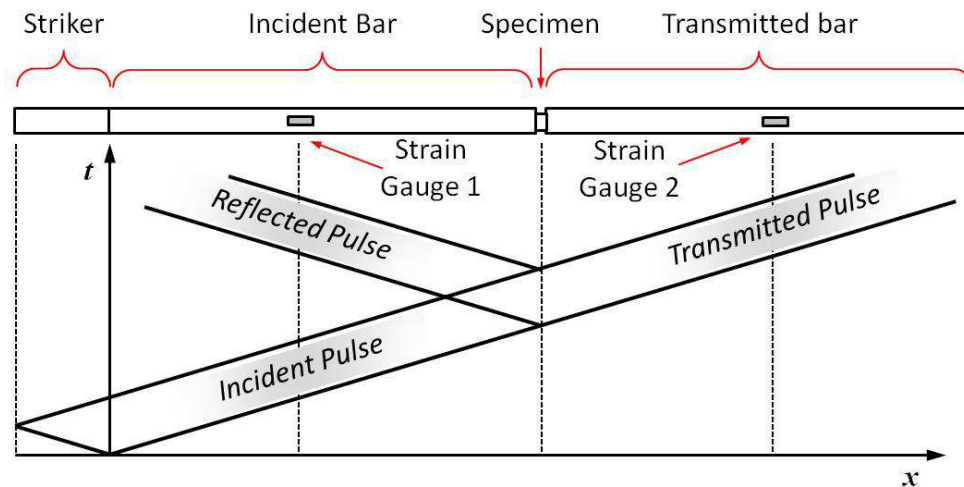
Figure 1-12: Time vs. distance diagram of the elastic wave propagation during a SHPB compression test. $\varepsilon_i, \varepsilon_r$ and ε_t represent the incident, reflected and transmitted pulses respectively.

As shown in Figure 1-12, when the striker contacts the incident bar, a compressive pulse propagates within the striker and incident bar. Upon reaching the free surface of the striker, the compressive pulse reverses sign and direction and travels back into the striker as a tensile release wave. This incident compressive strain pulse, ε_i, determined in duration by the length of the striker, travels through the incident bar to the specimen interface. Upon reaching the specimen, a portion of the incident pulse is reflected, ε_r, and a portion passes through the specimen and into the transmitted bar, ε_t. The amount of reflection and transmission are a direct result of the difference in impedance defined by the loading bars and specimen geometries and material properties. These three strains and impedance relationship can be derived in the following equations.

Governing Equations

The following equations are used to derive one dimensional motion of elastic wave propagation. The solution to the 1D wave equation will be the basis for the derivation of stress and strain of the specimen during compression tests using the SHPB apparatus. The elastic stress wave can be mathematically described by looking at a small section, dx, of the bar shown in Figure 1-13.
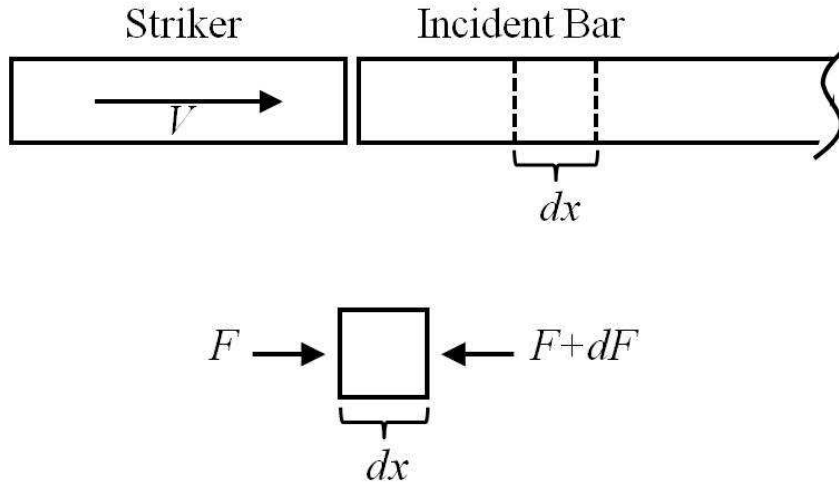
Figure 1-13: Differential area of the loading bar in the SHPB subjected to a force, F.

Newton's second law,

$$\sum F = ma \qquad (1.9)$$

where the sum of the forces, F, is equal to the mass, m, times the acceleration, a, can be applied to the condition in Figure 1-13, if we substitute the mass term with the differential distance along the bar, dx, whose area is A and density is ρ. Equation (1.9) can be rewritten as

$$-F + F + dF = \rho A dx a \qquad (1.10)$$

and since $F = \sigma A$, Equation (1.10) becomes

$$-\sigma + \sigma + \frac{\partial \sigma}{\partial x} dx = \rho dx a \qquad (1.11)$$

and after rearranging, it reduces to

$$\frac{1}{\rho}\frac{\partial\sigma}{\partial x}dx = a \tag{1.12}$$

The acceleration from Equation (1.12) can be rewritten in differential form as

$$\frac{1}{\rho}\frac{\partial\sigma}{\partial x}dx = \frac{\partial^2 u}{\partial t^2} \tag{1.13}$$

Since this is an elastic stress, Hooke's laws applies and the stress term can be written as

$$\sigma = E\varepsilon = E\frac{\partial u}{\partial x} \tag{1.14}$$

Substituting Equation (1.14) into Equation (1.13),

$$\frac{\partial^2 u}{\partial x^2}\frac{E}{\rho} = \frac{\partial^2 u}{\partial t^2} \tag{1.15}$$

The longitudinal elastic wave speed, C, is related to the elastic modulus and material density as

$$C = \sqrt{\frac{E}{\rho}} \tag{1.16}$$

which can be substituted into Equation (1.15) to result in

$$\frac{\partial^2 u}{\partial x^2}C^2 = \frac{\partial^2 u}{\partial t^2} \tag{1.17}$$

The second order partial differential, Equation (1.17), is the one dimensional wave equation [38] used to analyze elastic stress waves. D'Alembert's solution to the one dimensional wave equation is written as [39]

$$u(x,t) = f(x - Ct) + g(x + Ct) \tag{1.18}$$

where $u(x,t)$ is the displacement with the function $f(x - Ct)$ corresponds to a wave travel in the positive direction, and the function $g(x + Ct)$ corresponds to a wave traveling in the negative direction. As such, the displacement in the incident bar (designated by a subscript 1) , $u_1(x,t)$, and transmitted bar (designated by a subscript 2), $u_2(x,t)$, can be written as

$$u_1(x,t) = f(x - C_b t) + g(x + C_b t) = u_i + u_r \tag{1.19a}$$

$$u_2(x,t) = h(x - C_b t) = u_t \tag{1.20a}$$

where u_i, u_r, and u_t are the incident, reflected, and transmitted particle displacements, respectively and C_b represents the longitudinal wave speed in the bars, which is equivalent in the incident and transmitted bars. The strain in the bars can be derived by differentiating Equations (1.19a) and (1.20a) with respect to distance, written as

$$\varepsilon_1(x,t) = \frac{\partial u_1}{\partial x} = f'(x - C_b t) + g'(x + C_b t) = \varepsilon_i + \varepsilon_r \tag{1.19b}$$

$$\varepsilon_2(x,t) = \frac{\partial u_2}{\partial x} = h'(x - C_b t) = \varepsilon_t \tag{1.20b}$$

The particle velocity, U, can be derived by differentiating Equations (1.19a) and (1.20a) with respect to time, written as

$$U_1(x,t) = \frac{\partial u_1}{\partial t} = -C_b f'(x - C_b t) + C_b g'(x + C_b t) = C_b(-\varepsilon_i + \varepsilon_r) \qquad (1.19c)$$

$$U_2(x,t) = \frac{\partial u_2}{\partial t} = -C_b h'(x - C_b t) = -C_b \varepsilon_t \qquad (1.20c)$$

The forces acting on the bars can be written as

$$F_1 = A_b \sigma_1 = A_b E_b \varepsilon_1 = A_b E_b (\varepsilon_i + \varepsilon_r) \qquad (1.21)$$

$$F_2 = A_b \sigma_2 = A_b E_b \varepsilon_2 = A_b E_b \varepsilon_t \qquad (1.22)$$

where the subscript b denotes properties of the loading bars. Once the incident bar, specimen, and transmitted bar reach a state of equilibrium, the force in the incident bar, F_1, and transmitted bar, F_2, are considered equal, thus

$$\varepsilon_t = \varepsilon_i + \varepsilon_r \qquad (1.23)$$

These three pulses are measured using a set of strain gauges mounted on each loading bar. The strain gauges are connected to a signal conditioning amplifier (Vishay 2310B) which controls the excitation voltage of the gauges and amplifies the signal. The voltages are recorded using a high speed digital oscilloscope. A more detailed description of the apparatus can be found elsewhere [40]. A typical record is shown in Figure 1-14.
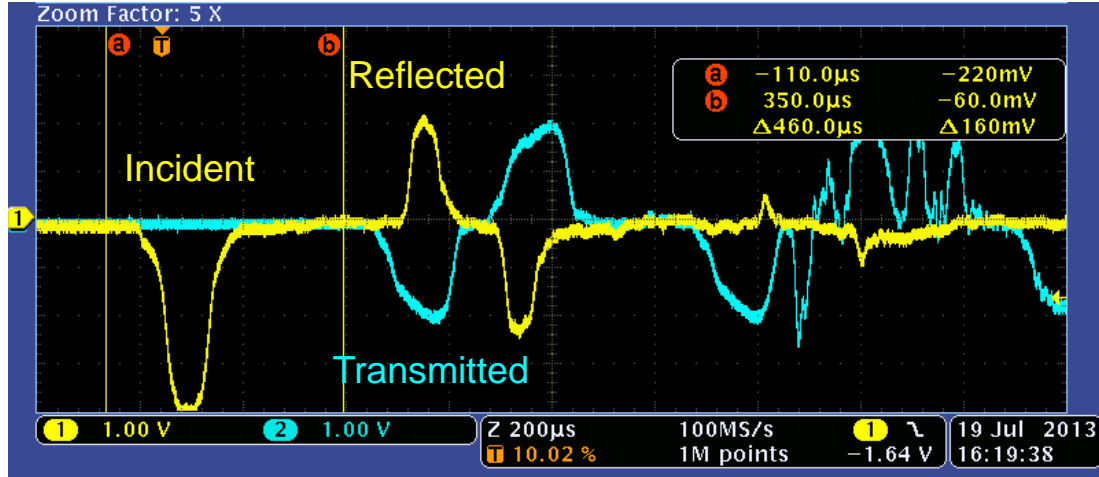
Figure 1-14: Typical strain gauge record from a SHPB compression test. The yellow curve is the record from the strain gauge mounted on the incident bar and the blue curve is the record of the strain gauge mounted on the transmitted bar.

Since the forces in the bars are in equilibrium across the specimen, the stress in the specimen can be equated to either Equation (1.21) or (1.22), written as

$$F_2 = F_s \rightarrow A_b \sigma_2 = A_s \sigma_s \rightarrow \sigma_s = \frac{A_b \sigma_2}{A_s} \rightarrow \sigma_s = \frac{A_b E_b \varepsilon_t}{A_s} \tag{1.24}$$

where the subscript s denotes the specimen. The strain rate in the specimen can be described as

$$\dot{\varepsilon}_s = \frac{\frac{\partial u_s}{\partial x}}{\partial t} = \frac{\frac{\partial u_s}{\partial t}}{\partial x} = \frac{U_1 - U_2}{l_s} \tag{1.25}$$

where the l_s is the length of the specimen. Substituting Equations (1.19c), (1.20c), and (1.23) into Equation (1.25), the strain rate in the specimen can be rewritten as

$$\dot{\varepsilon}_s = \frac{2 c_b \varepsilon_r}{l_s} \tag{1.26}$$

31

Integrating Equation (1.26) leads to the expression for strain in the specimen, written as

$$\varepsilon_s(t) = \frac{-2c_b}{l_s} \int \varepsilon_r(t)\, dt \qquad (1.27)$$

The amplitude of the stress can also be determined using the conservation of momentum which states that impulse is equivalent to the change in momentum, written as

$$F dt = d(mU) \qquad (1.28)$$

where U is the particle velocity. The force and mass terms can be rewritten as

$$\sigma A dt = d(\rho A dx U) \qquad (1.29)$$

and simplifying leads to

$$\sigma = \rho C U \qquad (1.30)$$

For the case where the striker and incident bar are of the same material, U is half the impact velocity. Again, equating the forces, an impedance match between the bars and specimen can be described as

$$F_b = F_s \rightarrow \rho_b C_b U_b A_b = \rho_s C_s U_s A_s \qquad (1.31)$$

Assuming that the particle velocities must also be equivalent, $U_b = U_s = U$, since they are in intimate contact at all times, the equation reduces to

$$\rho_b C_b A_b = \rho_s C_s A_s \qquad (1.32)$$

When this equation holds true, there will be a continuous passage of the wave between media. If the equation is not equivalent, then wave reflections are definite.

Equations (1.30) through (1.32) are useful when setting up SHPB experiments for estimating the specimen stress based on striker velocity and to ensure that the stress does not exceed yield strength of the loading bars. Since the particle velocity is half the striker velocity, the specimen stress can be written in terms of striker velocity, V, as

$$\sigma_s = \frac{\rho_b C_b A_b}{2A_s} V \tag{1.33}$$

The impedance matching in Equation (1.32) is particularly important when dealing with low or high temperature setups, discussed in more detail below.

Low and High Temperature Testing

When running SHPB compression tests at low or high temperatures, a set of tungsten bars is inserted between the loading bars and the specimen. This configuration ensures that minimal heat transfer occurs into the loading bars, thus keeping the properties constant. A picture of the tungsten inserts mounted between the loading bars is shown in Figure 1-15. Prior to testing, the specimen is held in place by the tungsten insert bars. The tungsten bars are heated along with the specimen and are not in contact with the incident and transmitted bars. Upon firing, a pneumatic actuator moves the incident and transmitted bars into position so that contact is made with the heated tungsten bars for only several milliseconds prior to loading.
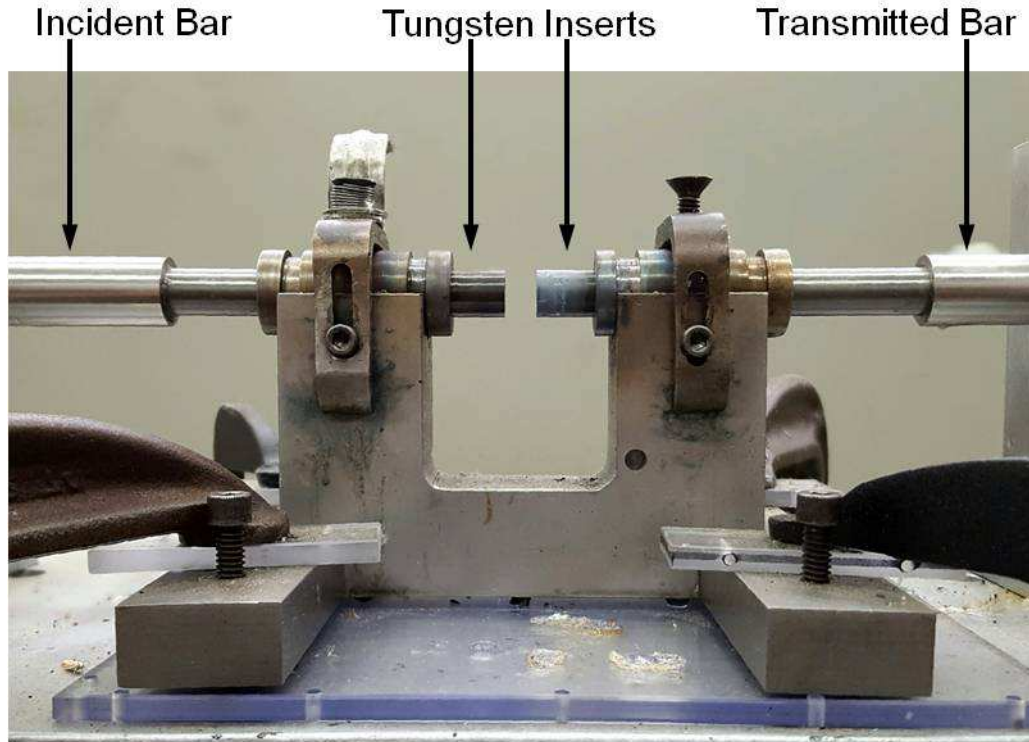
Figure 1-15: Tungsten insert setup mounted between loading bars on the SHPB for compression testing at low or high temperatures. The tungsten bars create a barrier between the incident and transmitted bars, which are used to measure strain and must have known constant properties.

The diameter of the tungsten inserts is an important consideration in order to prevent unwanted wave reflections at the tungsten insert/loading bar interface and achieve accurate results. The loading bars and tungsten bars must have an equivalent impedance [41], such that $\rho_T c_T A_T = \rho_M c_M A_M$, where the subscripts T and M represent the tungsten inserts and the maraging steel loading bars, respectively. Since the tungsten carbide bars are extremely difficult to machine, it is best to acquire a sample of the material prior to ordering specific dimensions so that accurate measurements of waves speeds can be done and the bar diameters can be obtained without additional in house grinding operations.

The longitudinal and shear waves speeds presented in Table 1 were measured using a nondestructive ultrasonic wave reflection technique, whose method is described elsewhere [42,43].

Table 1-1: Elastic constants of A572 Grade 50 low carbon steel.

Using Ultrasonic Wave Technique			
Material	Maraging	Tungsten	A572
$C_{longitudinal}$ (m/s)	5767	6790	5950
C_{shear} (m/s)	3035	4080	3255
Poissons Ratio	0.31	0.22	0.29
Youngs Modulus (Pa)	1.94E+11	5.85E+11	2.13E+11
Shear Modulus (Pa)	7.43E+10	2.40E+11	8.28E+10
Bulk Modulus (Pa)	1.69E+11	3.45E+11	1.66E+11
Density (kg/m^3)	8065	14431	7814

From the longitudinal and shear wave speeds in addition to the density, Poisson's ratio, v, Young's modulus, E, Shear modulus, G, and Bulk modulus, K, can be determined using the following relations, respectively

$$v = \frac{1 - 2\left(\frac{C_S}{C_L}\right)^2}{2 - 2\left(\frac{C_S}{C_L}\right)^2} \tag{1.34}$$

$$E = \frac{C_L^2 \rho (1+v)(1-2v)}{(1-v)} \tag{1.35}$$

$$G = C_S^2 \rho \tag{1.36}$$

$$K = \frac{E}{3(1-2v)} \tag{1.37}$$

For testing at low temperatures, a basin for filling with liquid nitrogen was fitted in the tungsten bar holder, as shown in Figure 1-16. Using this method, specimen temperature is decreased to approximately 77K.
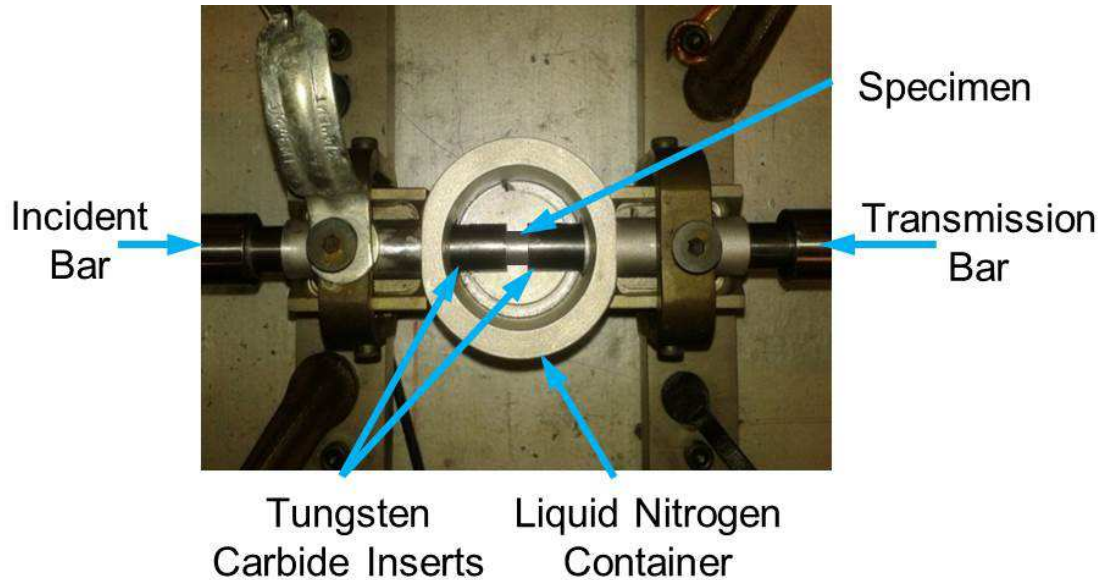
Figure 1-16: Low temperature setup on SHPB for compression testing at liquid nitrogen temperatures. The tungsten bars create a barrier between the incident and transmitted bars, which are used to measure strain and must have known constant properties.

An induction heating system is fitted to the SHPB for high temperature testing which was done up to temperatures of 923K. Specimen temperature was monitored using K-type thermocouple wires pinch welded to the outer diameter of the tungsten close to the specimen interface.

Typical SHPB Compression Test Results

Again, specimen dimensions are of utmost importance. For SHPB compression testing, the specimen should meet certain requirements for accurate results. Smaller

specimens are recommended in order to minimize the radial inertia, which is proportional to the square of the specimen radius, more details of which have been previously outlined [34]. The inertia effects are eliminated when the specimen length to diameter aspect ratio is chosen as

$$L/D = \sqrt{\frac{3v}{4}}$$
(1.38)

where Poisson's ratio, v, assumed to be equal to 0.333, results in a L/D ratio of approximately 0.5 [44]. Specimen L/D ratios were kept to 0.5 in this study, while it has been suggested that the rate of change of energy within the specimen would imply that the optimal L/D ratio is equal to $\sqrt{3/4}$ to reduce axial and radial inertia [45]. The final length of the specimen was achieved by surface grinding to ensure planar surfaces and parallel contact with the loading bars. Specimen surfaces were coated with graphite lubricant to reduce friction and prevent barreling of the specimen. When using the tungsten bars, specimen dimensions were approximately 0.3750 in. in diameter and 0.1875 in. in length.

The diameter was maintained close to 80% of the mating bar diameter to reduce the effects of radial and longitudinal inertia and friction [46] and reduce the impedance mismatch. Shorter length specimens also have the advantage of reaching equilibrium in shorter time periods. One way in which the loading condition in the specimen can reach steady state quicker, is to reduce oscillations in the load train by implementing a pulse shaper between the striker and incident bar. It has been shown that this can promote sample equilibrium faster than steep square pulses [47]. Pulse shapers in this study were made of aluminum 6061.

The record of the strain gauge voltages is captured using a high speed digital oscilloscope. One channel is used for the incident bar strain gauge, recording the incident and reflected pulse, and a second channel is used for the transmitted bar strain gauge, recording only the transmitted pulse. These voltage signals are stored as .csv files and transferred to the computer via a USB storage device. Data analysis consists of three separate matlab programs; Read_Data_SHPB.m, Clean_strain_pulses.m, and Calculate_Specimen_Stress_Strain_SHPB.m which are available in the appendix section. The first program, Read_Data_SHPB.m, reads the raw data, which contains time and voltage, and coverts the voltage into strain. The strain as a function of voltage is written as

$$\varepsilon = \frac{4V}{V_s G_C (GF)} \qquad\qquad (1.39)$$

where V is the measured voltage, V_s is the supplied voltage from the strain gauge amplifiers, G_c is the gain applied by the amplifier, and GF is the gauge factor, which is 3.3 for these particular gauges. The gain can be adjusted to amplify the signal to increase the voltage signal for lower rate testing or reduce the signal for higher rate testing in order to keep the signal within a desired range. The program outputs three separate text files containing line by line, time and strain, for each pulse; incident, transmitted, and reflected.

After the raw voltage signals are converted to strains, a second program is utilized, Clean_strain_pulses.m, which reads, line by line, the three text files generated from the first program. This program takes a running average of data points (smoothing) in order to smooth the high frequency oscillations inherent in the test and then reduces the number

of data points (blocking). Again, the program outputs three text files for each of the three separate strain pulses.

The third matlab program used for data analysis, Calculate_Specimen_Stress_Strain_SHPB.m, first aligns the incident, transmitted, and reflected strain pulses using a standard deviation method. Secondly, it calculates the stress, strain rate, and strain of the specimen, utilizing equations (1.24) (1.26), and (1.27) respectively, and required inputs of the specimen dimensions. A typical oscilloscope record of the strain gauge signals is shown in Figure 1-17.
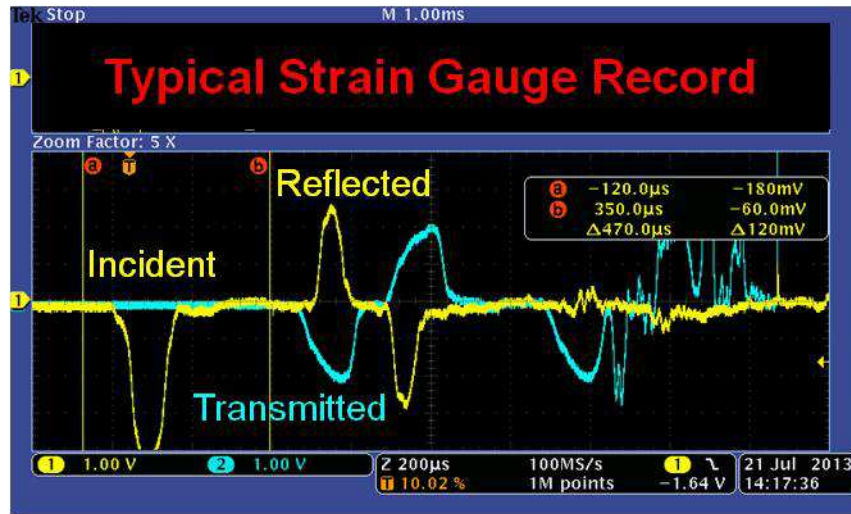
Figure 1-17: Typical record of voltage outputs from strain gauges mounted on the incident and transmitted bars of the SHPB. Note that the compressive incident and transmitted pulses are negative and the tensile reflected pulse is positive.

Note that the incident and transmitted pulse are recorded as negative voltages and the reflected pulse is positive. This is because the strain gauge registers compressive strains as negative and tensile strains as positive. These voltage signals are converted to strains,

smoothed and blocked, and aligned using the three matlab programs. Figure 1-18 shows

the alignment of the smoothed and blocked strain pulses.
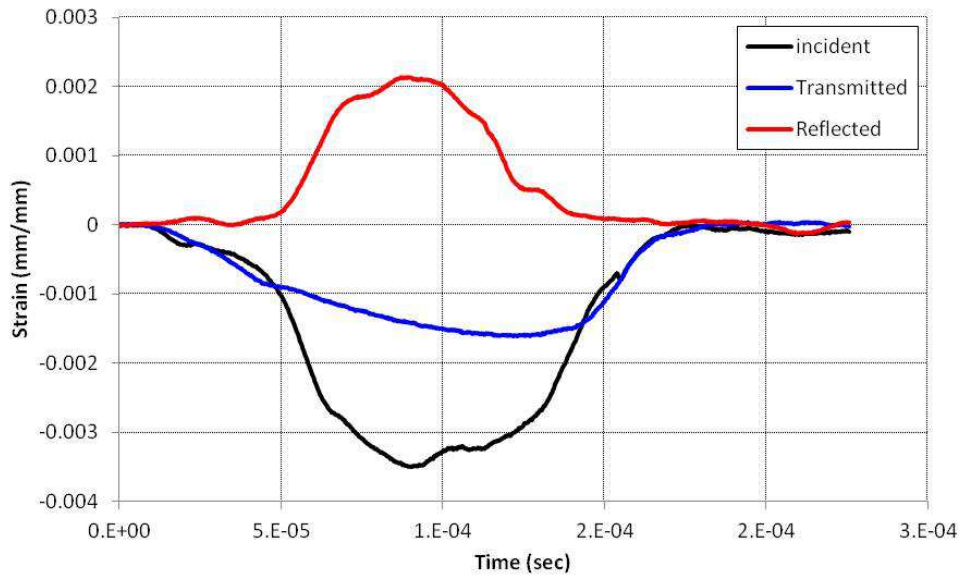
Figure 1-18: Alignment of the three strain pulses during a SHPB compression test.

To facilitate the alignment process, the reflected strain pulse can be compared with
the transmitted minus the incident strain pulse, as these are equivalent, as seen in
Equation (1.23), paying attention to the leading edge of the pulses, as shown in Figure
1-19.
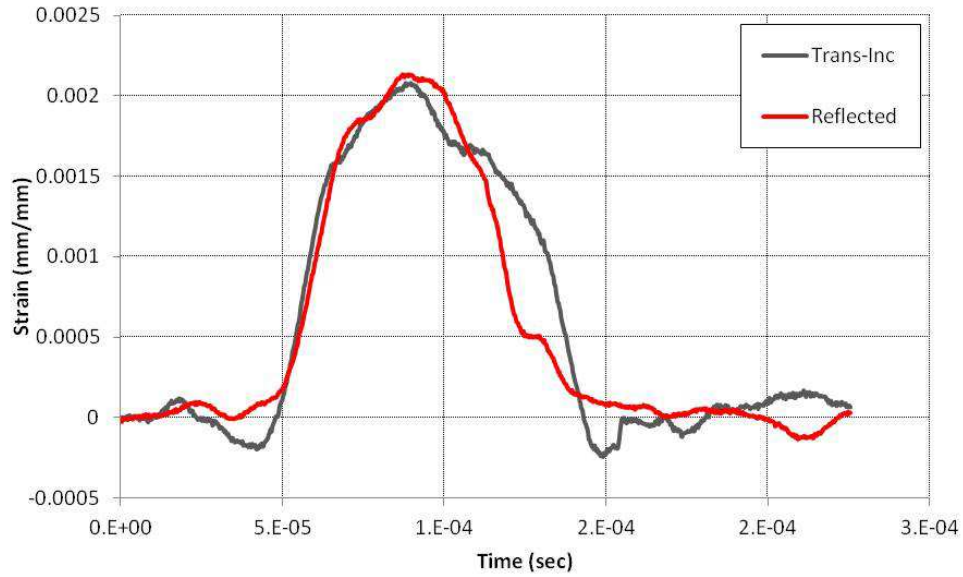
Figure 1-19: Alignment of the reflected strain pulse (red) and the transmitted pulse minus the incident strain pulse (grey). Good alignment is achieved when the leading edges of the pulses are coincident.

The strain rate for this test is determined by fitting a straight line to the strain vs. time data, as shown in Figure 1-20.
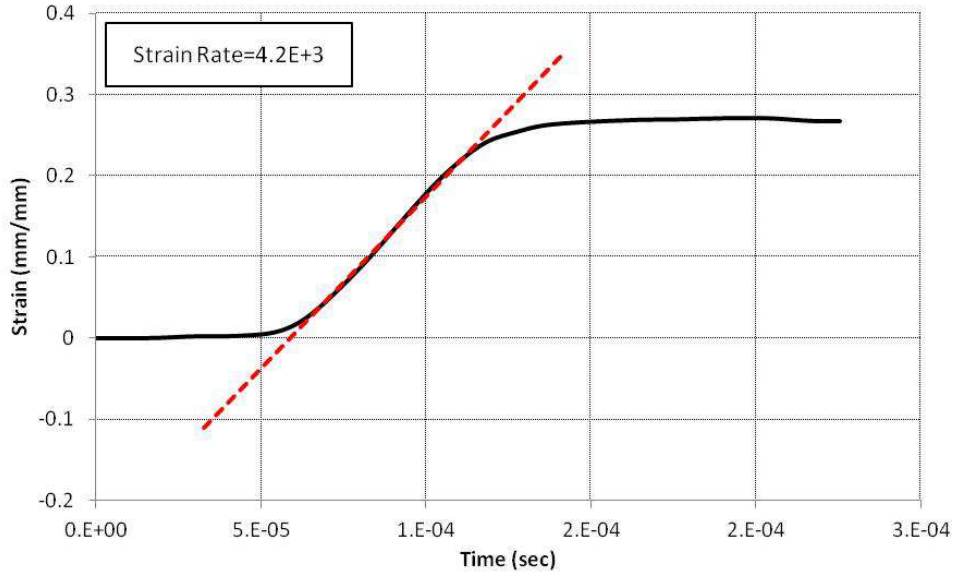
Figure 1-20: Specimen strain vs. time plot from which the strain rate can be determined by linear curve fitting.

After aligning the strain pulses, the strain and stress can be determined using Equations (1.27) and (1.33) and results can be plotted. Figure 1-21 shows a typical stress-strain curve before (red) and after (black) smoothing and blocking procedures.
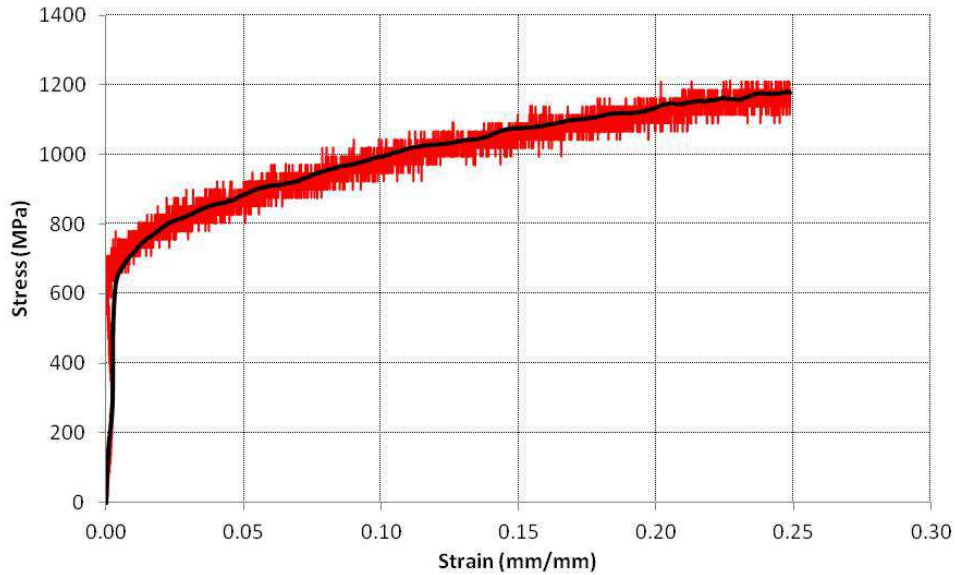
Figure 1-21: Stress vs. strain curves of a typical SHPB compression test. The red curve is the raw stress-strain data, and the black curve is the smoothed and blocked stress-strain data.

The dynamic compression tests using the SHPB result, in general, in a spread of data. While the testing apparatus may be completely sound in operation, the results really come down to the data analysis. After importing the raw data and converting the measured voltage vs. time to strain vs. time, all three strain pulses must be aligned. The alignment time of each pulse is adjusted so that the onset of the deviation from zero strain in all three pulses occurs at the same time. Alternatively, the slope of the leading edge of the reflected strain pulse (ε_r) can be aligned with the slope of the leading edge of the transmitted minus the incident (ε_t-ε_i). Problems arise because of inherent vibrations in the bars resulting in a somewhat noisy signal prior to the actual strain pulse. The time that the actual strain pulse begins can be difficult to determine. Small adjustments in the pulse time (~1-2 μs) can lead to variations in the overall level of the stress-strain curve.

Because of this, it is best to run multiple SHPB tests and take an average of the results. This will provide confidence and undisputable validity to the experimental results. Figure 6-1 shows three stress-strain curves of compression tests. The strain rates varied between 4.4E+3 s^{-1} to 4.8E+3 s^{-1}, however overlapping of all three curves occurs.
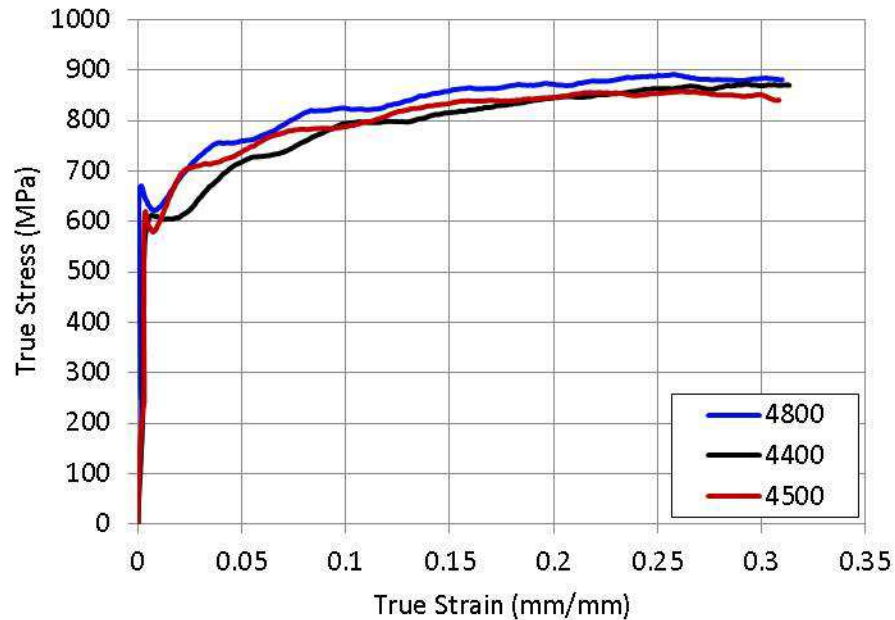
Figure 1-22: Three true stress-true strain curves of compression tests at room temperature using the SHPB.

For averaging the results into one single curve, the data is first compiled into a single data set of stress and strain, and then sorted by increasing strain using the built in sort feature in excel. This is plotted as a single curve, and a polynomial trend line is fitted to the data, as shown in 6-2.
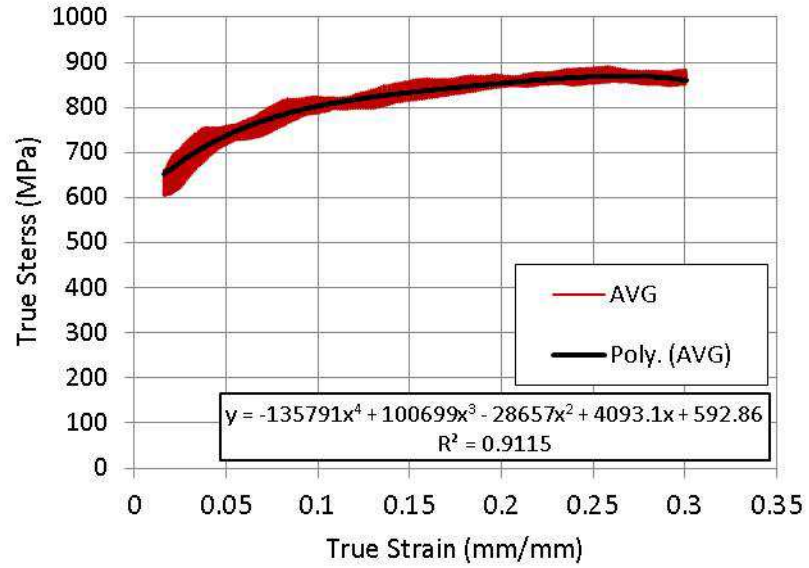
Figure 1-23: All three stress-strain data as a single data set with a polynomial curve fit of the plastic portion.

As shown in Figure 6-3 the trend line is plotted with the original three stress-strain curves, with an average strain rate of 4.6E+3 s^{-1}. The red trend line shown should be utlitzed for data analysis and modeling purposes.
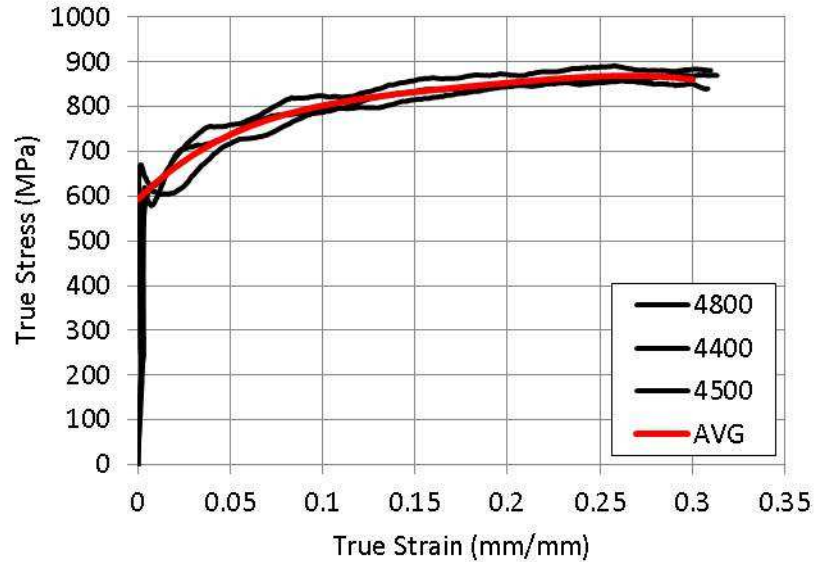
Figure 1-24: Averaged stress-strain curve plotted with the original three curves.

1.4.3. **Dynamic Compression Testing (High Strain Rate)**

Impact loading of steel is a subject that has been studied widely; it has been established that high strain rate loading of steel will result in a change of both the microstructure as well as the mechanical properties which individually affect the residual life of the material. Research has also been performed to assess blast loading and deformation effects, particularly those of low carbon steel, which is considered a primary reinforcing phase of civil structures. Furthermore, research in shock wave analysis, while in general utilizes the finite element method to provide solutions for the dynamic response of the structures [39], requires implementation of microstructure constitutive models to accurately capture changes in mechanical properties during high strain rate loading. Various techniques are being used to provide these models with material input parameters and allow for the recovery of previously impacted specimens suitable for

46

further analysis; see reviews by Field et al. [1] and Ramesh [2]. These techniques include drop weight testing, split Hopkinson pressure bar (SHPB), Taylor impacts, plate impacts, and explosive loading. In these tests, SHPB produces elastic-plastic wave propagation, with maximum strain rates typically up to the range of 10^4 s^{-1}.

To reach strain rates greater than 10^4 s^{-1}, explosives, laser pulse techniques, and plate impacts are utilized. The outcome of these high rate experiments are typically used for obtaining Hugoniot curves, measuring spall strength, post impact mechanical testing, and measuring phase change, the latter two of which are of concern in this work. Using explosives has the advantage of being directly measureable in a TNT equivalent scale, however requires difficult acquisition of explosives and special facilities to accommodate their detonation which for some, is not always feasible. Laser induced shock loading has several advantages and disadvantages. One advantage is that the pulse duration is easily adjustable down to the picoseconds range. The second advantage is that the stress levels can reach to the 100 GPa range, which is not achievable by other methods. Laser pulse shock loading however has a disadvantage in that the laser diameter is extremely small and limits the user to only post-impact imaging, and closes the door for further specimen extraction for further testing. The most common type of shock loading tests conducted are flyer plate impact experiments using a light gas gun system. The flyer plate is driven down a barrel by the release of compressed gas and impacts a target disc. The target disc is normal to the projectile path. The impact of the projectile against the target produces a shock wave within the material which is often measured using manganin stress gauges bonded between the target and a backing plate, as shown in Figure 1-25.
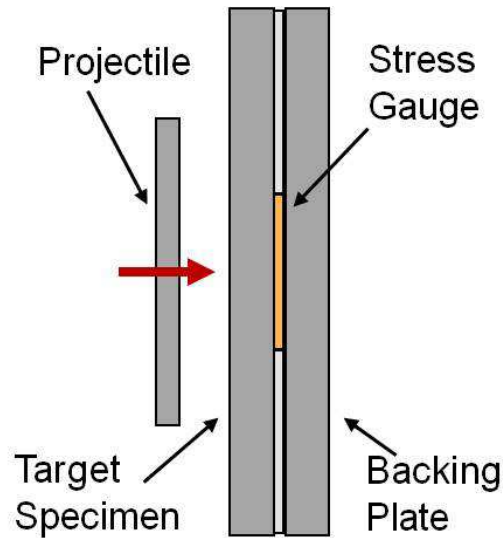
Figure 1-25: Schematic of a normal and planar plate impact configuration with a stress gauge bonded between the target specimen and a backing plate.

The shock loading tests used in this study were conducted using a single stage light gas gun (SSLGG) and are considered "symmetric" plate impacts experiments. This describes a plate impact test that utilizes the same material for the projectile and target, such that the stress wave propagation in both the projectile and the target travel at the same speed and amplitude, and are thus symmetric and identical.

Prior to impact, all the particles in the projectile have a velocity equal to the launch velocity, V, which is measured with lasers perpendicular to the barrel just before impact. Upon impact with the target, the particle velocity in the projectile is reduced, and the particle velocity in the target (initially at rest) is increased until the particle velocity in both the projectile and target are equal, as shown in Figure 1-26. In the case of a symmetric impact, the stresses are also equal.
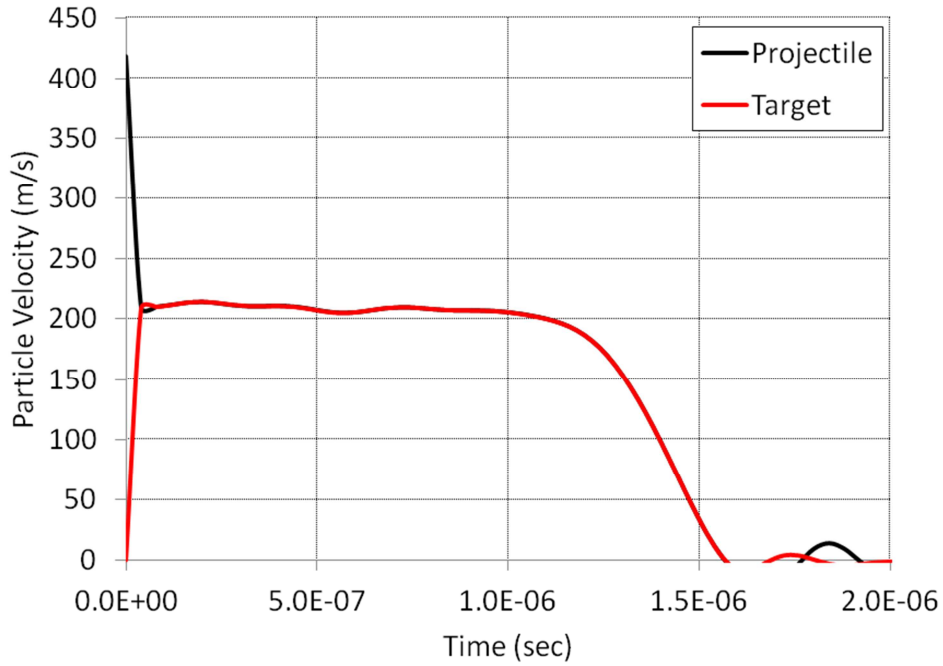
Figure 1-26: Particle velocity profiles generated from finite element simulation of a plate impact at 418 m/s

This rapid increase in particle velocity produces a compressive elastic wave, and if the magnitude is sufficiently high to induce plastic deformation, it is followed by a compressive plastic wave propagating both in the projectile and the target in equal and opposite directions. Figure 1-27 shows the longitudinal wave propagation diagram for a symmetric plate impact experiment.
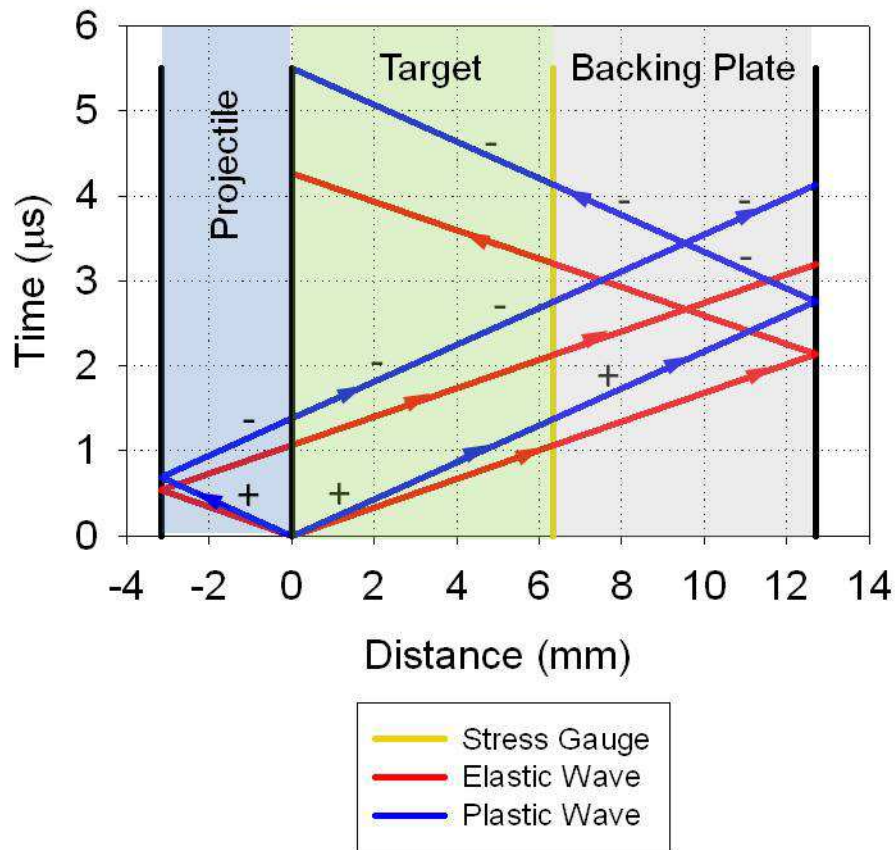
Figure 1-27: Lagrangian time-distance wave propagation diagram for symmetric plate impact experiments. The yellow line shown in the legend designates the interface between the target and backing plate where the stress gauge is bonded. The red lines are the elastic waves and the blue lines are the plastic waves. Positive and negative signs designate compressive (+) and tensile (-) waves.

As Figure 1-27 shows, at the projectile and target interface (*x=0*) starting from time zero, a compressive elastic and plastic wave propagate into the projectile and target, designate by red and blue lines with "+" signs, respectively. The back surface of the projectile is typically supported by a low impedance plastic or foam or freely supported by air. This lower impendence interface or free surface causes the compressive wave to reverse signs as it reflects back into the projectile traveling now as a tensile wave

bringing the stress state back to zero [39]. As shown in Figure 1-27, the duration of the stress pulse can be altered by varying the thickness of the projectile, d. The stress wave duration can be approximated as [39]

$$t_d = \frac{2d}{U_s} \tag{1.40}$$

As the initial compressive wave passes through the target and back plate, it is followed by the tensile release wave generated from the back surface of the projectile. Upon reaching the free surface of the backing plate, the initial compressive wave reflects as a tensile wave. These two tensile waves, will cross paths at a location determined by the impactor and target/backing plate thicknesses, and create a state of tension along that plane. This will typically result in an internal tensile failure of the material known as spall fracture. An example of the fracture is shown in Figure 1-28.

Figure 1-28: Spall fracture in the backing plate from a plate impact test at 12 GPa.

The experiments within this work were designed such that the spall fracture always occurs within the sacrificial backing plate such that the target plate can be used for post impact analysis.

A stress wave generated by planar symmetric plate impact typically has a generally square pulse shape with several distinct features as depicted in Figure 1-29.
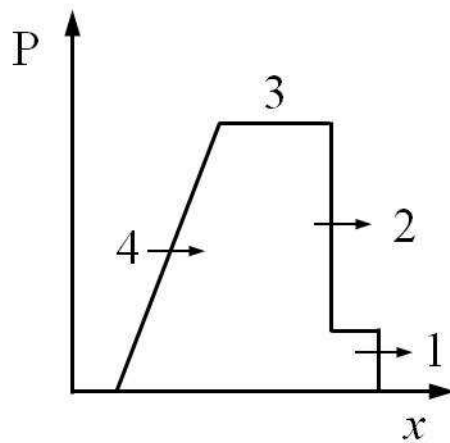
Figure 1-29: Schematic of a shock wave generated in a plate impact test with several distinct features; 1. elastic wave front; 2. plastic wave front; 3. peak pressure duration; 4. release portion of wave.

The simplified wave shown in Figure 1-29 is led initially by an elastic precursor wave, 1, travelling at the longitudinal wave speed. The amplitude of the elastic precursor is the dynamic elastic limit of the material. In a uniaxial strain state, the amplitude of transition into plastic deformation during compressive loading is called the "Hugoniot Elastic Limit" (HEL). The HEL is related to the maximum resolved shear stress though the relation [2,7,48]

$$\sigma_{HEL} = \left[\frac{1-\nu}{1-2\nu} \right] 2\tau \qquad\qquad (1.41)$$

The HEL is clearly shown in the experimental stress-time plots shown in Figure 1-30 for two tests at different impact velocities.
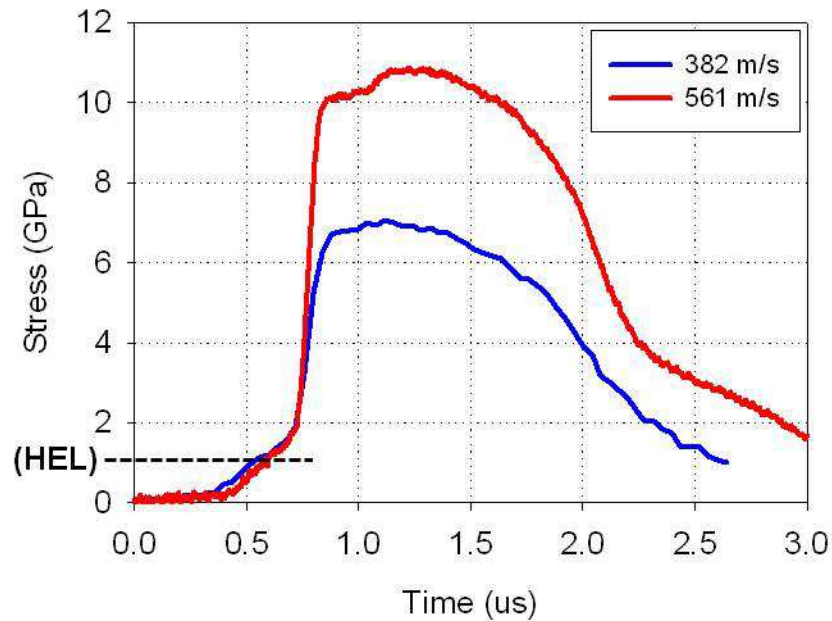
Figure 1-30: Stress history of two impacts at velocities of 382 m/s and 561 m/s.

The curves shown in Figure 1-30 had peak amplitudes of approximately 7 GPa and 11 GPa, yet both exhibit the same amplitude HEL of approximately 1 GPa. However, it has been shown that the HEL amplitude does decay with distance within the specimen [7,39]. Following the elastic precursor, a plastic wave front, 2, is generated which travels at the shock velocity, U_s, of the material of which the peak stress duration, 3, is controlled by the projectile thickness. This pressure pulse is brought back to a state of zero stress by the trailing release wave, 4. Other researchers have developed methods which alter this

profile, for shockless high pressure impacts, known as isentropic compression experiments (ICE), in an effort to reduce temperature rise during shock loading by the use of functionally graded impedance impactors [49-51].

Starting with the conservation of momentum, the maximum impact pressure, P, can be described as a function of the shock velocity, U_s, and particle velocity, U_p, written as

$$P_1 = \rho_{o1} U_{s1} U_{p1} \tag{1.42a}$$

$$P_2 = \rho_{o2} U_{s2} U_{p2} \tag{1.42b}$$

The shock velocity is defined by the well known equation of state (EOS) which relates the shock velocity, U_{s1} to the particle velocity, U_{p1},

$$U_{s1} = C_{b1} + S_1 U_{p1} \tag{1.43a}$$

$$U_{s2} = C_{b2} + S_2 U_{p2} \tag{1.43b}$$

where C_b is the bulk wave speed and S is an empirical constant, and the subscripts 1 and 2 represent the projectile and target, respectively. Utilizing Equations (1.42-1.43) the impact pressure can be calculated from the particle velocity. Since the projectile and target are made of the same materials in this study, these equations can be simplified by equating several variables, where $C_{b1} = C_{b2} = C_b$, $\rho_{o1} = \rho_{o2} = \rho_o$, and $S_1 = S_2 = S$, and the target is initially at rest so that $U_{p2} = 0$. Substituting Equations (1.43a) and (1.43b) into (1.42a) and (1.42b) and setting $P_1 = P_2$, the particle velocity in the projectile and target are

$$U_p = \frac{1}{2}V \tag{1.44}$$

which shows that, for a symmetric impact, the particle velocity is exactly half of the initial projectile velocity. Further details of this derivation are provided by Meyers [39]. The projectile velocity can then be directly related to the stress using Equations (1.42) and (1.44). This can be shown graphically by plotting in a stress-particle velocity space, as shown in Figure 1-31. An extensive amount of shock Hugonoit data is available by LANL [3].
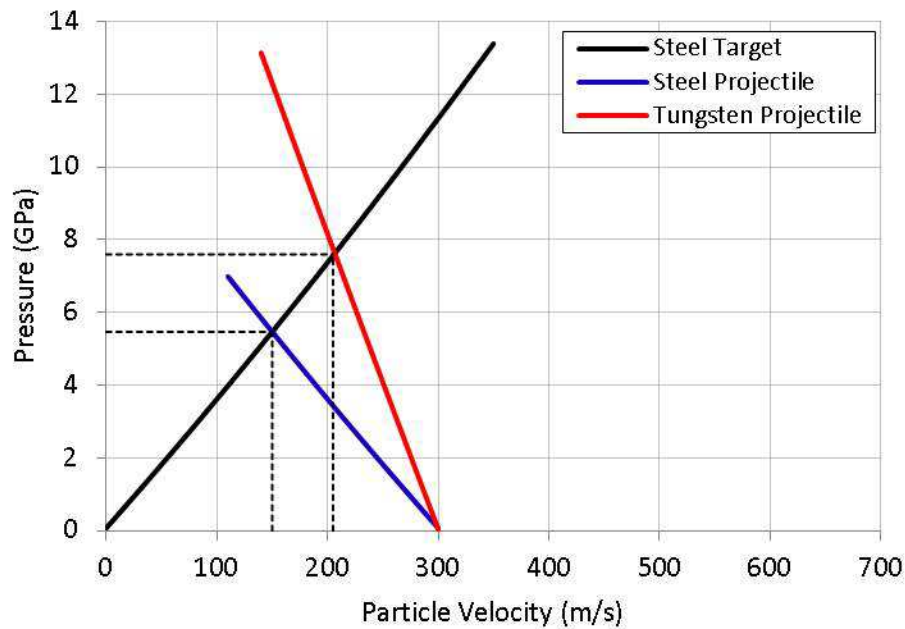
Figure 1-31: Pressure vs. particle velocity for steel target (black) and 300 m/s projectiles made of steel (blue) and another made of tungsten carbide (red). Data from [3]

Figure 1-31 shows the pressure-particle velocity relationship for an impact of a steel target (black curve) for two cases; a steel projectile with an impact velocity of 300 m/s

(blue curve) and a tungsten carbide projectile also with an impact velocity of 300 m/s (red curve). The blue and red curves representing the projectile are mirrored curves about the y-axis, such that there intersection with the x-axis starts from the initial projectile velocity and not from zero. As the figure shows, for the same initial projectile velocity of 300 m/s, the stress in the target steel can be substantially increased from 5.5 GPa up to 7.5 GPa.

The target material will remain in a state of compression until the trailing tensile wave releases it back to the original stress state. The diameter of the projectile disc and the target disc are several times larger than the thickness, such that the material remains in a state of uniaxial strain and the radial waves are delayed until the full longitudinal stress wave is measured [52-54]. Several resources are available which describe methods to "catch" radial waves in a sacrificial momentum trap ring surrounding the specimen [55-57] or employ the use of non-circular flyer plates [58] or tapered specimen edges [7,57] in order to eliminate reflection back into the center of the specimen to ensure a state of 1D strain at all times. The thickness of the projectile and target disc are designed such that the tensile waves reflected from the free surfaces cross paths within a sacrificial backing plate, eliminating the potential of spall fracture in the target disc to be studied. The compressive and tensile wave propagation in the specimen are shown in the time series schematics in Figure 1-32.
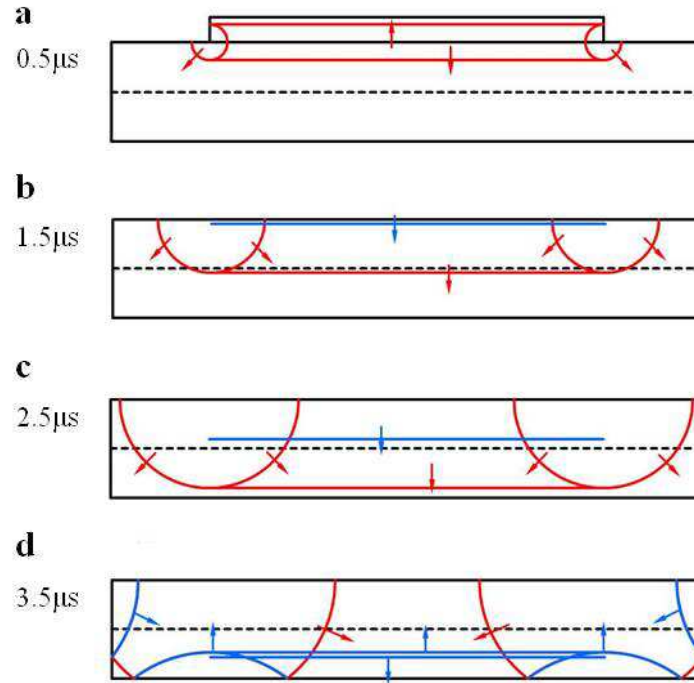
Figure 1-32:   Time series schematics of planar and radial wave propagation in a symmetric planar plate impact test at different time steps.   Red lines are compressive waves and blue lines are tensile waves.

As Figure 1-32 shows, upon impact a compressive wave is generated in both the projectile and target. From the edges of the projectile, radial waves propagate into the target specimen.   The plate impact experiments are considered to be a uniaxial strain loading condition within the time domain prior to radial waves traveling to the center region of the disc.   The dimensions of the target disc are much larger in the radial direction than in the direction of loading and as such, the radial strains are zero and non-zero strain only occurs in the loading direction; written in true strain as

$$\varepsilon_x = \ln\frac{V}{V_0}$$ (1.45)

The stress in the uniaxial strain loading can be derived from hydrostatic and deviatoric components. The hydrostatic pressure, P, is written as

$$P = \frac{1}{3}\left(\sigma_x + \sigma_y + \sigma_z\right)$$ (1.46)

and since the specimen is symmetric about the loading direction (x-axis), $\sigma_y = \sigma_z$, Equation (1.46) can be rewritten as

$$P = \frac{1}{3}\left(\sigma_x + 2\sigma_y\right) = \sigma_x - \frac{2}{3}\left(\sigma_x - \sigma_y\right)$$ (1.47)

The maximum shear stress is written as

$$\tau = \frac{1}{2}\left(\sigma_x - \sigma_y\right)$$ (1.48)

Substituting Equation (1.48) into Equation (1.47) and solving for stress in the impact direction;

$$\sigma_x = P + \frac{4}{3}\tau$$ (1.49)

This stress is measured using in plane piezoresistive manganin stress gauges bonded between the target and backing plate, which will be discussed in more detail in Chapter 2.

A set of equations to describe the motion of a shock wave in terms of the stress, density, and energy across the shock front can be described by the conservation of mass, momentum, and energy assuming that equilibrium exists on either side of the shock front. This set of equations is known as the Rankine-Hugoniot conservation equations [39,52-54,59]. A shock wave is a considered a discontinuous surface which has no apparent thickness, across which there is a discontinuity in pressure, density, and temperature. The conservation equations can be developed by considering regions of material directly ahead of shock front and directly behind the shock front, designated by subscript 0 and 1,

respectively. These equations can be written in there appropriate one dimensional form being that the plate impact tests are considered to be uniaxial strain loading.

The conservation of mass states that the mass ahead of the front and behind the front are equal. Considering an area, A, whose particle velocity and density of the material ahead of and behind the shock front are u_0 ,ρ_0 and u_1 ,ρ_1, respectively, the

The mass ahead of the shock front is written as

$$A\rho_0\left(U_s - u_0\right)dt \tag{1.50a}$$

and the mass behind the shock front is

$$A\rho_1\left(U_s - u_1\right)dt \tag{1.50b}$$

Equating the Equations (1.50a) and (1.50b) and dividing both sides by area and time, *Adt*, the equation reduces to

$$\rho_1\left(U_s - u_1\right) = \rho_0\left(U_s - u_0\right) \tag{1.51a}$$

If the material is initially at rest, then $u_0=0$, and Equation (1.51a) can be written as

$$\rho_1\left(U_s - u_1\right) = \rho_0 U_s \tag{1.51b}$$

Equation (1.51b) is the conservation of mass in one dimension for a material which is initially at rest.

The conservation of momentum states that the change in momentum across the shock front is equal to the impulse imparted per unit cross-sectional area. The momentum is

product of the mass and velocity, in this case the particle velocity, u. The impulse is product of the difference in force across the shock front and time. Using the mass from Equation (1.50a) and (1.50b), and the particle velocity ahead of and behind the front the momentum across the shock front can be written as

The momentum ahead of and behind the shock front is written as:

$$\left[A\rho_0 \left(U_s - u_0 \right) dt \right] u_0 \tag{1.52a}$$

$$\left[A\rho_1 \left(U_s - u_1 \right) dt \right] u_1 \tag{1.52b}$$

The impulse is written as:

$$\left[\left(P - P_0 \right) A \right] dt \tag{1.53}$$

Equating the Equation (1.52a) and (1.52b) with Equation (1.53), the conservation of momentum is thus written as:

$$\left[A\rho_1 \left(U_s - u_1 \right) dt \right] u_1 - \left[A\rho_0 \left(U_s - u_0 \right) dt \right] u_0 = \left[\left(P - P_0 \right) A \right] dt \tag{1.54a}$$

Since the target material is initially at rest, setting $u_0=0$, and $P_0=0$, and substituting in Equation (1.51b) to eliminate the unknown density, ρ_1, the conservation of momentum equation can be reduced to:

$$P = \rho_0 U_s u_1 \tag{1.54b}$$

From the conservation of momentum Equation (1.54b) the pressure or particle velocity of the material under impact loading can be determined if either the stress or particle velocity is measured during plate impact testing.

The conservation of energy states that the work done by the shock load is equal to the increase of internal and kinetic energy across the shock front. The work done can be written in the form

$$W = (PA)(udt)$$
(1.55)

where the product PA is the force applied over a distance, udt. The total energy is the sum of the kinetic and internal energy written in basic form as:

$$E_{total} = \left(\frac{1}{2}mV^2 \right) + \left(E_{internal/unit\ mass} \cdot m \right)$$
(1.56)

Substituting in the mass defined by Equations (1.50a) and (1.50b) the conservation of energy can be written as

$$
\begin{aligned}
(P_1 A)(u_1 dt) &- (P_0 A)(u_0 dt) \\
&= \left\{ \frac{1}{2} \left[A\rho_1 (U_s - u_1) dt \right] u_1^2 + E_1 \left[A\rho_1 (U_s - u_1) dt \right] \right\} \\
&- \left\{ \frac{1}{2} \left[A\rho_0 (U_s - u_0) dt \right] u_0^2 + E_0 \left[A\rho_0 (U_s - u_0) dt \right] \right\}
\end{aligned}
$$
(1.57a)

Again, the particle velocity ahead of the shock front in the undisturbed material can be set to zero, $u_0=0$, and the area and time, Adt, can be divided out, from which Equation (1.57a) reduces to:

$$P_1 u_1 = \frac{1}{2}\rho_1 \left(U_s - u_1\right) u_1^2 + E_1\rho_1 \left(U_s - u_1\right) - E_0\rho_0 U_s \tag{1.57b}$$

Utilizing the conservation of mass, Equation (1.51b), further reduction can be done resulting in a final form of the conservation of energy in terms of pressure, particle velocity, density, and shock velocity.

$$P_1 u_1 = \frac{1}{2}\rho_0 U_s u_1 + \rho_0 U_s \left(E - E_0\right) \tag{1.57c}$$

The three expression defining the conservation of mass (1.51b), the conservation of momentum (48b), and the conservation of energy (1.57c), for a material which is initially at rest, contain five unknown variables; pressure, particle velocity, shock velocity, density, and energy. A fourth equation is needed to solve this set of equations. The following expression, known as the Equation of State (EOS) of the material, is a relation between the shock velocity and the particle velocity of the material written as:

$$U_s = C_b + S_1 u + S_2 u^2 + \ldots.S_n u^n \tag{1.58}$$

where C_b is the sound velocity at zero pressure, and S_n are empirical parameters determined by fitting the equation to experimental data. For most metals, a linear form of the equation is sufficient. Applying a linear form of Equation (1.58) to the conservation of momentum presented in Equation (1.54b), the pressure can be directly related to the particle velocity as:

$$P = \rho_0 \left(C_b u_1 + S_1 u_1^2\right) \tag{1.59}$$

From Equation (1.59), the shock parameter, S_1, can be determined from experimental data of symmetric plate impact tests of materials with known sound velocities, in which the projectile velocity and target stress are measured. This curve, represented by Equations (1.51b), (1.54b), (1.57c), and (1.58), is known as the Hugoniot of the material and is typically represented in stress-volume or stress-particle velocity space. An extensive collection of the shock Hugoniot data for all types of materials was documented by LASL data center [3], of which a plot of several material Hugoniots is shown in Figure 1-33.
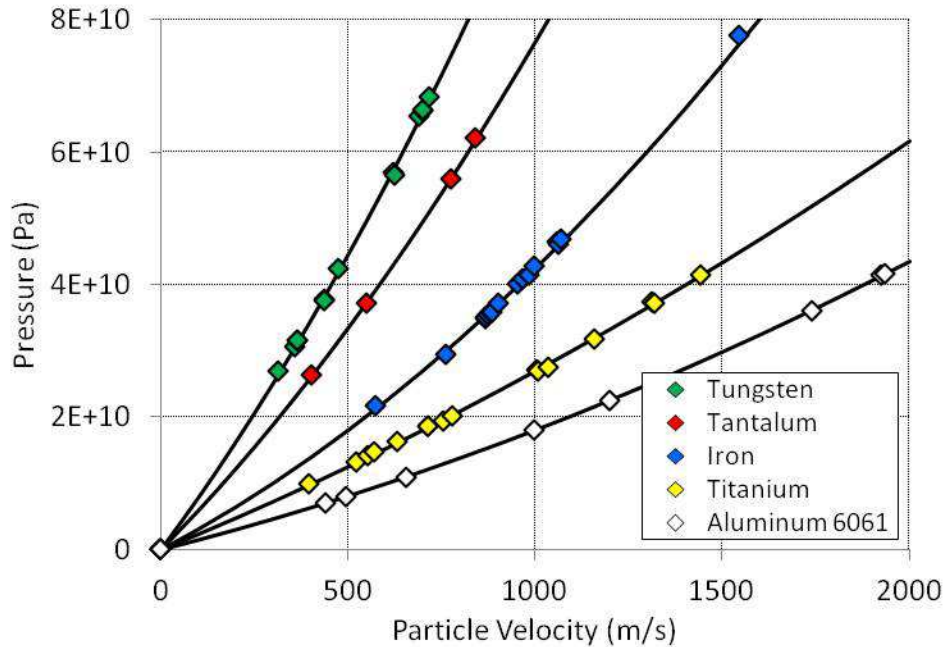
Figure 1-33: Material Hugoniots for several metals represented in pressure vs. particle velocity space. Data acquired from [3]

Fitting Equation (1.59) to the data points in Figure 1-33, the sound velocity and shock parameter can be determined, and are presented in Table 1-2. Values of C_b determined

from curve fitting the data are comparable to values when calculating the bulk wave

speed from the longitudinal and shear wave speeds using the expression

$$C_b = \sqrt{C_L{}^2 - \frac{4}{3}C_S{}^2}$$ (1.60)

Table 1-2: Sound velocity at zero pressure and shock parameter determined from curve fitting Equation (1.26) to data points shown in Figure 1-33.

	Tungsten	Tantalum	Iron	Titanium	Aluminum
ρ (kg/m^2)	19235	16656	7856	4527	2703
C_b (m/s)	3948	3437	3782	5103	5316
S	1.37	1.17	1.63	0.86	1.36

The conservation of mass, momentum, and energy in Equations (1.51b), (1.54b), and

(1.57c), respectively, can be conveniently implemented into finite difference methods by

first rewriting the relations in differential form in order to solve numerically through

distance and time. All three equations follow the notion of an accumulation rate which is

equal to the input rate minus the output rate. The conservation of mass can be written as

[1]

$$\frac{D\rho}{Dt} + \rho \nabla u = 0$$ (1.61a)

and in one dimension, $\frac{\partial}{\partial y}u = \frac{\partial}{\partial z}u = 0$, so Equation (1.61a) is written as

$$\frac{D\rho}{Dt} + \frac{\partial u}{\partial x} = 0$$ (1.61b)

The Eulerian coordinate x can be transformed into the Lagrangian coordinate X by

$$\rho_0 \partial X = \rho \partial x \tag{1.62}$$

thus multiplying and dividing both sides of Equation (1.61b) by density and applying the transformation in Equation (1.62), the conservation of mass is rewritten as

$$\frac{\rho_0}{\rho^2} \frac{\partial \rho}{\partial t} + \frac{\partial u}{\partial X} = 0 \tag{1.63}$$

The total strain can be written and differentiated with respect to time as

$$\varepsilon = 1 - \frac{\rho_0}{\rho} \ \rightarrow \ \frac{\partial}{\partial t}(\varepsilon) = \frac{\partial}{\partial t}\left(1 - \frac{\rho_0}{\rho}\right) \ \rightarrow \ \frac{\partial \varepsilon}{\partial t} = \frac{\rho_0}{\rho^2} \frac{\partial \rho}{\partial t} \tag{1.64}$$

Applying Equation (1.64), Equation (1.63) can be more conveniently expressed in terms of strain as

$$\frac{\partial \varepsilon}{\partial t} + \frac{\partial u}{\partial X} = 0 \tag{1.65}$$

Equation (1.63) and (1.65) represent the conservation of mass in one dimensional Lagrangian form. The same procedure can be applied to the conservation of momentum, written in Eulerian form as [39]

$$\rho \frac{Du}{Dt} = -\nabla P \tag{1.66a}$$

and in one dimension written as

$$\rho \frac{du}{dt} + \frac{\partial P}{\partial x} = 0 \tag{1.66b}$$

Again, transforming into Lagrangian spacial coordinates using Equation (1.62), the conservation of momentum is written as

$$\rho_0 \frac{du}{dt} + \frac{\partial P}{\partial X} = 0 \tag{1.67a}$$

When including the shear stress term, Equation (1.67a) can thus be written as

$$\rho_0 \frac{du}{dt} + \frac{\partial \sigma}{\partial X} = 0 \tag{1.67b}$$

where the stress, σ, is defined by pressure, P, and shear stress, τ, in Equation (1.49). The pressure from Equation (1.49) can also be written in terms of total strain as [7,60]

$$P = \frac{K\varepsilon}{\left(1 - S\varepsilon\right)^2} \tag{1.68}$$

where K is the bulk modulus of the material, and S is the empirical constant found curve fitting experimental data using Equation (1.58) or (1.59).

Likewise, the conservation of energy can be written in differential Lagrangian form as

$$\frac{dE}{dt} + P\frac{dV}{dt} = 0 \tag{1.69}$$

These three conservation Equations, (1.65), (1.67), and (1.69), can be solved numerically through distance and time using coding in standard computer programs or those found in complex 3D dynamic finite element analysis programs such as LS-DYNA. The concepts and equations detailed in this section are applied throughout this work for determining deformation characteristics of low carbon steel during shock load deformation.

1.5. Deformation of Metals

The particular features of plastic deformation, fracture, or failure of a material can be directly associated with their specific crystal structure and is most often intimately tied with dislocation activity. Therefore, when discussing the deformation of a particular metal under extreme loading conditions, whether it is high strain rate and/or high or low temperatures, a basic knowledge of crystallography and plastic deformation is necessary in order to understand the influence of different loading conditions. Much of the information contained within the following sections is fundamental and common knowledge within the field of materials science. This information can be found in any basic mechanics of materials or metallurgy text book. References for the following sections included text written by Reed-Hill [61], Hull and Bacon [62], Smallman and Bishop [63], and Dieter [64] for basic concepts presented, while more in depth details are referenced throughout.

1.5.1. Basic Crystal Structures

Figure 1-34 shows the three most common crystal structures of metals; the body-centered cubic (BCC), the face-centered cubic (FCC), and the hexagonal close-packed (HCP).
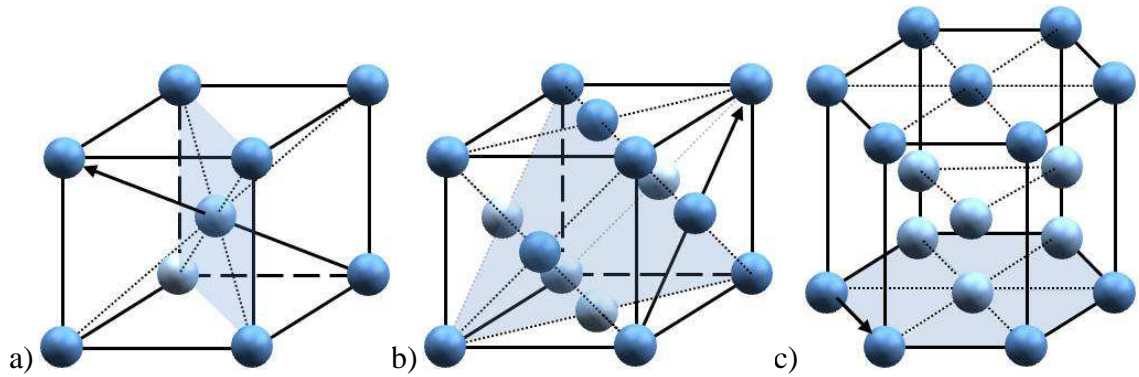
Figure 1-34: Common crystal structures of metals. a) Body-centered cubic structure showing the $(1\bar{1}0)$ plane and the $[1\bar{1}1]$ direction. b) Face-centered cubic structure showing the (111) plane and the $[\bar{1}01]$ direction. c) Hexagonal close-packed structure showing the (0001) plane and the $[11\bar{2}0]$ direction.

The BCC structure is made up of 8 atoms residing at each corner of the cubic structure with an addition atom at the center, resulting in 2 lattice points per unit cell. Each side of the cube is of equivalent length (lattice constant), a, whose angles are all 90 degrees. The atoms are in contact along the cube diagonals, i.e. in the $\langle111\rangle$ directions, as shown in Figure 1-34a with an arrow in the $[1\bar{1}1]$ direction, and is considered the close-packed direction. Because they are in contact, the distance is equal to 4 atomic radii, from which the lattice parameter can be calculated as $a = 4r/\sqrt{3}$. There is not close-packed plane in the BCC lattice, however the closest packed plane is the $\{110\}$. Slip occurs on the $\{110\}$, $\{112\}$, and $\{123\}$ planes all along the $\langle111\rangle$ directions for a total of 48 slip systems. Some common metals with a BCC structure include iron, molybdenum, tungsten, and vanadium.

The FCC structure is made up of atoms residing at each corner as well as 6 additional atoms occupying each face of the crystal, for a total of 4 lattice points per unit cell. The atoms are in contact along the face diagonals, the $\langle 011 \rangle$ close-packed directions, for example along the $\left[\bar{1}01 \right]$ direction shown in Figure 1-34b. From this, the lattice parameter can be determined as $a = 2r\sqrt{2}$. The close-packed plane is of the $\{111\}$ type, also shown in Figure 1-34b, which contains 3 close-packed directions.

The HCP unit cell is shown in Figure 1-34c. The top, bottom, and center planes, referred to as the basal planes, are the close-packed planes. Typically slip will occur on this plane, the $\left[0001 \right]$ plane shown in Figure 1-34c, and along one of the 3 close-packed directions, $\left(11\bar{2}0 \right)$ also shown in the figure. Slip along the prismatic and pyramidal planes is far less common, and therefore is typically restricted to a total of 3 independent slip systems.

The material used in this research is a low carbon steel with a primarily α-ferrite microstructure (BCC) with dispersed colonies of pearlite, as shown in Figure 1-35.
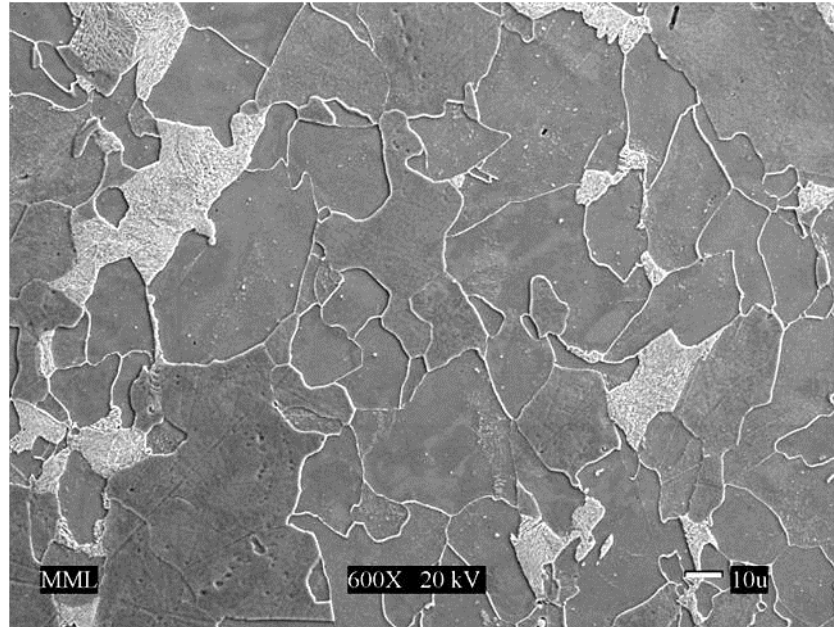
Figure 1-35: Low carbon steel SEM micrograph showing dispersed pearlite grains in a primarily α-ferrite microstructure.

Therefore, the details of the subsequent sections will focus primarily to the BCC crystal structure.

1.5.2. **Plastic Deformation**

Imperfections or defects in crystals consist of point, line, planar, and surface or volume defects. These defects are responsible for accommodating strain when applied loads cause plastic deformation. There are three basic ways in which plastic deformation can occur in crystals. First, individual atoms can move from thermal activation in a process known as diffusional creep. Second, line defects, entire planes of atoms can displace through the lattice, known as dislocation slip. Third, planar defects, atoms within the crystal can shift to produce a uniform shear of the lattice, and this process is known as mechanical twinning. The latter two concepts, dislocation slip and mechanical

70

twinning will be discussed in detail in the following subsections, whose primary factors influencing these types of deformation mechanism being temperature and strain rate. The basic principles of plastic deformation are presented in the following subsections in order to introduce basic concepts needed for an understanding of the work presented in the subsequent chapters.

1.5.3. **Dislocation Slip**

The two types of dislocations formed during plastic deformation are edge and screw dislocations. An edge dislocation is seen as an extra half plane of atoms inserted into an otherwise perfect lattice arrangement, as shown in Figure 1-36a.
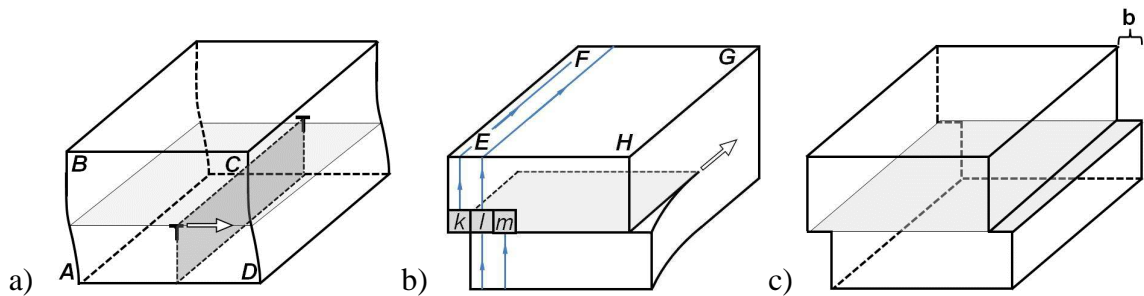
Figure 1-36: a) Edge dislocation b) Screw dislocation c) full Burger's vector step due to dislocation slip

This half plane of atoms moves under an applied shear stress perpendicular to its plane and results in plastic deformation as a result atomic displacement. Three steps of the movement of an edge dislocation are shown in Figure 1-37, looking at the plane *ABCD* from Figure 1-36a.
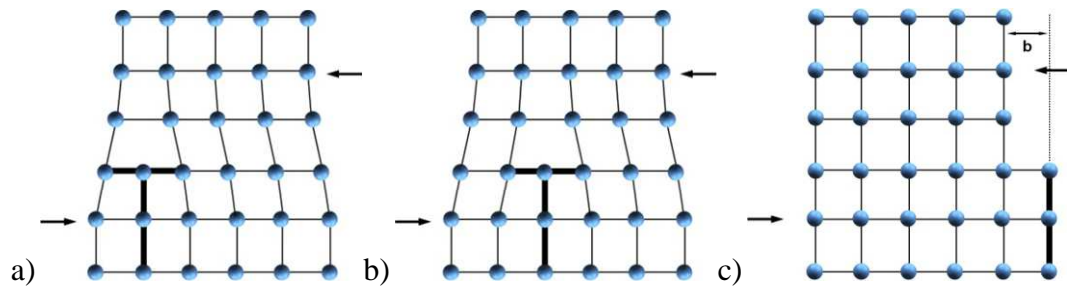
Figure 1-37: Movement of an edge dislocation.

A screw dislocation will result in the same displacement of atoms, however does not require the movement of a half plane of atoms. Instead, a screw dislocation results in a displacement planes of atoms with respect to planes of atoms lying below the slip plane, as shown in Figure 1-36b. The term "screw" is used to describe the spiral of atoms round the dislocation line. From Figure 1-36b, if a path is followed around the crystal from atom position k, the path will lead to atom position m, likewise if continued from m to l, the path will lead around the circuit to position n and so on. Three steps of the movement of a screw dislocation are shown in Figure 1-38, looking down at plane *EFGH* which is above the slip plane from Figure 1-36b.
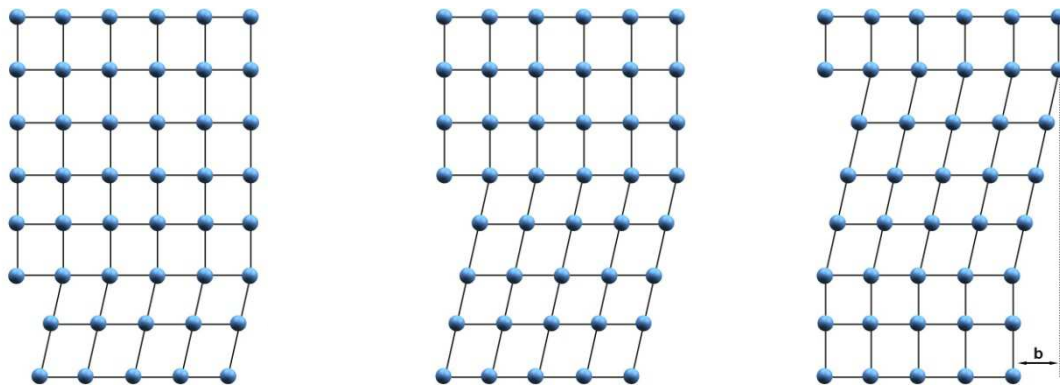
Figure 1-38: Movement of a screw dislocation.

An edge dislocation results in a displacement of atoms normal to the dislocation line and a screw dislocation results in a displacement of atoms parallel to the dislocation line, both of which have a magnitude of displacement called the Burger's vector, as shown in Figure 1-36c. The norm of the Burger's vector is dependent upon the direction in which the dislocation acts, and can be written as

$$\|b\| = \frac{a}{2}\sqrt{h^2 + k^2 + l^2}$$ (1.70)

where a is the lattice constant, and h, k, and l are the miller indices of the direction.

It is energetically favorable for a dislocation to travel, or slip, in crystallographic directions which are closest packed due to the minimum distance the dislocation plane must travel until reaching the next atomic position, known as the slip direction. The plane on which the dislocation lies must contain the close-packed direction. The preferential slip planes are ones that have the highest density of atoms, or those which have the widest spacing. The plane on which the dislocation lies and the direction in which the dislocation is moving defines a slip system. For BCC metals, the $\langle 111 \rangle$ direction is the close-packed direction and the slip plane is either the $\{112\}$ or the $\{110\}$. As the applied stress is increased, the plastic deformation increases, therefore the number of dislocation within the material also increases. This increase in dislocation density creates large stress fields within the material. The dislocation density has been shown to be the root cause for increases in yield stress, or work hardening of metals. The stress is related to the square of the dislocation density through the equation

$$\sigma = \sigma_o + \kappa \rho^{1/2}$$ (1.71)

where κ is a constant, ρ is the dislocation density (cm^{-2}), and σ_o is the stress when the density is extrapolated to zero [61].

As stated above, the dislocation will slip in the material with the application of shear stress. The stress applied to the dislocation to initiate motion is influenced by several factors. The temperature and strain rate both affect dislocation motion which can be attributed to influencing the stress field impeding the dislocation motion. This stress field can be split according to the barrier type impeding the dislocation motion; short range, long range, and drag components. The total flow stress required for dislocations to move is a summation of these stress components, written as

$$\sigma = \sigma_A + \sigma_{TH} + \sigma_D \tag{1.72}$$

where σ_A, σ_{TH}, and σ_D are the athermal, thermal, and drag stress components, respectively [66,67].

In BCC metals, short range stress barriers, those less than 10 atomic diameters [22], are controlled by the resistance of the actual lattice and point defects within. This stress is controlled by the strain rate and temperature, and is thus called thermal stress, σ_{TH}. Long range barriers, those greater than 10 atomic diameters, are controlled by stress fields from forest dislocations and grain boundaries [69], and thermal energy is not sufficient to aid in overcoming these obstacles.

In BCC metals, as described elsewhere [66-68], the thermal stress is due to the lattice itself which acts as the main resistance to dislocation motion, and the dislocation spacing should therefore be on the same order as the lattice spacing, therefore $l \approx b$. For FCC metals, the main source of short range barriers are forest dislocations, therefore as the dislocation density is increased, the dislocation mean free path decreases which is

described through the relation $l = 1/\sqrt{\rho}$ by several authors [8,9]. The stress field in the

lattice can be visualized for an edge dislocation in the schematic of Figure 1-39.
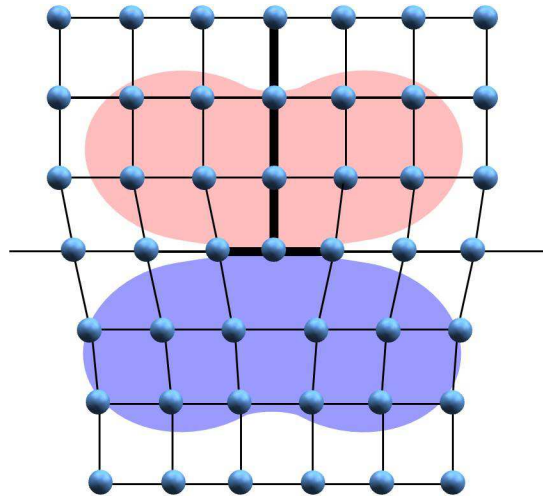
Figure 1-39: Stress field surround an edge dislocation.

The distortion in the surrounding lattice caused by the dislocation creates an elastic

stress field. Above the slip plane a compressive stress is developed due to the addition of

the extra half plane of atoms. Below the slip plane a tensile stress is developed due to the

lattice distortion attempting to retain the proper lattice spacing.

The stress required to overcome the long range barriers are not affected by the strain

rate, and are only indirectly affected by temperature through the elastic shear modulus,

and is thus called the athermal stress component, σ_A. As the strain rate is increased, the

sensitivity of the flow to strain rate increases. This has largely been thought to be due to

dislocation drag caused by scattered phonons or solute atoms in the lattice [23,70].

However, it has been shown that the increase of stress in the 10^3-10^4 s^{-1} range is not

caused by dislocation drag, but rather by an increased dislocation generation rate [71],

while others have shown that the shift from thermally-activated to viscous drag

mechanism occurs at strain rates on the order of 10^5-10^7 s^{-1} [23,24]. The athermal and thermal stress components are shown in Figure 1-40.
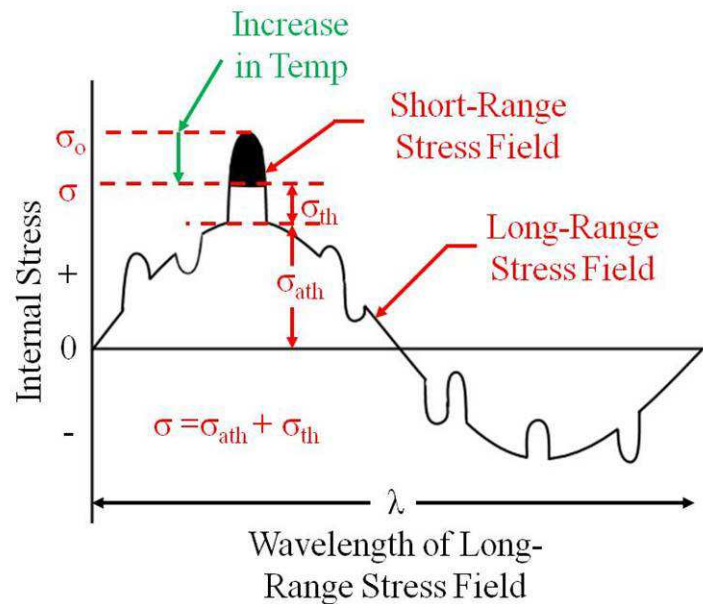
Figure 1-40: Long range and short range internal stress field a dislocation must overcome in order to glide [25].

As shown in Figure 1-40, the term σ_o is the flow stress required for a dislocation to overcome a barrier when there is no available thermal energy, i.e. at a temperature of 0 K. As the temperature is increased, the short range stress field is reduced until reaching a saturation limit for the temperature influence at which point only the long range, or athermal stress, is relevant. Increasing the temperature beyond this point has no further effect on the flow stress value.

Several mechanisms exist which facilitate the motion of dislocations. These mechanisms arise in order to reduce the energy necessary to allow the dislocation to move. Firstly, it should be known that a dislocation does not typically move as a

perfectly rigid line. It wavers as it passes through the lattice moving from one low energy position to the next.

Dislocation climb occurs when the dislocation plane intersects an impurity, interstitial atom, vacancy, or intersecting another dislocation. At high temperatures, the entire dislocation, or a portion of it, can move perpendicular out of its slip plane in order to glide to the next lattice position. The vertical steps created by climb of a portion of the dislocation line are called jogs. This is shown for an edge dislocation in Figure 1-41a and for a screw dislocation in Figure 1-41c. Pure screw dislocations alone cannot climb, however edge type jogs along the screw dislocation can provide sites to climb [62]. Steps in the dislocation line which do not move the dislocation out of its original slip plane are called kinks. This is shown for an edge dislocation in Figure 1-41b and for a screw dislocation in Figure 1-41d.
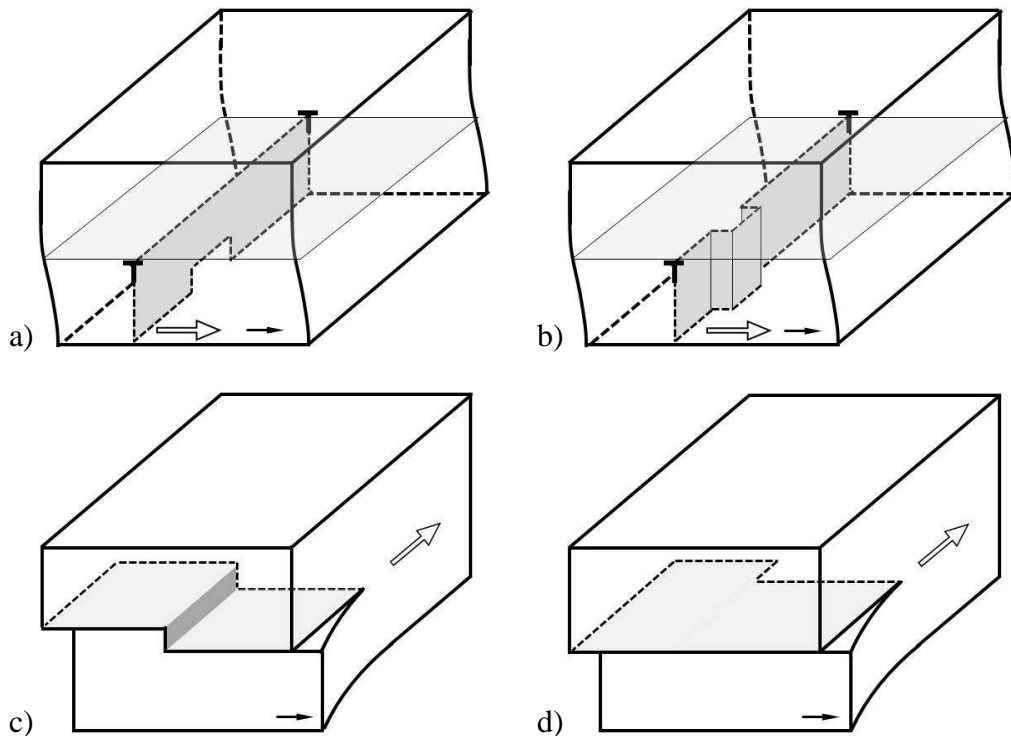
Figure 1-41: a) Edge dislocation with 2 jogs (edge orientation) resulting in a portion of the dislocation to climb one Burger's vector to a parallel slip plane. b) Edge dislocation

with 2 kinks (screw orientation) advancing a portion of the dislocation to the next lattice position. c) Screw dislocation with a single jog (edge orientation) resulting in a portion of the dislocation to act on a slip plane one Burger's Vector above the original slip plane. d) Screw dislocation with a single kink (edge orientation) advancing the dislocation line to the next lattice position along the same slip plane.

The kinks will form when the dislocation in unable to lie in one energy minimum position. Both jogs and kinks possess the same Burger's vector as the dislocation line on which they occur [62]. The preferential position of a dislocation is a location at which its energy is minimized, known as a Peierl's valley. As the dislocation moves between lattice positions, it must exceed the frictional stress created by moving between lattice positions, known as the Peierl's-Nabarro stress. Half way between positions shown in Figure 1-37a and Figure 1-37b the dislocation energy is at a maximum. Instead of the dislocation moving entirely from one position to the next, smaller increments of the total dislocation line can move between positions by the lateral movement of kinks. The glide of an edge dislocation by the lateral motion of kink pairs is shown in the steps of Figure 1-42.

c) A B C D   d) A B C D
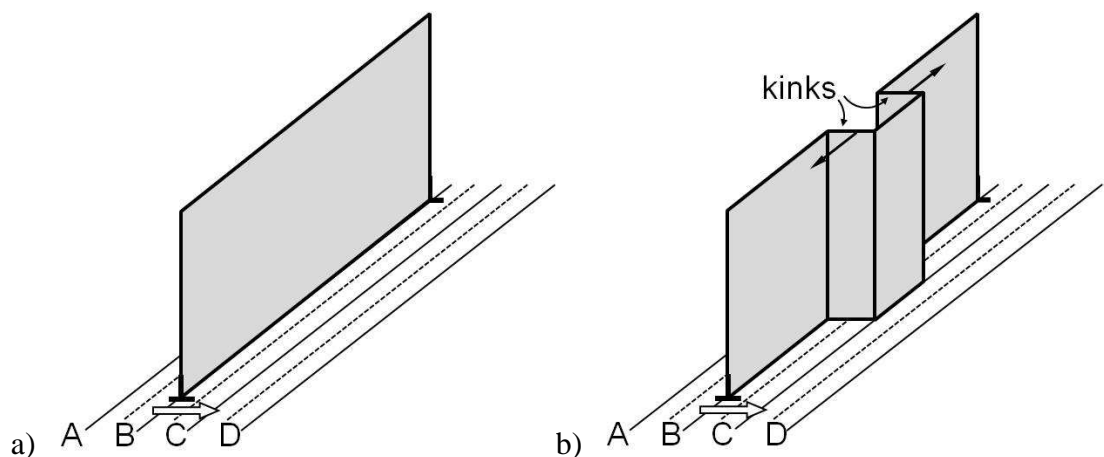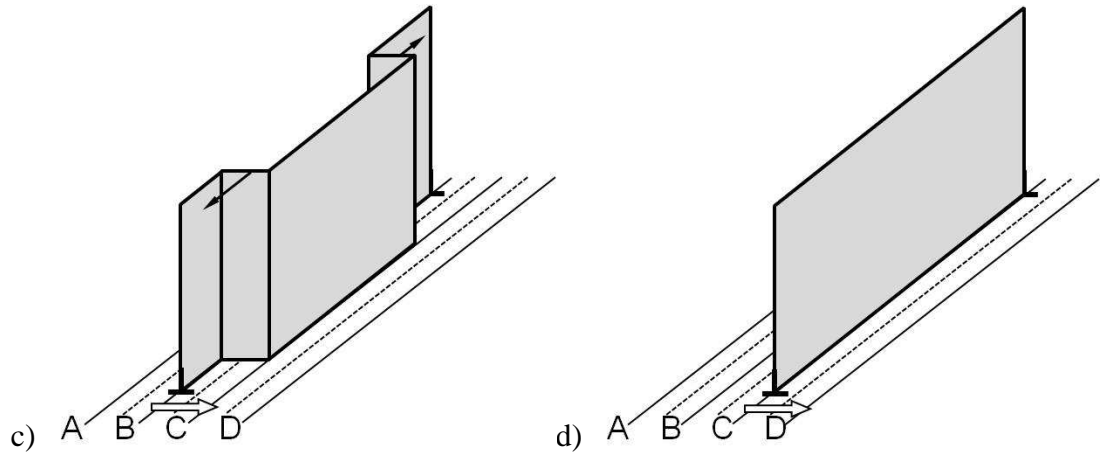
Figure 1-42: a) a perfect edge dislocation half plane lying in the Peierl's valley position b b) a pair of kinks formed on the dislocation, advancing a portion of the dislocation to position c. c) Lateral motion of the pair of kinks advancing the dislocation to the next lattice position. d) edge dislocation completely translated to position c by the motion of kink pairs. Solid and dotted lines represent Peierl's minimums and maximums, respectively.

Note that the component of the dislocation line that make up the kinks, shown in Figure 1-42, are parallel to the burgers vector, making them screw orientation. Instead of the entire dislocation line moving rigidly from position B to position C, smaller sections of the dislocation line can translate to position C by the lateral movement of the kinks. Since the motion of kinks only involve a small number of atoms, the energy required is relatively low, and can be sustained by thermal activation [65]. Since the energy to move a kink is lower than that to move an entire dislocation rigidly, kink mobility promotes dislocation glide at low temperatures. It has been established that BCC metals exhibit a strong temperature dependence at low temperatures. When the Peierl's barrier is large, as in the case of BCC metals, and there is minimal thermal energy available, glide will take place by nucleation and motion of kink pairs [72,73].

Kink nucleation and motion is particularly important when dealing with low temperature or high strain rate loading conditions. It has been shown that the maximum

energy required to nucleate a partial dislocation is less than that for a perfect dislocation at high stresses [11]. Furthermore, at low temperatures the jump frequency of partial dislocations is higher than for perfect dislocations resulting in a preferential glide of partial dislocations rather than dislocations with a full Burger's vector. These characteristics of partial dislocation nucleation and propagation can provide a means of deformation twin nucleation and growth, as will be discussed in the following section.

It has been shown that the dislocation motion is dependent both on temperature and strain rate. The dislocation will move from one lattice position to the next in a periodic energy potential field, as shown in Figure 1-42, by "jumping" the maximum Peierl's energy barrier at a specific jump frequency. The jump frequency of a dislocation to move one burgers vector by the lateral motion of kink pairs when the length of kink pairs is significantly smaller than the distance between kink pairs is given as [74]

$$f_k = f_f \exp\left(\frac{-2W_k + \tau b^3}{kT}\right)$$ (1.73)

where W_k is the formation energy of a single kink, k is Boltzmann's constant, T is temperature, f_f is approximately equal to the Debye frequency, b is Burger's vector, and τ is the applied shear stress. The frequency at which a dislocation moves a burgers vector

$$f_d = \frac{\dot{\varepsilon}}{\rho b^2}$$ (1.74)

where $\dot{\varepsilon}$ is the strain rate, and ρ is the dislocation density. As shown in Equations (1.73) and (1.74), the jump frequencies from one Peierl's valley position to the next are functions of both temperature and strain rate.

The imposed strain rate must be matched by the dislocation activity; i.e. for a specific dislocation density, and burger's vector. The strain can is related to the dislocation density through the Orowan equation as

$$\varepsilon = \rho b l \tag{1.75}$$

where ρ is the density of perfect dislocations and b is a full Burgers vector. Differentiating the strain, Equation (1.75), the strain rate is written as

$$\dot{\varepsilon} = b\rho \frac{\partial l}{\partial t} + bl \frac{\partial \rho}{\partial t} \tag{1.76}$$

where the derivative $\dfrac{\partial l}{\partial t}$ is the velocity of dislocations and $\dfrac{\partial \rho}{\partial t}$ is the generation rate. The velocity can be rewritten in terms of the jump frequency and distance travelled, in this case a Burger's vector, as

$$\frac{\partial l}{\partial t} = v = f_d b \tag{1.77}$$

The velocity, and therefore the jump frequency, of a perfect dislocation has upper limits. Consequently, for a given dislocation density, dislocation slip alone has a limit to the level of strain rate it can accommodate. The second term in Equation (1.76), the generation rate supplements dislocation slip by increasing the dislocation density. In order to match the strain rate, the dislocations may require a higher jump frequency, which can be accomplished by dissociation into partial dislocations. The jump frequency of partial dislocations is higher than that of perfect dislocation and can therefore accommodate higher strain rate loadings, higher stresses, and lower temperatures. Furthermore, it has also been shown that at high applied stresses, the energy required to nucleate partial dislocations is less than that required to nucleate full perfect dislocations

[74]. Equation (1.76) can thus be rewritten in terms of perfect and partial dislocations for impact loading conditions as

$$\dot{\varepsilon} = b_o \rho_o \frac{\partial l}{\partial t} + b_p l \frac{\partial \rho_p}{\partial t} \qquad (1.78)$$

where the existing perfect dislocations will glide and the generation rate of perfect dislocations was eliminated, assuming all new dislocations are partial. This condition leads to the preexisting perfect dislocations reaching a maximum velocity, and the generation of partial dislocations in the material, setting up a condition which is preferential for twin formation.

Several authors have shown that straining BCC metals prior to high strain rate impact loading can decrease or completely suppress the formation of deformation twins [6-10]. This has been shown experimentally and has been attributed to the increase in mobile dislocation density. The increased number of mobile dislocations in the material is sufficient to relieve the strain in the short time periods of impact loading without the need for the additional strain relief process of twinning. This observation and hypothesis can be explained in terms of the dislocation velocity and dislocation generation rate. In an annealed material, the dislocation density is relatively low; therefore in order to accommodate the imposed strain rate, each dislocation must travel at an average velocity approaching the maximum. While dislocations velocity were originally proposed to be travelling with the shock wave front, Gilman [75], however, argues that supersonic velocities are not possible because it implies dislocations have an infinite angular momenta, which also disproves the use of the shear wave velocity as a limiting value. Gilman provided an equation for maximum velocity as

$$v_{0\_max} = \left(1/\pi\right)\left(G/\rho\right)^{1/2}$$

<div align="right">(1.79)</div>

where G is the shear modulus and ρ is the density of the material. Using Equation (1.79), the maximum velocity in low carbon steel with G=82 MPa, and a material density of ρ=7814 kg/m^3, the limiting velocity is $v_{0\_max} = 1036$ m/s. For annealed iron with a dislocation density of 10^{12} m^{-2}, and a burgers vector of b=2.485Å, and the generation rate set to zero, $\dfrac{\partial \rho}{\partial t} = 0$, the velocity of dislocations would have to be approximately 2000 m/s to accommodate an impact at a strain rate of $\dot{\varepsilon} = 5.0E + 5$. If the material is pre-strained by 3%, increasing the mobile dislocation density to 10^{13} m^{-2}, the imposed strain rate can be achieved with an average dislocation velocity of 200 m/s without the need for the generation of new dislocations.

1.5.4. Deformation Twinning in the BCC Lattice

Deformation at of BCC metals at low temperatures or high strain rates cannot always be accommodated purely by dislocation slip. At high strain rates, the dislocation generation rate and glide velocity are not alone sufficient to match the imposed strain rate. Therefore, a second mode of deformation is activated to accompany the slip process, known as deformation or mechanical twinning. An example of deformation twins can be seen in the micrograph of low carbon steel which has been impacted at 9 GPa; see Figure 1-43.
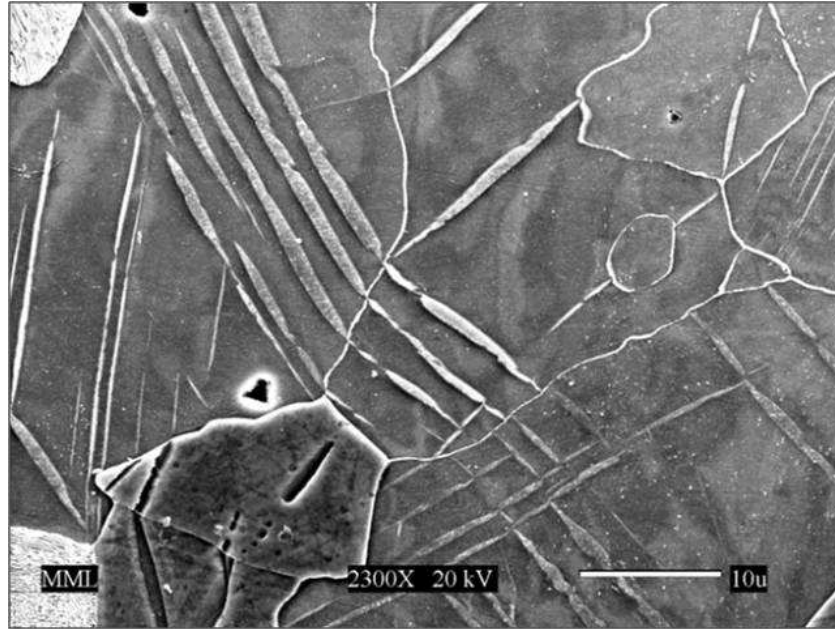
Figure 1-43: SEM micrograph of low carbon steel which was impacted at 9 GPa showing deformation twins within the ferrite grains.

The reorientation of the lattice within the twinned region allows the twins to be revealed when etched and viewed under light or scanning electron microscopes as opposed to dislocation lines which require transmission electron microscopy. It has been shown that the amount of twinning during impact loading is directly proportional to the level of impact stress in BCC metals; see Chapters 3 and 4.

A twin is a section of the lattice which has been reoriented with respect to the orientation of the lattice within the grain it is formed. The twinning process can occur by a homogeneous shear of parallel and consecutive planes in a manner by which each layer is sheared an amount proportional to the distance to the original habit plane. Wasilewski [76] has also shown that a twin can be formed by a local "shuffle" of atoms in which two planes of atoms move opposite each other to result in the same orientation shift with respect to the parent lattice as that formed by a progressive shearing process. In BCC

metals, the most common twinning system involves the <111> and the {112} type direction and plane, respectively. For complete details of all possible twinning features can be found in the extensive review by Christian and Mahajan [77].

Figure 1-44a shows the $(1\bar{1}2)$ planes inside two BCC latt ices. Rotating the view of the lattice such that the $[110]$ direction is directly out of the page, i.e. the line connecting the B position atoms, the lattice is viewed normal to the (110) plane, as shown in Figure 1-44b.
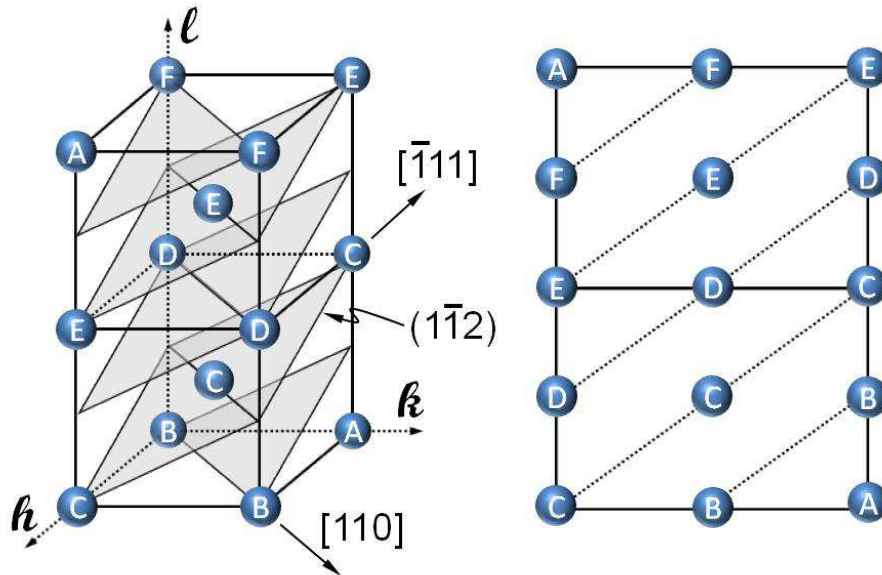
Figure 1-44: 3D model of two BCC crystal lattices and b) the lattice rotated with the (110) plane normal to the page and the $(1\bar{1}2)$ planes connecting atoms of the same lettering. Redrawn from Hull and Bacon [2]

Rotating the view again, the lattice shown in Figure 1-44b can be oriented such that the $(1\bar{1}2)$ planes are horizontal, as shown in the perfect lattice of Figure 1-45.
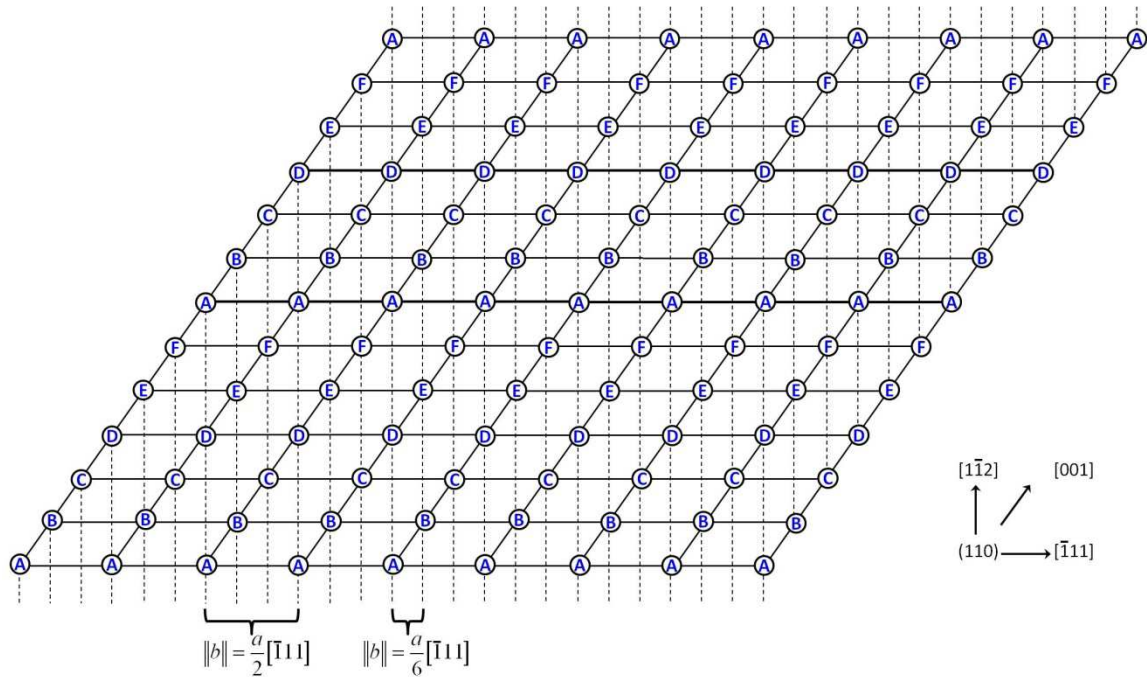
Figure 1-45: Perfect BCC crystal structure projection of the (110) plane

As Figure 1-45 shows, the stacking sequence of the 112 planes in a BCC lattice is ABCDEFABCDEFAB... As mentioned previously, the twinned region can be accomplished by the glide of $\frac{a}{6}[111]$ partial dislocations on successive $\{112\}$ planes. The partial dislocations can be directly emitted from grain boundaries, or can occur from dissociation of existing perfect dislocations. Several dislocation models exist which explain the existence of the partial dislocations necessary to form a twin. Cottrell and Bilby proposed a twin dislocation model, known as the pole mechanism, involving a

$\frac{1}{6}\left[11\overline{1}\right]$ glissile partial dislocation revolving or spiraling around a $\frac{1}{3}[112]$ sessile partial

dislocation (pole) from the dissociation of a screw dislocation reaction

$$\frac{1}{2}[111] \rightarrow \frac{1}{3}[112] + \frac{1}{6}\left[11\overline{1}\right]$$

However, this reaction was discredited by suggesting that the $\frac{1}{6}\left[11\overline{1}\right]$ twin dislocation

would be annihilated by the nucleation of a dipole of $\frac{1}{6}\langle111\rangle$ partials [77] and for the

fact that this reaction is energetically unfavorable [63]. Hirth and Lothe [78] instead

suggested dissociation for the pole mechanism by the reaction

$$\frac{1}{2}[111] \rightarrow \frac{1}{3}[221] + \frac{1}{6}\left[\overline{1}\,\overline{1}1\right]$$

Priestner and Leslie [79] suggest a reaction resulting from the attraction of dislocations

on different slip planes leading to the formation of a single sessile dislocation

$$\frac{1}{2}\left[\overline{1}11\right] + \frac{1}{2}\left[1\,\overline{1}1\right] \rightarrow [001]$$

where the $[001]$ sessile dislocation would lead to a local stress concentration from pile-

ups, and in turn dissociate into multiple partials, some of which lie along the $\left[\overline{1}11\right]$

direction and form a twin. Sleeswyk [80] proposed that a $\frac{1}{2}\langle111\rangle$ edge dislocation may

split into three equivalent partials

$$\frac{1}{2}\left[11\overline{1}\right] \rightarrow \frac{1}{6}\left[11\overline{1}\right] + \frac{1}{6}\left[11\overline{1}\right] + \frac{1}{6}\left[11\overline{1}\right]$$

and similarly by Ogawa who suggested that the partials may spread onto successive

$\{112\}$ planes [81]. This last model described by partial edge dislocations is shown in the

following figures where a progressive shear of the parent lattice will produce a shear offset; i.e. plastic deformation, equal to *kh*, where *k* is the twinning shear, and *h* is the average thickness of the twin lamella. For BCC crystals twinning is most readily formed on the $\{112\}$ planes in the $\langle111\rangle$ direction which has a *k* equal to $1/\sqrt{2}$ [7,21]. Each layer of atoms shifts 1/3 burgers vector, equivalent to $a/6\langle111\rangle$. As such, the twinning shear in BCC material can be derived as the ratio of the length of the Burger's vector of the partial dislocation, $a/6\langle111\rangle$, to the interplanar spacing of the $\{112\}$ twinning planes [45]. Twinning by progressive shear of the parent lattice is shown in Figure 1-46 through Figure 1-48. The first stacking fault is created by the glide of an $\dfrac{a}{6}\left[\bar{1}11\right]$ partial dislocation on the $\left(\bar{1}12\right)$ plane, labeled as "1st Layer" in Figure 1-45.
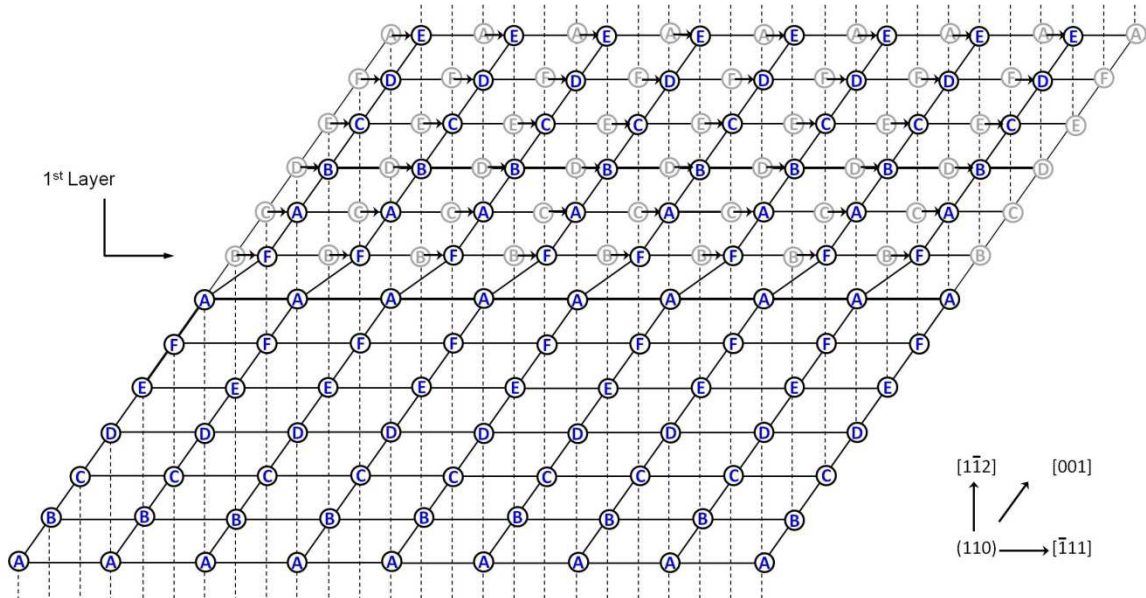
Figure 1-46: 1 layer fault produced by glide of an $\dfrac{a}{6}\left[\bar{1}11\right]$ partial dislocation

Another $\frac{a}{6}\left[\bar{1}11\right]$ partial dislocation glides above the "1st Layer" on the adjacent

$\left(\bar{1}12\right)$ plane, labeled as "2nd Layer", and another on the "3rd Layer" creating a stable 3

layer twin.

Figure 1-47: 2 layer fault produced by glide of two $\frac{a}{6}\left[\bar{1}11\right]$ partial dislocations
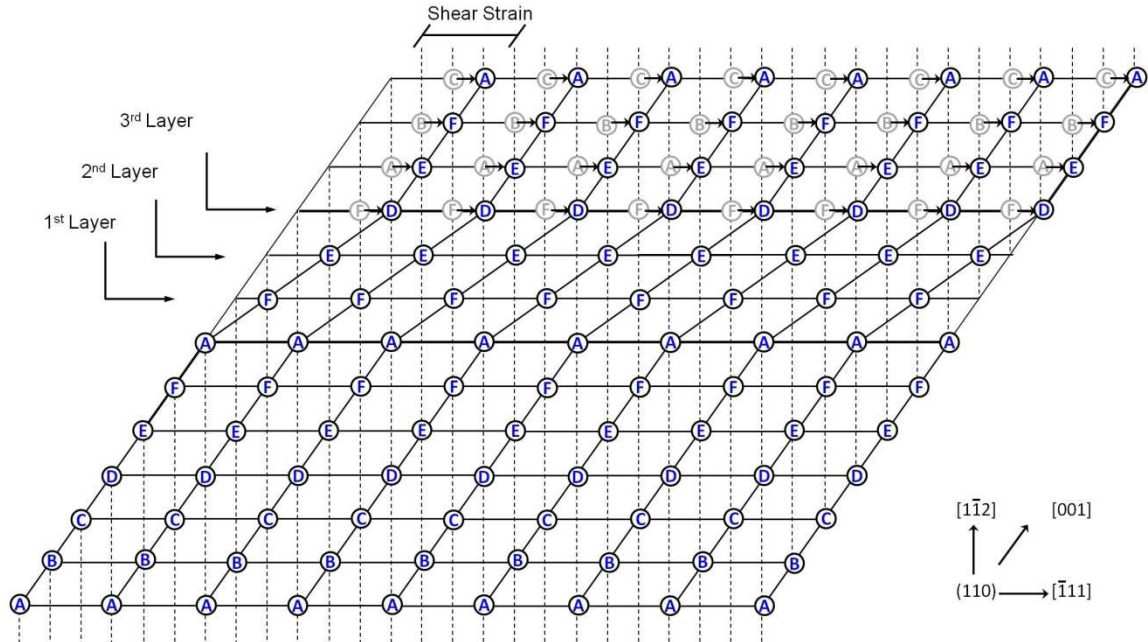
Figure 1-48: 3 layer twin produced by glide of three $\frac{a}{6}\left[\bar{1}11\right]$ partial dislocations.

As the twin region continues to grow, additional layers are added to the structure. Figure 1-49 shows a thicker, six layer twin. The arrows indicate the $\left[001\right]$ direction in the twin and parent lattice. The green highlighted sections show the mirror patern across the twin plane.
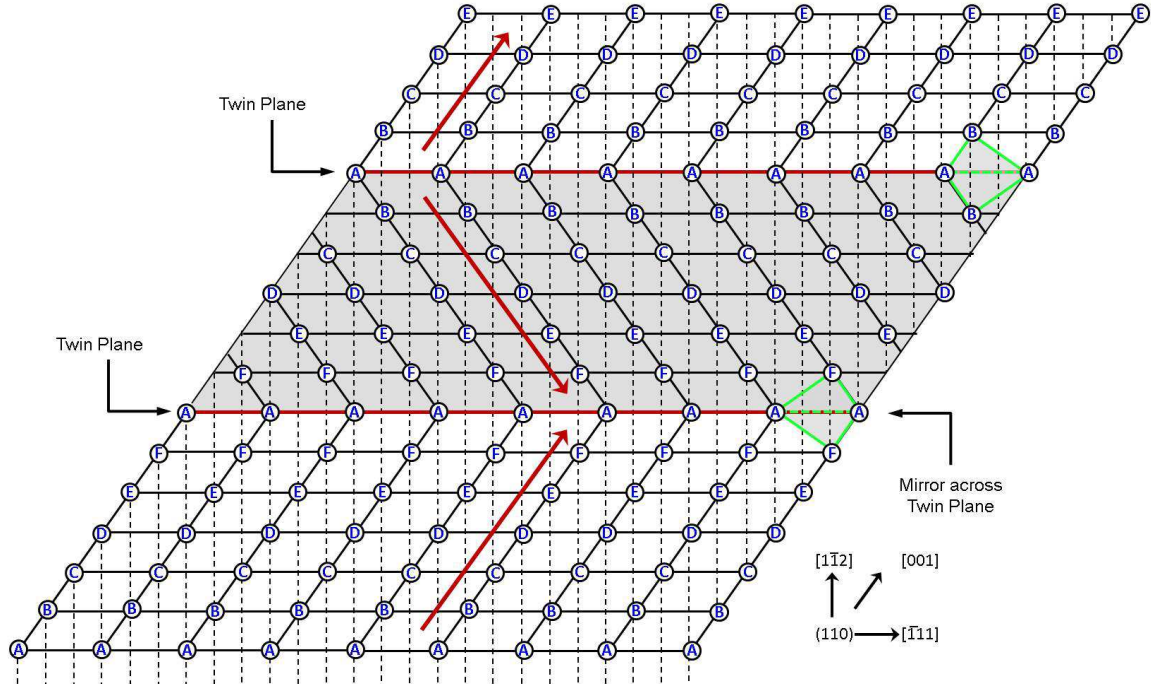
Figure 1-49: 6 layer twin. Bold red arrows indicate the the $[001]$ direction in the parent and twin lattice. The highlighted green sections show the mirror across the twinning plane.

As discussed by Wasilewski [76], twin formation can occur by two different processes; progressive shear of the parent lattice or by an atomic shuffle within the lattice, both of which create the same atomic arrangement within the twinning planes. As shown in the figures above, the progressive shear results in a shear strain equal to *kh*. However, a local rearrangement or "shuffle" process will produce no overall plastic deformation, as is shown in Figure 1-50, where no displacement of atoms occurs on either side of the twinned region.
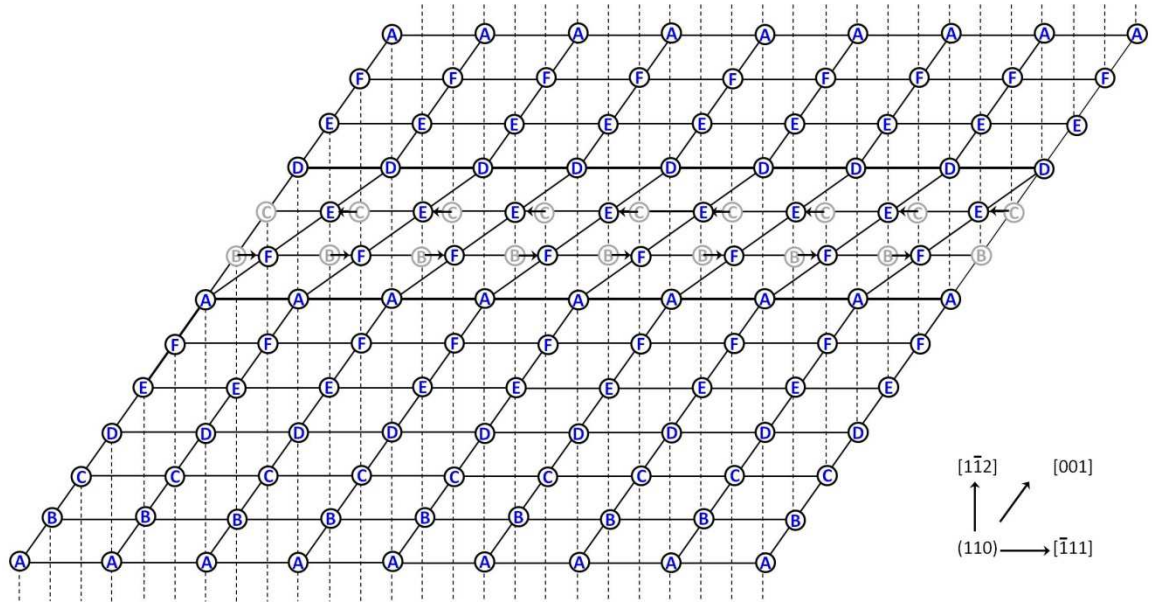
Figure 1-50: Twinned region by the local "shuffle" of atoms resulting in no plastic deformation based on Wasilewski's theory [76].

As shown in the above figures, further deformation will result in the twin to thicken as additional partial dislocations glide on successive planes. Twinning will occur in BCC metals when dealing with low temperatures or high strain rates, as in the case of plate impacts, due to the fact that twins are formed by partial dislocation glide which are more operative at these conditions, as discussed previously. The stress criteria for twin nucleation will be discussed in detail in Chapter 4.

1.6.   **Dissertation Overview**

This dissertation describes the experimental and numerical work performed in order to complete the objectives of this research, as described in Section 1.1. Chapter 2 describes the development of the single stage light gas gun including the background and

purpose and the design of all major components. Chapter 3 describes the effects of impact loading on low carbon steel in terms of microstructure, particularly deformation twinning, and mechanical properties. A model was utilized to simulate plate impact loading in order to predict twin volume fraction as a function of impact stress. Chapter 4 describes the twin nucleation process in low carbon steel. A dislocation based twin nucleation criteria was developed for low carbon steel in order to extend modeling to materials that have been previously strained. Chapter 5 describes the effects of impact loading on the post-impact dynamic flow stress. A flow stress model based on thermal and athermal stress contributions was modified to include the effects of impact loading by including dislocation and deformation twinning contributions. Chapter 6 outlines the major conclusions of this research and provides future recommendations. This is followed by the appendices which include gas gun operating procedures, mechanical drawings, and Matlab code for data analysis.

1.7. **References**

[1]   Field, J.E., Walley, S.M., Proud, W.G., Goldrein, H.T., Siviour, C.R., International Journal of Impact Engineering 30 (2004) 725–775.

[2]   Ramesh, K.T. "High Strain Rate and Impact Experiments" Part D.33. Springer Handbook of Experimental Solid Mechanics. 2008

[3]   Marsh, S. P., editor, "*LASL Shock Hugoniot Data*," University of California Press, CA, (1980).

[4]   Meyers, M.A., Benson, D.J., Vöhringer, O., Kad, B.K., Xue, Q., Fu, H.-H., Constitutive description of dynamic deformation: physically-based mechanisms, Materials Science and Engineering. A322 (2002) 194–216.

[5]   Visser, W., Sun, Y., Gregory, O., Plume, G., Rousseau, C-E., Ghonem, H., Deformation Characteristics of Low Carbon Steel Subjected to Dynamic Impact Loading, Materials Science and Engineering. A528 (2011) 7857–7866.

[6]   De Resseguier, T., Hallouin, M., Stress relaxation and precursor decay in laser shock-loaded iron, Journal of Applied Physics 84 (4) (1998) 1932–1938.

[7]   Johnson, J.N., Rohde, R.W., Dynamic deformation twinning in shock-loaded iron, Journal of Applied Physics. 42 (11) (1971) 4171–4182.

[8]   Armstrong, R. W. and Worthington, P. J., in Metallurgical Effects at High Strain Rates. p. 401, (edited by R. W. Rohde, B. M. Butcher. J. R. Holland and C. H. Karnes), Plenum. New York (1973).

[9]   Meyers, M.A., Benson, D.J., Vöhringer, O., Kad, B.K., Xue, Q., Fu, H.-H., Constitutive description of dynamic deformation: physically-based mechanisms, Materials Science and Engineering. A322 (2002) 194–216.

[10]   Meyers, M.A., Vöhringer, O., Lubarda, V.A., The onset of twinning in metals: A constitutive description, Acta Materialia 49 (2001) 4025–4039.

[11]   Karaman, Sehitoglu, Gall, Chumlyakov, Maier. Deformation of single crystal Hadfield steel by twinning and slip, Acta Mater. 48 (2000) 1345-1359.

[12]   Biggs, W.D., Pratt, P.L., The Deformation and Fracture of Alpha-Iron at Low Temperatures, Acta Metallurgica 6 (1958) 694-703.

[13]   Lindley, T.C., The effect of a prestrain on the low temperature mechanical properties of a low carbon steel, Acta Metallurgica. 13 (1965) 681-689.

[14]   Rosenfield, A.R., Averbach, B.L., Cohen, M., Twinning Occurrence in Iron Single Crystals, Acta Metallurgica. 11 (1963) 1100-1101

[15]   Churchman, A.T., Cottrell, A.H., Yield Phenomenon and Twinning in α-Iron, Nature 1951.

[16]   Mahajan, S., Bartlett, A.F., Influence of Prior Mechanical and Thermal Treatments on Shock Induced Substructures in Molybdenum, Acta Metallurgica. 19 (1971) 1111-1119.

[17]   Mahajan, S., Effects of Existing Substructure on Shock-Twinning Behavior of Iron, Physica Status Solidi. Vol 2, Issue 2, (1970) 217-223.

[18]   Smida, T., Bošanský, J., Deformation twinning and its possible influence on the ductile brittle transition temperature of ferritic steels, Materials Science and Engineering. A287 (2000) 107–115.

[19]   Jolley, W., Hull, D., Effect of Prestrain and Strain Aging on the Brittle Fracture of 3.25% Silicon Iron, Acta Metallurgica 12 (1964) 1337-1352.

[20]   Biggs, W.D., Pratt, P.L., The Deformation and Fracture of Alpha-Iron at Low Temperatures, Acta Metallurgica 6 (1958) 694-703.

[21]   L.E. Murr, M.A. Meyers. "Shock-induced deformation twinning in tantalum." *Acta Materialia* 45.1 (1997): 157-75.

[22]   Thermally Activated Deformation of Metals. Conrad. *Journal of Metals*. 1964. pg 582-588

[23] High strain-rate response of commercially pure vanadium. Nemat-Nasser, Guo. *Mechanics of Materials*. 32 (2000) pp. 243-260.

[24] Spirdione, J., et al. "Role of pearlite colonies on the dynamic flow stress of low carbon steel." *Materials Science and Engineering: A* 679 (2017): 446-454.

[25] G. R. Johnson and W. H. Cook, "A Constitutive Model and Data for Metals Subjected to Large Strain, High Strain Rates and High Temperatures," in *Proc. 7th Int. Symp. on Ballistics*, Hague, Netherlands, 1983.

[26] Zhao, Y. H., et al. "Influence of specimen dimensions and strain measurement methods on tensile stress–strain curves." *Materials Science and Engineering: A* 525.1 (2009): 68-77.

[27] B. Hopkinson, "A Method of Measuring the Pressure Produced in the Detonation of High Explosives or by the Impact of Bullets," *Philosophical Transactions of the Royal Society A,* vol. 213, pp. 437-457, 1914.

[28] R. Davies, "A Critical Study of the Hopkinson Pressure Bar," *Philosophical Transactions of the Royal Society of London A,* vol. 240, no. 821, pp. 375-457, 1948

[29] H. Kolsky, "An Investigation of the Mechanical Proprties of Materials at very High Rates of Loading," *Proc. Phys. Soc. B,* vol. 62, pp. 676-700, 1949.

[30] J. Krafft, A. Sullivan and C. Tipper, "The Effect of Static and Dynamic Loading and Temperature on the Yield Stress of Iron and Mild Steel in Compression," *Proceedings of the Royal Society of London A,* vol. 221, no. 1144, pp. 114-127, 1954.

[31]   Lindholm, U. S., and L. M. Yeakley. "High strain-rate testing: tension and compression." *Experimental Mechanics* 8.1 (1968): 1-9.

[32]   Lewis, Jack L., and Werner Goldsmith. "A biaxial split Hopkinson bar for simultaneous torsion and compression." *Review of scientific instruments* 44.7 (1973): 811-813.

[33]   Klepaczko, J. "Application of the split Hopkinson pressure bar to fracture dynamics." *Proc. 2 nd Conf. Mechanical Properties of Materials at High Rates of Strain, Oxford, England, Mar. 1979,*. 1980.

[34]   W. Chen and B. Song, Spilt Hopkinson (Kolsky) Bar - Design, Testing and Applications, New York, New York: Springer, 2011.

[35]   A. T. Owens, "Development of a Split Hopkinson Tesnsion Bar for Testing Stress-Strain Response of Particulate Composites Under High Strain Rates of Loading," Aubrun Univerisity, Auburn, Alabama, 2007.

[36]   [7] K. D. Robertson, S.-C. Chou and J. H. Rainey, "Design and Operating Characteristics of A Split Hopkinson Pressure Bar Apparatus," Army Materials and Mechanis Reserach Center, Watertown, Massachusetts, 1971.

[37]   [8] M. A. Kaiser, "Advancements in the Split Hopkinson Bar Test," Virginia Polytechnic Institute and State University, Blacksburg, Virginia, 1998

[38]   L.-L. Wang, Fondations of Stress Waves, New York, New York: Elsevier, 2007.

[39]   Meyers, M.A., "*Dynamic Behavior of Materials*," John Wiley & Sons Inc., New York. (1994).

[40]   Spirdione, Justin. "Microstructure-dependent dynamic flow stress in metallic alloys." (2015).

[41]   Rand, James. An analysis of the split Hopkinson pressure bar. NOLTR 67-156 (1967)

[42]   Goni, Miguel, and Carl-Ernst Rousseau. "On the Use of Ultrasonic Pulse-Echo Immersion Technique for Measuring Real Attenuation." *Experimental Mechanics of Composite, Hybrid, and Multifunctional Materials, Volume 6*. Springer International Publishing, 2014. 255-257.

[43]   Plume, Gifford. "Response of materials to various shock loading conditions generated by plate impact experiments." (2013).

[44]   Chen, Weinong W., and Bo Song. "Dynamic characterization of soft materials." *Dynamic Failure of Materials and Structures*. Springer US, 2009. 1-28.

[45]   Samanta, S. K. "Dynamic deformation of aluminium and copper at elevated temperatures." *Journal of the Mechanics and Physics of Solids* 19.3 (1971): 117in1123-122in4135.

[46]   Gama, Bazle A., Sergey L. Lopatnikov, and John W. Gillespie. "Hopkinson bar experimental technique: a critical review." *Applied Mechanics Reviews* 57.4 (2004): 223-250.

[47]   Frew, D. J., MICHAEL J. Forrestal, and W. Chen. "Pulse shaping techniques for testing brittle materials with a split Hopkinson pressure bar." *Experimental mechanics* 42.1 (2002): 93-106.

[48]   Scapin, Martina. *Shock-wave and high strain-rate phenomena in matter: modeling and applications*. Diss. Politecnico di Torino, 2013.

[49] Chhabildas, Lalit C., Lee Davison, and Yasuyuki Horie. *High-pressure shock compression of solids VIII: The science and technology of high-velocity impact*. Vol. 8. Springer Science & Business Media, 2005.

[50] Asay, J., Clint A. Hall, and Marcus Knudson. "Recent advances in high-pressure equation-of-state capabilities." *Sandia National Report, SAND2000-0849C* (2000).

[51] Meyers, M., et al. "Dynamic response of single crystalline copper subjected to quasi-isentropic laser and gas-gun driven loading." *Journal de Physique IV (Proceedings)*. Vol. 134. EDP sciences, 2006.

[52] Davison, L., D.E. Grady, M. Shahinpoor, "*High-pressure Shock Compression of Solids II*," Springer, New York. (1996).

[53] Zhernokletov, M.V., B.L. Glushak, "*Material Properties under Intensive Dynamic Loading*," Springer, New York. (2006).

[54] Kanel, G.I., S.V. Razorenov, V.E. Fortov, "*Shock-wave Phenomena and the Properties of Condensed Matter*," Springer, New Yorrk. (2004).

[55] Bourne, N. K., W. H. Green, and D. P. Dandekar. "On the one-dimensional recovery and microstructural evaluation of shocked alumina." *Proceedings of the Royal Society of London A: Mathematical, Physical and Engineering Sciences*. Vol. 462. No. 2074. The Royal Society, 2006.

[56] Gray III, George T. "Shock recovery experiments: an assessment." *Shock compression of condensed matter* (1989): 407-414.

[57]   Lassila, D. H., and G. T. GRAY III. "Effects of shock prestrain on the dynamic mechanical behavior of tantalum." *Le Journal de Physique IV* 1.C3 (1991): C3-19.

[58]   Machcha, Ashok R., and Sia Nemat-Nasser. "Effects of geometry in pressure–shear and normal plate impact recovery experiments: Three-dimensional finite-element simulation and experimental observation." *Journal of applied physics* 80.6 (1996): 3267-3274.

[59]   Isbell, William M. *Measuring the Dynamic Response of Materials*. London: Imperial College Press, 2005.

[60]   Taylor, John W. "Dislocation dynamics and dynamic yielding." *Journal of Applied Physics* 36.10 (1965): 3146-3150.

[61]   Reed-Hill, Robert E., and Reza Abbaschian. "Physical metallurgy principles." (1973).

[62]   Hull, Derek, and David J. Bacon. *Introduction to dislocations*. Butterworth-Heinemann, 2001.

[63]   Smallman, Raymond E., and Ray J. Bishop. *Modern physical metallurgy and materials engineering*. Butterworth-Heinemann, 1999.

[64]   Dieter, George Ellwood, *Mechanical metallurgy*. New York: McGraw-Hill, 1961.

[65]   Messerschmidt, Ulrich. *Dislocation dynamics during plastic deformation*. Vol. 129. Springer Science & Business Media, 2010.

[66]   Direct measurement of isothermal flow stress of metals at elevated temperatures and high strain rates with application to Ta and Ta-W alloys. S. Nemat-Nasser, J.B. Isaacs. *Acta Metallurgica*. Vol. 45, No. 3. (1997) pp. 907-919.

[67]   Flow stress of FCC polycrystals with application to OFHC Cu. S. Nemat-Nasser, Y. Li. *Acta Mater*. Vol 46, No. 2. (1998) pp. 565-577.

[68]   Effect of dislocation density evolution on the thermomechanical response of metals with different crystal structures at low and high strain rates and temperatures. G.Z. Voyiadjis, F.H. Abed. *Arch. Mech*. 57, 4. (2005) pp. 299-343.

[69]   Temperature and high strain rate dependence of tensile deformation behavior in single crystal iron from dislocation dynamics simulations. Tang, Marian. *International Journal of Plasticity*. Nov 2013.

[70]   Handbook of Materials behavior Models. Section 5. Physically based Rate- and Temperature-Dependent Constitutive Models for Metals, Nemat-Nasser. 2001. pg 387-397.

[71]   Effects of prestrain on high temperature impact properties of 304L stainless steel. Lee, Lin, Chen, Yang. *J. Mater. Res*., Vol 25, No. 4, Apr 2010. pp 754-763.

[72]   Gordon, P. A., et al. "Screw dislocation mobility in BCC metals: the role of the compact core on double-kink nucleation." *Modelling and Simulation in Materials Science and Engineering* 18.8 (2010): 085008.

[73]   Swinburne, T. D., et al. "Theory and simulation of the diffusion of kinks on dislocations in bcc metals." *Physical Review B* 87.6 (2013): 064108.

[74]   Ferreira, P.J., Vander Sande, J.B., Amaral Fortes, M., Kyrolainen, A., Microstructure Deveolopment during High-Velocity Deformation, Metallurgical and Materials Transactions. A 35A (2004) 3091-3101.

[75]   J. Gilman. The Limiting Speeds of Dislocations. Metall. Mater. Trans A. 31. (2000) 811.

[76] Wasilewski, R.J., Mechanism of bcc twinning: Shear or shuffle?, Metallurgical Transactions. 1 (1970) 2641–2643.

[77] Christian, John Wyrill, and Subhash Mahajan. "Deformation twinning." *Progress in materials science* 39.1 (1995): 1-157.

[78] Hirth, John P., and Jens Lothe. *Theory of dislocations*. John Wiley, New York, 1982.

[79] Priestner, R., and W. C. Leslie. "Nucleation of deformation twins at slip plane intersections in BCC metals." *Philosophical Magazine* 11.113 (1965): 895-916.

[80] Sleeswyk, A. W. "½< 111> screw dislocations and the nucleation of {112}< 111> twins in the bcc lattice." *Philosophical Magazine* 8.93 (1963): 1467-1486.

[81] Ogawa, K. "Edge dislocations dissociated in {112} planes and twinning mechanism of bcc metals." *Philosophical Magazine* 11.110 (1965): 217-233.

CHAPTER 2

DEVELOPMENT OF A SINGLE STAGE LIGHT GAS GUN

2.1.   Motivation

This chapter describes the development of a single stage light gas gun for plate impact experiments. This project started as an analytical study of structural materials subjected to shock waves as an interest from the blast mitigation group of the department of homeland security.   This work focuses on identifying deformation and damage mechanisms of the reinforcing low carbon steel (LCS) phase of civil structures subjected blast loading. These mechanisms govern the post-impact residual life. A program has been carried out in the MMRL focusing on various microstructure factors including prior deformation by cold rolling and post-impact performance.

The work focuses on identifying microstructural variations in steel discs subjected to impact pressures comparable to close range explosive loads. This range is defined by determining peak overpressure, P, due to spherical blast loading of explosive charges, see Figure 2-1, as a function of distance from the blast, R, and an equivalent charge weight of TNT, W, expressed as [22]

$$P = \frac{1772}{\left(R^3/W\right)^3} - \frac{114}{\left(R^3/W\right)^2} + \frac{108}{\left(R^3/W\right)} \tag{2.1}$$

where R is the distance from the blast and W is the weight of TNT in kg.
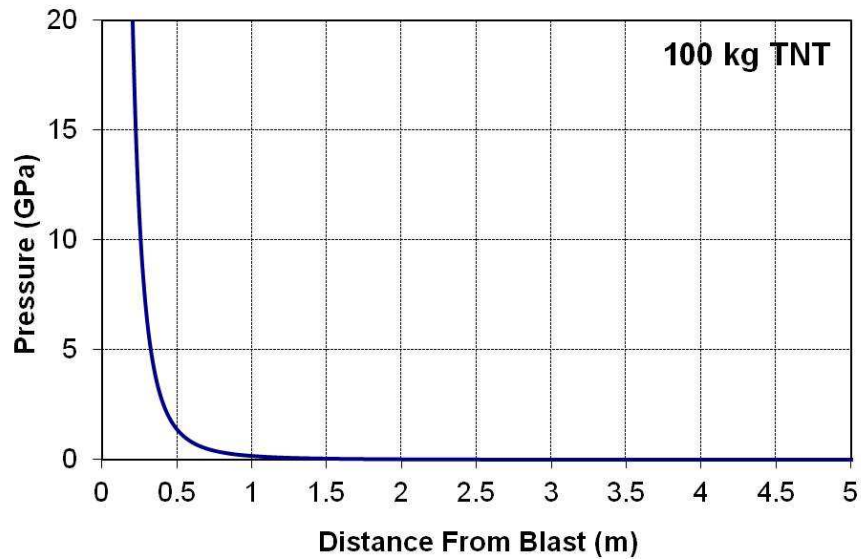
Figure 2-1: Pressure vs. distance for a 100kg TNT detonation

The simulated explosive pressure range is achieved using the single stage light gas gun system designed and built in the MMRL. The benefit of such an apparatus over conventional explosive testing is in the lab setting repeatability and ability to adjust the loading conditions, such as stress magnitude, loading duration, and temperature.

2.2.   **Background**

The term "light gas gun" is derived from the nature of the gas utilized in driving the projectile. Typically the pressure chamber is filled with a gas with a low molar (atomic) mass gas, typically either hydrogen or helium, which has a lower atomic weight and

higher speed of sound than air and a higher volumetric expansion coefficient, thus producing a faster projectile velocity.

For lower velocities, up to approximately 1000 m/s, single stage gas gun systems are employed. The term single stage refers to the single pressure chamber used for launching the projectile. This system consists of a pressure chamber, a pressure release valve, and a barrel. The compressed gas is released using a fast acting valve or rupture diaphragm and drives the projectile down the length of the barrel. Upon exiting the barrel, the projectile impacts the target specimen and is then recovered in a deceleration chamber. A simplified schematic of a single stage gas gun is shown in Figure 2-2.
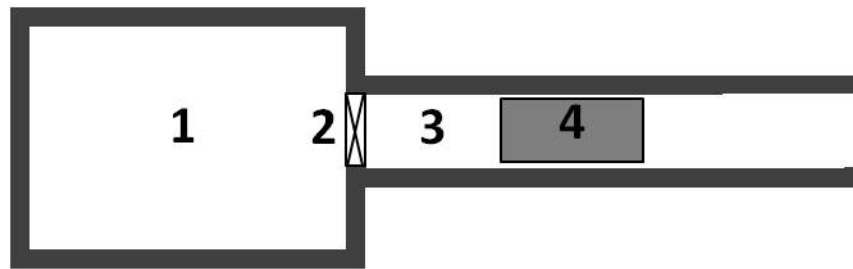
Figure 2-2: Schematic of a single stage light gas gun with components labeled; 1. Pressure chamber; 2.Fast acting valve; 3. Barrel; 4. Projectile.

For velocities higher than 1000 m/s, two stage gas gun systems are utilized, as shown in Figure 2-3. The first stage consists of a powder chamber which accelerates a piston using of gun powder or a light explosive. This piston then travels through the second stage pump tube and compresses a light gas ahead of it, creating extremely high pressures. This high pressure gas is then used to drive the projectile down the length of the barrel.
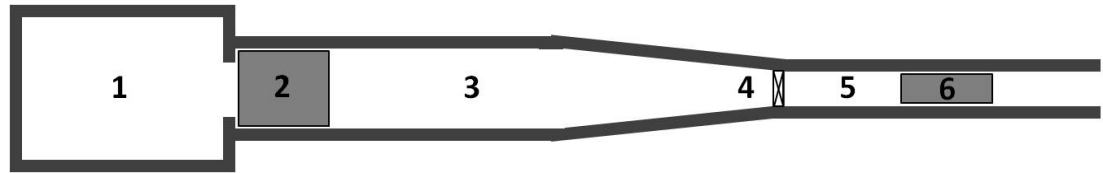
Figure 2-3: Schematic of a two stage light gas gun with components labeled; 1. Powder chamber (stage 1); 2. compression piston; 3. pump tube filled with light gas(stage 2); 4. Diaphragm; 5. launch tube or barrel; 6. projectile.

While the two stage gas gun system has the advantage of achieving higher velocities, this type of gun requires a large facility to accommodate the additional length of the pressure chambers and barrel, as the length of the apparatus can be in excess of 55 feet [1,2]. They also require sacrificial driving pistons to be machined for each experiment. There exist numerous sources in literature which describe designs and applications for single stage and two stage light gas guns [1, 2,12-18] as well as three stage gas guns [23].

The most common experiment using gas guns are planar plate impacts. The impactor plate is carried down the barrel of the gas gun by a sacrificial sabot at a velocity, V, and impacts a target disc which is at rest whose face is normal to the projectile trajectory. Upon impact, the particle velocity in the target and impactor plate equalize, thus producing a compressive shock wave in both materials. A general schematic of the impact setup is shown in Figure 2-4.
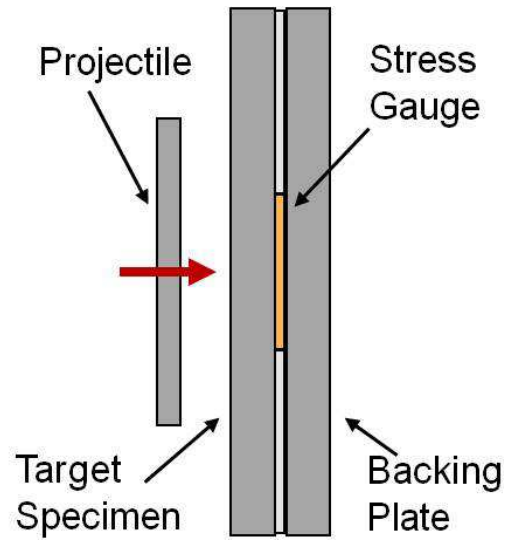
Figure 2-4: Schematic of a normal and planar plate impact configuration with a stress gauge bonded between the target specimen and a backing plate.

In Figure 2-4, a stress gauge is bonded in the target between the target specimen and a backing plate which measures the incident compressive stress wave as a function of time. The projectile velocity can be varied by adjusting the input pressure to the gas gun. After several trials, a trend of projectile velocity (at constant mass) as a function of input pressure can be plotted, as shown in Figure 2-5.
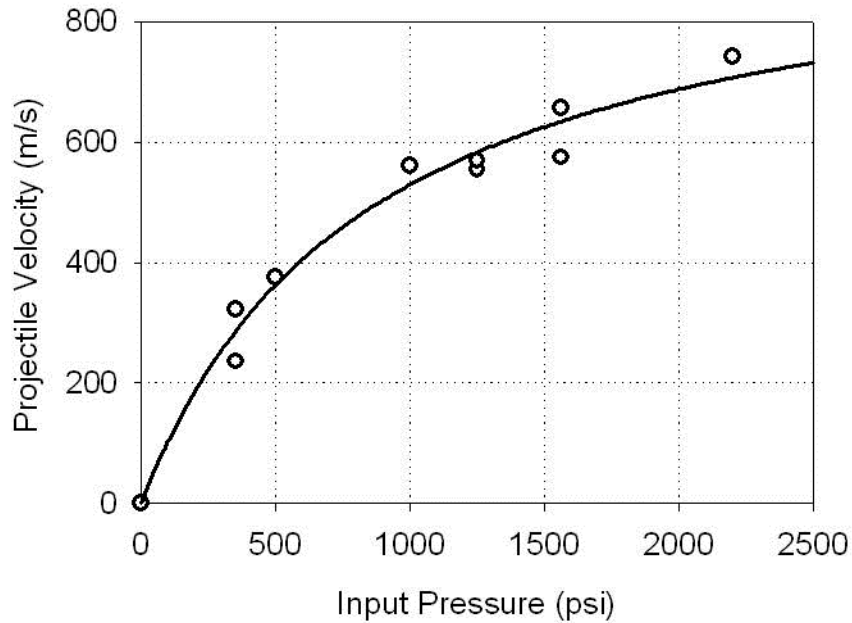
Figure 2-5: Projectile velocity vs. main chamber input pressure for projectile weights between 170-185g.

The velocity largely depends upon the design of the sabot with the overall weight being a major factor. Other considerations such as tolerance between the barrel, sealing or piston rings, lubricant, and material coefficient of friction are also key components affecting velocities.

2.3.   Gas Gun

The gas gun designed and built in the MMRL is characterized as a single stage light gas gun and is shown in Figure 2-6. The basic concept of the gas gun design are similar to those found in literature with several features, such as the breach system and vacuum

configuration, setting it apart from the common designs. The overall length of the entire assembly is approximately 16ft with additional space required behind the catch camber. All components of the pressure chamber and pressure control system are designed with 17-4PH stainless steel which has a yield strength of 145,000 psi (1000MPa) in condition A, up to 200,000 psi (1379 MPa) in condition H900 [3] depending on the specific heat treatments.
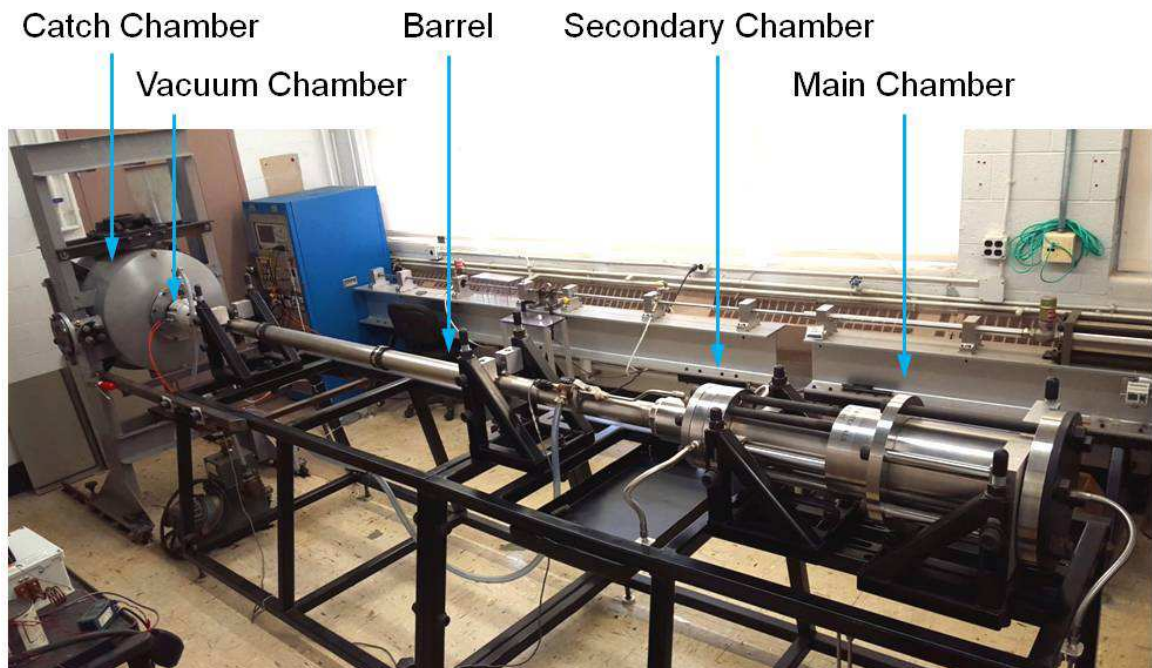
Figure 2-6: Single Stage Light Gas Gun (SSLGG) designed and built in the Mechanics of Materials Research Lab (MMRL) at URI.

The gas gun designed in the MMRL has proven to be an effective tool in studying shock waves in metals and through several design iterations of sabots, velocity systems and vacuum design arrangements, has reached a level of repeatability required for experimental accuracy. All major components of the pressure chamber were designed and assembled within the MMRL and machined by an outside vendor. The remaining components of the assembly were designed, machined and assembled by the MMRL.

The gas gun has 5 main components which will be discussed in detail within the following sections

1. (Section 2.3.1) Pressure Chamber

2. (Section 2.3.2) Pressure Control System

3. (Section 2.3.3) Barrel and Vacuum Target Fixture

4. (Section 2.3.4) Specimen Catch Chamber

5. (Section 2.3.5) Diagnostic System

2.3.1. **Pressure Chamber**

The pressure chamber is the component of the gas gun which contains the driving gas used to launch the projectile. The main pressure chamber consists of two sections tubing specified to standard sizes; NPS8 schedule 160 pipe and a NPS5 schedule 160 pipe coupled together with a machined pressure neck/coupler and a back plate as shown in the 3D model of Figure 2-7. The pressure chamber is supported on the main frame of the gas gun by two sub frames which have a height adjustment screws attached to the mounting blocks, as shown in Figure 2-8.
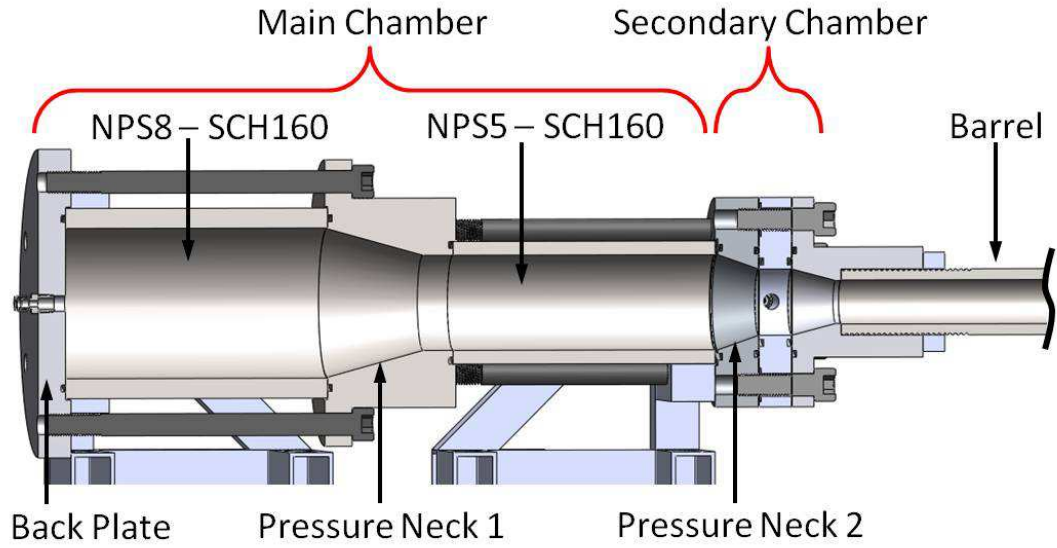
Figure 2-7: 3D model of the pressure chambers of the SSLGG.
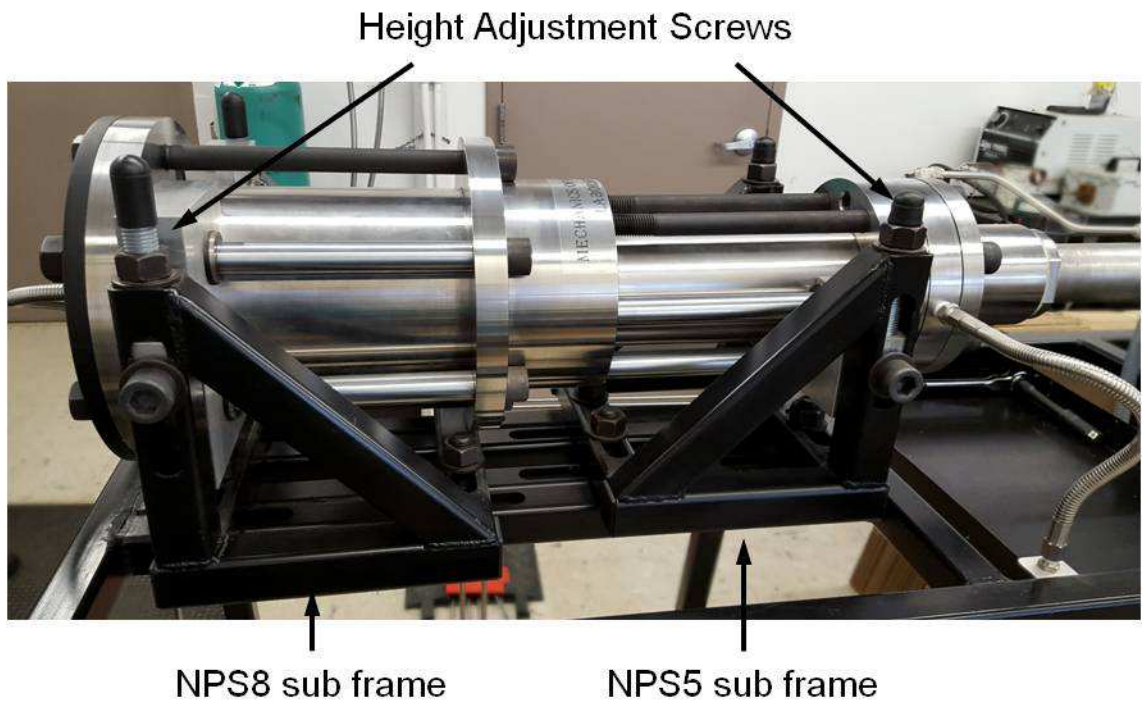
Figure 2-8: **Sub** frame supports for the pressure chamber section of the gas gun.

The volume of the main pressure chamber is approximately 750 in^3 and the volume of the barrel is 376 in^3. As the projectile moves down the barrel, the capacity is increased to 1126 in^3. The large capacity of the pressure chamber allows the gas to expand down the barrel behind the projectile and still retain 66% of its original input pressure.

As seen in the schematic of the pressure chamber in Figure 2-7, tapered transitional regions between differing pipe diameter sections were made. The fluid velocity across the pressure necks increase in velocity and decrease in pressure due to continuity. Abrupt decreases in diameters create a contraction in the fluid flow area, known as vena contracta, and cause eddies in the flow in the barrel entrance. The optimal design would be to have the pressure chamber the same diameter as the barrel; however this is not a feasible solution, as it would nearly double the length of the assembly. Instead, two pressure necks within the main chamber were utilized in order to decrease the diameter from the largest section, the NPS8 pipe, down to the rupture discs, and another tapered section within the barrel mount.

The pressure chamber is designed for an input pressure limit of 6,000 psi. This pressure is the maximum pressure that a tank of helium supplies. The design principles of the cylinders are based on closed end, thick walled cylinders, with an internal pressure, p_1, and an external atmospheric pressure p_2=0. The stresses can be determined from the loading condition for a thick walled cylinder as shown in Figure 2-9.
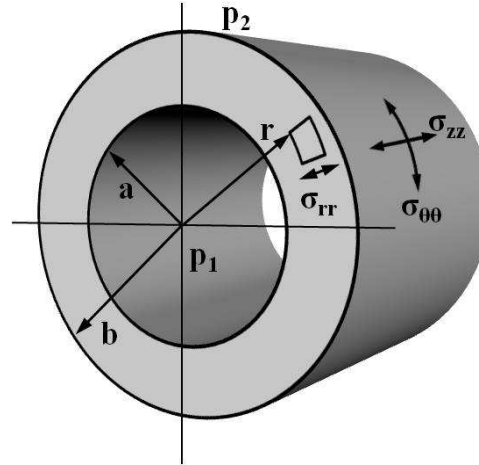
Figure 2-9: Stress components for a thick walled cylinder with internal pressure p_1.

The stress components developed within a thick walled cylinder are expressed as [4];

$$\sigma_{\theta\theta} = p_1 \frac{a^2 \left(r^2 - b^2 \right)}{r^2 \left(b^2 - a^2 \right)} \tag{2.2}$$

$$\sigma_{\theta\theta} = p_1 \frac{a^2 \left(r^2 + b^2 \right)}{r^2 \left(b^2 - a^2 \right)} \tag{2.3}$$

$$\sigma_{zz} = p_1 \frac{a^2}{b^2 - a^2} \tag{2.4}$$

$$\tau_{max} = \frac{\sigma_{max} - \sigma_{min}}{2} \tag{2.5}$$

where σ_{rr}, $\sigma_{\theta\theta}$, and σ_{zz} are the radial, hoop, and longitudinal stresses, respectively. The cylinder is subjected to an internal pressure of p_1 has an internal radius a and an outer radius b. Setting the radius, r, for the inner and outer radius, the minimum and maximum stress components in each cylinder of the pressure chamber are tabulated in Table 1.

Table 2-1: Principal stress components in the main pressure chamber cylinder

	NPS5		NPS8	
Principal Stress	inner wall	outer wall	inner wall	outer wall
σ_{rr} (psi)	-6,000	0	-6,000	0
$\sigma_{\theta\theta}$ (psi)	24,068	18,068	25,804	19,804
σ_{zz} (psi)	9,034	9,034	9,902	9,902
τ_{max} (psi)	15,034	9,034	15,902	9,902

Considering the minimum yield stress of 17-4PH stainless steel is 145,000 psi, the safety factor of the cylinders expressed as the ratio of yield stress to applied stress is calculated and the results are shown in Table 2.

Table 2-2: Factor of safety for main pressure chamber cylinders

	NPS5		NPS8	
Safety Factor	inner wall	outer wall	inner wall	outer wall
σ_{rr}	23	-	23	-
$\sigma_{\theta\theta}$	6	8	5	7
σ_{zz}	15	15	14	14
τ_{max}	9	15	9	14

As shown in Table 3, the lowest safety factor of 5 occurs with the hoop stress in the NPS8 pipe of the main pressure chamber. This is still a conservative value since the yield stress of the material was assumed to be that associated with the heat treatment of condition A.

The strain components in the pressure vessel can be computed in a similar manner. The strain components are expressed as [4];

$$\varepsilon_{rr} = \frac{1}{E}\left[\sigma_{rr} - \nu\left(\sigma_{\theta\theta} + \sigma_{zz}\right)\right] \tag{2.6}$$

$$\varepsilon_{\theta\theta} = \frac{1}{E}\left[\sigma_{\theta\theta} - \nu\left(\sigma_{rr} + \sigma_{zz}\right)\right] \tag{2.7}$$

$$\varepsilon_{zz} = \frac{1}{E}\left[\sigma_{zz} - \nu\left(\sigma_{rr} + \sigma_{\theta\theta}\right)\right] \tag{2.8}$$

with a Poisson's ratio of 0.272 and an elastic modulus of 28.5E6 psi (197E3 MPa) the strains can be calculated and shown in Table 3.

Table 2-3: Principal Strain components in the main pressure chamber cylinders of the SSLGG.

	NPS5		NPS8	
Principal Strain	inner wall	outer wall	inner wall	outer wall
ε_{rr} (in./in.)	-0.001	0.000	-0.001	0.000
$\varepsilon_{\theta\theta}$ (in./in.)	0.001	0.001	0.001	0.001
ε_{zz} (in./in.)	0.000	0.000	0.000	0.000

From the strain values shown in Table 2-3, corresponding displacements can be determined. The maximum displacement of the cylinders is approximately 0.009 in., which is within the limits of the machining tolerances (± 0.010 in.), therefore no binding or leaking from seals at interfaces will occur.

Each section of the chamber is held together by six grade 8 alloy steel 1"-8 bolts with a class 3A fit which have a minimum tensile strength of 170,000 psi. Designing for an

input pressure of 6,000 psi yields a pressure of 301,592 lbs on the chamber end cap. Divided over the six bolts yields 64,000 psi on each bolt.

The end cap of the pressure chamber, Figure 2-10, can be considered as a circular flat plate with a circular hole in the center with fixed edge boundary conditions, as shown in Figure 2-11.
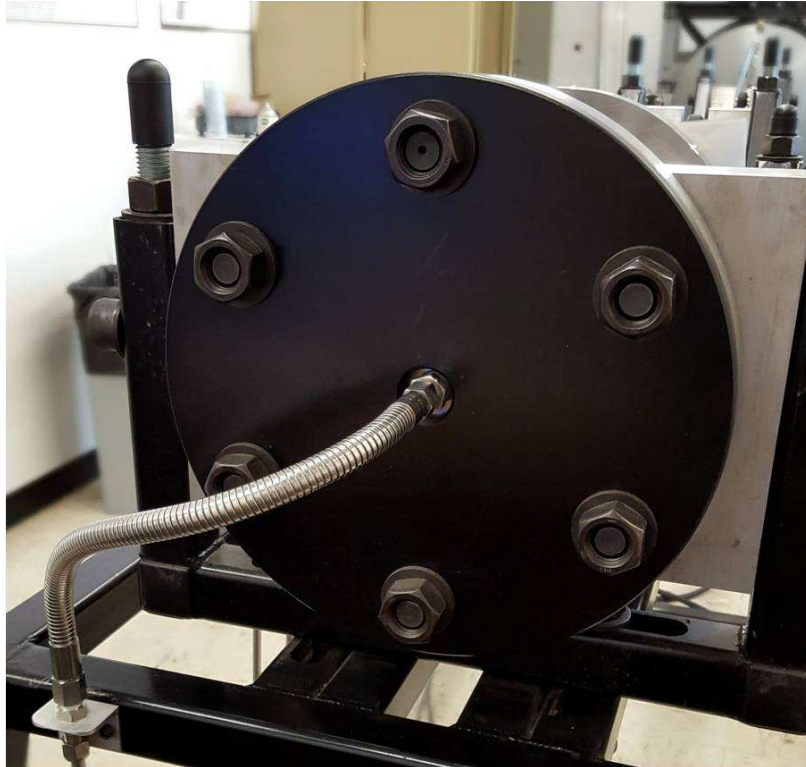
Figure 2-10: End caps of the main pressure chamber held on by six 1"-8 bolts threaded into the 17-4PH SS back plate with an additional D2 tool steel plate held on by six grade 8 nuts.
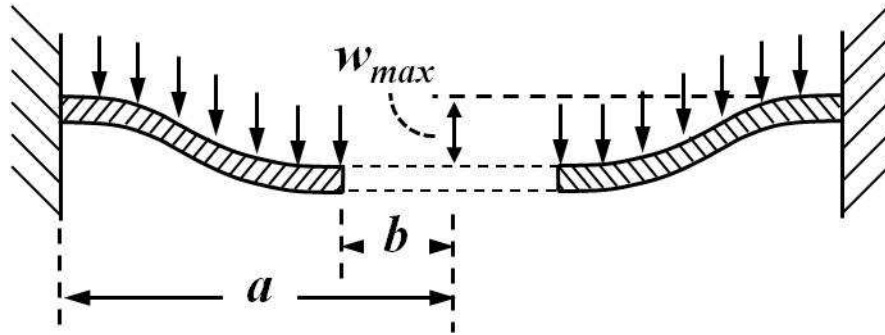
Figure 2-11: Loading and boundary condition for pressure chamber end cap [19].

The plate has a diameter, a, inside the chamber walls of 8 in. and a hole tapped for 1/2 in. NPT fitting, which has a diameter, b, of approximately a 0.8 in. and is uniformly loaded by an internal pressure of 6,000 psi. The majority of the plate is 1.250 in. thick, however is only 1.045 in. thick at the o-ring groove. The maximum stress and deflection can be calculated as [19]

$$\sigma_{max} = k\frac{pa^2}{h^2}$$
(2.9)

$$w_{max} = k_1\frac{pa^4}{Eh^3}$$
(2.10)

where the constants k and k_1 are based on the ratio a/b and h is the thickness, set to 1.000 in. Timoshenko [19] has published values of k and k_1 for several ratios. Extrapolating his values to a ratio $a/b=10$, gives values of approximately 0.83 and 0.28 for k and k_1, respectively. Solving for the maximum stress when the pressure chamber is filled to 6,000 psi yields a maximum stress of $\sigma_{max} = 73,400\,\text{psi}$ and a maximum deflection of $w_{max} = 0.013\,\text{in}$. This is still less than half of the yield strength of the 17-4PH stainless steel end cap when loaded to 6,000 psi. This is a higher estimate of the predicted stress

considering that the hole in the center of the plate is plugged with a high strength connector. This hole however, in addition to the low safety factor of 2, is a potential source for leaks when the plate deflects at high pressures. For this reason, an additional plate, 0.750 in. thick, made of D2 tool steel was added. The additional plate reduces the maximum stress to $\sigma_{max} = 24,877\,\text{psi}$ and the maximum deflection to $w_{max} = 0.002\,\text{in.}$ which increases the factor of safety to over 5.

2.3.2. Pressure Control System

The gas being used in the light gas gun is helium which is filled via high pressure helium tanks, the maximum pressure of which is 6,000 psi. The feed lines are made of 3/8 in. stainless steel seamless tubing with 0.065 in. wall thickness connected with stainless steel Swagelok fittings. The gas feed system is rated for a 6,200 psi allowable working pressure. A high pressure manifold and regulator was installed for a multiple tank reservoir since the gas gun uses large quantities of gas during high pressure tests; see Figure 2-12. The control panel for filling the gas gun is shown in Figure 2-13. The panel includes two digital pressure gauges (Dwyer DPG-111) which have a 5000 psi limit with 1 psi increments and an accuracy of 0.25%. The gauges monitor the pressure in the main and secondary chambers. The control panel has three valves for controlling the gas. The control panel includes a dump valve, Valve 3 in Figure 2-13, which evacuates the entire system of its pressure in the event that there is an error with the experimental setup and the test needs to be cancelled.
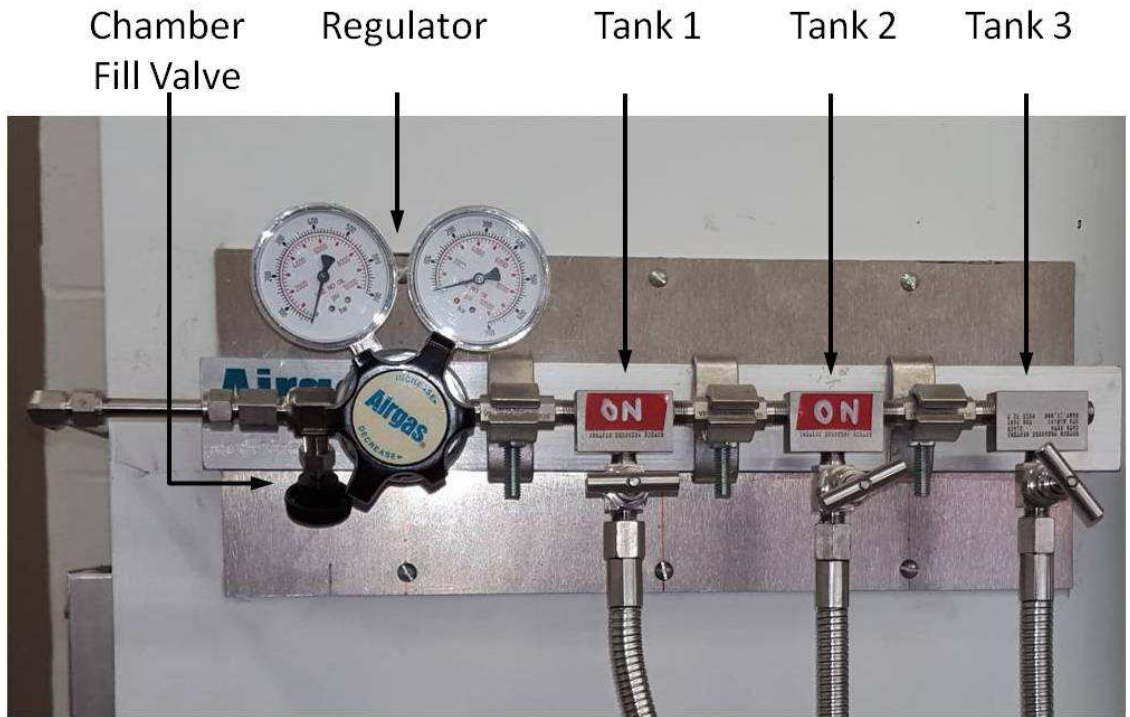
Figure 2-12: Gas regulator and a three tank manifold for a high capacity gas reservoir
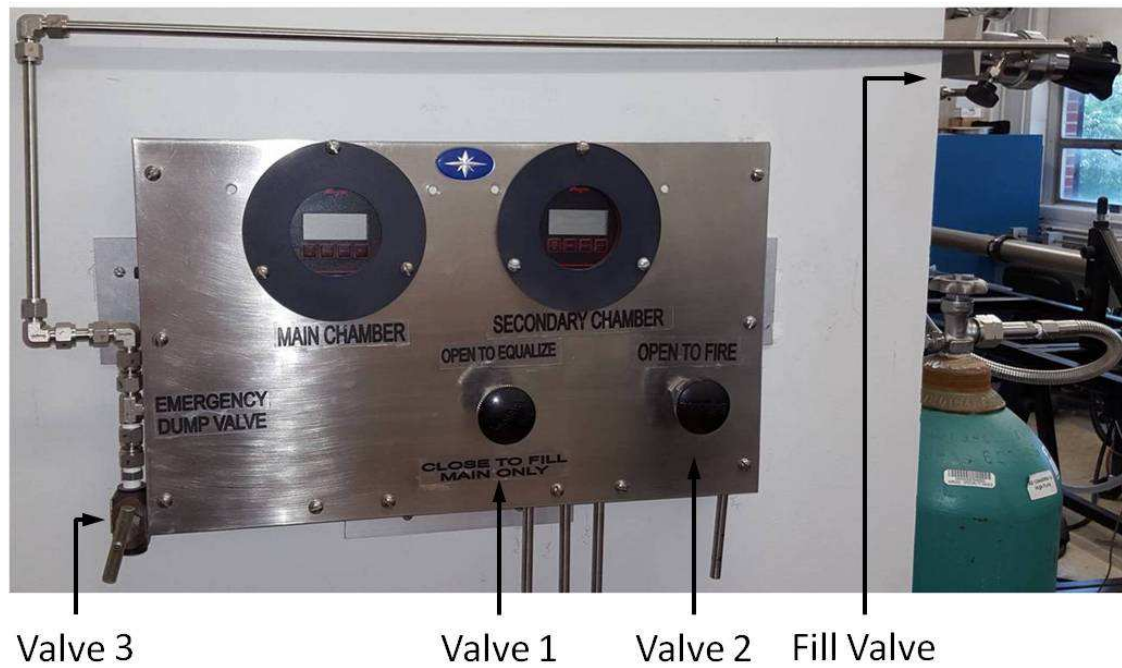
Figure 2-13: Gas gun pressure control panel. Valve 1 is used to close the feed to the secondary chamber. Valve 2 is used to release the pressure from the secondary chamber

to fire the gas gun. Valve 3 is used to evacuate the entire system without firing the gas gun.

The gas gun is triggered using a pressure release section consisting of two sets of rupture discs enclosing the secondary pressure chamber, similar to that used by Gupta et al. [20] and Sikka [21]. A close up 3D model of this system is shown in Figure 2-14.
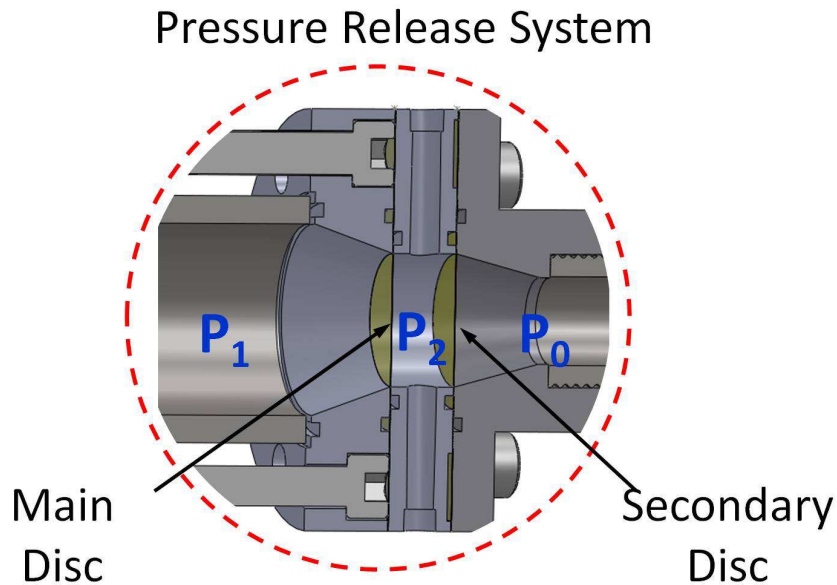
Figure 2-14: Gas gun pressure release system for controlled launch of projectiles.

As shown in Figure 2-14, two sets of rupture discs are used to separate the secondary chamber (P_2) from the main chamber (P_1) and the barrel section (P_0). The advantage of this double rupture disc setup is that it provides a consistent and controllable release of pressure to the projectile, where as a single rupture disc setup, typically used in shock tubes, the pressure is continuously increased until the disc ruptures. The single rupture

disc setup only allows for blast pressures at increments equal to the rupture disc break pressures. The current design allows the user to control the pressure to the level required by the specific experiment. The system works on a pressure differential to break the discs and launch the projectile.

A typical procedure for this pressure control is as follows. As shown in Figure 2-14, pressures associated with the main chamber, secondary chamber, and barrel section are designated by P_1, P_2, and P_0, respectively. With valve 1 in the fully opened position, gas is fed into the main and secondary chambers simultaneously such that P_1 and P_2 are equivalent. Once the pressure, P_2, in the secondary chamber is at the desired level, the gas feed to the secondary chamber is closed with valve 1; see Figure 2-13. Gas is then fed only to the main chamber until the pressure, P_1, is such that $P_1 > P_{rupture} > P_1 - P_2$. Once the desired main chamber pressure is reached, valve 2 is opened to bleed pressure from the secondary chamber and launch the projectile.

Applying specific pressures to the outlined procedure, if the main chamber is to be pressurized to $P_1 = 800$ psi, the rupture discs should be set to break at approximately $P_{rupture} = 1,000$ psi. First, gas is fed into main and secondary chambers until $P_1 = P_2 = 800$ psi. After closing of the secondary chamber, Valve 1 in Figure 2-13, gas is fed into only the main chamber until the pressure $P_1 = 1600$ psi. Now the difference between main and secondary is 800 psi and between secondary and atmosphere is 800 psi; both below $P_{rupture}$. The gas gun is now ready to launch the projectile. Valve 2 is now opened to begin bleeding the pressure from the secondary chamber and the pressure differential across the diaphragms of the main and secondary chamber will exceed the rupture pressure and both sets of discs will break, launching the projectile.

The rupture discs are made of thin (0.004 in.) polyester sheets. The rupture disc breaking pressure, $P_{rupture}$, is varied by increasing the number of sheets used in each section. Initial trials of determining the rupture strength per sheet in this particular configuration showed that each rupture disc breaks between 70 and 100 psi. From this range of rupture pressures per sheet, an accurate relationship of the number of sheets to be used for a given input pressure is determined. A relationship between gas pressure and number of rupture discs is shown in Figure 2-15.
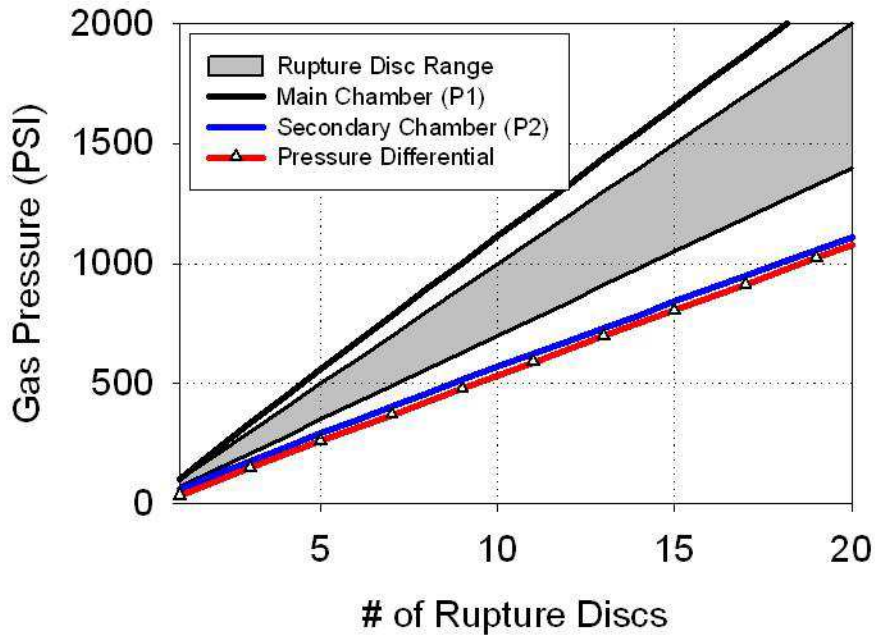
Figure 2-15: Gas pressure vs. number of rupture discs used in the trigger system of the SSLGG. The black curve represents the main chamber pressure, The red curve represents the secondary chamber pressure, and the blue curve represents the pressure differential between the two chambers. The grey area shows the upper and lower limit for the differential pressure at which the rupture discs break.

2.3.3. Barrel and Vacuum Target Fixture

The barrel section is made of seamless 316 stainless steel tubing measuring 10 ft in length with an inner diameter of 2in. and a wall thickness of 0.5in . To reduce friction and increase projectile velocity, the ID of the barrel was honed to a surface finish of 8RA or better.

The barrel is supported on the main frame by a set of two sub frames. Each sub frame is equipped with height adjustment screws. The barrel is directly supported by a set of polyurethane wheels so that the barrel section can be rolled forward when uncoupling the pressure release system to change out rupture discs; see Figure xxx.
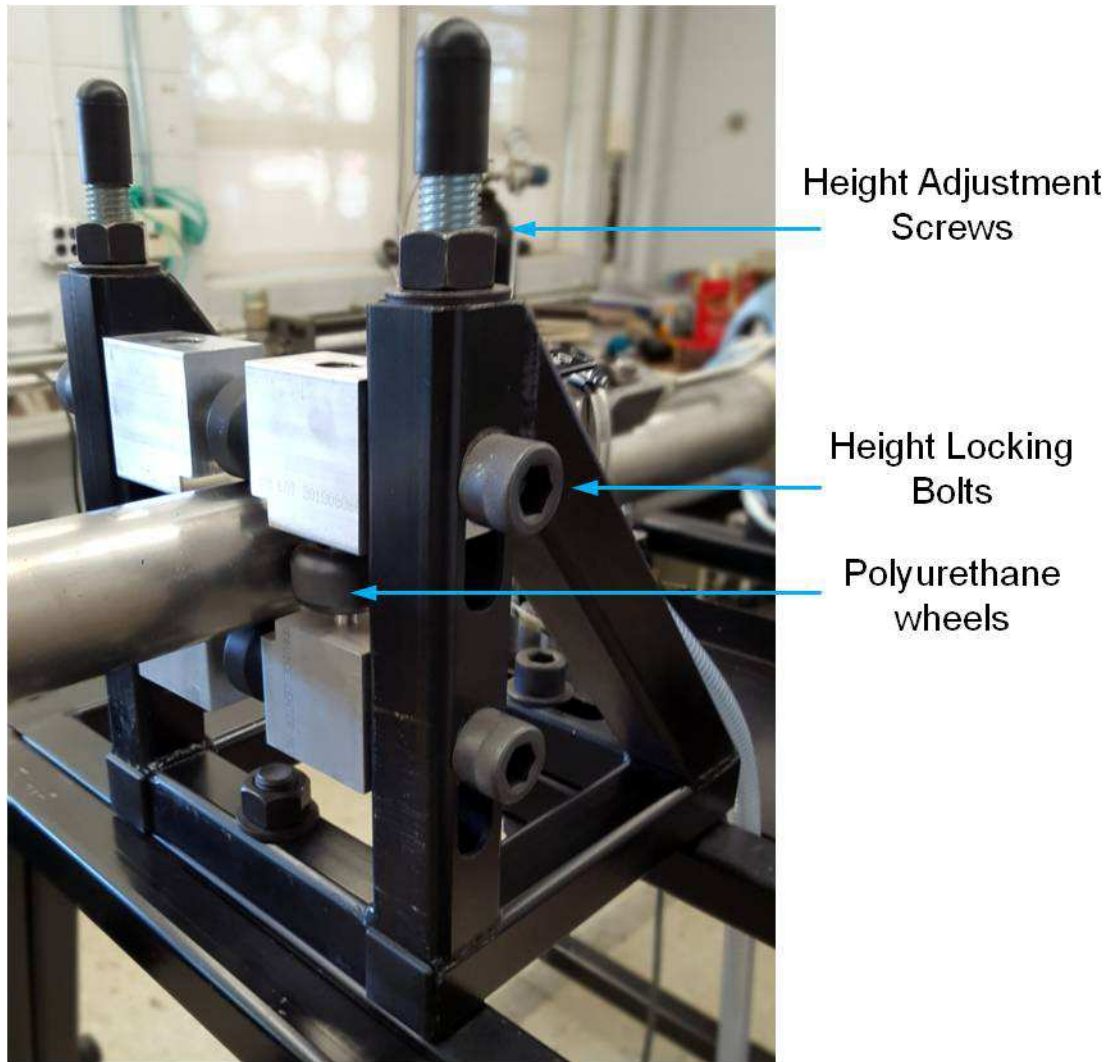
Figure 2-16: Barrel support sub frames showing height adjustment screws and wheel supports

Prior to acquiring the barrel section, a study was done to determine the optimal length of the barrel. Using Newton's second law, the basic equations of motion, and the ideal gas law, the projectile velocity was incrementally determined as a function of the pressure drop in the barrel and distance including the effects of drag, and is shown in Figure 2-17.
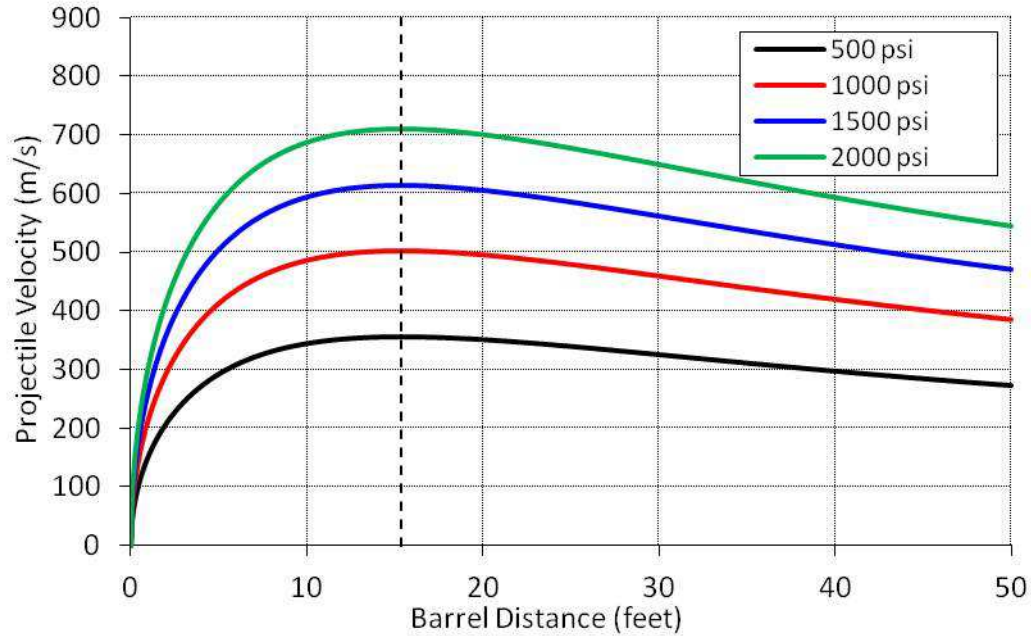
Figure 2-17: Preliminary calculations of projectile velocity vs. position in the barrel for several input pressures.

As shown in the figure above, the projectile eventually begins to decelerate due to the drag and friction forces and the loss of driving pressure as the volume and pressure of the driving gas changes. The optimal length for this particular volume chamber is approximately 15ft. For constraints of the facility, the barrel was limited to 10ft. However, the difference in velocities between the 10ft and 15ft length barrels is only 3%.

Again, applying equations (2.2) through (2.5) to the barrel section, the stress components and safety factors can be determined and are shown in Table 2-4 and Table 2-5.

Table 2-4: Principal stress components in the Barrel section

Principal Stress	Barrel	
	inner wall	outer wall
σ_{rr} (psi)	-6,000	0
$\sigma_{\theta\theta}$ (psi)	15,600	9,600
σ_{zz} (psi)	4,800	4,800
τ_{max} (psi)	10,800	4,800

Table 2-5: Factor of safety for the barrel section

Safety Factor	Barrel	
	inner wall	outer wall
σ_{rr}	23	-
$\sigma_{\theta\theta}$	9	15
σ_{zz}	29	29
τ_{max}	13	29

As shown in Table 2-4 and Table 2-5, the a pressure input of 6,000 psi would lead to a maximum hoop stress of 15,600 psi with the lowest safety factor of 9, which again is conservative given that the barrel is continuously bleeding pressure out of the barrel end.

Attached to the end of the barrel is a vacuum chamber which also serves as the target fixture and mount for the velocity lasers; see Figure 2-18.
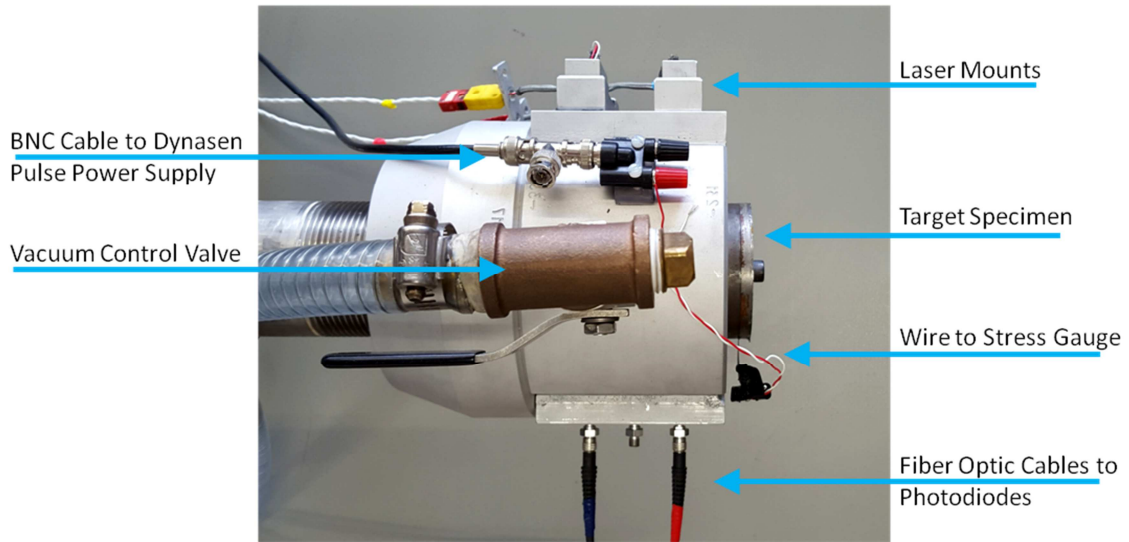
Figure 2-18: Vacuum chamber and target and velocity laser mount at end of the SSLGG barrel.

As seen at the top of Figure 2-18, the velocity lasers are mounted directly to the vacuum chamber. These lasers pass a beam perpendicular to the barrel mouth. The light from the lasers are received by fiber optic cables attached on the other side of the vacuum chamber. This light is collected in high speed photodiodes, which converts light intensity into voltage recorded on the oscilloscope. The ports in the vacuum chamber for both the lasers and the fiber optic cables are sealed by glass windows and O-rings.

The entire barrel section and target mount is maintained under vacuum using a mechanical vacuum pump which evacuates the barrel and target fixture into the 10^{-3} torr range. The vacuum serves two purposes. First, a vacuum is drawn between rupture disc 2 and the projectile to load the projectile. Secondly, the vacuum serves to reduce the drag on the projectile to increase the velocity as well as to prevent premature air shock or disturbance of the target specimen. This is especially important to ensure a planar impact

with the target specimen. The target specimen is mounted directly to the end of the vacuum chamber, and the face of the target specimen creates a vacuum seal against an O-ring embedded groove at the end of the vacuum fixture; Figure 2-19.
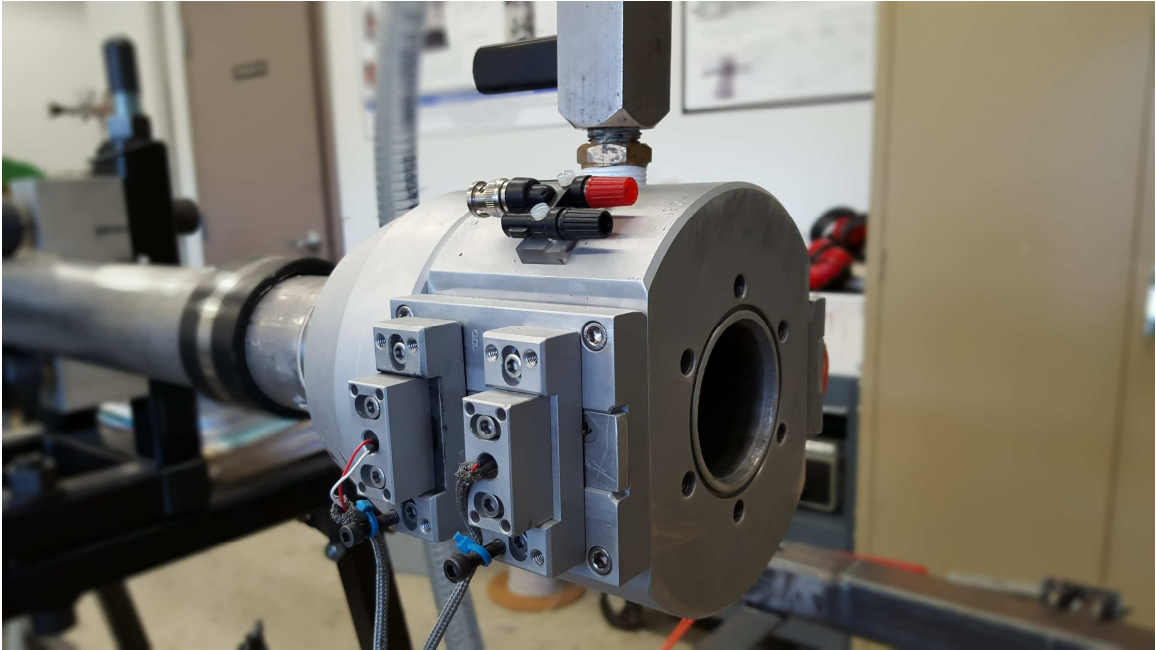
Figure 2-19: Vacuum chamber mouth at which the target specimen is mounted.

The distance from the end of the barrel mouth to the face of the target is such that the 5in long projectile remains partially within the barrel section upon impacting the target. This ensures that the target plate and impactor plate are consistently planar during impact.

2.3.4.   Specimen Catch Chamber

During the plate impact test, the specimen is impacted at the end of the vacuum chamber and the projectile and target package must be soft recovered in order to preserve the specimen integrity and to not introduce secondary impact effects. A catch camber is

located at the end of the barrel. The chamber itself is mounted on linear sliders and attached to the gas gun frame with a separate steel rail that is attached to a shock absorber system. This provides the necessary blow back of the chamber to allow the pressure relief of the excess helium while still containing any debris from the plastic sabot; see Figure 2-20.
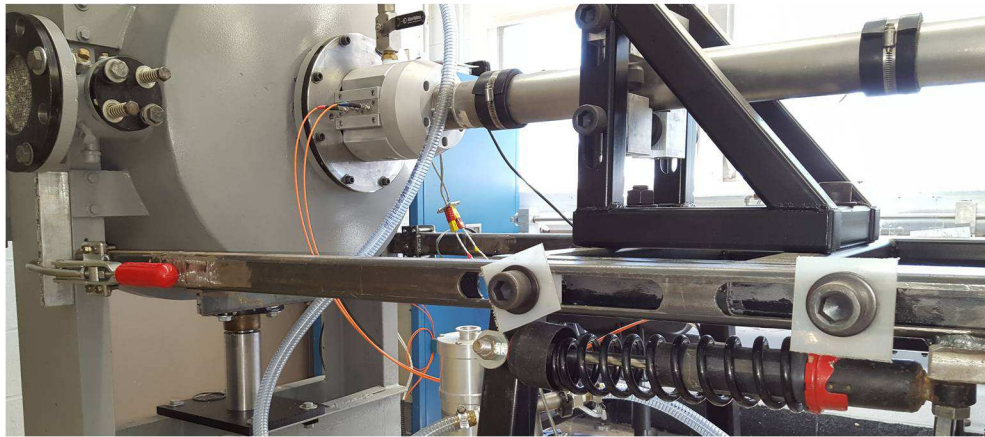
Figure 2-20: Shock absorber system for blow back of catch chamber during pressure release.

Within the catch chamber, a specimen catch box is mounted to upper and lower 2in. diameter solid steel posts. This catch box is filled with a high density, non-hardening clay in order to decelerate the target plate as seen in Figure 2-21.
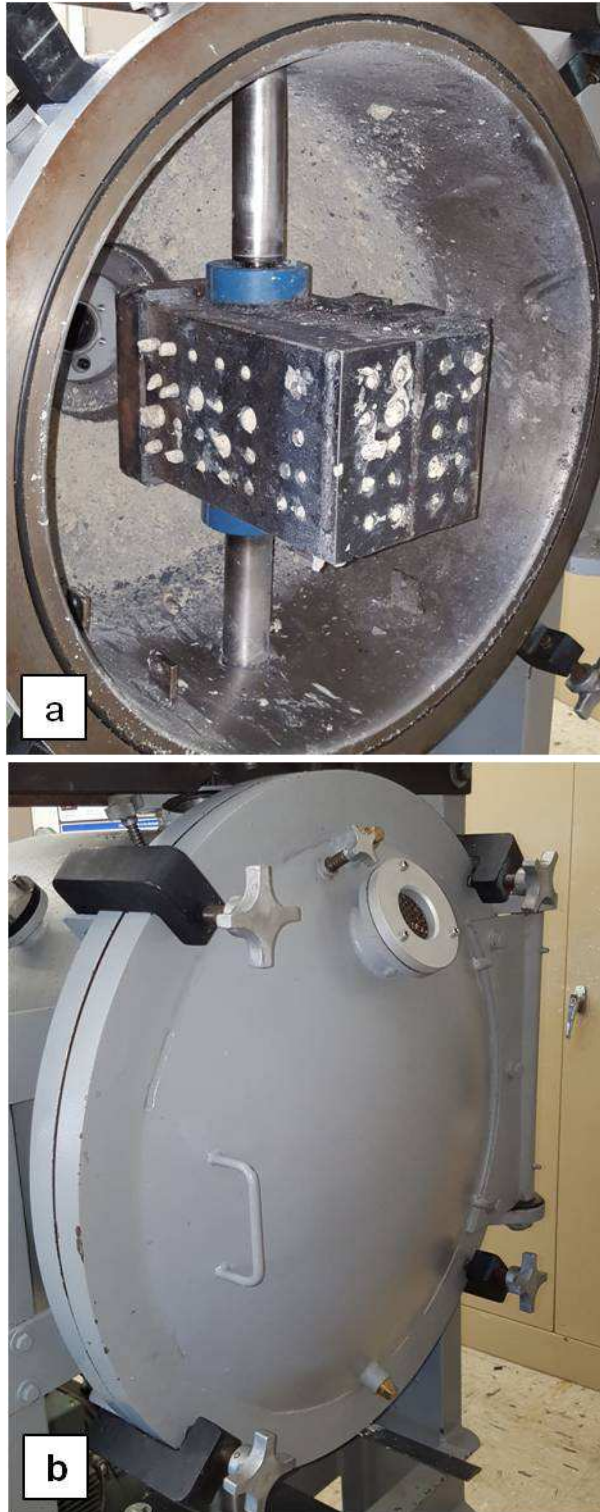
Figure 2-21: a) Specimen Catch Box filled with high density non-hardening oil based clay for soft recovery of specimens and b) specimen catch chamber access door

Containing the catch box assembly and absorbing clay outside of the vacuum avoids interference with the vacuum quality and laser and fiber optic ports due to the clay outgassing and splatter. This reduces the downtime of maintenance of the vacuum chamber and catch chamber between each experiment.

2.3.5. **Diagnostic System**

Recording the plate impact event is done using a Tektronix DPO3034 high speed digital phosphorus oscilloscope. This is a 4 channel oscilloscope with a 300MHz bandwidth and a sample rate of 2.5 GS/s. The resolution of the oscilloscope is more than sufficient for these plate impact experiments given that the oscilloscope records at 2.5 samples per nanosecond, while the rise time of the incident stress pulse is on the order of 100ns. The recording start time is triggered via the velocity lasers mounted at the end of the SSLGG barrel. The trigger position in the oscilloscope is set such that data is captured 400μs prior to the event and for 1.6ms after the data record is triggered to ensure that the entire event is captured. When the oscilloscope is triggered to record from the velocity lasers, it simultaneously sends an output trigger signal via BNC cable to the Dynasen pulse power supply to excite the stress gauge. A schematic of the full diagnostic system is shown in Figure 2-22, the components of which will be described in the following sections.
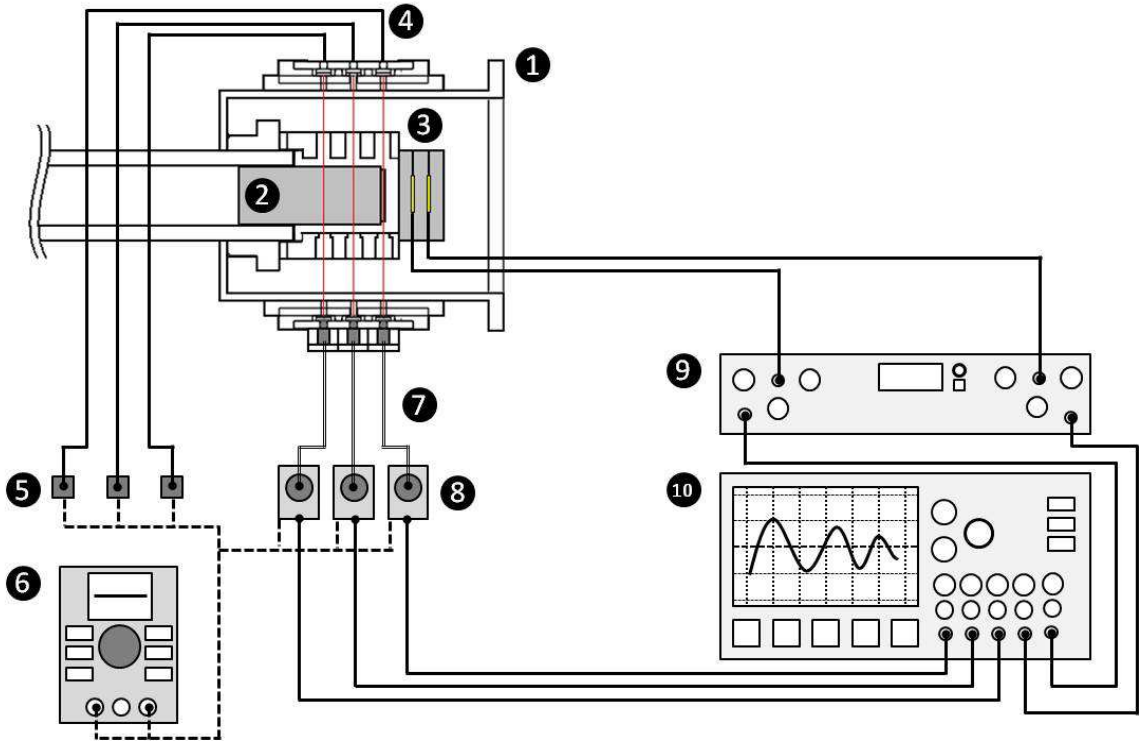
Figure 2-22: Schematic of gas gun diagnostic system for measuring impact velocity and stress. Components are labeled as 1. vacuum chamber, 2. barrel and projectile, 3. target package with manganin stress gauges, 4. lasers, 5. laser drivers, 6. DC power supply, 7. fiber optic cables, 8. photodetectors, 9. Dynasen stress gauge power supply, 10. digital oscilloscope.

All of the electronics for the velocity and stress measurement are mounted in a separate electrical stack. The stack is located in close proximity to the barrel exit and catch chamber in order to reduce the cable length needed for the stress gauge. The control panel has power switches for each individual component, shown in Figure 2-23.
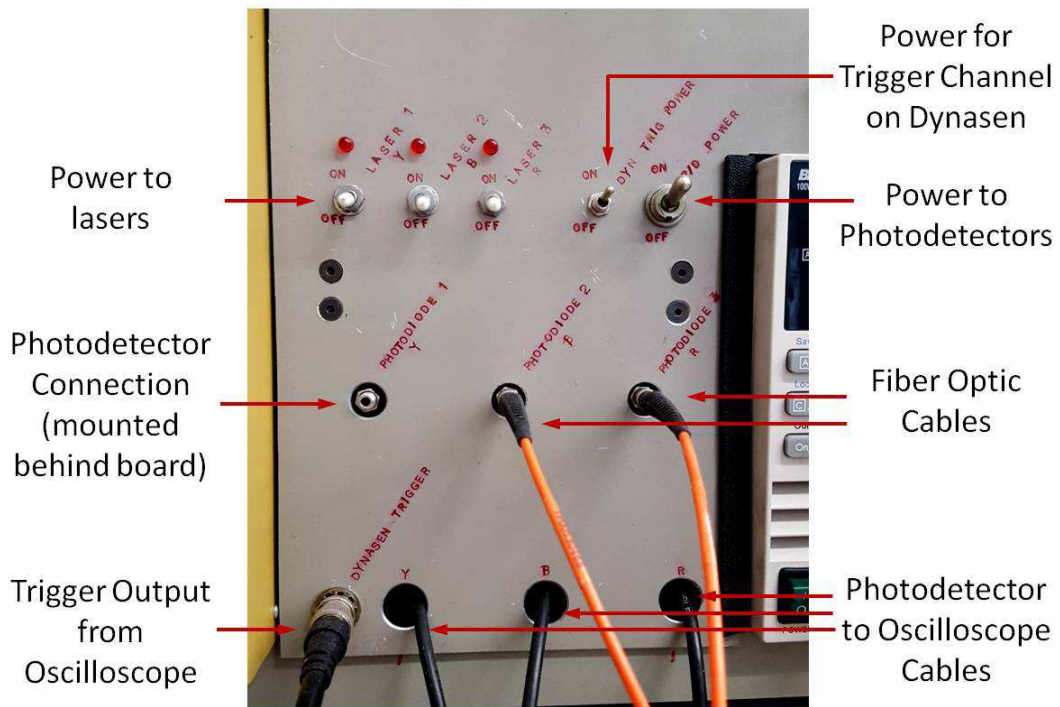
Figure 2-23: Diagnostics control panel for the gas gun. Each channel is labeled Y/B/R which correspond the color coordination of each channel on the oscilloscope. The photodetectors are mounted directly to the back of the panel, with connections on front to attach the fiber optics.

The control panel has individual power switches for each laser with indicating LEDs, while the photodetectors share the same power switch. The switch labeled "DYN TRIG POWER" is used the power switch for the trigger channel output of the oscilloscope feeding into the trigger input of the Dynasen power supply. The switch amplifies the signal from the oscilloscope up to the required 9 volts needed for triggering the Dynasen power supply. Each photodetector is mounted directly to the panel, with connectors in front for directly attaching the fiber optic cables. Each photodetector has its own output cable feeding into separate channels on the oscilloscope mounted above. All channels are labeled with designations Y/B/R, corresponding to the yellow, blue, or red color coordination of each channel on the oscilloscope. The DC power supply is mounted

133

directly to the right of the panel which supplies the necessary 9 volt source for the lasers, photodetectors, and trigger channel.

2.3.5.1. **Velocity Measurement**

The projectile velocity is measured using a set of high power lasers and photodetectors mounted perpendicular to the barrel between the barrel mouth and the target specimen, as seen in Figure 2-18. With reference to the schematic shown in Figure 2-22, a 9 volt DC power supply powers a set of constant current laser drivers (5), which drive the 660nm lasers (4). The laser light is received by high speed photodetectors (8), via fiber optic cables (7) mounted across the barrel mouth, opposite to the lasers. The photodetectors convert the intensity of incident light into a voltage which is recorded on the high speed oscilloscope (10). The through beams are sequentially interrupted by the passing projectile (2). This causes the voltage output from the photodiodes to drop to zero. A typical screen shot of the signal from the photodetector voltage output is shown in Figure 2-24.
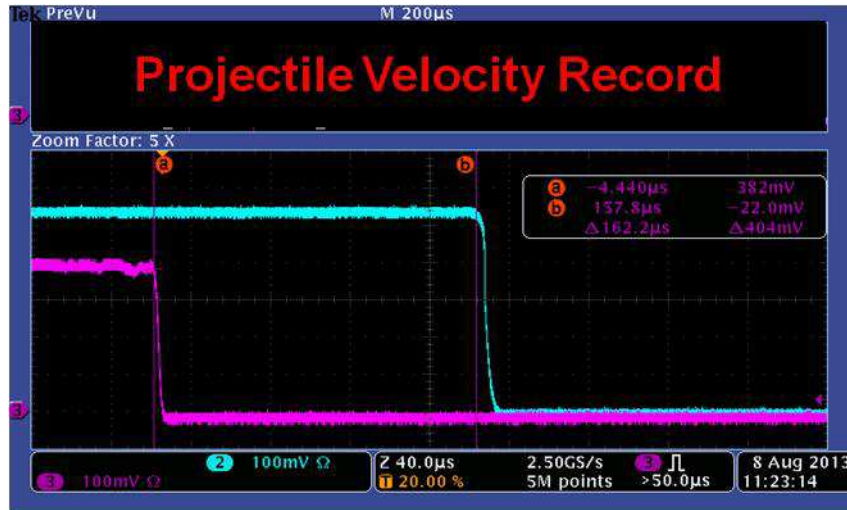
Figure 2-24: Typical recording of voltage drop of photodetectors when a projectile interrupts the laser signal.

With known distances between the lasers, and determining the time between voltage drop from the photodetector signal, the projectile velocity just prior to impact can be determined. Several other methods exist by which the projectile velocity can be measured, such as the flash x-ray measurement technique [12] or by the use of velocity shorting pins [9,13,15-18]

The laser signals are received using ThorLabs high speed reverse-biased silicon photodetectors (DET10A). The measured output current is linearly proportional to input optical power. When coupled with a 50 terminator, the response time of the photodetector is as little as 1ns. These detectors are capable of receiving light between 200 and 1100 nm in wavelength. The responsivity, which is a measure of the electrical output per optical input, of the photodetector for the given wavelengths is shown in Figure 2-25.
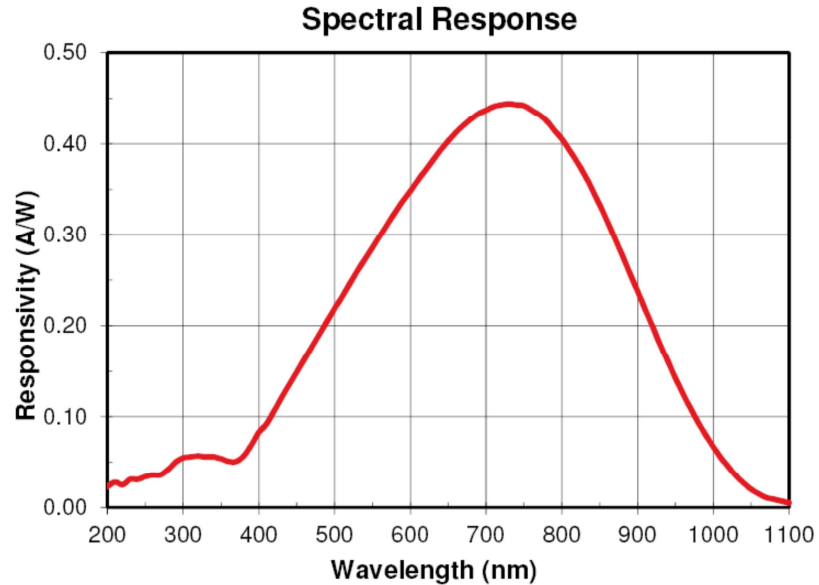
Figure 2-25: Responsivity of ThorLabs DET10A photodetector for a range of wavelengths [5]

Based on the responsivity of the photodetectors used, the lasers selected are 660nm wavelength (LPC-826) diodes with a maximum power output of 250mW. By using 660nm wavelength lasers, it is still within the visible spectrum making alignment an easier task and, staying close to the peak wavelength, the output voltage of the photodetector is maximized. In order to achieve the maximum output voltage of the photodetectors, proper alignment of the lasers is necessary. The fiber optic cables have a very low acceptance angle, therefore the lasers mounts have the ability for fine lateral and tilt adjustments; see Figure 2-26. (Note: Extreme caution should be taken and eye protection should be worn when using these high power lasers as eye damage can occur.)
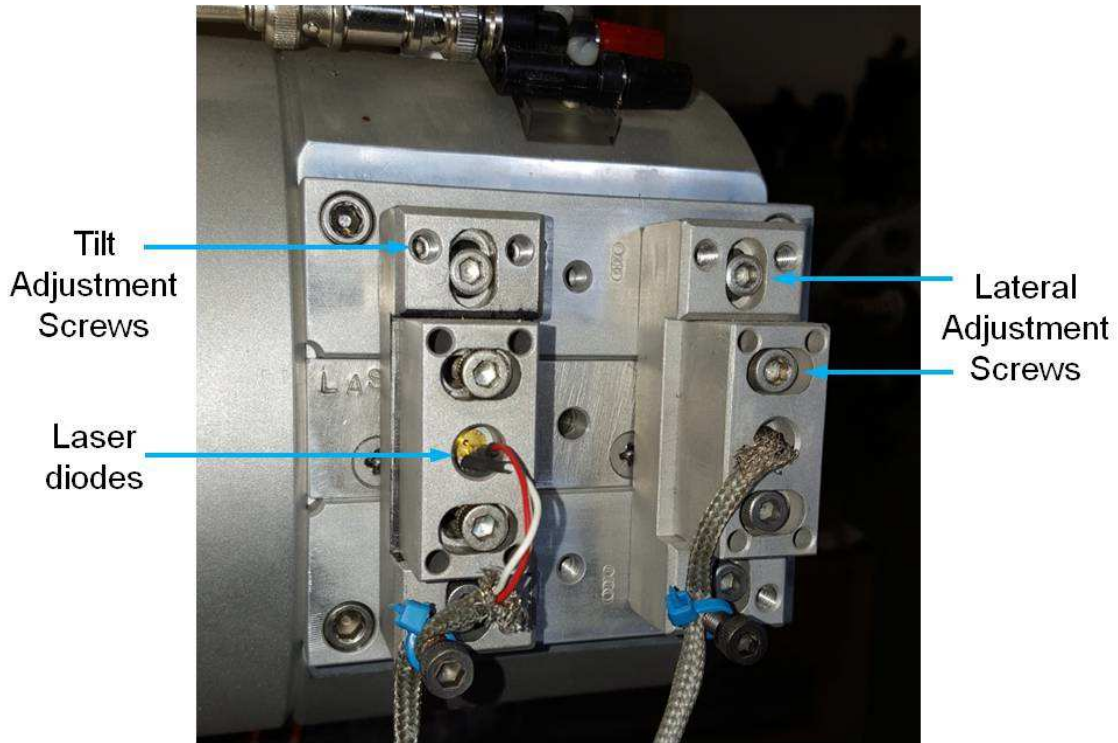
Figure 2-26: Laser mounts for velocity measurement system.

2.3.5.2.   **Stress Measurement**

The stress during plate impacts is measured using piezoresistive manganin foil stress gauges bonded between the target specimen and a backing plate in a manner ensuring that the gauge grid is oriented perpendicular to the loading direction. Manganin is composed of 83-87% copper, 12-13% manganese, and 0-4% nickel [7]. This material has a low temperature resistivity coefficient and a large piezoresistance coefficient, making this material ideal for measuring large changes in stress without capturing effects of temperature rise associated with high strain rate experiments. The thin foil gauge has been shown to be optimal for measuring in plane stress during uniaxial strain shock experiments, as opposed to manganin wire gauges which also tend to capture the

transverse stress along the gauge's width [8,9]. In addition, the foil gauges tend to be thinner than wire gauges, resulting in less interference of the shock wave within the target assembly [8].

The stress gauges used in this study are 50Ω manganin gauges (J2M-SS-210FD-050/SP60) manufactured by Micro-Measurement, a sub division of Vishay. The foil is 0.0005in. thick and has an active grid area of 0.210in. by 0.250in. This gauge is encapsulated in a 0.0008in. thick polymide (Kapton) film. A picture of the manganin gauge grid is shown in Figure 2-27.
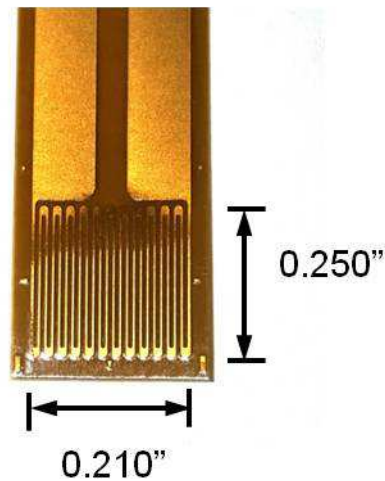
Figure 2-27: Piezoresistive 50Ω manganin foil stress gauge (J2M-SS-210FD-050/SP60) grid used in plate impact experiments.

The maximum stresses achieved in the current work were up to 16 GPa. Stress limitations exist with the use of manganin stress gauges bonded within metallic specimens. The manganin must be encapsulated within a non-conductive layer, such as polyamide, epoxy, or PTFE layers, when using conductive target and backing plates, however there does exists a threshold for certain materials at which the insulating layer becomes conductive, creating a bridge between the gauge and the conductive specimen.

It has been shown that the pressure limit for kapton is around 9 GPa [10]. The gauge however is bonded in the specimen with layers of epoxy, which has been shown to have a transition pressure of approximately 23GPa, which can be further increased by adding thin layers of PTFE between the gauge and specimen [11].

The gauges are excited using a constant voltage pulse power supply (Dynasen KC2-50/0.050-300). This power supply can operate with a single or double gauge set up, with voltages up to 300 volts for pulse width durations up to 1500μs. The power supply is trigger using an auxiliary output channel from the oscilloscope which supplies a trigger channel on the power supply with 9 volts (6-100 volt limit). The 50Ω gauge is excited by the power supply by a 50Ω coaxial cable to ensure impedance matching. The voltage signal is then recorded by the oscilloscope using the 75Ω output from the power supply for the fastest response times (20ns) and a 75Ω terminator to reduces wave reflections, as shown in Figure 2-28. Complete details of the operating and setup procedure of the power supply are provided in the instruction manual [6].
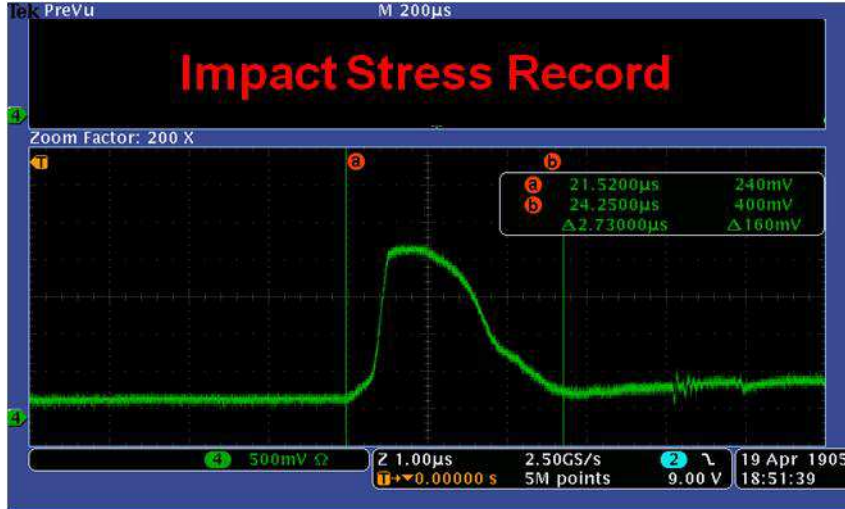
Figure 2-28: Screen shot of the oscilloscope showing an impact stress record for an impact with projectile velocity of 400 m/s

In order to convert the recorded voltage signal into a stress-time plot, the first step is converting the change in voltage to a relative change in stress gauge resistance. In this work, two methods were used for comparative purposes. The first method employed was the procedure outlined by the Dynasen manual provided with the pulse power supply [6]. The stress gauge signal was transferred via a 75Ω coaxial cable utilized the 75Ω unattenuated bridge output from the pulse power supply applying a 75Ω termination at the oscilloscope. As such, the first calibration equation, relating the change in voltage of the calibrated signal, ΔV_c, to the initial gauge resistance, R_o, is expressed as

$$K_{75} = \left[\frac{\Delta V_c}{\left(\dfrac{R_1}{R_o + R_1}\right) - \left(\dfrac{R_1}{R_G + \Delta R_o + R_1}\right)} \right] \qquad (2.11)$$

140

ΔR_o is the change in gauge resistance and R_1 is the resistance of the 3 additional legs completing the Wheatstone bridge. The relative change in resistance of the gauge is then expressed as

$$\left(\frac{\Delta R}{R_o}\right)\% = \left[\frac{R_1}{R_o}\left(\frac{1}{\dfrac{R_1}{R_o + R_1} - \dfrac{V_s}{K_{75}}}\right) - 1 - \frac{R_1}{R_o}\right] \times 100 \qquad (2.12)$$

The change of the gauge resistance can be used to determine the impact stress using the calibration curve provided by Dynasen [6]. The calibration equation from Dynasen written in units of GPa, is expressed as

$$\sigma = \frac{5\left(\dfrac{\Delta R}{R_o}\right) - 0.052\left(\dfrac{\Delta R}{R_o}\right)^2 + 0.00002\left(\dfrac{\Delta R}{R_o}\right)^4}{10} \qquad (2.13)$$

Rosenberg also provides a calibration equation for manganin gauges written as [9]

$$\sigma = A_o + A_1\left(\frac{\Delta R}{R_o}\right) - A_2\left(\frac{\Delta R}{R_o}\right)^2 + A_3\left(\frac{\Delta R}{R_o}\right)^3 + A_4\left(\frac{\Delta R}{R_o}\right)^4 \qquad (2.14)$$

with $A_o = 0.572$, $A_1 = 29.59$, $A_2 = 95.20$, $A_3 = -312.74$, and $A_4 = 331.77$ where the stress is in GPa. A plot of these calibration curves is shown in Figure 2-29.
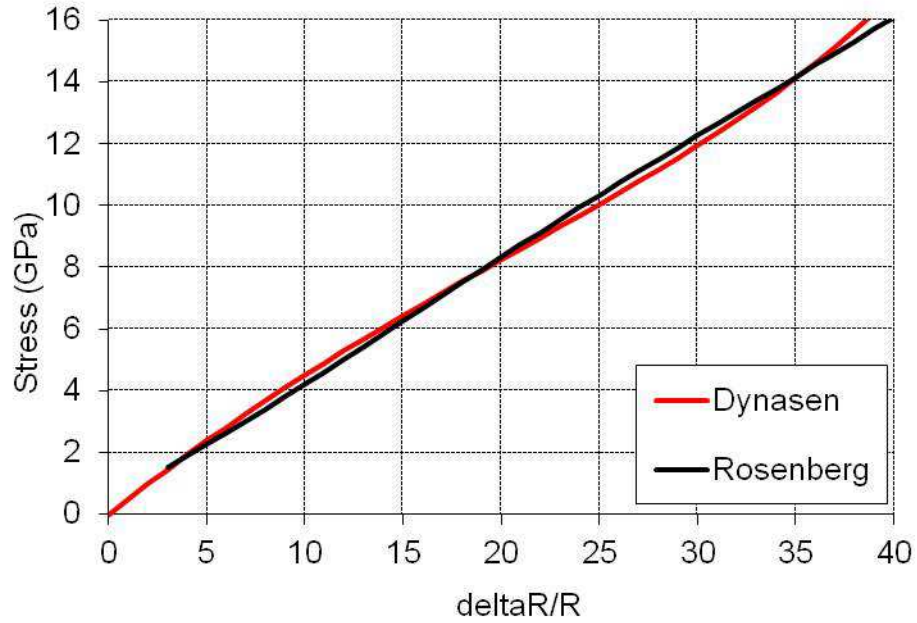
Figure 2-29: Calibration curves for manganin stress gauge

As shown in Figure 2-29, there is only a slight variation between Dynasen's and Rosenberg's calibration curves and when utilizing either curve, there are negligible differences in the stress results. The stress was calculated using both calibration curves provided by equations (2.13) and (2.14). A typical stress curve using these methods is shown in Figure 2-30.
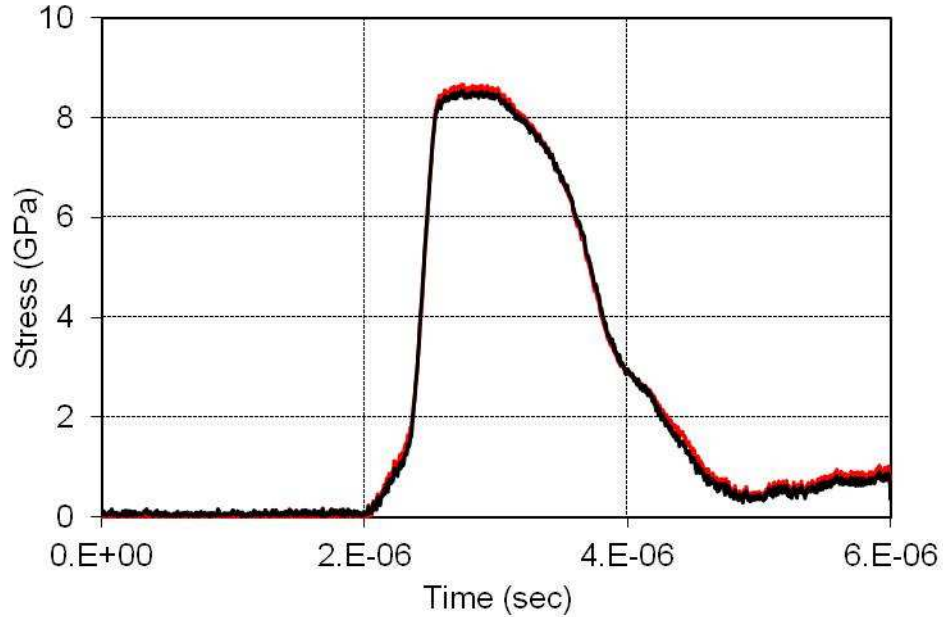
Figure 2-30: Stress results from a plate impact test utilizing calibration curves provided by Dyansen (black curve) and Rosenberg (red curve).

2.3.6. **Projectile and Target Specimen**

The projectile for the plate impact experiments consist of the impactor plate, 1.750in. in diameter and 0.125in. thick, bonded to the front of a carrier assembly called a sabot, typically made of a plastic material. The sabot is a sacrificial component that is demolished each experiment and serves only to carry the impactor plate at a fixed angle down the barrel to the target specimen. The barrel section inner diameter of the gas gun is 2.037in. The tolerance between the sabot and the barrel ID has to be such that the sabot is free to slide yet can still provide an adequate seal for the pressurized driving gas. If there is an excess amount of gas blowing by the projectile, it could potentially interfere with the target specimen by dislodging it from its holder. The projectiles for the plate

143

impact tests took several design iterations until a final design proved to be robust enough to be subjected to the high pressure driving gas as well as consistent in dimensions.

Initial attempts were made to decrease sabot production time by using a design made by a rapid prototype machine. While intricate designs were possible in order to reduce overall mass and contact area between the barrel and the sabot, the layered ABS plastic sabots from the rapid prototype machine were not strong enough to endure the high pressures needed for higher pressure plate impact experiments. Figure 2-31 shows two preliminary rapid prototyped designs
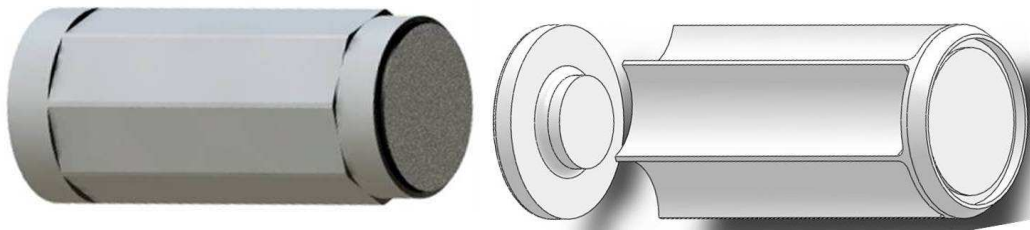
Figure 2-31: Two preliminary rapid prototype designs of sabots.

Using conventional machining, several UHMV polyethylene sabots were made. While the strength of the material and the low coefficient of friction were adequate, the high thermal expansion during the turning process created problems when attempting to keep a tight tolerance with the barrel.

The final design of the sabots is made of gray PVC material. High strength and machinability, this material has proven to be consistent for predicting projectile velocities. To compensate for the high coefficient of friction, a light oil lubricant is used in the barrel. The sabot consists of a main body made from a PVC tube turned to

approximately 2.030in. outside diameter with the inner diameter machined to 1.468in. The front and back of the main body tube are capped with PVC plugs to hold the driving pressure and to hold the impactor plate. The total weight of the sabot and impactor plate is approximately 185 grams. Figure 2-32 shows a schematic of the projectile assembly.
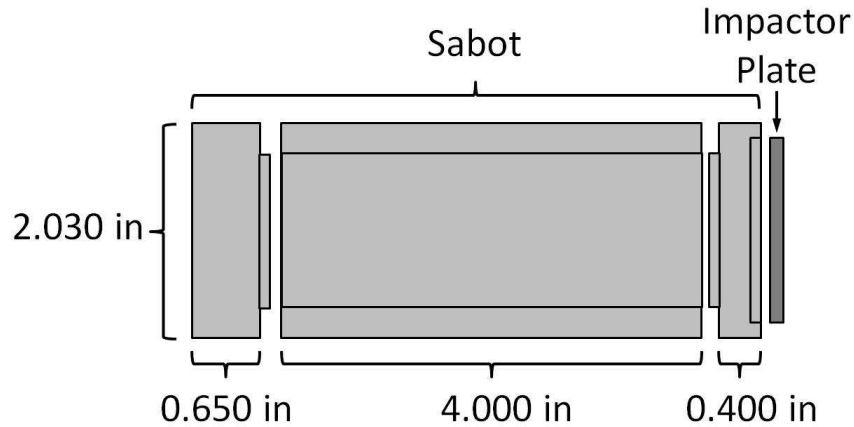
Figure 2-32: Components and dimensions of the final sabot design machined from gray PVC.

This sabot/impactor plate assembly is driven down the barrel of the gas gun and impacts the target specimen. The target is mounted perpendicular to the projectile direction at the end of the vacuum chamber attached to the barrel. An O-ring between the vacuum chamber and target face create the vacuum seal in the chamber. This configuration eliminates the need for electrical feedthroughs into the vacuum chamber for the stress gauge. Figure 2-33 shows the target setup mounted to the gas gun.
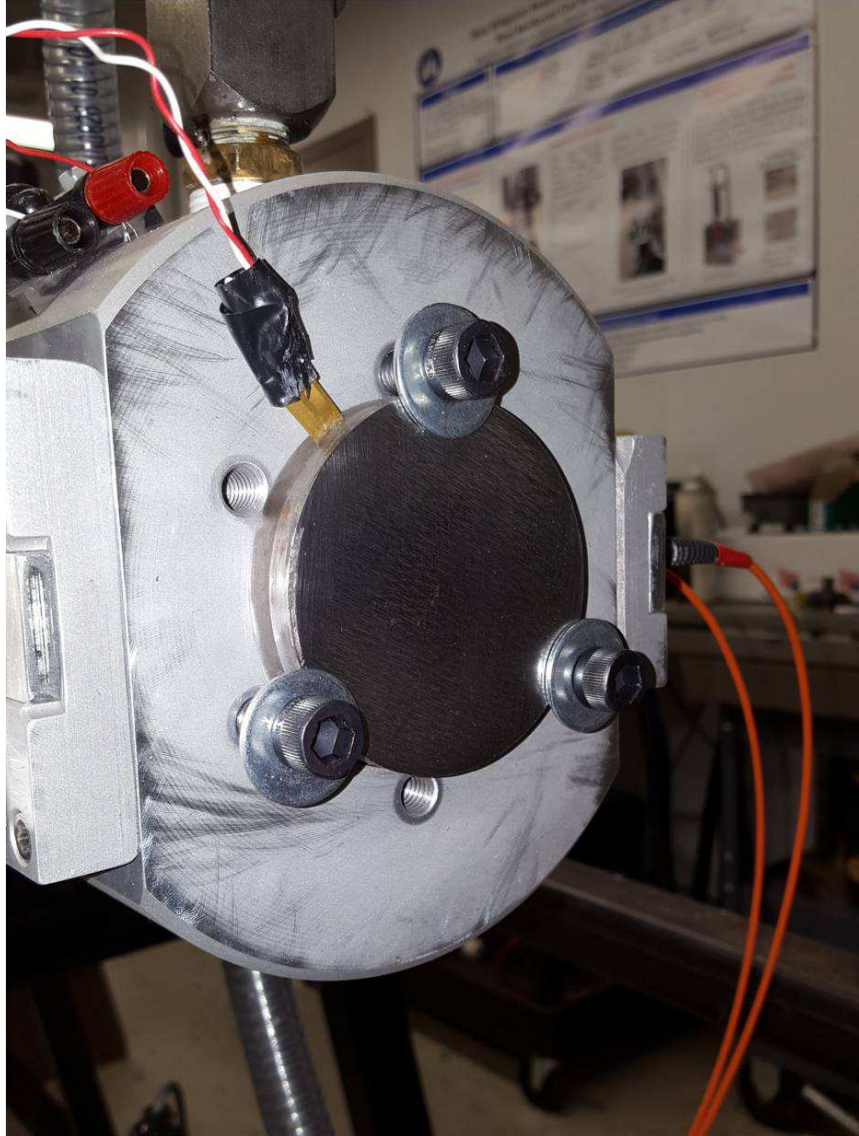
Figure 2-33: Target mounted the end of the vacuum chamber of the gas gun.

As shown in Figure 2-33, the specimen is held in by three 3/8"-16 bolts. These bolts have the cross section behind the bolt head turned down to a diameter of approximately 0.0625in, as shown in Figure 2-34.

Figure 2-34: 3/8"-16 bolt used for mounting the target to the vacuum chamber. The diameter has been turned down to 1/16in. to reduce the force to break during impact of the specimen.

This allows for the bolts to break when the projectile exerts a static pressure of approximately 4MPa. Nylon bolts were initially used, however extraction of the stud proved to be cumbersome, as the break always occurred just below the surface of the vacuum chamber face.

The distance between the barrel exit and the target face is shorter than the sabot, which allows the sabot to remain partially in the barrel to eliminate free flight ensure a planar impact. The faces of the target and backing plate were surface ground to ensure planarity between the impact face and the grid of the stress gauge, which is bonded between the target and the backing plate using a two part epoxy. The gauge setup within the target is shown in the schematic of Figure 2-35 and the picture of Figure 2-36.
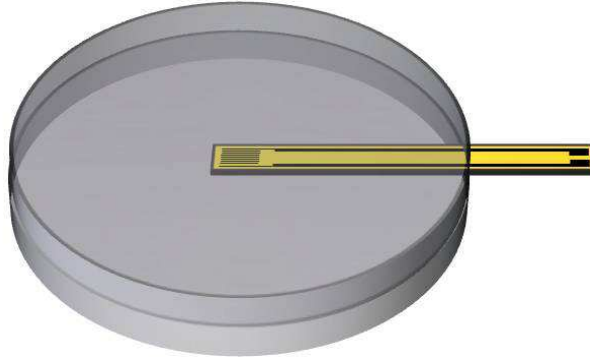
Figure 2-35: Schematic showing the embedded stress gauge bonded centrally between the target and backing plate using two part epoxy.

Figure 2-36: Picture of a target specimen ready for testing with the stress gauge bonded and with wire leads soldered to the stress gauge tabs.

The target disc was machined to 0.250in., which is double the thickness of the impactor disc. The backing plate was ground to a minimum thickness of 0.275in. This ensures that the spall plane does not occur within the target, and the sacrificial backing plate always fails by spall fracture during these tests.

2.4.   References

[1] Jeelani, S., et al. *Two-Stage Light-Gas Gun Installation for Hypervelocity Impact Studies*. No. TR-73-3. NORTH CAROLINA STATE UNIV AT RALEIGH, 1973.

[2] Jones, A_H_, W. M. Isbell, and C. J. Maiden. "Measurement of the Very-High-Pressure Properties of Materials using a Light-Gas Gun." *Journal of Applied Physics* 37.9 (1966): 3493-3499.

[3] AK Steel. Product Bulletin 17-4 PH-B-08-01-07

[4] Boresi, Arthur P., and Omar M. Sidebottom. *Advanced Mechanics of Materials*. 4th ed. New York: Wiley, 1985. Print.

[5] "*DET10A(/M) Si Biased Detector User Guide*" .ThorLabs. Revision E, 2015.

[6] "*Piezoresistive Pulse Power Supply Model CK2-50/0.050-300 Instruction Manual*," Dynasen Inc., (1996).

[7] Yiannakopoulos, G. *A review of manganin gauge technology for measurements in the gigapascal range*. No. MRL-TR-90-5. Materials Research Labs Ascot Vale (Australia), 1990.

[8] Rosenberg, Z., and Y. Partom. "Longitudinal dynamic stress measurements with in-material piezoresistive gauges." *Journal of applied physics* 58.5 (1985): 1814-1818.

[9] Rosenberg, Z., D. Yaziv, and Y. Partom. "Calibration of foil-like manganin gauges in planar shock wave experiments." *Journal of Applied Physics* 51.7 (1980): 3702-3705.

[10] Graham, R. A. "Shock-induced electrical switching in polymeric films." *Megagauss Physics and Technology*. Springer US, 1980. 147-150.

[11] Rosenberg, Z., A. Ginzberg, and E. Dekel. "High shock pressure measurements using commercial manganin gauges." *International Journal of Impact Engineering* 36.12 (2009): 1365-1370.

[12] Mitchell, A. C., and W. J. Nellis. "Diagnostic system of the Lawrence Livermore National Laboratory two-stage light-gas gun." *Review of scientific instruments* 52.3 (1981): 347-359.

[13] Raiser, G., R. J. Clifton, and M. Ortiz. "A soft-recovery plate impact experiment for studying microcracking in ceramics." *Mechanics of Materials* 10.1 (1990): 43-58.

[14] Field, J. E., et al. "Review of experimental techniques for high rate deformation and shock studies." *International journal of impact engineering* 30.7 (2004): 725-775.

[15] Meyers, M.A., "*Dynamic Behavior of Materials*," John Wiley & Sons Inc., New York. (1994).

[16] Zhernokletov, M.V., B.L. Glushak, "*Material Properties under Intensive Dynamic Loading*," Springer, New York. (2006).

[17] Chhabildas, Lalit C., Lee Davison, and Yasuyuki Horie. *High-pressure shock compression of solids VIII: The science and technology of high-velocity impact*. Vol. 8. Springer Science & Business Media, 2005.

[18] Antoun, Tarabay. *Spall fracture*. Springer Science & Business Media, 2003.

[19] Timoshenko, Stephen P., and Sergius Woinowsky-Krieger. *Theory of plates and shells*. McGraw-hill, 1959.

[20] Satish C. Gupta, R.G. Agarwal, J.S. Gyanchandani, S. Roy, N. Suresh, S.K. Sikka, A. Kakodkar And R. Chidambaram, A Single Stage Gas Gun For Shock Wave Studies, In Shock Compression of Condensed Matter–1991, edited by S.C. Schmidt, R.D. Dick, J.W. Forbes and D.G. Tasker, Elsevier, Amsterdam, 1992, Pages 839-842

[21] Sikka, S. K. "Behaviour of materials under shock loading conditions." *Bulletin of Materials Science* 15.1 (1992): 35-46.

[22] Ngo, T., et al. "Blast loading and blast effects on structures–an overview." *Electronic Journal of Structural Engineering* 7 (2007): 76-91.

[23] Piekutowski, A. J., and K. L. Poormon. "Development of a three-stage, light-gas gun at the University of Dayton Research Institute." *International journal of impact engineering* 33.1 (2006): 615-624.

CHAPTER 3

DEFORMATION CHARACTERISTICS OF LOW CARBON STEEL SUBJECTED TO DYNAMIC IMPACT LOADING

W. Visser[a], Y. Sun[a], O. Gregory[b], G. Plume[a], C-E. Rousseau[a], H. Ghonem[a,*]

[a] Department of Mechanical Engineering, University of Rhode Island, Kingston, RI 02881, USA
[b] Department of Chemical Engineering, University of Rhode Island, Kingston, RI 02881, USA
* Corresponding author. Tel.: +1 401 874 2909; fax: +1 401 874 2925.
E-mail address: ghonem@egr.uri.edu (H. Ghonem).

3.1.   **Abstract**

The effects of impact loading on changes in microstructure have been studied in low carbon steel.   Low to moderate shock loading tests have been carried out on steel specimens using a single stage gas gun with projectile velocities ranging from 200 to 500 m/sec. Stress history at the back face of the target specimen and projectile velocity prior to impact were recorded via manganin stress gauges and velocity lasers, respectively. A Johnson-Cook constitutive material model was employed to numerically simulate the material behavior of low carbon steel during impact and obtain the particle velocity at the impact surface as well the pressure distribution across the specimens as a function of impact duration. An analytical approach was used to determine the twin volume fraction as a function of blast loading. The amount of twinning within the α-ferrite phase was measured in post-impact specimens. A comparison between experimental and numerical stress histories, and analytical and experimental twin volume fraction were used to optimize the material and deformation models and establish a correlation between impact pressure and deformation response of the steel under examination. Strain rate controlled tensile tests were carried out on post-impact specimens. Results of these tests are discussed in relation to the effects of impact loading on the yield and ultimate tensile strength as well as the hardening and strain energy characteristics.

Keywords: Low Carbon Steel, Shock, Impact Loading, Twinning, Post-Impact

3.2.   **Introduction**

Impact loading of steel is a subject that has been studied widely for structural applications and material characterization. It has been established that high strain rate

loading of steel will result in a change of both microstructural and mechanical properties which individually affect the residual life of the material. Vast amounts of research has been done in order to assess blast loading and deformation effects, much of it being on steel as it is a primary reinforcing phase of structures. Research in blast analysis, while in general utilizes the finite element technique to provide solutions for the dynamic response of the structures [1], requires implementation of microstructure constitutive models required to accurately capture changes in mechanical properties during high strain rate loading.

In order to replicate the pressure profile and high strain rate deformation caused by explosive loading and recover intact specimens suitable for further testing and analysis, various techniques exist of which Field et al. [2] provide a detailed review. Some basic techniques which are of main concern to material characterization are drop weight testing, split Hopkins pressure bar, Taylor impacts, plate impacts, and explosive loading. While SHPB tests produce elastic-plastic wave propagation, the maximum strain rates achieved are typically in the range of 10^4 s^{-1}. Plate impact tests are often used to replicate explosive loading due to the fact that the strain rates, greater than 10^4, and planar shock waves achieved clearly simulate that of explosive shock wave loading. During plate impacts at high velocities, a state of one dimensional strain is produced until lateral release waves from the edge of the projectile and target specimen reach the center of the impact area. To achieve the highest velocities, above 1km/s, two and three stage gas guns are used. These techniques are typically used for obtaining Hugoniot curves, measuring spall strength, post-impact mechanical testing, and measuring phase change, the latter of which is the concern of the work presented herein.

An important aspect in the post-impact analysis of materials is the phase change of the microstructure, which is generally incorporated into analytical modeling in order to predict deformation response. Recent studies, by Gregory et al. [3], of recovered pipe bomb fragments provided basis for characterization of plain carbon-steel subject to high rate deformation. They observed metallurgical variations of the steel in order to estimate explosive loading severity. It was found that explosive loading resulted in elongation in grains in both the α-ferrite and pearlite phases, intersecting slip bands and cross slip, as well as mechanical twin formation. Firrao et al. [4] subjected stainless steel to plane shock wave loading by means of spherical plastic explosives with varying charge weights and varying charge-target distances. Changes in microstructure on the impact surface included oxidations, partial melting at grain boundaries, isolated slip bands, and mechanical twins in areas around fragment impact points. Changes through the thickness of the specimen were limited to mechanical twins in discontinuous layers bordering the exposed surface, but never across the entire thickness. Through X-ray analysis it was found that dislocation density remains unchanged, proving that deformation by dislocation slip, and subsequently plastic yielding, was not reached, which is also evident through measurement of thickness variations. Based upon observed twinning and estimated explosive pressures, Firrao et al. [4] were able to calculate critical stress required for twinning, and proved that twin nucleation occurs prior to yielding. De Resseguier and Hallouin [5] studied iron disks of different thickness submitted to shock loading by means high-power laser pulses. Post shock studies of the iron microstructure revealed significant twin formation. Using a constitutive twinning model proposed by Johnson and Rohde [6] accurate predictions of twin volume fraction and elastic-plastic

response of the material have been made [5,7]. They used plate impacts to examine shock-loaded iron and analytically predict twin volume fraction in recovered specimens as a function of impact stress. Atroshenko et al, [8] examined the strengthening properties of materials, including copper, aluminum, titanium, and steel, due to spherical loading by means of explosives, and uniaxial loading using a light gas gun. The strength of the material was measured as a function of distance from the impact using microhardness measurements. In all materials except aluminum, microstructure refinement and increases in hardness occurred. Smida and Bosansky [9] provide experimental and fractographical analysis of ferritic structural steel in order to provide a correlation between the role of deformation twins and mode of fracture. Tensile and Charpy impact tests were carried out and the occurrence of deformation twins on the fracture surface were studied. Murr et al. [10] observed profuse mechanical twinning in Tantalum when subjected to shock wave deformation of magnitudes up to 45 GPa. From post-impact testing, shock hardening was observed which have been attributed to twins as barriers to plastic deformation.

Deformation in BCC materials by means of shock loading is described as being composed of the competing mechanisms of slip and twinning. Murr et al. [10] rationalize that critical twinning stress is highly dependent upon and directly proportional to the stacking-fault energy. Their work examined twin formation during shock loading and twinning effect on the post-shock mechanical response of Tantalum. Murr et al. found that twinning was more predominant at the impact surface than at the back surface. Post-shock testing consisted of quasi-static and dynamic compression tests as well as microhardness measurements. The rationale of slip-twinning transition was explained

through experimental observations and a mechanistic model proposed by Armstrong and Worthington. A model was presented to predict the critical threshold stress for twin initiation which is based upon the Swegle-Grady relationship, grain-size and temperature. Meyers et al. [11,12] recognize the fact that twin initiation and growth is closely tied to dislocation motion which is highly strain rate and temperature sensitive. They note that twinning can have two significant effects upon plastic deformation; it increases the work hardening rate by creating more barriers, effectively subdividing the grains, and it contributes to plastic deformation due to twinning shear. Meyers briefly describes the effects of strain rate, temperature, grain size, texture, and stress state effects upon twinning nucleation. The model used is based upon a similar theory for FCC material in Murr's study of Tantalum [10], in which dislocation pile-ups are a key aspect to twin nucleation. Equations for critical shear stress for twining are presented for BCC, FCC, and HCP materials, all of which are dependent upon strain rate, temperature, and the Hall-Petch relation for grain size. They describe that the twins per grain is a function of stress which is independent of temperature and strain rate and the amount of twins will increase monotonically with increasing stress. The evident common aspect in all these works is the twin formation in steel during high strain rate loading. A correlation however does not exists between blast conditions, i.e. strain rate and stress state, and twin volume fraction, from which a unique criteria defining material integrity can be established. This criterion is the objective of this study. For this purpose, the effect of blast loading up to strain rates of 10^5 s^{-1}, on the microstructure deformation mechanisms of low carbon steel will be examined. Discs of low carbon steel were subjected to high velocity impact loading using a light gas gun. Impact specimens were analyzed by

measurement of microstructural variations and mechanical properties. Attempts are made to study the deformation pattern in steel using material and deformation models. Results of this analysis are linked with the experimental work in order to assess the validity of the approach. Prediction of impact loading conditions will be achieved through a relationship between twin volume fraction and impact stress history and linked to post-impact mechanical properties. An experimental procedure was used to impact low carbon steel specimens and experimental observations of microstructure. In addition, numerical methods used and means of obtaining accurate results are described. An analytical model of dynamic deformation based upon slip and twinning is described and results are compared with experimental findings.

3.3.   **Material and Experimental Procedure**

The as received microstructure of the low carbon steel, as shown in Figure 1, consists of primarily α-ferrite phase with colonies of pearlite. The pearlite colonies are made of α ferrite and Fe_3C cementite lamellas; Figure 3-1. Average grain size is 50 μm with 9% volume fraction of the pearlite phase. Tensile tests of as received material showed yield strength of the material to be 348 MPa at 0.2% offset at room temperature with a Young's modulus of 197 GPa. Preparation of all specimens was done by mechanical polishing to 1 micron and chemical etching using 5% nital solution.
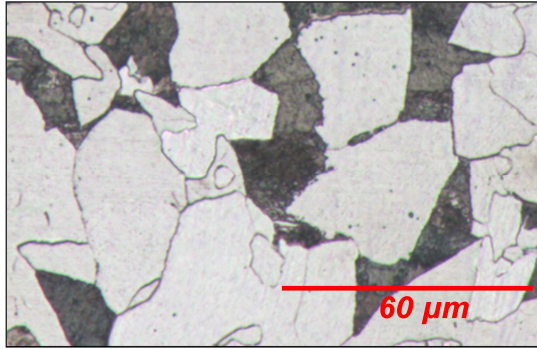
Figure 3-1: Optical micrograph of as received A572 grade 50 structural steel. Lighter grains are α-ferrite, and darker grains are pearlite

This material was prepared into round discs by electro discharge machining and tested by subjecting it to different impact loads using a single stage light gas gun. A series of five plate impact experiments have been carried out using a single stage light gas gun; Figure 3-2a. Fixed back conditions, Figure 3-2b, were employed in order to minimize energy loss and provide means for recovering post impact specimens; Figure 3-2c provides a schematic of the experimental set up. The projectile measurements are 31.75mm diameter and 3mm thick, while the target disk and backing plate measurements are 57.15mm diameter and 6mm thick. The target dimensions allowed for tensile specimens to be machined from deformed specimens for possible mechanical testing.
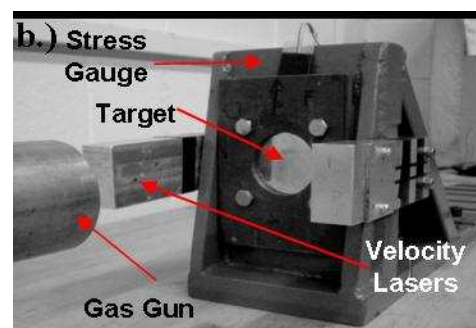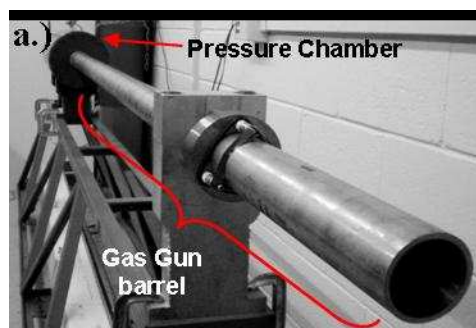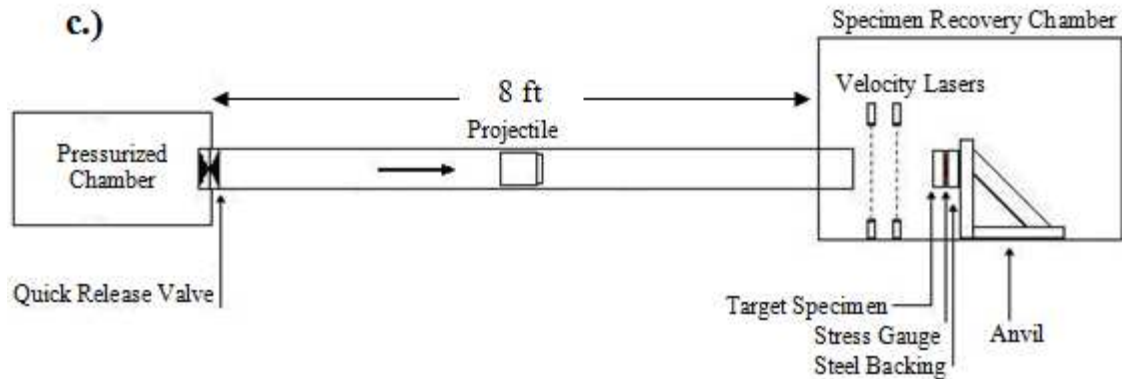
Figure 3-2: a.) Photograph of experimental gas gun and b.) fixed back apparatus for plate impact tests.   c.) Schematic of gas gun and target apparatus

Projectile velocities ranging from 200 to 500 m/sec were measured using two lasers which were mounted perpendicular to the projectile and in front of the target.   Input pressure was used to control projectile velocities and magnitude of impact loads.   Input pressure of Helium gas was used to control projectile velocities and achievable stress levels.   Longitudinal stress histories were recorded using manganin stress gauges bonded centrally between the back surface of the target disk and a steel backing plate.

Typical results of normal stress versus time curves are shown in Figure 3, for the five different impact velocities.   These curves, generated from data recorded from the back surface of the impacted target disk, are characterized by four distinct features; the elastic precursor, the plastic wave, the peak stress level and duration, and the unloading wave. The Hugoniot elastic limit, σ_{HEL}, which is the amplitude of the initial elastic wave, is related to the shear stress, τ, through the relation:

$$\sigma_{HEL} = 2\tau \left[\frac{1-\nu}{1-2\nu} \right] \tag{1}$$

where ν is Poisson's ratio. From the impact stress-time histories, the elastic limit for all curves is reached at 1 GPa. A σ_{HEL} of 1 GPa corresponds to a 0.285 GPa maximum resolved shear stress, and for shear stress greater than this, it is suggested that dislocation slip accommodates plastic deformation [6].

The time between impact and that at which the stress gauge at the back surface begins to register the elastic wave can be estimated using the velocity of the elastic precursor. The wave speed of the elastic precursor, $C_{Elastic}$, is described as [13]:

$$C_{Elastic} = \sqrt{\frac{E(1-\nu)}{\rho(1+\nu)(1-2\nu)}} \tag{2}$$

where E, and ρ are the elastic modulus and material density, respectively. Using the calculated elastic wave speed with a 6 mm thick specimen, the elastic wave will reach the back surface in 1.03 µsec. If the projectile and target are of the same material, identical waves will simultaneously propagate in both. The projectile will stay in contact with the specimen until the elastic wave in the projectile reflects off of the free surface and returns to the contact surface. The projectile and target will remain in contact for the time duration, $t_{Contact}$, determined as [13]:

$$t_{Contact} = \frac{2L_P}{C_{Elastic}} \qquad\qquad (3)$$

where L_P is the projectile thickness. Since the projectile is half the thickness of the target specimen, they will separate in the same time the elastic wave reaches the back of the target, at 1.03 μsec.
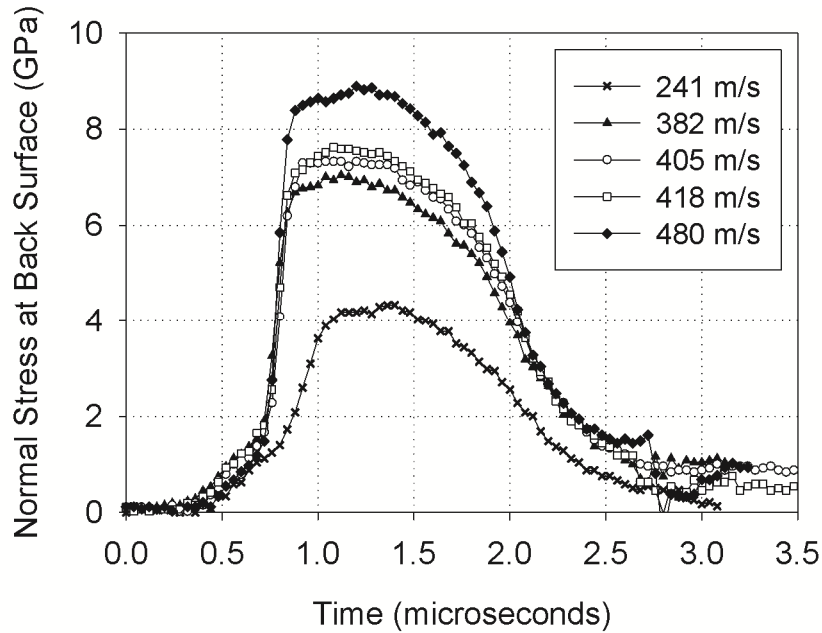
Figure 3-3: Impact Stress data recorded at the back surface of target disk

Each of the stress-time curves shown in the Figure 3-3 will be compared to that obtained numerically as will be detailed in a later section, for the same impact condition and will be used as a reference for obtaining particle velocity at the impact surface. Simulated particle velocity of the target impact surface will be used as an input into

analytical constitutive equations formulated as the basis of the Johnson and Rohde, in order to calculate twin volume fraction as a function of local shear stress and time.

3.1.   Experimental Results

Post impact target specimens show that plastic deformation took place in the impacted area and back surface as accompanied with an increase in total diameter of the target disk. The area of impact was discolored suggesting a large and rapid increase in temperature on the front surface during impact. Specimen surfaces were ground flat using a surface grinder under coolant, and polished and etched. Optical microscopy was conducted on post impact test specimens and the results show the presence of mechanical twins within the α-ferrite grains; see Figure 3-4. Micrographs of the cross-section just below the impact surface showed a lack of twins, which suggests that the temperature rise was high enough to suppress twin formation in the contact region.
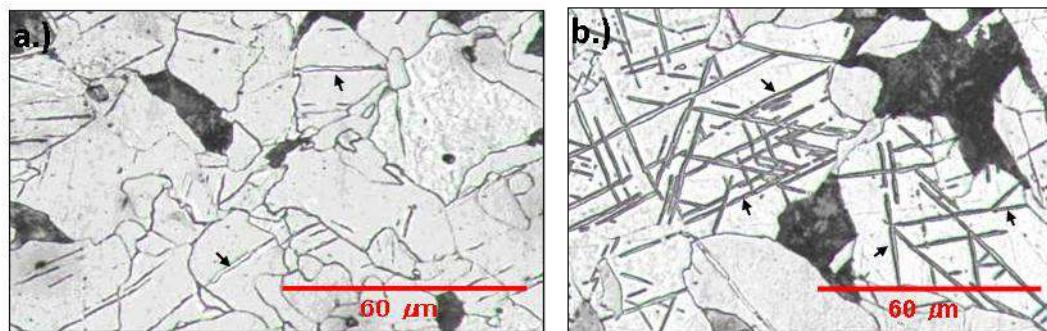
Figure 3-4: Example of optical micrographs of post impact steel specimens a.) 7 GPa peak stress yielding 3.4% twins, b.) 9 GPa peak stress yielding 4.3% twins. Lighter grains are α-ferrite, and darker grains are pearlite; black arrows indicate deformation twins.

Results of these optical micrographs show that all of the twins are of lenticular shape, which is indicative of the mechanism by which the twins form. The majority of the grains have parallel twins extending between grain boundaries. However, there are also large amounts of twin-twin interaction in which twins terminate at other twins, or continue through the intersections, which suggests formation on multiple planes [14]. Volume fraction of the twins was calculated using ASTM E562-05, standard test method involving systematic manual point count method [15]. This count provides an average estimation of twin volume fraction which was correlated to impact stress, as shown in Table 1. Figure 3-5 shows that macro hardness is also positively correlated to impact stress.

Table 3-1: Peak impact stress and measured twin volume fraction

Impact stress (GPa)	0.00	4.34	7.05	7.63	7.30	8.90
Mean Twin V_f (%)	0.00	1.93	3.38	3.73	4.05	4.16
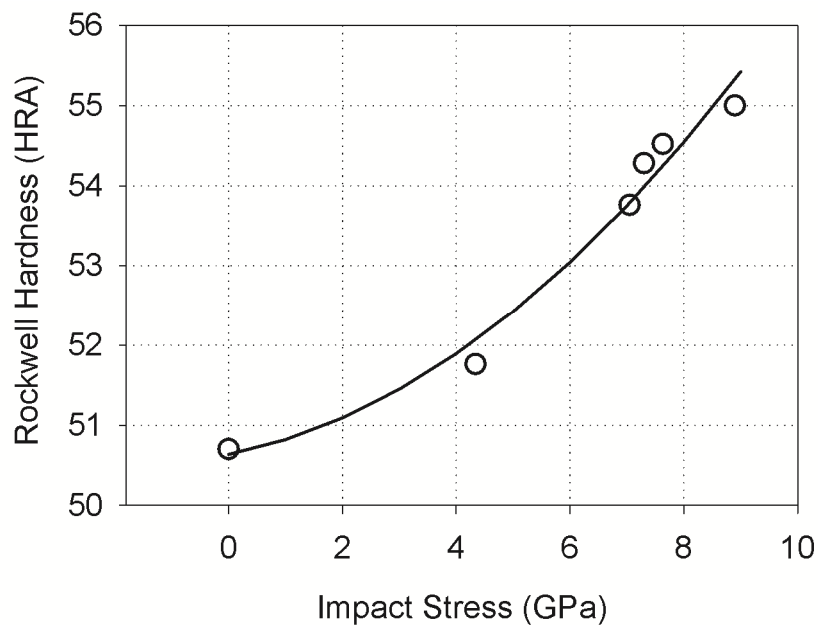
Figure 3-5: Post-impact macro hardness as a function of impact stress

The increase in hardness, which indicates an increase in yield strength of the material, can be attributed to strain hardening [16], and to presence of twin-matrix interfaces, which provide additional barriers for further dislocation slip. There may exist a unique relationship between the twinning and hardness properties, however since hardness also increases in the absence of twinning, no attempt has been made in this study to examine the unique relationship between hardness and twinning.

3.4.   **Numerical and Analytical Analysis**

The analysis of the impact process will be carried out first by calculating the particle velocity for each impact condition. This velocity will then be utilized to calculate the corresponding deformation field and corresponding twin volume fraction.

3.1.1.   *Particle Velocity Simulation*

Dynamic-explicit finite element simulation was used to model plate impacts. Simulation of impact conditions provides knowledge of impact wave parameters as well as a description of the blast related stress distribution within the impacted steel. Input parameters for boundary and loading conditions are obtained from experimental procedures. From the simulation, the longitudinal stress distribution is matched with experimental stresses recorded. Once good correlation exists, particle velocity at the impact surface is extracted from numerical results and used as an input for analytical

modeling of twin volume fraction as a function of impact loading. In order to obtain stress histories in accordance with experimental results, parameters for a rate dependent model were required. For this purpose, the Johnson-Cook (JC) constitutive model [17] was used to express the equivalent Von-Mises tensile flow stress as a function of the equivalent plastic strain, strain rate, and temperature. This stress is expressed as [13,17]

$$\sigma = \underbrace{\left(A + B\varepsilon^n\right)}_{\text{Strain hardening}} \underbrace{\left[1 + C\ln\left(\frac{\dot{\varepsilon}}{\dot{\varepsilon}_0}\right)\right]}_{\text{Strain rate effect}} \underbrace{\left[1 - \left(\frac{T - T_r}{T_m - T_r}\right)^m\right]}_{\text{Temperature dependency}} \tag{4}$$

where σ is the Von-Mises tensile flow stress, which is the applied stress in the loading direction for the uniaxial tensile test case; ε is the equivalent plastic strain, which equals the strain in the loading direction for the uniaxial tensile test case; A, B and n are material constants to characterize the strain hardening behavior of the material; C is the material constant to describe the strain rate effect; and m is the material constant to describe the temperature dependency. Values for material constants, Table 2, were optimized using a room temperature stress-strain curve of the as received material obtained from the work of Maciejewski et al. [16]; see Figure 3-6.
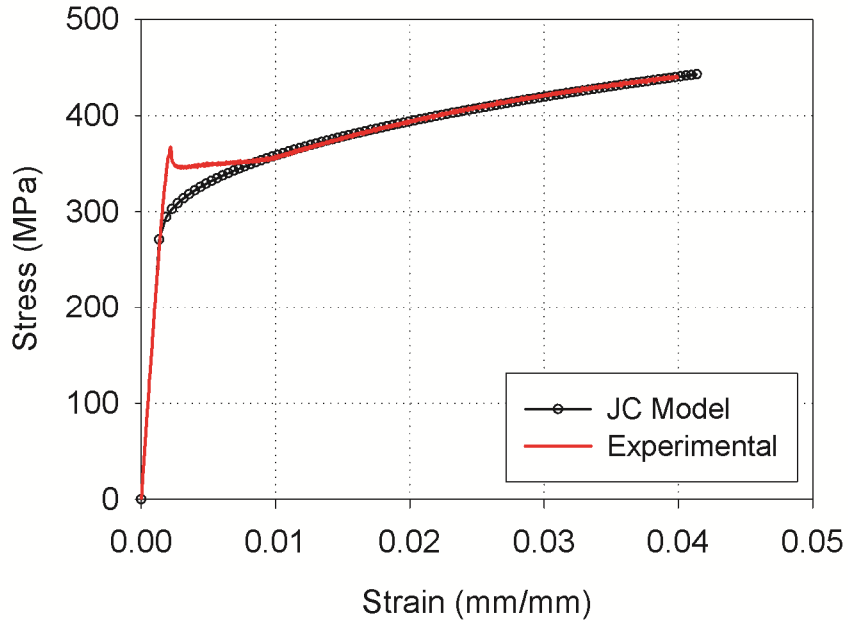
Figure 3-6: Stress strain curve of as received material plotted with JC model output. The curve was obtained at room temperature with a strain rate of 5×10^{-6} s^{-1}.

Table 3-2: Material properties and JC model constants for use in Finite Element Simulation

Young's Modulus	Poisson's ratio	Density	Inelastic Heat Fraction	Specific Heat
200 GPa	0.3	7850 kg/m^3	0.864	0.465 KJ/kg*K
A	B	C	n	m
348	900	0.032	0.434	1

Once the parameters for equation 4 are optimized, simulation of the plate impact is preceded. To obtain comparable σ_{HEL} during simulation, the constant A is adjusted from the static to the dynamic yield strength of the material. In this simulation, symmetry of the impacted test specimen permits simulation of only one quarter of the specimen, as illustrated in Figure 3-7a; however model boundary and loading conditions replicate that of the actual experiment, as illustrated in Figure 3-7b.
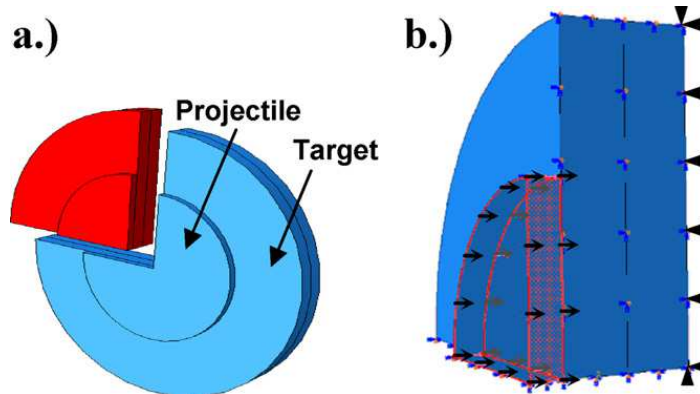
Figure 3-7: Quarter plate model of axis-symmetrical target disk, and predefined velocity imparted on flyer plate in finite element simulation

Step time period was 3 μsec and included adiabatic heating effects. The model was symmetrically bounded on edges to prevent rotation and translation on the cross-sectional areas. The displacement and rotation of the surface of the backing plate was fixed in the axial direction corresponding to experimental setup. The temperature of the parts and the velocity of the projectile were defined as a predefined field. The mesh is standard hex type element CD38R with 12,416 and 1,848 elements in the target and flyer plate, respectively, and is approximately 1x1 mm on the surface and refined to 0.375 mm in the axial direction.

Numerical stress history of the target specimen during impact show comparable profiles to experimental impact results. In this profile, three important components which must be captured accurately, pressure rise time, impact duration, and maximum stress, all exhibit good fit with experimental data. Figure 3-8 shows numerically generated stress profiles during impact at the back surface of the target specimen compared with experimental results.
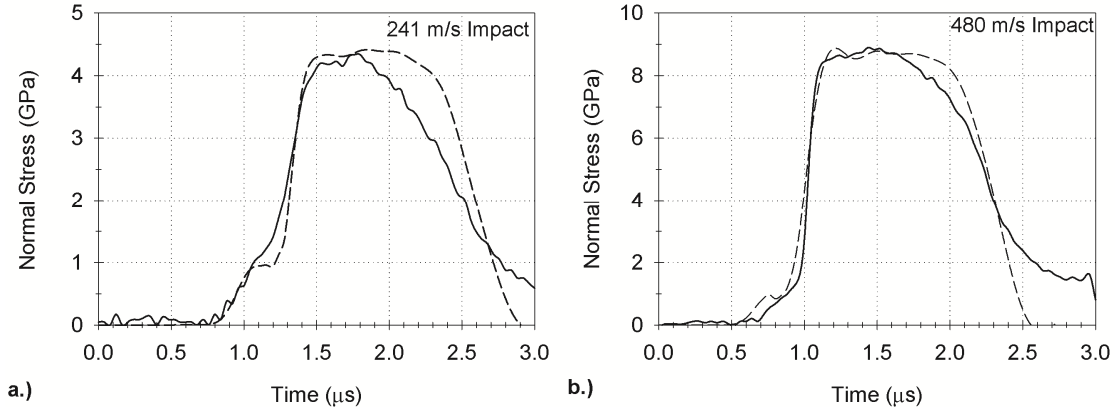
Figure 3-8: Experimental (solid line) and numerical (dashed line) stress history data matching for two impact cases. Graph legends pertain to projectile velocity.

Results show good correlation between rise time, peak stress, and σ_{HEL} amplitude. Linear and quadratic bulk viscosity parameters in the dynamic explicit step were adjusted in order to reduce noise in the numerical solution. Furthermore, the linear and quadratic bulk viscosity parameters damp high frequency ringing and smear the shock front across several elements to prevent collapse under high velocity gradients. Once good agreement between numerical and experimental stress-time curves is achieved, the simulated maximum particle velocity at the front surface of the specimen can be used as an input for calculation of twin volume fraction. An approach to carry out these calculations is described in the following section.

3.1.2. *Twin Volume Fraction Calculation*

The twin region can be simply described as an area of stacking faults enclosed by partial dislocations. Two ways in which this can occur are discussed by Wasilewski [18]. Wasilewski suggests that twins can form by progressive shear of the parent lattice or by a

close atomic shuffle within the lattice, both of which will end in the same arrangement within the twinning planes; Figure 3-9. Twinning by progressive shear of the parent lattice will produce a shear offset, of which plastic deformation results, Figure 3-9a, while a local rearrangement or shuffle will produce no shear offset, Figure 3-9b. It is assumed that formation of the twin by homogeneous shear will produce a shear offset equal to *kh*, where *k* is the strength of the simple shear, also known as the *twinning shear*, and *h* is the average thickness of the twin lamella. For bcc crystals the twinning is most readily formed on the {112} planes in the (111) direction which has a twinning shear equal to $1/\sqrt{2}$ [6]. The two modes can be distinguished by observation of the shape of the twins formed. Twins by shear will be lenticular in shape while those created by shuffle will be prismatic [18]. Based upon the characteristic lenticular shape of the twins formed in this study, they are assumed to be produced by progressive shear of the parent lattice, as in opposition to the theory of atomic shuffle.
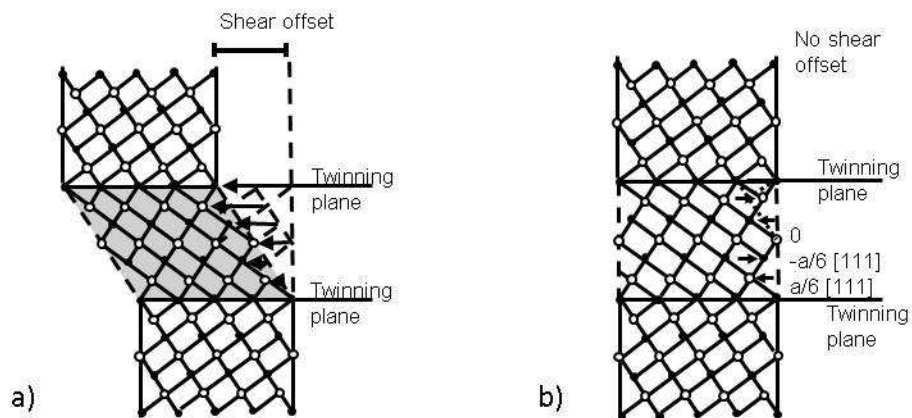
Figure 3-9: a.) Twin formation by progressive shear of the parent lattice, and b.) twin formed by successive alternating "shuffle" of atoms by sequence $+a/6[1\bar{1}1], -a/6[1\bar{1}1], 0$.

From the works of Wasilewski [18] and Johnson and Rohde [6], it is inherent that twins form by local rearrangement of atoms resulting in a shear offset, as opposed to local shuffling. In order to analytically predict twin volume fraction, these two points are considered and a modified form of a deformation model based on the work of Johnson and Rohde [6] was therefore applied here. This deformation model incorporates slip and twinning mechanisms previously described [18,19,20] and will be used to calculate twin volume fraction in the material for the given loading conditions. The assumptions and observation from these previous studies are described in the constitutive model in which total plastic strain is composed of both dislocation slip and deformation twinning, and the twin volume fraction and growth rate are functions of corresponding shear stress. The dynamic response and deformation twinning of low carbon steel under impact loading is described by the laws of mass and momentum conservation, which are written as

$$\frac{\rho_0}{\rho^2}\frac{\partial \rho}{\partial t} + \frac{\partial u}{\partial X} = 0 \tag{5}$$

$$\rho_0 \frac{\partial u}{\partial t} + \frac{\partial \sigma}{\partial X} = 0 \tag{6}$$

where ρ_0 is initial density, ρ is an evolved density, and u is particle velocity during impact at time t at a distance of X from the impact surface. The stress, σ, component can be defined by a contact pressure P, and shear stress τ, and is expressed as

$$\sigma = P + \frac{4}{3}\tau \tag{7}$$

where;

$$P = \rho(C + Su)u \tag{8}$$

and

$$\dot{\tau} = \mu(\dot{\varepsilon}_t - 2\dot{\gamma}) \tag{9}$$

where μ is shear modulus, C and S are wave speed constants, and ε_t is total strain in the wave direction and is given by:

$$\varepsilon_t = 1 - \frac{\rho_0}{\rho} \tag{10}$$

γ is the plastic shear strain on the plane of maximum shear stress described as the summation of slip and twinning strains,

$$\gamma = \gamma_s + \gamma_{tw} \tag{11}$$

Plastic strain due to twinning, and that due to slip are expressed as

$$\gamma_{tw} = k(\alpha - \alpha_0) \tag{12}$$

$$\gamma_s = \frac{1}{2}\varepsilon_t - 2k\alpha - \alpha_0 - \tau_s/\mu \tag{13}$$

respectively, where k is twinning shear, α is the volume fraction of twins, α_0 is initial twin volume fraction, and τ_s is the shear stress required for slip. Volume fraction of twinned material is given by

$$\alpha = \left(\alpha_0^{1/m} + \frac{1}{t_c} \int_0^t v(\tau) dt \right)^m \tag{14}$$

where t_c is characteristic time, which is a constant controlling the rate of twin density, and $m=3$ is for growth of twins both through the thickness and radial directions. The dimensionless growth rate of twins, $v(\tau)$, is expressed as

$$v(\tau) = \tau/\tau_T - 1 \quad \tau \geq \tau_T \tag{15}$$

where τ_T is shear stress required for twinning. This set of equations provides a method of calculating twin volume fraction as a function of shear stress. The results of this model in terms of average twin volume fraction versus impact stress are compared with experimental results, and are shown in Figure 3-10.
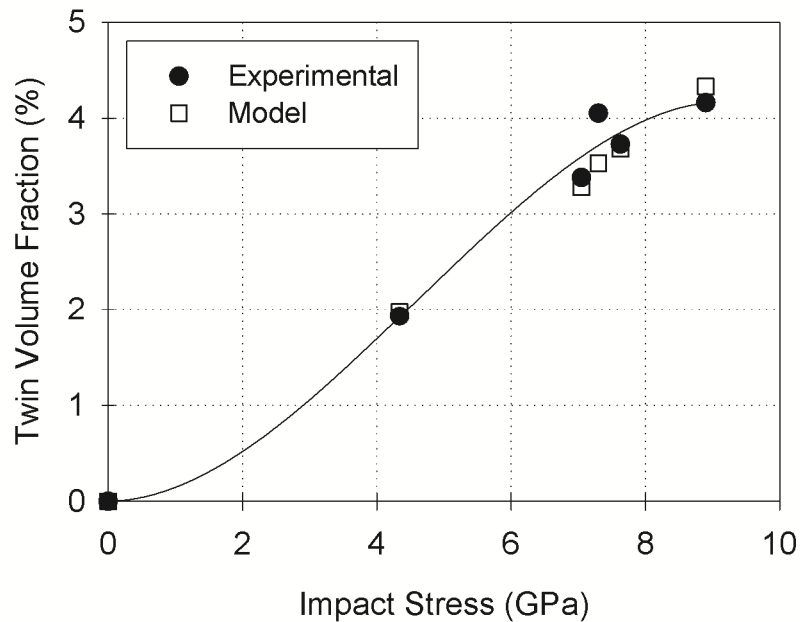
Figure 3-10 Comparison of experimentally measured and analytically computed twin volume fraction within α-ferrite grains as a function of impact stress.

Analytical model predictions show similar trends to experimental measurements for the given stress range. The linearity of the experimental and calculated data in Figure 10 apparently deviates from this trend at higher stresses as the twin volume fraction seems to saturate in the material, or other deformation mechanisms begin to dominate. While the relationship between impact stress and twin volume fraction may be satisfied within the given conditions, shear banding and phase transformation have been observed to occur at extremely high pressures [4,21], and the criteria may no longer be valid. Further study of the material at higher stresses and strain rates are underway by the authors in order to extend the deformation criterion and set limits for its applicability.

3.5.　　**Post-Impact Residual Strength**

The influence of twin volume fraction on the residual strength of the material is examined through strain rate controlled monotonic tensile tests and has been compared to the response of the as-received condition. For this purpose, post-impact steel discs were ground and polished flat to a nominal thickness of 3 mm and cut into dog-bone specimens. Geometry and dimensions of the specimen as being cut from the impacted disc are illustrated in Figure 3-11. Testing was carried out at room temperature using a servo hydraulic mechanical test system and strain values were recorded using a knife edge extensometer mounted in the gauge section of the test specimen. Testing of as-received material was carried out at two strain rates; 10^{-5}/s and 20^{-5}/s. Results show no strain rate dependency at this rate and temperature. All post-impact specimens were tested at 20^{-5}/s.
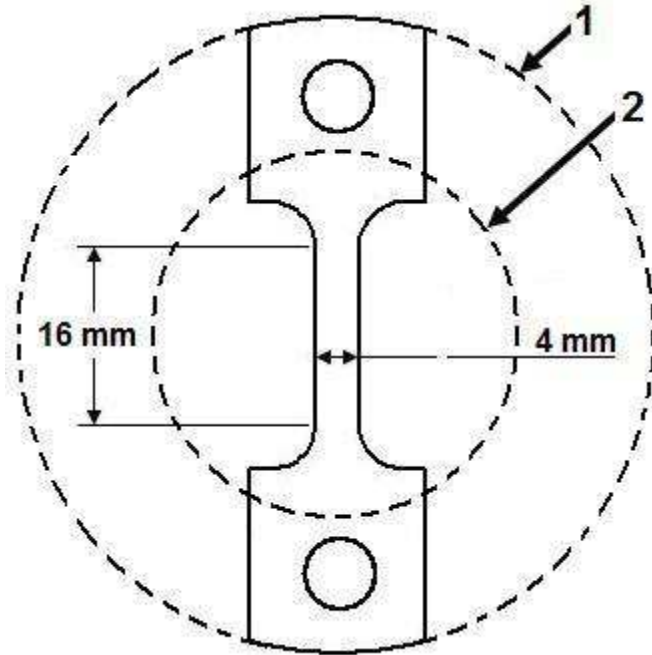
Figure 3-11: Tensile specimen (3mm thick) cut from impact region 2, of target disk 1

It was observed that as-received specimens began necking at 20% strain, while the post-impact specimens began necking in the range of 10%-20%, depending on the impact stress history. Engineering stress-strain curves for the as-received material are presented in Figure 3-12.
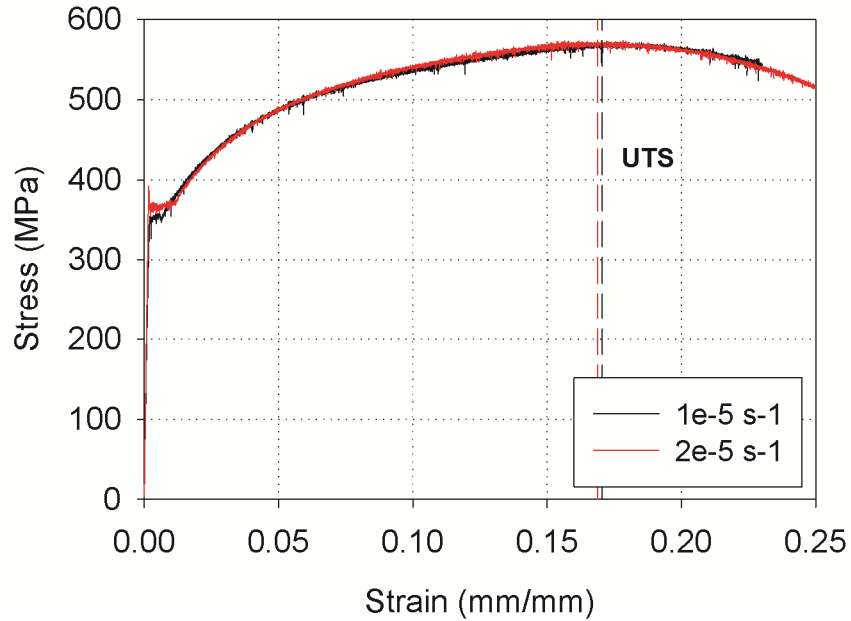
Figure 3-12: Stress-strain curves of as-received material tested at strain rates of 1e-5 s^{-1} and 2e-5 s^{-1}

These curves show clear upper and lower yield points, Lüders extension [22] and serrated plastic flow resembling characteristics of Portevin-Le Châtlier effects [23]. Despite the serrated characteristics, the amplitude of serration is minimal in comparison to the magnitude of the general stress level, and is considered insignificant in the overall analysis of the curves. Engineering stress-strain curves of the post-impact tensile specimens, categorized by impact velocity and volume fraction of twins, are presented in Figure 3-13.
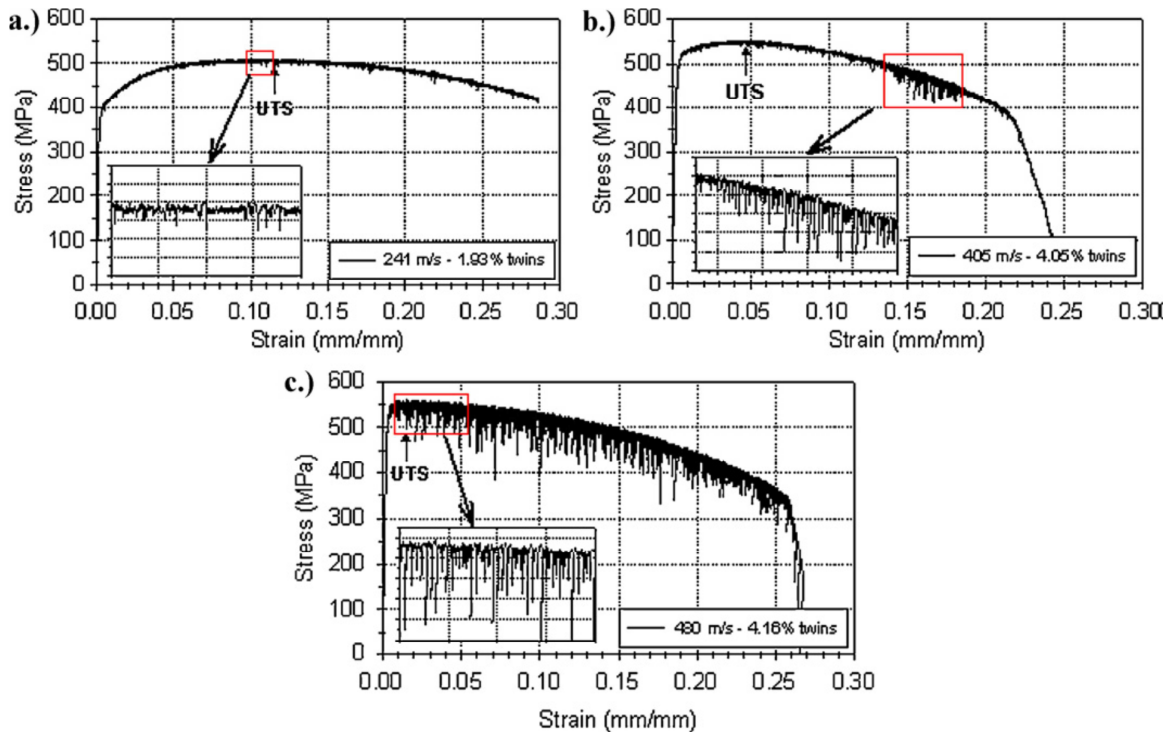
Figure 3-13: Stress–strain curves of post-impact steel specimens. Graph legends pertain to projectile velocities at which the steel was impacted and resultant twin volume fraction. Inset graph shows detailed view of serration characteristics.

Post-impact mechanical response of the material showed an increase in yield strength and slight increase in the ultimate strength, and a decrease in the work hardening. A comparison between yield and UTS for different twin volume fractions is shown in Figure 3-14.
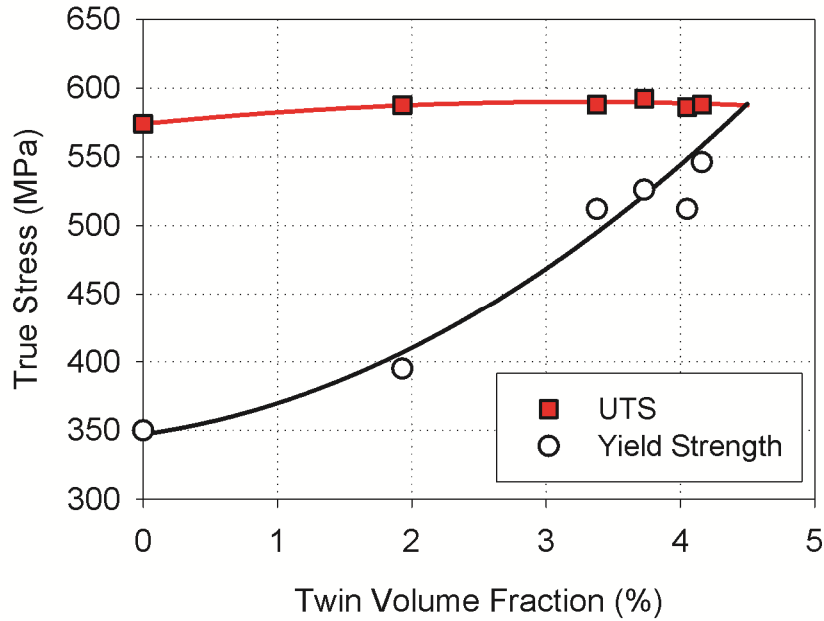
Figure 3-14 Ultimate tensile strength and yield stress of post-impact tensile specimens as a function of twin volume fraction.

This figure shows that as twin volume fraction increases, the yield stress approaches the ultimate strength of the material. The convergence of these curves indicates that the plastic hardening characteristics are becoming less prominent. Figure 3-14 and Figure 3-15 suggests that an increase in twin volume fraction results in a decrease in the ability of the material to store defects during post-impact plastic deformation, which is represented by the loss in work hardening [21] and in the loss of available strain energy up to UTS. Furthermore, quantitative and qualitative interpretation of mechanisms governing elastic-plastic response and instability of the material can be made by comparing the as-received and post-impact stress-strain characteristics.
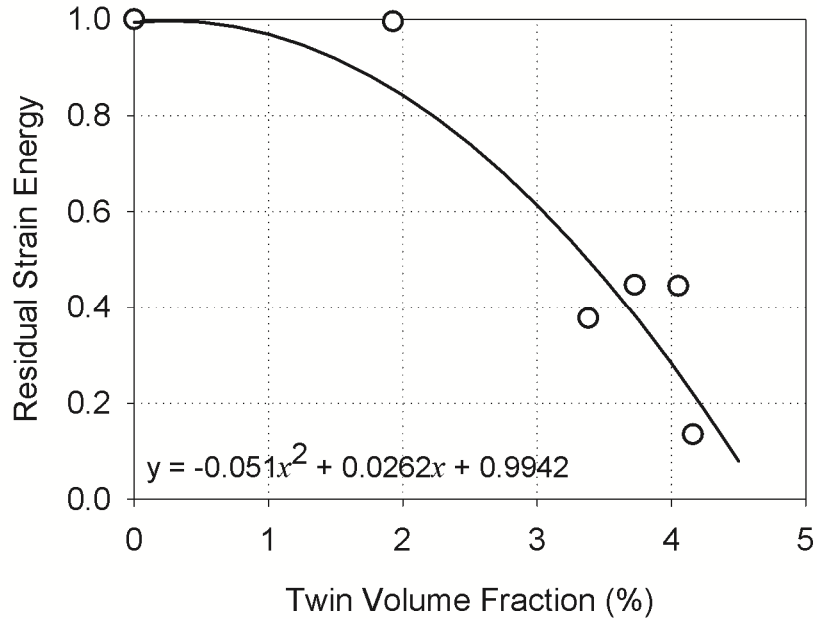
Figure 3-15 Residual strain energy ratio versus twin volume fraction. The ratio is in reference to the as-received condition with no twins. Strain energy is measured as area under the curve up to strain at UTS.

The as-received and the post-impact stress-strain curves both exhibit serrated flow characteristics which have been observed and reported in low carbon and stainless steels [22,24]. Post-impact specimens lack an upper and lower yield point and are characterized by presence of serrations. These serrations can occur in the event of an increase in dislocation density or velocity or both [25]. This increase can be attributed to dislocations within deformation bands locking and unlocking and can be distinguished by three different profiles; type-A, type-B, and type-C [25,26], as illustrated in Figure 3-16.
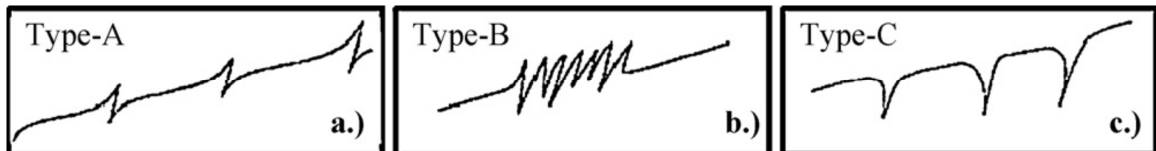
Figure 3-16: Typical segments of a stress-strain profile with a.) type-A, b.) type-B, and c.) type-C serrations.

Type-A serrations are characterized by periodically spaced yield points which increase in size and spacing with further straining. This process is controlled by the formation and propagation of deformation bands along the gage section [26]. Increases in stress are due to large solute atmospheres which prevent unpinning of dislocations, while the creation of new dislocations suddenly decreases the stress. Each successive deformation band requires higher stress to activate. Type-B serrations are characterized by quickly fluctuating peaks and valleys lying along the general level of the stress-strain curve. In this case, in contrast to type A, the serrations are the result of the propagation of deformation bands rather than formation of new bands. In order to maintain the applied strain rate, an increase in dislocation density, and in turn, a decrease in average dislocation velocity results in segregation of solute atoms. The slow moving dislocations become locked rapidly until the stress increases and breaks the dislocation free again, thus allowing the band to propagate. This process continues within the deformation band until it has run through the entire gage section or has encountered another band [25]. Type-C serrations are characterized by distinct yield drops occurring below the general level of the stress-strain curve. This process is controlled by unlocking of pinned dislocations. Inhomogeneous deformation due to stress concentrations created at barriers, such as grain or twin boundaries, result in localized regions of a higher strain rate. This creates additional drag on the atmosphere of dislocations and in turn, frees dislocations and reduces the stress. The sudden availability of mobility decreases the average dislocation velocity in the deformation band and sets up a condition for solute atoms to relock the dislocations and repetition of the process [25].

The type-C load drops, as well as the general softening behavior characterizing the post-impact stress-strain curves can be attributed to Sleeswyk's emissary dislocation mechanism [28]. As Figure 4b shows, several of the twins, while lenticular shaped, have blunted ends. This is evidence that the twinning shear is accommodated by slip in the matrix [24]. The incoherent twin boundary can be schematically visualized in Figure 3-17.
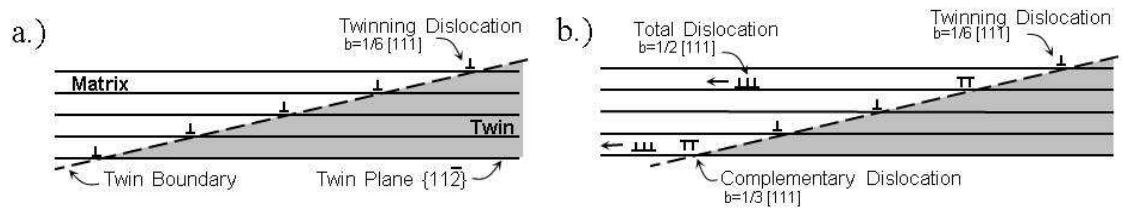
Figure 3-17 (a.) Incoherent twin boundary composed of twinning dislocations on {1 12} planes, and (b.) dissociation of twinning dislocation as the matrix accommodates slip [24].

During tensile testing, slip in the matrix can emanate from available dislocations which make up the incoherent twin boundary; Figure 3-17 a). This dislocation boundary supports a high energy configuration surrounding the twin. As further straining continues, the matrix accommodates plastic deformation by slip of these dislocations upon dissociation of every third dislocation

$$\tfrac{1}{6}[1\,1\,1] \rightarrow \tfrac{1}{2}[1\,1\,1] - \tfrac{1}{3}[1\,1\,1]$$

as shown in Figure 3-17 b). A 1/2 [111] total dislocation glides away from the twin, leaving behind a 1/3 [111] complementary dislocation, and drastically lowers the configuration energy. Thus, as further plastic deformation continues, the energy is

reduced locally allowing for dislocation pile-ups to break through the twin boundary, as can be seen in the stress reduction of Figure 3-13c. If the matrix is not able to accommodate the shear, then a crack may develop in the twin boundary region. The cracking can be seen in Figure 3-18, as they are formed both along the ferrite-pearlite interface, and within the ferrite grains [27], both which occur parallel to the twinning direction. This suggests that the presence of twins in the microstructure influences the not only the elastic-plastic response, but also the characteristics of the failure mechanism.
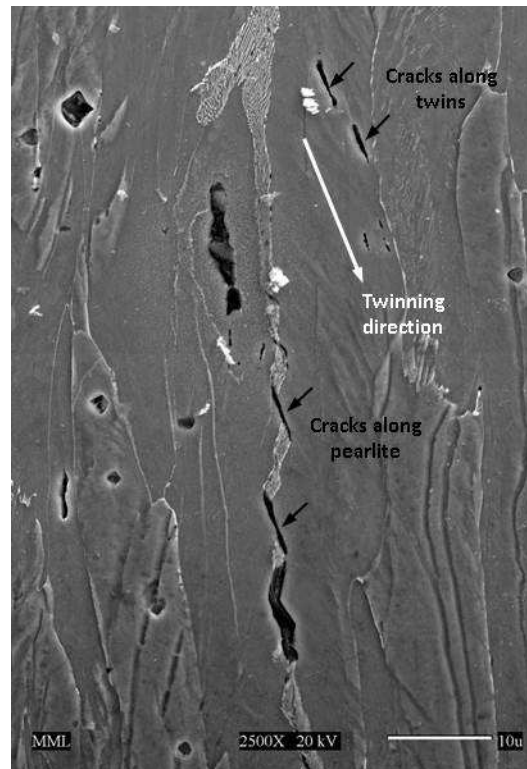
Figure 3-18: SEM micrograph of necked region in post-impact tensile specimen. Cracking occurred along the ferrite–pearlite and twinning interfaces during post-impact tensile testing. All of the cracks within this region are oriented in the twinning direction, suggesting that twins play a role during fracture.

The as-received tensile curves show type-B serrations occurring from the onset of yield through the entire plastic stress-strain curve. Post-impact specimens with less than 4% twins also exhibit type-B serrated flow with a random minority of type-C load drops, as shown in detail in the inset of Figure 3-13a. Figure 3-13b shows, as the volume fraction of twins increases to 4%, the stress-strain curve transitions from type-B to type-C serrations upon further straining [25]. A detailed view of the type-B to type-C transition is shown in the inset of Figure 3-13b. Although this transition is after the UTS, it still acts as an indication that twin interactions are becoming a dominant mechanism for locking mobile dislocations. As the volume fraction of twins increases further, as shown in Figure 3-13c, the majority of the serrations are of type-C.

Since type-C serrations occur from unlocking of pinned dislocations, the transition from B to C indicates could suggest that the material has reached a point where all stored dislocations are locked up due to the presence of twinned regions [21]. During post-impact straining, the networks of locked dislocations between twinned regions break free, causing successive load drops. This change in stress-strain characteristics suggests that the material has transitioned to a point of instability when 4% or more twins exist in the microstructure.

3.6.   **Conclusions**

The objective of the study is to present a correlation between high rate impact and microstructure variation of low carbon steel. Five plate impact experiments were carried out and post impact microscopy shows deformation mechanisms occurring during shock

loading of low carbon b.c.c. steel. The coupling of numerical simulations and the analytical constitutive model act as a tool for defining impact history and predicting post-impact microstructure. Results of this study can be briefly summarized as follows:

1. A direct and unique relationship between impact stress and volume fraction of twins has been experimentally established.

2. Microscopic observation of impact specimens indicate that slip and mechanical twinning are two competing deformation mechanisms occurring during high rate loading of low carbon steel. The lenticular shape of the twins indicates that the twin formation mechanism is by progressive shear of the parent lattice. As impact stress increases, another twinning plane becomes active, and results in large amounts of intergranular twin-twin interactions.

3. Based on microscopic observations, an analytical twinning model aiming at predicting twin volume fraction incorporating both slip and twinning mechanisms has been applied and shown to accurately calculate twin volume fraction. This model was coupled with a rate dependent model implemented into numerical procedures and was capable of capturing deformation response and twin formation during impacts for the given stress range.

4. Quantitative analysis of the post-impact stress-strain curves clearly shows an increase in both yield and ultimate strength, which indicates an increase in stored dislocations in the microstructure as a result of impact loading. However, while the yield and UTS both benefit from shock loading, the available strain energy is drastically reduced; up to 87%. If this trend is extrapolated further, it will show

that the yield and ultimate tensile strength converge, thus eliminating available energy.

5. It is apparent that as the shock loading is increased, new twinning planes are activated. Qualitative analysis provides insight into the dislocation-twinning interaction during plastic deformation. Low impacted specimens reveal small fluctuations in stress-strain response representing that of type-B serrations. At higher impact levels, the presence of multiple twinning planes and twin-twin interactions results in the transition of type-B serrations to type-C load drops during plastic deformation. This suggests that twin-twin interactions play a significant role in controlling plastic deformation, which is responsible for instability within the microstructure.

6. The twins play an important role in the direction of cracking during failure. They provide new interfaces at which cracks may initiate and propagate, and also control the direction of crack propagation.

3.7. **Acknowledgments**

3.8. **References**

[1] J.Y. Richard Liew. "Survivability of steel frame structures subject to blast and fire." *Journal of Constructional Steel Research*. 64 (2008) 854-866.

[2] J.E. Field, S.M. Walley, W.G. Proud, H.T. Goldrein, C.R. Siviour. "Review of experimental techniques for high rate deformation and shock studies." *International Journal of Impact Engineering*. 30 (2004) 725-775.

[3] O. Gregory, J. Oxley, J. Smith, M. Platek, H. Ghonem, E. Bernier, M. Downey, C. Cumminskey. " Microstructure characterization of pipe bomb fragments." *Materials Characterization.* 61.3(2010) 347-354.

[4] D. Firrao, P. Matteis, G. Scavino, G. Ubertalli, M.G. Ienco, G. Pellati, P. Piccardo, M.R. Pinasco, E. Stagno, R. Montanari, M.E. Tata, G. Brandimarte, S. Petralia. "Mechanical twins in 304 stainless steel after small-charge explosions." *Materials Science and Engineering*. A 424 (2006) 23-32.

[5] T. De Resseguier, M. Hallouin. "Stress relaxation and precursor decay in laser shock-loaded iron." *J. Appl. Phys.* 84.4 (1998): 1932-38.

[6] J.N. Johnson, R.W. Rohde. "Dynamic deformation twinning in shock-loaded iron." *J. Appl. Phys.* 42.11 (1971): 4171-82.

[7] J.W. Taylor. "Dislocation Dynamics and Dynamic Yielding." J. Appl.Phys. 36.10 (1965): 3146-50

[8] S.A. Atroshenko, N.S. Naumova, S.A. Novikov. "Influence of high-velocity impact on metals." *International Journal of Impact Engineering*. 33 (2006) 62-67.

[9] T. Smida, J. Bošanský. "Deformation twinning and its possible influence on the ductile brittle transition temperature of ferritic steels." *Materials Science and Engineering*. A287 (2000) 107-115.

[10] L.E. Murr, M.A. Meyers. "Shock-induced deformation twinning in tantalum." *Acta Materialia* 45.1 (1997): 157-75.

[11]   M.A. Meyers, O. Vöhringer, and V.A. Lubarda. "The onset of twinning in metals: A constitutive description." *Acta Materialia* 49 (2001): 4025-39.

[12]   M.A. Meyers, D.J. Benson, O. Vöhringer, B.K. Kad, Q. Xue, H.-H. Fu. "Constitutive description of dynamic deformation: physically-based mechanisms." *Materials Science and Engineering*. A322 (2002) 194-216.

[13]   V. Panov. "Modeling of Behavior of Metals at High Strain Rates" PhD Thesis. Cranfield University. (2005)

[14]   S. Mahajan. "Accommodation at deformation twins in bcc crystals." Metallurgical Transactions A. 12A (1981) 379-386.

[15]   L. Jiang, J. Jonas, R. Mishra, A. Luo, A. Sachdev, S. Godet. "Twinning and texture development in two Mg alloys subjected to loading along three different strain paths." *Acta Materialia*. 55 (2007) 3899-3910.

[16]   K. Maciejewski, Y. Sun, O. Gregory, H. Ghonem. "Time-Dependent Deformation of Low Carbon Steel at Elevated Temperature." (Submitted for Publication)

[17]   G.R. Johnson, W.H. Cook. "A constitutive model and data for metals subjected to large strains, high strain rates and high temperatures." In*: Proceedings of the Seventh International Symposium on Ballistic*, La Hague, Netherlands. (1983) 541–547.

[18]   R.J. Wasilewski. "Mechanism of bcc twinning: Shear or shuffle?" Metallurgical Transactions. 1 (1970) 2641-2643.

[19]   J.W. Christian, S. Mahajan. "Deformation twinning." *Progress in Materials Science* 39 (1995): 1-157.

[20]   S. Mahajan. "Interrelationship between slip and twinning in B.C.C. crystals." *Acta Metallurgica*. 23 (1975) 671-684.

[21]   L.M. Dougherty, E.K. Cerreta, E.A. Pfeif, C. Trujillo, G.T. Gray. "The impact of peak shock stress on the microstructure and shear behavior of 1018 steel." *Acta Materialia* 55 (2007) 6356-6364.

[22]   E. Pink, S. Kumar. "Patterns of serrated flow in low-carbon steel." *Materials Science and Engineering.* A201 (1995) 58-64.

[23]   K. Renard, S. Ryelandt, P.J. Jacques. "Characterisation of Portevin-Le Chatelier effect affecting an austenitic TWIP steel based on digital image correlation." *Materials Science and Engineering.* A527 (2010) 2969-2977.

[24]   Reed-Hill, Robert E. *Physical Metallurgy Principles.* 2nd ed. New York: Nostran, 1973. 611-660.

[25]   D. Fahr. "Analysis of stress-strain behavior of type 316 stainless steel." ORNL/TM-4292 (1973), Oak Ridge National Laboratory report.

[26]   P. Rodriguez. "Serrated Plastic Flow." *Bulletin of Material Science*. Vol. 6, No. 4, (1984) 653-663.

[27]   N. Narasaiah, K.K. Ray. "Small crack formation in a low carbon steel with banded ferrite-pearlite structure." *Materials Science and Engineering.* A392 (2005) 269-277.

[28]   A.W. Sleeswyk. "Twinning and the Origin of Cleavage Nuclei in α-Iron." *Acta Metallurgica.* 10 (1962) 803-812.

CHAPTER 4

TWIN NUCLEATION IN COLD ROLLED LOW CARBON STEEL SUBJECTED TO PLATE IMPACTS

W. Visser, H. Ghonem*

_____

Department of Mechanical Engineering, University of Rhode Island, Kingston, RI 02881, USA

∗ Corresponding author. Tel.: +1 401 874 2909; fax: +1 401 874 2925.
                    E-mail address: ghonem@egr.uri.edu (H. Ghonem).

4.1.   **Abstract**

Shock loading tests have been carried out on low carbon steel specimens using a single stage gas gun with projectile velocities ranging from 200 to 800 m/sec. In addition to dislocation slip, twinning was observed to be a contributing deformation mode. Similar impact tests were performed on specimens that have been previously subjected to cold rolling and it was shown that pre-straining increases the threshold stress for twin formation under shock loading. Efforts are made to determine the critical stress and strain rate required for twinning in cold rolled specimens. For this purpose a set of compression tests were performed on as-received and pre-strained specimens using a split Hopkinson pressure bar at various strain rates. These tests were carried out at liquid nitrogen temperatures where the thermal activation of dislocations is assumed to be higher than that for twin nucleation. Results of these tests are combined with FE analysis to provide knowledge of the twin stress as a function of pre-strain and strain rate. In addition, post-impact specimens were examined to identify characteristics of the deformation induced twins. It is shown that more than one {112} <111> type twin system is active at high stress levels as evident by the non-parallel nature of twins formed at the higher impact pressures. This observation was incorporated into a constitutive model based on one dimensional wave and conservation equations for predicting twin volume fraction by resolving the shear stress in multiple directions and applying twin growth equations for each plane. Results of this model show similar trends when compared with experimental outcomes for as-received and pre-strained steel.

4.2.   Introduction

The study of high strain rate loading is important for a wide array of uses from manufacturing needs such as explosive forming processes to end-use applications such as safety of structural members and crumple zone materials in vehicle components. In order to effectively design for such events, experimental testing of related materials is required over a range of strain rates and temperatures to facilitate in the development of constitutive models and in the understanding of the evolution of microstructure features. Several techniques exist by which these experiments can be conducted in small scale laboratory settings, of which Field et al. [1] and Ramesh [2] have described in detail. These tests include compression and tension tests using a drop weight, split Hopkinson pressure bar (SHPB), Taylor impacts, plate impacts using single or two stage gas guns, and small scale explosive loading of plates. From these methods, strain rates in the range of 10^1 s^{-1} up to 10^6 s^{-1} can be achieved.

Of all the metals which have been subject to dynamic testing, steel is the most common. The cost, variety, strength, and availability have allowed steel to be a widely used metal in structural engineering. For this reason, vast amounts of research on all types of steel have been carried out. One common aspect in all high strain rate testing of steel is evident; deformation can occur by two processes, dislocation slip and/or mechanical twinning. Visser et al. [3] have shown that the volume fraction of twins is directly proportional to the applied stress through a series of plate impacts in low carbon steel. Firrao et al. [4] were able to calculate critical stress required for twinning based on observed twinning and explosive pressures, and proved that twin nucleation occurs just before the onset of yielding. Karaman et al. [5] determined the dependence of the stress-

strain response on slip and twinning as a function of crystal orientation, from which they suggest that twinning occurs by pile ups of dislocations from which partial separation occurs. De Resseguier and Hallouin [6] shock loaded iron using high-power lasers pulses and found significant twin formation in post-shock specimens. A constitutive twinning model proposed by Johnson and Rohde [7] was implemented to determine twin volume fraction and elastic-plastic response by Taylor [8]. Several studies have been done in order to determine the role of deformation twins on the mode of fracture [9][10], while Biggs and Pratt [11] established a correlation between deformation twins and the mode of fracture. Visser et al. [3] have shown that twins have some influence on the direction of crack path during subsequent quasi-static loading of impacted steel.

Armstrong and Worthington [12] presented a mechanistic model based on experimental observations explaining the slip-twinning transition. Meyers [13] [14] discusses the influence of strain rate, temperature, grain size, and stress state on twin initiation and showed that twin nucleation is related to dislocation motion which in turn is strain rate and temperature sensitive. A model was proposed, on the basis of the Swegle-Grady relationship, to predict the critical stress for twin nucleation in which dislocation pile-ups are considered a key aspect; see also the work of Murr and Meyers [15] on FCC Tantalum. This critical stress has also been examined for FCC, BCC, and HCP materials. Equations for critical shear stress for twining are presented [13] for BCC, FCC, and HCP materials, all of which are dependent upon strain rate, temperature, and the Hall-Petch relation for grain size. They found that the twin density is a function of stress, independent of temperature and strain rate and the amount of twins will increase monotonically with increasing stress.

Mechanical twinning is known to occur in low carbon steel at high strain rates at room temperature as well as at low strain rates at low temperatures. Several authors have shown that pre-straining at room temperature prior to low temperature deformation will inhibit deformation twin nucleation. Lindley [16] has shown that twins are suppressed in low carbon steel when testing at -196°C after a prior pre-straining of 3%, 5%, and 8% at room temperature. Biggs and Pratt [11] were able to determine yield stress for slip at -183°C in alpha-iron by suppressing twins through pre-straining to 2% at room temperature. Rosenfield et al. [17] have shown that 1% pre-straining suppresses twins in single crystal iron during tensile testing at -195°C. Churchman and Cottrell [18] showed that alpha-iron with less than 1% strain at room temperature deforms only by slip when testing at liquid air temperatures. Furthermore, Mahajan and Bartlett [19] proved that a 2% pre-strain was sufficient to suppress twin formation in molybdenum during room temperature shock loading of 9 GPa.

The above studies have also indicated that the volume fraction of twins is influenced by the dislocation configuration, which in turn is a function of the strain rate, temperature, dislocation density, and the overall duration and magnitude of stress. As the loading rate and stress level increase, the number of nucleated twins increases. This is due to the low density and heterogeneous network of mobile dislocations present in the as-received or annealed material which leads to a larger probability of twin nucleation sites. In the case of a material with a homogeneous distribution of dislocations, the propensity to twin becomes lower as plastic deformation can be accommodated by slip which is motivated by dislocation multiplication which more easily occurs by the double cross-slip mechanism [19]. By nucleating mobile dislocations and homogenizing the

dislocation network prior to high rate deformation, the plastic strain can be accommodated purely by dislocation slip [20]. Therefore, prior mobile dislocation density is indirectly proportional to the number of probable twin nucleation sites. This could indicate that the mobile dislocation density and the degree of uniformity have a direct correlation with the critical stress required to twin.

This concept, the correlation of dislocation density and homogeneity to twin stress, can be examined by varying the initial mobile dislocation density. This will lead to an alteration of the critical stress for twin nucleation, τ_{twin}, and should produce differing final volume fractions of deformation twins accordingly. These conditions can be achieved through different levels of pre-straining at low rates and at room temperature via cold rolling. Mahajan and Bartlett [19] and Mahajan [20] also recognized that the density of mobile dislocations can be increased and configuration be altered by increasing the initial pre-strain level. In order to investigate the strain rate effects on the critical twinning stress, a set of low temperature tests have been carried out using a Split Hopkinson Pressure Bar. Since the stress required for slip is increased above that for twinning at liquid nitrogen temperatures, τ_{twin} can be reached at lower strain rates than those achieved in room temperature plate impact tests. This can be attributed to the fact that cross-slip is a thermally activated process, becoming more difficult as the temperature is decreased [21].

The objective of this work is to establish a twin nucleation stress in pre-strained low carbon steel. This will be expressed as a stress based criteria which will be a function of strain rate and dislocation density. First, the steel in both the as-received (hot rolled) and pre-strained (cold rolled) conditions were characterized through optical microscopy and

quasi-static testing. A series of plate impact tests were conducted on these materials using a single stage gas gun, from which a relation between impact stress and twin volume fraction was determined. A coupled numerical and analytical approach was then used in order to model the mechanical response and microstructural evolution of the steel during impact events. A twin stress equation was developed on the basis of dislocation generation and velocity and utilized in numerical modeling to predict twin volume fraction during shock loading. Model parameters were determined through low temperature (SHPB) tests. Based on experimental evidence of twin systems present during shock loading, procedures are carried out in order to improve model accuracy in calculating twin volume fraction as a function of impact stress by including twin nucleation on multiple {112} twin systems.

4.3.   **Material**

The material used in this study is low carbon steel in a hot rolled condition with the microstructure consisting of primarily α-ferrite phase with dispersed colonies of pearlite. The pearlite colonies are made of α ferrite and Fe_3C cementite lamellas. Figure 4-1(b) shows an optical micrograph of the as-received steel which has been polished to a 1µm finish and etched using 5% nital solution for 7 seconds. Average grain size is between 25-35 µm with a 9% volume fraction of the pearlite phase.
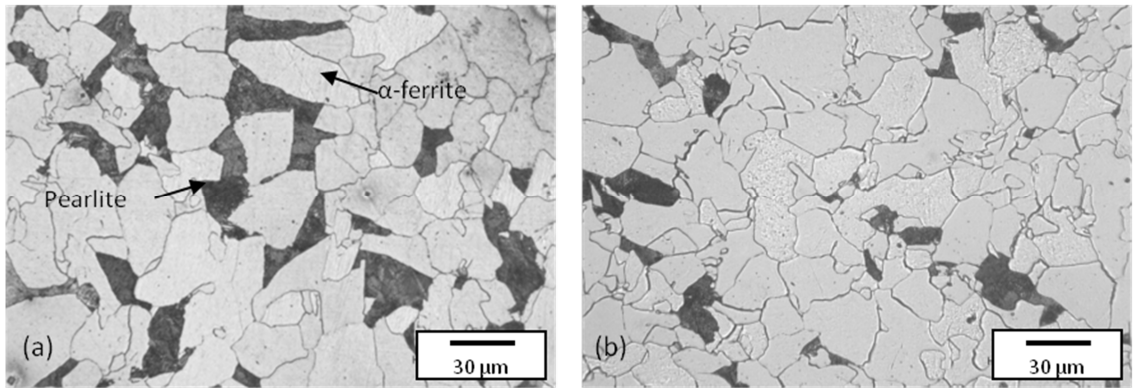
Figure 4-1: Optical micrographs of (a) the as-received A572 grade 50 low carbon steel. The lighter color phase is the ferrite and darker phase is the pearlite as indicated in the figure, and (b) 3% cold rolled steel showing no significant change in the grain size or it's aspect ratio.

Quasi-static compression tests showed the yield strength of the material to be 350 MPa at room temperature with a Young's modulus of 210 GPa. The longitudinal and shear wave speeds of the steel were measured using nondestructive ultrasonic wave reflection methods and results are shown in Table 4-1.

Table 4-1: A572 Grade 50 low carbon steel material properties determined using ultrasonic wave technique

$C_{longitudinal}$ (m/s)	5950
C_{shear} (m/s)	3255
Poisson's ratio	0.286
Young's Modulus (Pa)	2.130E+11
Shear modulus (Pa)	8.279E+10
Bulk modulus (Pa)	1.662E+11

From these wave speeds Poisson's ratio and elastic moduli were calculated, which confirmed the quasi-static tensile results. Test specimens were prepared in the as-received and pre-strained conditions. Pre-straining was done by cold rolling 1/2 inch plates at room temperature to strains of 1%, 3%, and 20%. As Figure 4-1(b) shows, no major changes in grain size or aspect ratio have occurred. Plate impact target specimens were cut into discs 3 inches in diameter, and 0.250 inch in thickness and projectile discs measuring 1.75 inches in diameter and 0.125 inches thick were used. SHPB specimen dimensions were 0.375 inches in diameter and 0.1875 inches thick. All specimen faces were surface ground to ensure planarity during testing.

4.4. **Plate Impact Testing and Results**

Plate impact experiments were conducted using a single stage gas gun with high pressure helium as the driving gas. In this system, projectile velocities ranging from 200 to 800 m/s are measured using a set of lasers and photo diodes which are mounted perpendicular to the barrel and between the end of the barrel and the front face of the target. Steel projectile plates were launched down the barrel using 4 inch long PVC sabots and remained partially in the barrel upon impact to eliminate tilt between target and projectile surfaces. The air in the barrel was evacuated using a mechanical vacuum pump. Target discs were mounted directly to the end of the vacuum chamber from which a vacuum seal is created. This mounting configuration also ensures a 1D planar impact. A top view of the target and the vacuum chamber attached to the end of the gas gun barrel are shown in Figure 4-2.
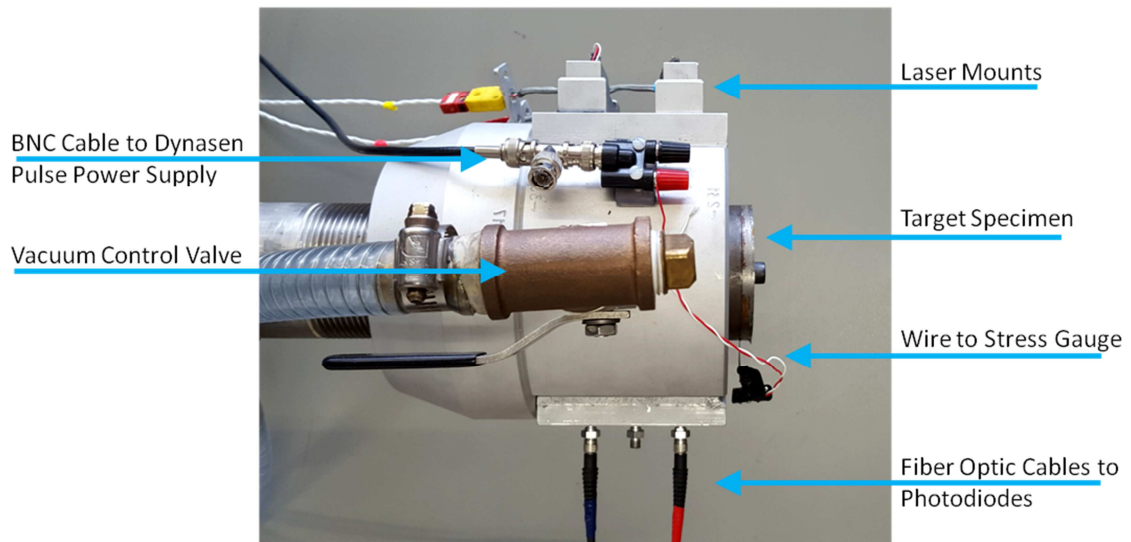
Figure 4-2: Top view target and vacuum chamber set up attached to the end of the gas gun barrel

Longitudinal stress histories were recorded using piezoresistive manganin foil stress gauges bonded centrally between the back surface of the target disc and a steel backing plate. The backing plate was machined slightly thicker to ensure that tensile reflection waves and spallation was captured in the sacrificial backing plate. The gauges were excited with 100 volts prior to impact using a Dynasen pulse power supply which was triggered by the first velocity laser. Stress and velocity data was recorded using a 300MHz digital phosphor oscilloscope at 2.5 GS/s. Figure 4-3 shows the stress histories of the steel samples recorded during the impact.
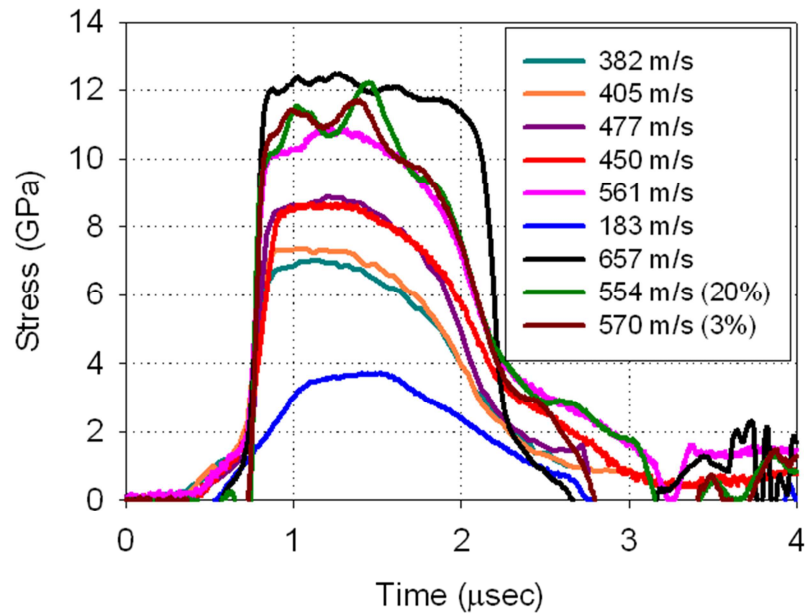
Figure 4-3: Room temperature plate impact stress-time profiles of steel specimens. Legend data corresponds to the velocity of the impactor plate and the (20%) and (3%) correspond to pre-strained steel specimens.

Impacted target specimens were sectioned, polished and etched to study the post-impact microstructure. SEM micrographs were taken perpendicular to the impact direction. In the as-received condition the α-ferrite grains deformed by slip and mechanical twinning and has previously been established that as the impact stress is increased, the volume fraction on twins increases [3]. As other studies have shown, twinning can be suppressed in BCC metals during impact loading by subjecting the material to quasi-static pre-straining which Mahajan [20] has observed to be due to a delay in the twin nucleation process.

As shown in Figure 4-4, at impact pressures similar to those used in the as received condition, pre-straining at 3% and 20% has completely suppressed twin formation.

However, the 1% pre-strained samples show the presence of few twins, Figure 4-4(b), in a manner indicating that the pressure level 10-11 GPa is close to the twin nucleation threshold.
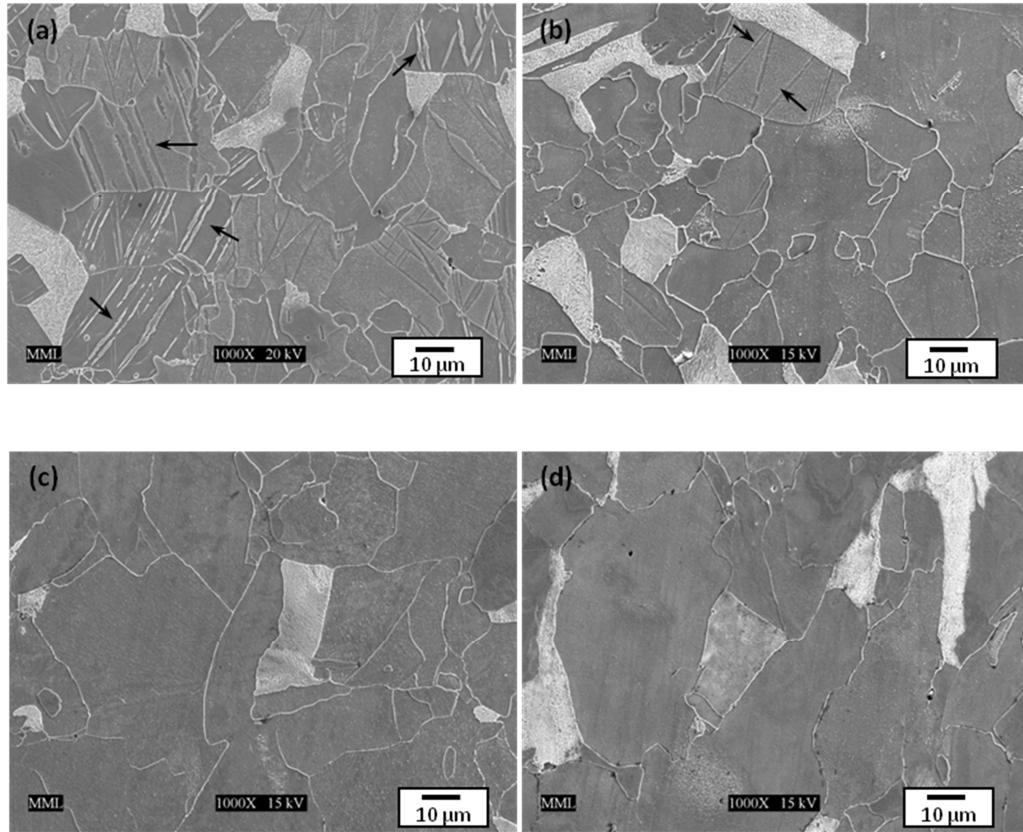
Figure 4-4: SEM micrographs of shock loaded as-received and pre-strained steel samples; white regions are the pearlite phase and dark regions are the ferrite phase; arrows indicating twins (a) as-received steel impacted at 12GPa resulting in 12% twin volume fraction, (b) 1% pre-strain steel impacted at 11 GPa resulting in 0.5% twin volume fraction, (c) 3% pre-strain steel impacted at 11GPa with no twins present, (d) 20% pre-strain steel impacted at 11GPa with no twins present.

As discussed by Wasilewski [22], twin formation can be described by two different processes; Twins can form by a progressive shear of the parent lattice or by an atomic shuffle within the lattice, both of which create the same arrangement within the twinning

planes. Twinning by progressive shear of the parent lattice will produce a shear offset; i.e. plastic deformation, while a local rearrangement or shuffle will produce no shear offset. Formation of the twin by homogeneous shear will produce a shear offset equal to kh, where k is the twinning shear, and h is the average thickness of the twin lamella. For bcc crystals twinning is most readily formed on the {112} planes in the $\langle 111 \rangle$ direction which has a k equal to $1/\sqrt{2}$ [7,21]. Each layer of atoms shifts 1/3 burgers vector, equivalent to $a/6\langle 111 \rangle$. As such, the twinning shear in BCC material can be derived as the ratio of the length of the Burger's vector of the partial dislocation, $a/6\langle 111 \rangle$, to the interplanar spacing of the {112} twinning plane [45]. A representation of three layer twin is shown in Figure 4-5.
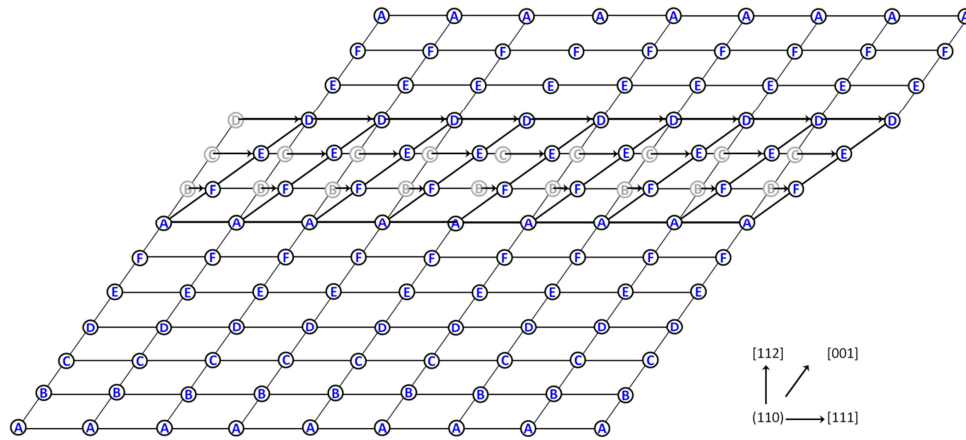
Figure 4-5: BCC structure viewed normal to the (110) plane showing the atomic shift on successive planes resulting in a twinned portion of the lattice

The operative mode of twining being shear or shuffle can be determined by observation of the shape of the twins formed. The lenticular shape of the twins indicates that the twins are formed by progressive shear of the parent lattice rather than prismatic twins arising from a local shuffle of atoms [22]. It should also be noted that the critical shear stress required to nucleate twins is much higher than the shear stress required for twin propagation. This can be explained by the lenticular shape of twins. The ratio of surface area to volume is very high when the twin is small. As the twin grows, the surface area to volume ratio decreases, hence less stress is required for twin growth, however the stress needed to propagate twins will increase as slip activity increases. The parallel nature of twin formation suggests that twins are forming on the same {112} type plane, however there does exist a large amount of twin-twin interaction. As the impact stress is increased a larger percent of the grains encompass twins forming on multiple types of {112} <111> systems, which is evident in Figure 4-4(a) and (b). Several methods exist to measure twin volume fraction the most accurate of which is electron backscatter diffraction [23-25]. The current work employs a manual point count method ASTM E562-05. Results of these measurements are shown in Figure 4-6.
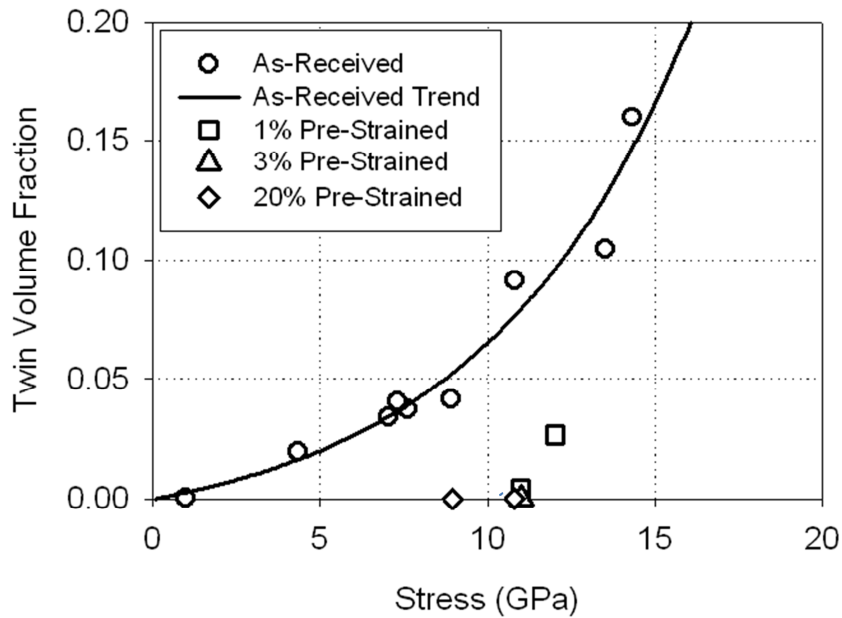
Figure 4-6: Twin volume fraction vs. impact stress measured from room temperature plate impact experiments for as-received and 1%, 3%, and 20% pre-strained low carbon steel.

As shown in this figure, twinning in the as-received steel occurs at stress levels as low as approximately 1 GPa and the volume fraction of twins increases exponentially to around 16% at 14GPa. Cold rolling to a strain of 1% resulted in a distinct increase in the twin nucleation stress to 11 GPa. An increase to 2.5% volume fraction occurred at 12 GPa. Results of tests conducted on the 20% cold rolled steel showed that that the twins are fully suppressed within the tested stress range up to 16 GPa; see Figure 4-4(c) and Figure 4-4(d). It can be argued that an increase in the critical twin stress results in a reduction of the amount of twins available to accommodate plastic deformation. Previous work [3,11] has shown that an increase in twin volume fraction leads to a decrease in the available energy to failure and elimination of twinning prevents fracture by cleavage. Work by

Hull [21] has shown that the initiation of cleavage fracture was coincident with the first twins formed. Therefore reduction in the final twin volume fraction may increase the post-impact strength by reducing the probability of crack initiation at twin boundary sites. The next section describes the work made to calculate the critical twin stress of cold rolled steel as a function of pre-strain and strain rate

4.5.   Modeling Twin Volume Fraction

Several models exist which deal with different aspects of the deformation twinning process. While much of the work is performed on FCC; see Kibey et al. [26], De Resseguier and Hallouin [6] and Meyers et al. [13,14] have examined BCC metals. In the current work a deformation model, based on the work of Johnson and Rohde [7], is used in order to analytically predict twin volume fraction occurring due to uniaxial strain during plate impact loading. The model is based on the assumption that twins form by a homogeneous progressive shear of the parent lattice rather than a local atomic "shuffle" process as described by Walisewski [22]. This model will be used to calculate stress and strain during impact loading based on the conservation of mass and momentum equations. Following the model description, a twin nucleation stress criterion will be described in conjunction which a series of numerical simulations and low temperature compression tests which were used to obtain required material parameters.

4.5.1.   Twin Model Formulation

The mechanical response during impact loading can be determined using one-dimensional stress-strain relations derived from basic equations in theory of elasticity and substitution into one-dimensional Lagrangian equations of wave motion [8], from which a set of equations is solved numerically to determine, strain, and particle velocity as functions of position and time. These equations can be written as:

$$\frac{\partial \varepsilon}{\partial t} + \frac{\partial u}{\partial X} = 0 \tag{1}$$

$$\rho_0 \frac{\partial u}{\partial t} + \frac{\partial \sigma}{\partial X} = 0 \tag{2}$$

where ε is the total longitudinal component of strain, u is particle velocity during impact at time t at a distance of X measured from the impact surface, ρ_0 is initial density, and σ is the normal stress component.

The initial particle velocity profile imposed at the front surface of the target specimen is a required input in order to explicitly solve equations (1) and (2) through time and distance. Finite element analysis of plate impacts is used in order to determine the particle velocity profile as shown in Figure 4-7 which is then simplified as a trapezoidal pulse to eliminate numerical fluctuations. The procedure by which the numerical simulation is executed is provided in more detail by Visser et al. [3].
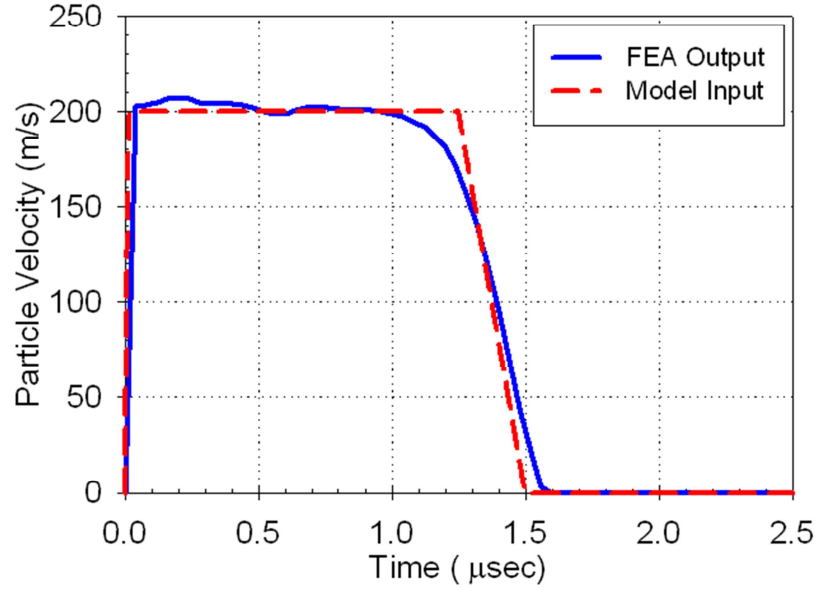
Figure 4-7: Particle velocity profile of the front surface of the target determined from FEA of a 400 m/s plate impact. Blue line is the FEA output, and the red dashed line is the simplified form of the profile for an input into equation (2).

The stress component σ, can be decomposed into hydrostatic and deviatoric components in terms of a pressure P and shear stress τ:

$$\sigma = P + \frac{4}{3}\tau \tag{3}$$

The pressure can be derived from the conservation of momentum equation; see Asay and Shahinpoor [27]:

$$P_1 - P_0 = \rho_0 \left(u_1 - u_0 \right) \left(U_S - u_0 \right) \tag{4}$$

where the subscripts 0 and 1 denote initial and current states, respectively. The shock velocity U_S is described as

$$U_S = C_0 + Su_1 \tag{5}$$

where C_0 is the longitudinal wave speed and S is the slope of the shock velocity-particle velocity curve. Combining equations (4) and (5), and for a material initially at rest the initial pressure P_0 and particle velocity u_0 terms drop from equation, which results in an equation for pressure during shock loading as:

$$P = \rho_0 u_1 \left(C_0 + Su_1 \right) \tag{6}$$

The resolved shear stress, τ, is written as:

$$\tau = \frac{1}{2}\left(\sigma_x - \sigma_y \right) \tag{7}$$

where the x and y subscripts denote the loading and transverse directions, respectively. From the generalized Hooke's law for linear isotropic elastic solids, the normal stress, σ_x, and transverse stress, $\sigma_y = \sigma_z$, relations are:

$$\sigma_x = \lambda\left(\varepsilon_x^e + \varepsilon_y^e + \varepsilon_z^e \right) + 2\mu\varepsilon_x^e \tag{8a}$$

$$\sigma_y = \lambda\left(\varepsilon_x^e + \varepsilon_y^e + \varepsilon_z^e \right) + 2\mu\varepsilon_y^e \tag{8b}$$

where λ is Lame's constant, μ is shear modulus, and the superscript e signifies the elastic strain component, which is determined as:

$$\varepsilon^e = \varepsilon^t - \varepsilon^p \tag{9}$$

The superscripts t and p designate total and plastic strain components. The plastic shear strain on the plane of maximum shear stress can be written as:

$$\gamma = \frac{1}{2}\left(\varepsilon_x^p - \varepsilon_y^p\right)$$

(10)

Due to radial symmetry about the loading axis, $\varepsilon_y = \varepsilon_z$, and since the plate impact loading is in a state of uniaxial strain, the total strain in the transverse direction is considered zero; $\varepsilon_y^t = 0$. Substituting equations (8)-(10) into (7) results in a shear stress equation of the form:

$$\tau = \mu\left(\varepsilon_x^t - 2\gamma\right)$$

(11)

Work by Wasilewski [22], Christian and Mahajan [28], and Klassen-Neklyudova [29] have shown that the total strain component in the constitutive model can be decomposed into elastic and plastic parts, of which the total plastic strain can be described as a summation of strain due to dislocation slip and deformation twinning:

$$\gamma = \gamma_s + \gamma_{tw}$$

(12)

The plastic strain due to twinning can be expressed as the shear offset due to a single twin multiplied by the total number of twins:

$$\gamma_{tw} = k\left(\alpha - \alpha_0\right)$$

(13)

where k is twinning shear, α is the volume fraction of twins, α_0 is initial twin volume fraction. The value for k is dependent upon the plane on which the twin forms. In the

case of BCC metals, the twinning system is on the {112} planes which has a twinning

shear of $k = 1/\sqrt{2}$ based on the plane spacing and atomic translation vector; Klassen-

Neklyudova [29]. The plastic strain due to slip is simply the total strain, ε_x^t minus the

elastic strain and the strain due to twinning:

$$\gamma_s = \frac{1}{2}\left(\varepsilon_x^t - 2k(\alpha - \alpha_0) - \tau_s/\mu\right) \tag{14}$$

where τ_s is the shear stress required for slip. The twin volume fraction and twin growth

rate are functions of corresponding shear stress which is solved explicitly through time

and space. Johnson and Rohde [7] have expressed the volume fraction of twinned

material as:

$$\alpha = \left(\alpha_0^{1/m} + \frac{1}{t_c}\int_0^t g(\tau)\,dt\right)^q \tag{15}$$

where t_c is a characteristic time, which is a constant controlling the rate of twin density,

and q is an exponent with values of 1, 2, or 3 to describe growth of twins through the

thickness, radial direction, or both [7]. The dimensionless growth rate of twins, $g(\tau)$, is

expressed as:

$$g(\tau) = \tau/\tau_{tw} - 1 \quad \tau \geq \tau_{tw} \tag{16}$$

The critical twinning stress τ_{tw} is the parameter which is of interest in this work.

Johnson and Rohde considered this stress to be a constant in their model formulations.

This is, however, a simplified approach and does not provide accurate results when

dealing with materials that have been previously cold rolled. Based on the work of Karaman et al. [5], Meyers et al. [13,14] and Christian and Mahajan [28] certain materials exhibit twin stresses that are dependent on material or loading parameters such as stacking fault energy, strain rate, and temperature. Without implementing initial material parameters and loading conditions, the model will over predict the twin volume fraction at higher strain rates and stresses, leading to a deviation from the actual stress-strain response.

4.5.2. **Critical Twinning Stress Formulation**

In developing an equation for the critical twin nucleation stress, two assumptions are made here. The first is that the formation of twins in the BCC structure occurs by gliding of partial dislocations on successive {112} type planes in the <111> direction. The second assumption is that during shock loading, the contribution of dislocation generation to the strain rate is occurring by the generation of primarily partial dislocations which, in turn, lead to twin formation, and any strain accommodation due to dislocation slip is occurring with perfect dislocations which are already preexisting in the material. The basis of the second assumption stems from the nucleation energy associated with perfect and partial dislocations. At high applied stresses, the Burgers vector of dislocations tend to be smaller, therefore, the nucleation of partial dislocations is preferential due to a lower free energy of nucleation at high strain rates and low temperatures. Furthermore, the partial dislocations are more operative at these conditions due to their higher jump frequency [30]. This is described in further detail by Ferreira et al. [31] who state that the onset of twinning occurs when the jump frequency of dislocation kink pairs f_k is greater

than the jump frequency of perfect dislocations f_d. However, the amount of twinning is still driven by the peak pressure and duration. It is therefore reasonable to rely on a stress based criteria as the driving nucleation force. Meyers [14] has studied the critical twinning stress and the slip-twin transition in FCC, BCC, and HCP metals as a function of temperature, strain rate, grain size and stacking-fault energy. These studies are based on dislocation emission, in which local stresses exceed the twinning stress due to the formation of dislocation pile-ups emitted by a Frank-Read type source. The critical twin stress in Meyers' work is obtained from the Johnston-Gilman equation describing dislocation velocity driven by the shear stress as [32]:

$$v = A\tau^m \exp\left(-\frac{Q}{RT}\right) \tag{17}$$

where Q is activation energy, R is universal gas constant, T is temperature, and A and m are constants. The time required to build up n dislocations traveling an average distance from dislocation source to barrier of l at velocity v is given as:

$$t = n\frac{l}{v} \tag{18}$$

Under conditions of uniaxial loading the stress is described by Hooke's law as:

$$\sigma = E\dot{\varepsilon}t \tag{19}$$

Substituting equations (17) and (18) into (19), the equation for twinning stress as a function of strain rate takes the form:

$$\sigma_T = K\dot{\varepsilon}^{\left(\frac{1}{m+1}\right)} \exp\left(\frac{Q}{(m+1)RT}\right) \tag{20}$$

211

$$K = \left(\frac{nlE}{A}\right)^{\left(\frac{1}{m+1}\right)} M^{\left(\frac{m}{m+1}\right)} \qquad (21)$$

where M is an orientation factor and E is the elastic modulus. This set of equations (17-21) describes a source for dislocation multiplication which produces a stress concentration needed to increase the stress above the critical value for twin nucleation, and is based on nucleation and motion of perfect dislocations which is based on the Johnston-Gilman velocity; equation (17). However, in BCC metals, where partial dislocations are more likely to nucleate at high strain rates, the dislocation generation rate, not the velocity, is the controlling factor.

While several models have been developed for the generation of dislocations during shock loading, the work presented in this paper is built on the work of Meyers [33] and Zaretsky [34,35]. The dislocation generation model originally proposed by Smith and Horbogen [36], has limitations due to the reliance on dislocations moving with the shock front at velocities slightly higher than the shock front velocity. The velocity of dislocations which, as seen in equation (17), is driven by the applied shear stress and can range between less than one meter per second to a maximum velocity which is limited by the velocity of sound in the material [30]. Atomistic simulations have shown that dislocations can actually move at velocities higher than the speed of sound [37], especially at lower temperatures where scattering of phonons is less pronounced [38], thereby reducing the viscous drag component. However, this may still be unlikely to happen due to the high Peierl's Nabarro stress in BCC metals. Gilman [39], however, argues that supersonic velocities are not possible because it implies dislocations have an

infinite angular momenta, which also disproves the use of the shear wave velocity as a limiting value. Gilman provides an estimate of the limiting velocity as:

$$v_{0\_max} = (1/\pi)(G/\rho)^{1/2}$$

(22)

where G is the shear modulus and ρ is the density of the material.

The description of dislocations velocity clearly limits the validity of the models proposed by Smith and by Horbogen [36]. The model of dislocation generation during shock loading proposed by Meyers [33] considers that stress relief occurs through a high homogeneous generation rate of dislocations just behind the shock front which only move short distances at subsonic speeds, resulting in dislocations left behind the front. Meyers also suggests that the strain accommodation during shock loading takes place by the movement of existing dislocations and by the generation of new dislocations, which Ferreira et al [31] have considered to be primarily partial screw dislocations.

Zaretsky [34] extended Meyers model by proposing that the dislocations generated are that of a smaller burgers vector (partial dislocations). The advantage of the model is that it needs no assumption of supersonic dislocation motion, or simultaneous creation of dislocations of opposite sign, and provides an explanation for the generation of deformation twins during shock loading based on high rate partial dislocation multiplication and emission.

Based on the models presented above, and the assumption that twins are formed by partial dislocation glide on successive planes, the total plastic strain can first be described as a summation of strain due to slip and due to twinning:

$$\varepsilon_{plastic} = \varepsilon_{slip} + \varepsilon_{tw} \tag{23}$$

Strain due to slip can be written in terms of density of perfect dislocations, ρ_o, burger's vector of a perfect dislocation (b_o=2.473E-10 m), and the average dislocation distance travelled, l. This is expressed by the Orowan equation as:

$$\varepsilon_{slip} = \rho_o b_o l \tag{24}$$

Taking the time derivative of equation (25) leads to:

$$\dot{\varepsilon}_{slip} = b_o \rho_o \frac{\partial l}{\partial t} + b_o l \frac{\partial \rho_o}{\partial t} \tag{25}$$

The two time derivatives on the right hand side represent the dislocation velocity, $\frac{\partial l}{\partial t}$, and the dislocation generation rate, $\frac{\partial \rho}{\partial t}$. The strain rate due to partial dislocations can be expressed in a manner similar to equation (25), thus, the total plastic strain is written as:

$$\dot{\varepsilon}_{plastic} = \underbrace{\left(b_o \rho_o \frac{\partial l}{\partial t} + b_o l \frac{\partial \rho_o}{\partial t} \right)}_{\dot{\varepsilon}_{slip}} + \underbrace{\left(b_p \rho_p \frac{\partial l}{\partial t} + b_p l \frac{\partial \rho_p}{\partial t} \right)}_{\dot{\varepsilon}_{tw}} \tag{26}$$

In equation (26), the strain rate due to dislocation slip is expressed by the dislocation density, ρ, Burger's vector, b, and dislocation velocity, v, where the subscripts o and p are representative of perfect and partial dislocations, respectively. At lower strain rates the velocity of dislocations is the controlling parameter, whereas at high strain rates dislocation generation rate dominates [33][40]. Based on the assumption that only partial dislocations are being generated at this loading rate, the velocity component from the

$\dot{\varepsilon}_{twin}$ term and the generation of perfect dislocations in the $\dot{\varepsilon}_{slip}$ term can be eliminated. Thus, equation (26) reduces to:

$$\dot{\varepsilon}_{plastic} = \underbrace{\left(b_o \rho_o \frac{\partial l}{\partial t} \right)}_{\varepsilon_{slip}} + \underbrace{\left(b_p l \frac{\partial \rho_p}{\partial t} \right)}_{\varepsilon_{tw}} \tag{27}$$

The strain rate in equation (27) can be related to the stress in power law form as seen in typical hardening plasticity models such as described by the one dimensional form of the Norton-Hoff model where plastic strain rate is related to stress as:

$$\dot{\varepsilon}_{plastic} = \left(\frac{\sigma}{\lambda^*} \right)^{N^*} \tag{28}$$

N and λ are material hardening parameters. Solving equation (28) for stress and substituting in equation (27) yields an equation for twin stress expressed as:

$$\sigma_T = \lambda \left(b_0 \rho_0 \frac{\partial l}{\partial t} + b_p l \frac{\partial \rho_p}{\partial t} \right)^{\left(\frac{1}{N} \right)} \tag{29a}$$

The velocity, v_0, is assumed to have a limit expressed in equation (22). Using binomial expansion, equation (29a) can be expanded and for simplicity in the resultant equation only the first and last term will be kept. Furthermore retaining the second term has little bearing on the overall trend of the resultant twin volume fraction results. Equation (29a) can then be rewritten as:

$$\sigma_T = \lambda \left(b_0 \rho_0 v_0 \right)^{1/N} + \lambda \dot{\varepsilon}^{1/N} \tag{29b}$$

This expression has the advantage of incorporating the initial state of the material in the form of dislocation density, and also includes the loading rate occurring during the impact event, both of which play a role in the twin nucleation process. This dependency of σ_T on the initial state of the material is shown experimentally from plate impact tests performed on cold rolled specimens in which very little twinning was present at high impact stresses, owing to an increase in σ_T.

4.5.3. **Critical Twinning Stress Parameters**

This section focuses on determining the material parameters listed in equation (29b). For this purpose a direct relationship between strain rate and stress corresponding to twin formation, are obtained using compression tests performed on as-received and pre-strained specimens using a split Hopkinson pressure bar at various strain rates. These tests were carried out at liquid nitrogen temperatures in order to decrease the thermal activation of dislocations thereby increasing the threshold stress for perfect dislocation slip to a level higher than that for twin nucleation.

SHPB Compression tests were performed at strain rates ranging from 10^2 to 10^4 s^{-1} and at a temperature of 77K. This data, coupled with microscopic analysis provides knowledge of the twinning stress. Since the stress required to form twins is considered independent of temperature for BCC metal [13], these values apply for room temperature impacts. Low temperature tests require special consideration in order to prevent the incident and transmission bars from changing temperature. This was done using tungsten carbide inserts between the specimen and incident and transmission bars. Contact time between the tungsten inserts and incident and transmission bars is reduced by using a

linear actuator system with a timing relay to move the bars in place 1 ms prior to firing, preventing any heat transfer between the bars and specimen [41].

Due to complex wave interactions that can arise from contacts between bars and tungsten inserts, the geometric impedances were carefully matched using ultrasonic wave technique to measure the wave speed of the bars. Specimen length to diameter ratios were kept to 0.5 to ensure a state of uniaxial stress and the diameter was maintained close to 80% of the mating bar diameter to reduce the effects of radial and longitudinal inertia and friction [42]. The mating surfaces were coated in dry graphite lubricant to reduce specimen barreling caused by friction.

Strain pulses were recorded via dynamic strain gauges on the incident and transmission bars and recorded using the oscilloscope previously mentioned and data analysis was done using Matlab. In order to produce deformation twins in the SHPB strain rate range, the specimens were cooled during the test in order to raise the critical stress for slip above that for twinning. Low temperature tests were conducted at temperature of 77K by submerging the specimen and tungsten inserts in a basin of liquid nitrogen as shown in Figure 4-8
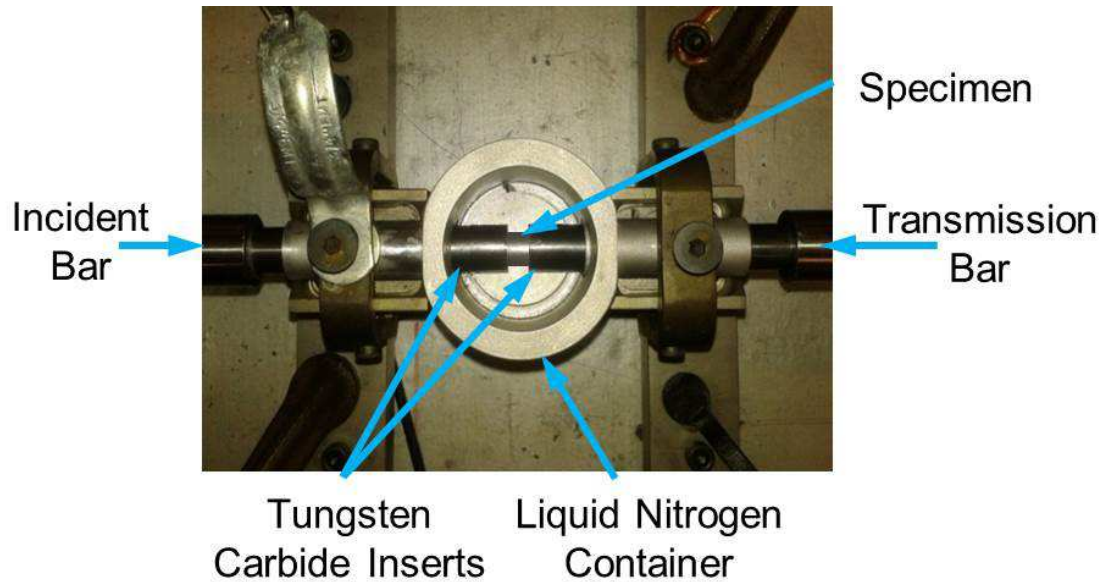
Figure 4-8: Low temperature setup on SHPB for compression testing at liquid nitrogen temperatures.

Stress-strain results of the low temperature tests are shown in Figure 4-9 for strain rates 1.5E+3 up to 7.4E+3 s^{-1}. By the nature of wave reflections in SHPB testing at high strain rates, oscillation in the plastic region of the stress strain curve is inherent. Therefore, each curve in Figure 4-9 is an average of two tests in order to insure accurate results, which have then been smoothed for data analysis.
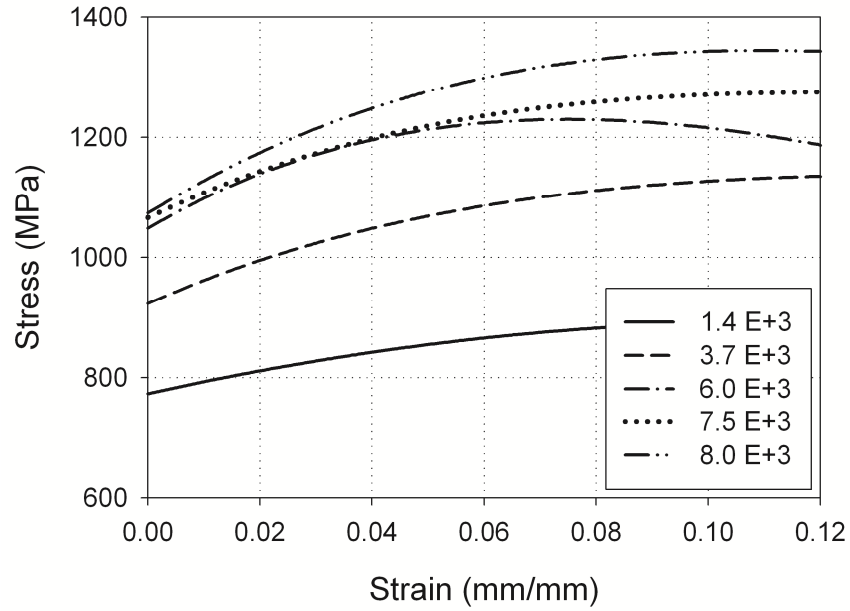
Figure 4-9: Typical dynamic stress-strain results from SHPB compression testing for as-received steel tested at 77K. Each smoothed curve shown is an average of multiple tests.

SHPB specimens from low temperature tests on the as-received steel were sectioned and polished to 1 µm finish and etched using 5% nital solution. Figure 4-10(a) shows the absence of twins at a strain rate of 1.5E+3 s^{-1}, while Figure 4-10(b) shows the presence of twins as the strain rate increases to 6.0E+3 s^{-1}.
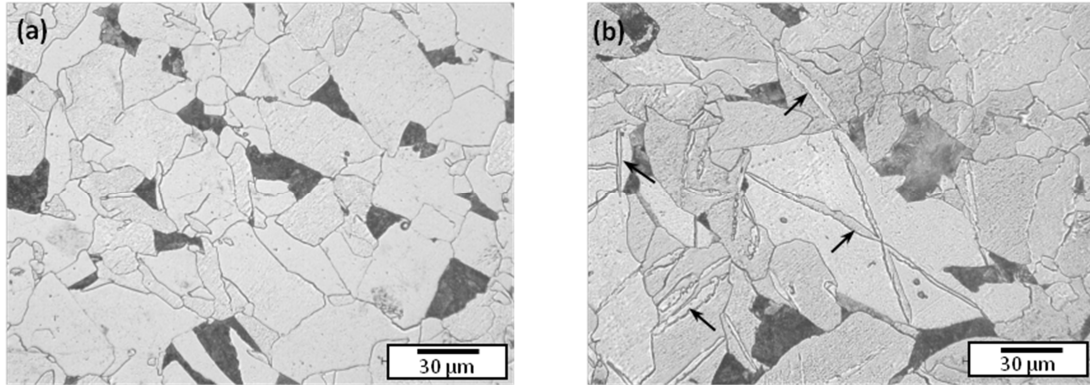
Figure 4-10: Optical micrographs of as-received steel deformed at 77K at strain rates of (a) 1520 s^{-1} (b) 6010 s^{-1}. Arrows indicate mechanical twins.

The twinning stress can be determined by fitting equation (29b) to the yield point from specimens which twinned during low temperature SHPB tests as shown in Figure 4-9. The dislocation density, ρ_0, is determined using data generated in the work of Conrad and Christ [43] on alpha-iron; see Figure 4-11.
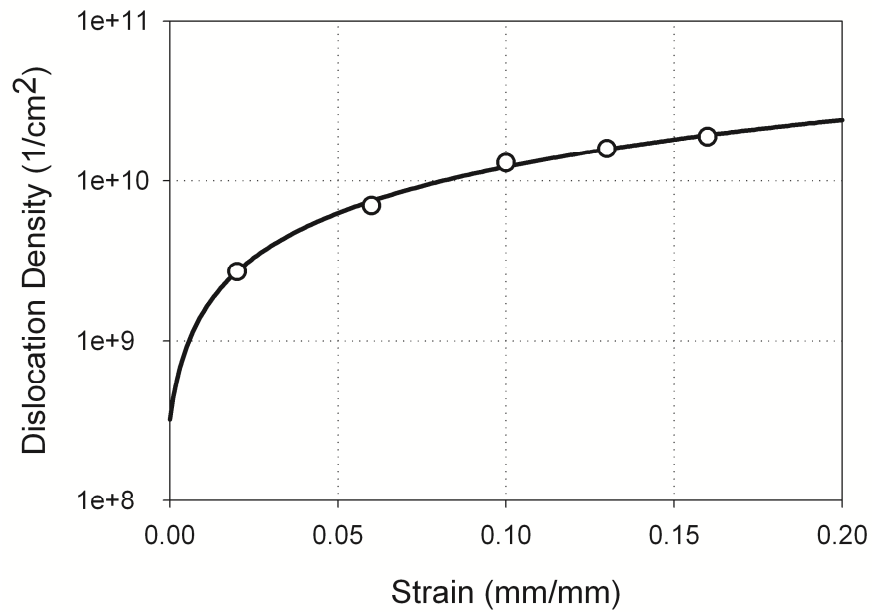
Figure 4-11: Dislocation density as a function of strain [43]

The maximum dislocation velocity, described by Equation (22), was determined from material properties shown in Table 1, and is calculated to be $v_0 =1035$ m/s. Equation (29b) was fit to the yield stress data from Figure 4-9 and is plotted in Figure 4-12, which shows the strain rate dependence of the critical twinning stress.
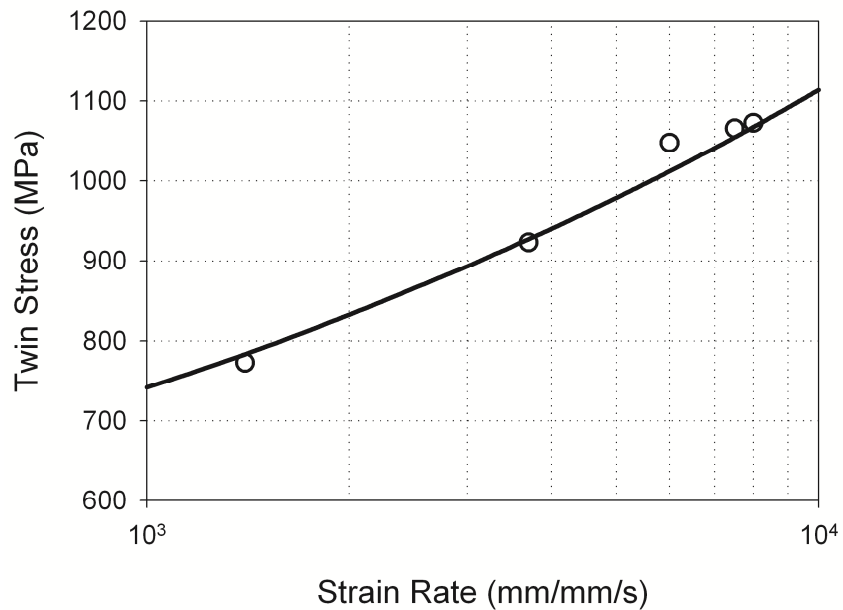
Figure 4-12: Twin stress vs. strain rate determined from low temperature SHPB compression tests for the as-received hot rolled steel. These values were taken at the yield point from curves in Figure 9.

The coefficients λ and N in equation (29b) are determined for as-received steel to be 85 and 4, respectively. In order to determine the twin stress at higher strain rates, the impact stress during plate impacts must be correlated with the strain rate. Finite element analysis of plate impacts has been done using Abaqus Explicit and was validated by comparing experimentally recorded stress history with that obtained numerically as shown in Figure 4-13(a). The simulation utilizes the built in Johnson-Cook material model for plastic deformation which has been previously described [3].
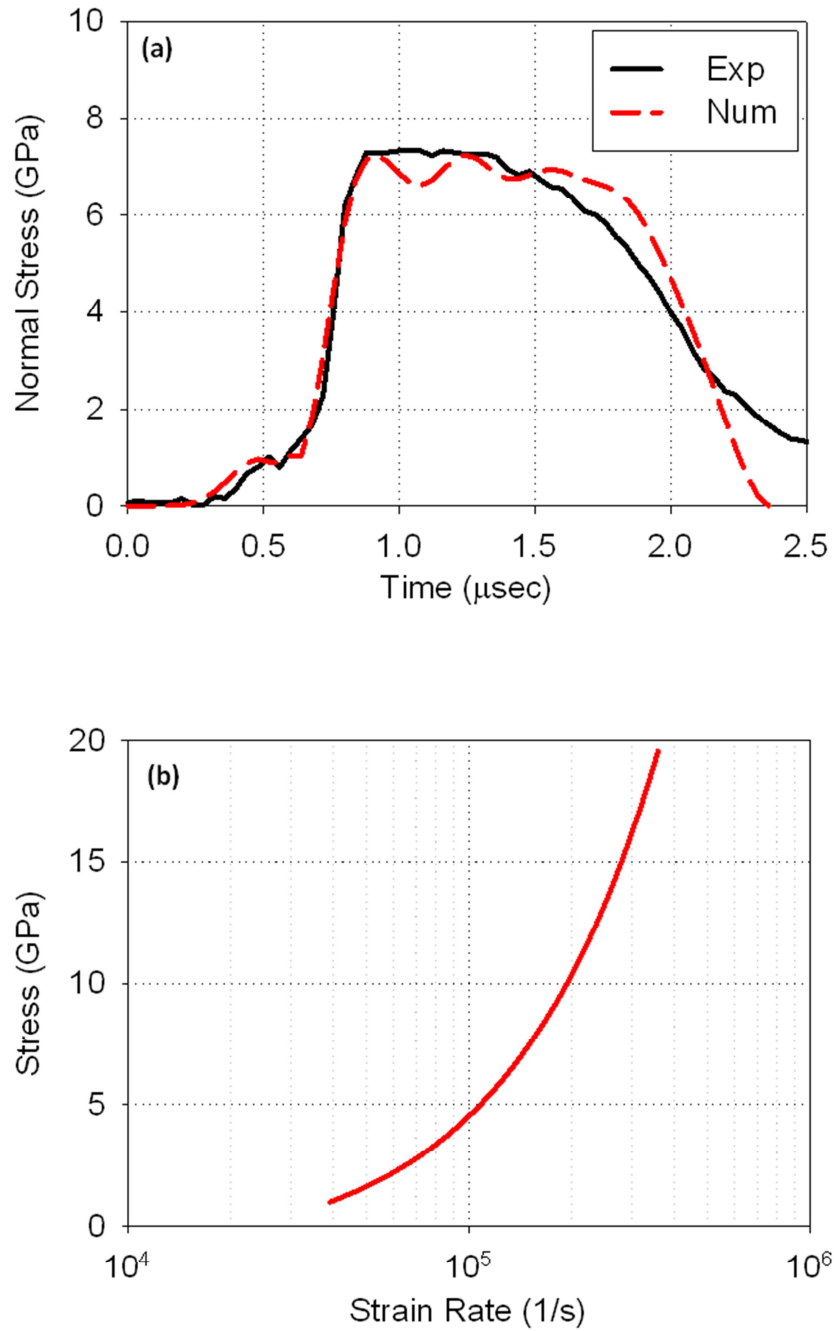
Figure 4-13: FEA of plate impact testing. (a) Comparison of numerical and experimental stress-time profiles obtained between the target and the backing plate. (b) Stress as a function of strain rate determined through FEA.

Figure 4-13(b) shows the impact stress plotted as a function of strain rate from FEA. This relationship is used to determine the strain rate corresponding to the stress required for the onset of twinning during impact loading. The intersection of the two curves, the twin stress curve in Figure 4-12 and the stress-strain rate curve in Figure 4-13(b), coincides with the stress corresponding to the initiation of twinning in the as-received steel as obtained in Figure 4-6. This result reflects the accuracy of extrapolating the twin stress equation to higher impact strain rates.

The onset of twin nucleation in the 1% cold rolled steel was experimentally determined to be around 11GPa, as seen in Figure 4-6. This stress value was correlated with strain rate using the FEA curve as shown in Figure 4-14. Using material properties from Table 1 and dislocation density from Figure 4-11, a twin stress versus strain rate curve for the 1% pre-strained material was matched with the experimental data point of 11 GPa by selecting N_1 equal to 2.56.
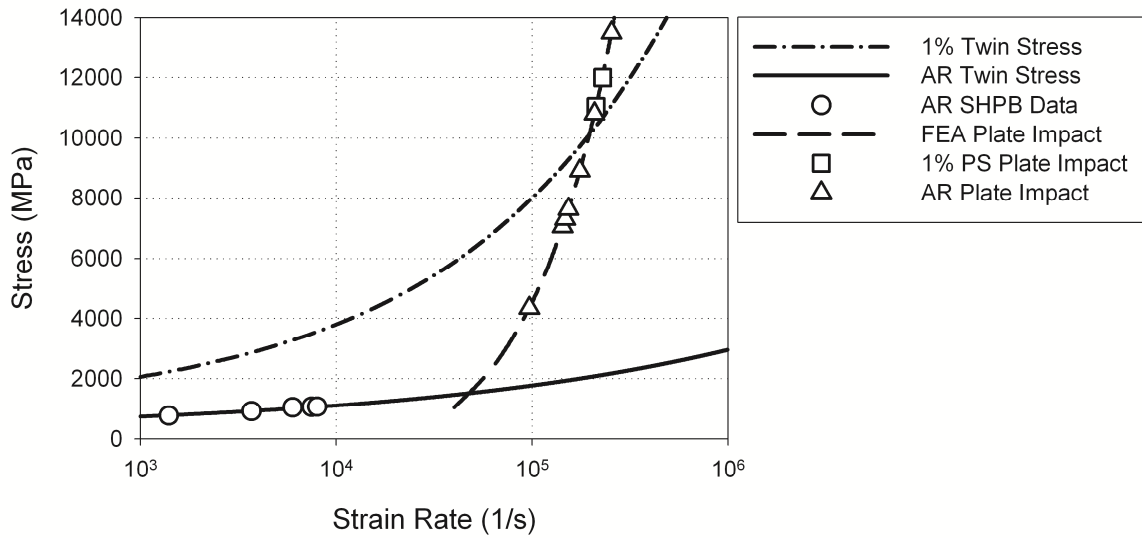
Figure 4-14: Critical twinning stress for as-received and 1% pre-strained steel. The long-dashed line denoted in the legend by FEA Plate Impact corresponds to the numerical results shown in Figure 13 (b) which are the stress-strain rates achieved during plate impact testing. Triangle and Square Data points along this curve represent the maximum stress achieved during plate impacts from Figure 3.

4.5.4. **Model Results and Discussion**

The equations developed in the previous section for the critical twin nucleation stress as a function of strain rate and pre-strain are implemented into the model developed in section 4.1. This form of the model is run using explicit time stepping numerical scheme for a series of input velocities ranging from 100 to 1000 m/s. The twin volume fraction is averaged across spatial increments at the end of time in each simulation. Based on the micrographs of impacted specimens, there appears to be a relation between impact stress and the number of active twinning systems. Therefore, in order to improve accuracy of the model predictions, multiple twin systems were considered in the simulation. The first twin system to become active in a single grain will be that which has the highest resolved

225

shear stress. This system is oriented 45 degrees to the loading direction and its acting

shear stress is calculated using equation (11). As the impact stress increases, the resolved

shear stress on planes deviating from 45 degrees would exceed the critical twin stress, σ_T,

thus allowing multiple twinning systems to become active. This is shown clearly in the

micrographs in Figure 4-15.
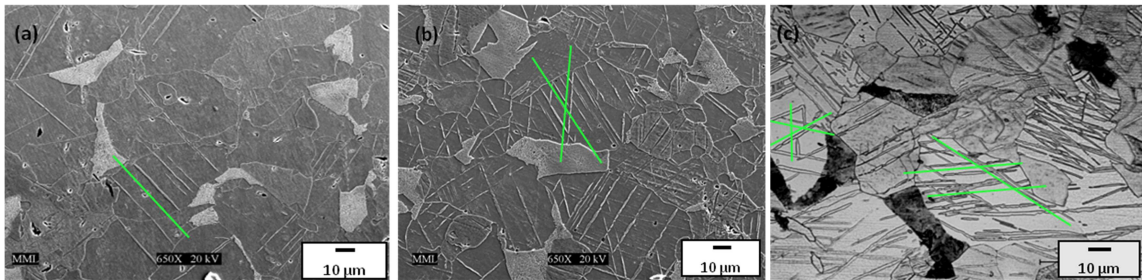
Figure 4-15: Micrographs of impacted steel specimens showing the evolution of multiple twinning systems as the impact stress is increased. (a) As-received steel impacted at 4 GPa with 1 primary twin system per grain; (b) As-received steel impacted at 8.5 GPa showing 2 twin systems per grain; (c) As-received steel impacted at 13 GPa showing 3 twin systems per grain.

For modeling purpose, it is assumed here that in a global sense, twining occurs only

on systems belonging to the {112} <111> family and that the critical twin stress for each

of these systems is the same. In order to achieve twinning on multiple planes, the normal

impact stress must be higher than that required to induce twining only on the system

oriented at 45 degrees with respect to the loading direction. This concept is accounted for

in the model by resolving the calculated shear stress component onto potential twin

planes. The first active twin plane is that in which the shear stress is maximum. Based

on the work of Mahajan [44] on twin-twin interaction and the work of Hull [21], several

twin systems can be considered. The angles between two types of twin planes are determined using equation (30) and are summarized in Table 4-2.

$$\cos\theta = \frac{(h_1 h_2) + (k_1 k_2) + (l_1 l_2)}{\sqrt{h_1^2 + k_1^2 + l_1^2} \cdot \sqrt{h_2^2 + k_2^2 + l_2^2}} \tag{30}$$

Table 4-2: Twin interaction systems associated with multiple twinning within one plane and angle between system 1 and system 2.

System 1	System 2	Angle
$(\bar{1}\bar{1}2)$ $\langle 111 \rangle$	$(1\bar{2}1)$ $\langle \bar{1}\bar{1}\bar{1} \rangle$	60°
$(\bar{1}21)$ $\langle 11\bar{1} \rangle$	$(2\bar{1}1)$ $\langle 11\bar{1} \rangle$	60°
$(\bar{2}11)$ $\langle \bar{1}\bar{1}\bar{1} \rangle$	(211) $\langle 1\bar{1}\bar{1} \rangle$	70°
$(\bar{1}21)$ $\langle 11\bar{1} \rangle$	$(12\bar{1})$ $\langle \bar{1}11 \rangle$	70°
(121) $\langle \bar{1}11 \rangle$	(112) $\langle \bar{1}\bar{1}1 \rangle$	30°

If any one of the twin systems in Table 4-2 is selected as the plane of maximum shear, i.e. 45 degrees to the loading direction, the shear stress can be resolved on the next planes as shown in Figure 4-16.
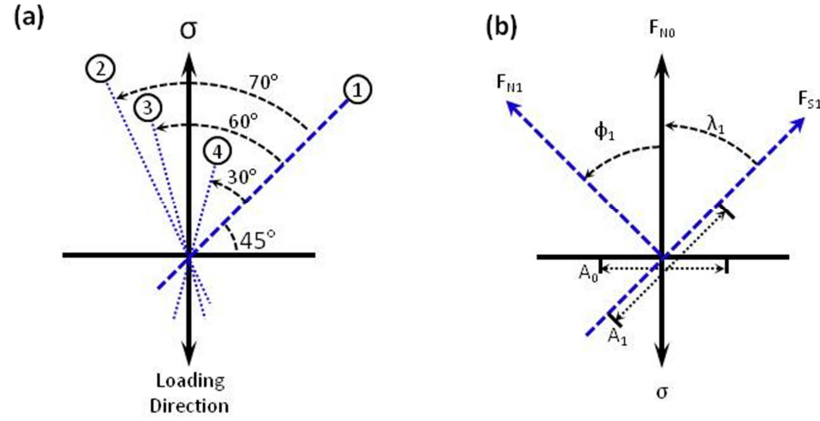
Figure 4-16: (a) Angles related to twin planes of which the normal impact stress is resolved upon. Planes 2, 3 and 4 are at 30°, 60°, and 70° with respect to Plane 1, of which shear stress is maximum. (b) Normal force F_{N0} resolved onto area A_1 resulting in shear force and normal force on a plane which is at an angle of λ_1 to the loading direction.

In order to calculate the twin volume fraction accurately, the additional shear stress matrices should be determined. This is done by resolving the shear stress with respect to the first active twin plane based on the angle between successive {112} type planes. From Figure 16 (b), it is shown that the forces due to impact loading can be resolved on the next twinning plane and direction defined by λ_1 which is the angle between the applied force and the twin direction, and φ_1 which is the angle between the applied force and the normal to the twin plane area A_1. The maximum shear stress τ_1 calculated in equation 11, is directly calculated from equation (11), and can further be defined as

$$\tau_1 = \sigma_0 \cos \lambda_1 \cos \phi_1 \tag{31}$$

Solving equation (31) for the normal stress, the shear stress on the second and third active planes can be defined in terms of the maximum shear stress calculated by equation (11) as

$$\tau_2 = \frac{\tau_1}{\cos \lambda_1 \cos \phi_1} \cos \lambda_2 \cos \phi_2 \qquad (32)$$

$$\tau_3 = \frac{\tau_1}{\cos \lambda_1 \cos \phi_1} \cos \lambda_3 \cos \phi_3 \qquad (33)$$

Since the pre-straining only affects the nucleation, and not the growth process [16], only the critical twinning stress needs to be adjusted and the same form of the growth equation, equation (16), can still be utilized in the model for pre-strained steel. If these three systems shown in Figure 4-16(a) are considered, three separate growth equations can be summed into a global twin volume fraction.

$$g_i(\tau_i) = \frac{\tau_i}{\tau_{twin}} - 1 \quad \tau_i \geq \tau_{twin} \quad i = 1,2,3,... \qquad (34)$$

$$\alpha_i = \left(\alpha_0^{1/m} + \frac{1}{t_c} \int_0^t g_i(\tau_i) \, dt \right)^m \quad i = 1,2,3,... \qquad (35)$$

$$\alpha_{total} = \sum \alpha_i \qquad\qquad i = 1,2,3,... \qquad (36)$$

This set of equations allows the twin growth rate on each plane to be increasing with respect to the resolved stress on each plane. As the input particle velocity is increased, the contribution of each plane becomes more prominent as the resolved shear stress exceeds the critical value. The model outputs of twin volume fraction vs. impact stress are compared with experimental data and are plotted in Figure 4-17.
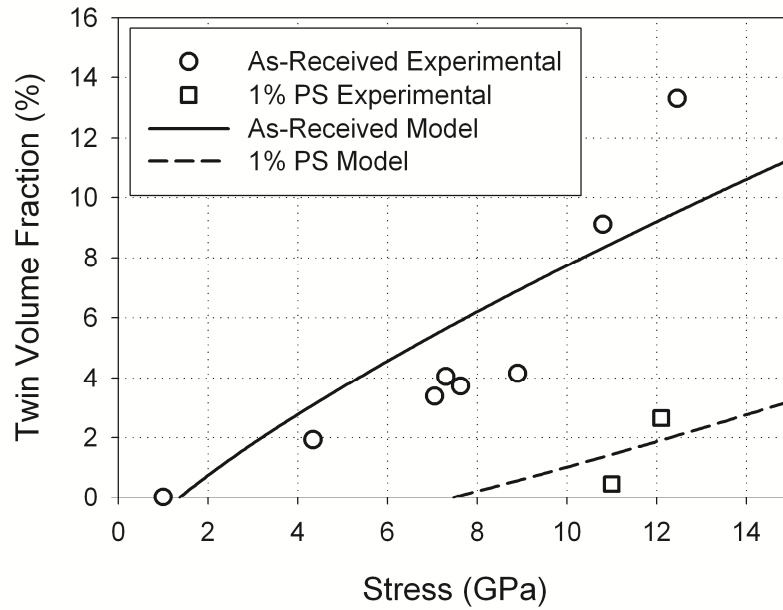
Figure 4-17: Experimental and analytical model results of twin volume fraction vs. impact stress.

While the model predictions compare well with experimental data for the as-received steel, it is necessary to provide additional experimental data for pre-strained material in order to improve the accuracy of the concept presented. The range of impact stress and twin volume fraction presented within this research prevents a view of the full trend which may ensue. Running the analytical model to higher stresses shows a general saturation of the twin volume fraction which is to be expected of any deformation phenomenon, however as impact stress is further increased in steel, other mechanisms such as adiabatic heating and phase transformation may influence the results, which have not been accounted for in this particular model. Limitations in testing methods available hinder the ability to reach higher maximum stresses during plate impacts used in this

work. Furthermore, greater accuracy in model parameters would require an extensive amount of TEM analysis. Nonetheless, through referenced work and experimental evidence presented here, it is evident that the twin stress is in fact a function of strain rate and more substantially, the level of pre-strain.

4.6.   **Conclusions**

Shock loading tests have been carried out on low carbon steel specimens using a single stage light gas gun. The material tested was in both the as received and pre-strained conditions. The study examined the high strain rate deformation mechanisms with emphasis on the role of twins and their correlation with impact pressure. Experimental and numerical work has been performed to determine the critical twin stress as a function of both pre-strain and strain rate. Major outcomes of this study are listed below.

1. Using a single stage light gas gun, deformation mechanisms in low carbon steel specimens subjected to plate impacts have been examined in as-received, hot rolled steel. It is observed that under this type of loading, twins are a contributing deformation mechanism and twin volume fraction exponentially increases with the impact pressure. The twin volume fraction was measured using standard point count method, the maximum of which was 16% occurring with an impact pressure of approximately 14 GPa.

2. High strain rate deformation mechanisms were examined in the same steel in pre-strained conditions. Pre-straining was completed using low strain rate, cold rolling procedures to strains of 1%, 3% and 20%. Impact loading was performed on specimens in the same direction as the pre-straining. It has been shown that the twin nucleation stress is proportional to the level of pre-strain. This has been explained in terms the dislocation network, density and configuration within the steel as modified by cold rolling prior to impact loading. A 1% pre-straining, has raised the threshold pressure for the onset of twin nucleation to 11 GPa.

3. Twin formation during high strain rate loading and/or low temperature loading was described based on a progressive shear of atoms rather than a local shuffle concept. This occurs by a shift of atoms on the $\{112\}$ planes in the $\langle 111 \rangle$ direction by a displacement 1/3 burgers vector for BCC metals. A minimum of 3 $\{112\}$ layers is required to form a stable twin for compatibility across the twin habit plane. It is assumed that at these loading conditions, the strain rate of the material is controlled by the velocity of preexisting perfect dislocations and by the generation of partial dislocations. The nucleation of partial dislocations is preferential at high applied stresses due to a lower free energy of nucleation at high strain rates and low temperatures. Furthermore, the partial dislocations are more operative at these conditions due to their higher jump frequency. These partial dislocations, if formed on successive planes, are responsible for the formation of the deformation twins.

4. An explicit form of the critical twin nucleation stress has been developed based on strain rate accommodation by perfect dislocations and partial dislocations. The form of the equation considers the velocity of perfect dislocations and the generation rate

of partial dislocations utilizing Gilman's limiting dislocation velocity equation and the Orowan strain rate relation.

5. Parameters for the critical twin nucleation stress in as-received steel and 1% pre-strained steel have been determined through plate impact tests and low temperature SHPB compression tests. The SHPB compression tests were carried out at liquid nitrogen temperatures. Under this type of loading, the thermal activation of dislocations is lowered, thereby increasing the threshold stress for perfect dislocation slip to a level higher than that for twin nucleation. At this low temperature condition, deformation twins are present at strain rates lower than that encountered in room temperature plate impact tests. As such, SHPB compression tests can be used to correlate strain rate and twin nucleation stress.

6. Observation of nonparallel and intersecting twins in grains led to a modification of a model originally presented by Johnson and Rohde. By assuming that deformation twinning is occurring primarily on {112} <111> systems, the applied stress was resolved on multiple planes. These stress components were then applied to separate twin growth equations to account for the multiple twin systems.

4.7.   **References**

[1]   Field, J.E., Walley, S.M., Proud, W.G., Goldrein, H.T., Siviour, C.R., International Journal of Impact Engineering 30 (2004) 725–775.

[2]   Ramesh, K.T. "High Strain Rate and Impact Experiments" Part D.33. Springer Handbook of Experimental Solid Mechanics. 2008

[3]   Visser, W., Sun, Y., Gregory, O., Plume, G., Rousseau, C-E., Ghonem, H., Deformation Characteristics of Low Carbon Steel Subjected to Dynamic Impact Loading, Materials Science and Engineering. A528 (2011) 7857–7866.

[4]   Firrao, D., Matteis, P., Scavino, G., Ubertalli, G., Ienco, M.G., Pellati, G., Piccardo, P., Pinasco, M.R., Stagno, E., Montanari, R., Tata, M.E., Brandimarte, G., Petralia, S., Mechanical twins in 304 stainless steel after small-charge explosions, Materials Science and Engineering. A424 (2006) 23–32.

[5]   Karaman, Sehitoglu, Gall, Chumlyakov, Maier. Deformation of single crystal Hadfield steel by twinning and slip, Acta Mater. 48 (2000) 1345-1359.

[6]   De Resseguier, T., Hallouin, M., Stress relaxation and precursor decay in laser shock-loaded iron, Journal of Applied Physics 84 (4) (1998) 1932–1938.

[7]   Johnson, J.N., Rohde, R.W., Dynamic deformation twinning in shock-loaded iron, Journal of Applied Physics. 42 (11) (1971) 4171–4182.

[8]   Taylor, J.W., Dislocation Dynamics and Dynamic Yielding, Journal of Applied Physics. 36 (10) (1965) 3146–3150.

[9]   Smida, T., Bošanský, J., Deformation twinning and its possible influence on the ductile brittle transition temperature of ferritic steels, Materials Science and Engineering. A287 (2000) 107–115.

[10]   Jolley, W., Hull, D., Effect of Prestrain and Strain Aging on the Brittle Fracture of 3.25% Silicon Iron, Acta Metallurgica 12 (1964) 1337-1352.

[11]   Biggs, W.D., Pratt, P.L., The Deformation and Fracture of Alpha-Iron at Low Temperatures, Acta Metallurgica 6 (1958) 694-703.

[12]   Armstrong, R. W. and Worthington, P. J., in Metallurgical Effects at High Strain Rates. p. 401, (edited by R. W. Rohde, B. M. Butcher. J. R. Holland and C. H. Karnes), Plenum. New York (1973).

[13]   Meyers, M.A., Benson, D.J., Vöhringer, O., Kad, B.K., Xue, Q., Fu, H.-H., Constitutive description of dynamic deformation: physically-based mechanisms, Materials Science and Engineering. A322 (2002) 194–216.

[14]   Meyers, M.A., Vöhringer, O., Lubarda, V.A., The onset of twinning in metals: A constitutive description, Acta Materialia 49 (2001) 4025–4039.

[15]   Murr, L.E., Meyers, M.A., Shock-induced deformation twinning in tantalum, Acta Materialia 45 (1) (1997) 157–175.

[16]   Lindley, T.C., The effect of a prestrain on the low temperature mechanical properties of a low carbon steel, Acta Metallurgica. 13 (1965) 681-689.

[17]   Rosenfield, A.R., Averbach, B.L., Cohen, M., Twinning Occurrence in Iron Single Crystals, Acta Metallurgica. 11 (1963) 1100-1101

[18]   Churchman, A.T., Cottrell, A.H., Yield Phenomenon and Twinning in α-Iron, Nature 1951.

[19]   Mahajan, S., Bartlett, A.F., Influence of Prior Mechanical and Thermal Treatments on Shock Induced Substructures in Molybdenum, Acta Metallurgica. 19 (1971) 1111-1119.

[20]   Mahajan, S., Effects of Existing Substructure on Shock-Twinning Behavior of Iron, Physica Status Solidi. Vol 2, Issue 2, (1970) 217-223.

[21]   Hull, D., Orientation and temperature dependence of plastic deformation processes in 3.25% silicon iron, Proc. R. Soc. A (1963) 274: 5-20.

[22] Wasilewski, R.J., Mechanism of bcc twinning: Shear or shuffle?, Metallurgical Transactions. 1 (1970) 2641–2643.

[23] Mason, T.A., Bingert, J.F., Kaschner, G.C., Wright, S.I., Larson, R.J., Advances in Deformation Twin Characterization Using Electron Backscattered Diffraction Data, Metallurgical and Materials Transactions. A 33A (2002) 949-954

[24] Gray III, G.T., Levescu, V., Cerreta, E.K., Mason, T.A., Maudlin, P.J., Bingert, J.F., Influence of shockwave obliquity on deformation twin formation in Ta, DYMAT (2009) 963-969

[25] Zeng, Z., Deformation Behaviour, Microstructure and Texture Evolution of CP Ti Deformed at Elevated Temperatures, PhD Thesis. Royal Institute of Technology. 2009

[26] Kibey, S., Liu, J.B., Johnson, D.D., Sehitoglu, H., Predicting twinning stress in fcc metals: Linking twin-energy pathways to twin nucleation, Acta Mater. 55 (2007) 6843-6851.

[27] Asay, J. R., and Mohsen Shahinpoor. *High-pressure Shock Compression of Solids*. New York: Springer-Verlag, 1993. Print.

[28] Christian, J.W., Mahajan, S., Deformation Twinning, Progress in Materials Science. 39 (1995) 1-157.

[29] Klassen-Neklyudova, M.V., Mechanical Twinning of Crystals. Consultants Bureau. Ney York (1964)

[30] R. Hull, C. Jagadish, R.M. Osgood, Jr., J. Parisi, Z.Wang, H.Warlimont. Dislocation Dynamics During Plastic Deformation. 2010

[31]   Ferreira, P.J., Vander Sande, J.B., Amaral Fortes, M., Kyrolainen, A., Microstructure Deveolopment during High-Velocity Deformation, Metallurgical and Materials Transactions. A 35A (2004) 3091-3101.

[32]   Johnston, W.G., Gilman, J.J., Dislocation Velocities, Dislocation Densities, and Plastic Flow in Lithium Fluoride Crystals, Journal of Applied Physics. 30 (2) (1959) 129-144

[33]   M. Meyers. A Mechanism For Dislocation Generation In Shock-Wave Deformation. Scripta Metallurgica. 12. (1978) 21-26

[34]   E. Zaretsky. Dislocation multiplication behind the shock front. J. Appl. Phys. 78 (6) (1995). 3740-47.

[35]   E. Zaretsky. Dislocation multiplication in F.C.C. metals at presence of high shear stress. Acta Metall. Mater. Vol 43. No. 1 (1994) 193-198.

[36]   J. P. Hirth and L. Kubin. Dislocations in Solids. Vol 15. The Netherlands: North-Holland, Ch 89. Dislocations in Shock Compression and Release. 2009, pp. 91–197.

[37]   P. Gumbsch, H. Gao. Dislocations faster than the speed of sound. Science. 283 (1999) 965-968.

[38]   D. Hull, and D. J. Bacon. *Introduction to Dislocations*. Oxford: Butterworth-Heinemann, 2001. Print.

[39]   J. Gilman. The Limiting Speeds of Dislocations. Metall. Mater. Trans A. 31. (2000) 811.

[40]   R.W. Armstrong, W. Arnold, F. Zerilli. Dislocation mechanics of copper and iron in high rate deformation tests. Journal Of Applied Physics. 105, (2009) 23511

[41]   Spirdione, J., Influence of Microstructure on the Dynamic Flow Stress in Metals, Master's Thesis, University of Rhode Island. (2014)

[42]   Gama, B.A., Lopatnikov, S. L., Gillespie Jr, J.W., Hopkinson bar experimental technique: A critical review, App Mech Rev. Vol 57. No 4. (2004) 223-250.

[43]   Conrad, H., Christ, B., Variation of Dislocation Density and Stored Energy with Grain Size, Commander Space Systems Division, United States Air Force. 1963

[44]   Mahajan, S., Accommodation at deformation twins in bcc crystals, Metallurgical Transactions. A 12A (1981) 379–386.

[45]   Niewczas, Marek. "Dislocations and twinning in face centred cubic crystals." *Dislocations in solids* 13 (2007): 263-364.

CHAPTER 5

DYNAMIC FLOW STRESS OF PRE-SHOCKED
LOW CARBON STEEL

W. Visser, H. Ghonem*

_____

Department of Mechanical Engineering, University of Rhode Island, Kingston, RI 02881, USA

∗ Corresponding author. Tel.: +1 401 874 2909; fax: +1 401 874 2925.
E-mail address: ghonem@egr.uri.edu (H. Ghonem).

5.1. **Abstract**

This study identifies the role of twin volume fraction in the dynamic stress-strain relationship of shock loaded low carbon steel. This relationship is modeled using thermal activation concepts based on dislocations interactions with thermal and athermal stress barriers. Model parameters are determined by first subjecting a set of as-received specimens as well as 3% pre-strained steel to shock loads of 6 GPa, and 11GPa employing a gas gun. These specimens as well as ones with no prior shock loading were subjected to dynamic compression tests at temperatures in the range 293K to 923K at strain rates between 1E+3 s^{-1} and 5E+3 s^{-1} using a split Hopkinson pressure bar. The resulting stress-strain curves were partitioned into thermal and athermal stress components. Results of this work show that the thermal stress component of both the as-received and pre-strained materials is insensitive to the corresponding impact strain history. The athermal stress component for as-received specimens which have been previously shock loaded is shown to be proportional to the loading pressure while for specimens which have been pre-strained before shock loading, the athermal stress displayed a constant value at the two load levels. This difference in athermal stress between as received and pre-strained materials is explained in terms of the deformation twin volume fraction generated as a function of the impact load. To validate model predictions, the calculated total flow stress for impact loads of 3.7GPa, 7GPa and 13GPa are compared with those generated experimentally. Results of this comparison are presented and discussed in relation to the proposed stress-strain formulations.

5.2. **Introduction**

Shock loading is a method utilized in many engineering applications such as explosive welding, forming, cutting, or bending operations. After such procedures, the resultant mechanical properties of the pre-shocked material are influenced by the induced microstructure features specific to the high strain rate loading condition. The use of these materials, in terms of design or simulation, requires constitutive laws which must acknowledge the microstructure variations brought about by the high strain rate deformation history. It is recognized that dynamic deformation of BCC microstructure can be accommodated, in addition to dislocation slip, by the formation of mechanical twins. Several authors [1-4] have investigated the role of deformation twins on the mechanical properties at these loading conditions and have shown that twins contribute to the observed increase in the flow stress. This has been attributed to the role of twin boundaries (TBs) as barriers for the motion of dislocations. Though observed experimentally, the effect of TBs on the flow stress at high strain rate loading has not been extensively studied in BCC materials.   In order to quantify the individual contribution of twins on the flow stress a constitutive stress-strain relationship should include explicit terms related to twins which could be expressed in terms of its volume fraction. Several flow stress models exist in literature such as the Johnson-Cook [5] or Zerilli-Armstrong [6]. Parameters of these models are, however, phenomenological in nature. Murr et. al [7] utilized a modified form of the Johnson-Cook model to describe the post-shock mechanical response of Tantalum. While capturing the flow stress characteristics of the shocked material, this model does not attempt to separate the contributions of the different shock induced microstructure features. Other approaches

such as the thermal activation theory [8-11] have been used to express the dynamic flow stress of metals over a range of strain, strain rate and temperature. This theory considers different types of barriers to dislocation motion, described as being short range and long range. Short range barriers which include phonons and Peirls-Nabarro stress, are dependent upon the strain rate and temperature loading conditions. Long range barriers include grain boundaries, secondary phases and dislocations on parallel slip planes [11,12]. The long range dislocation barriers are dependent on strain as well as microstructural features such as twins, grain boundaries, microstructural phases and interstitial alloy elements [10]. Using this approach, the flow stress could then be decomposed into its thermal and athermal components which would then provide a means to include the role of twins as an explicit term contributing to the overall flow stress.

The use of the thermal activation model concepts to identify the role of twins requires the experimental generation of the dynamic flow stress for a material with varying twin volume fraction. This can be achieved either through low strain rate loading at low temperatures or by shock loading. The deformation mechanisms associated with these two types of loadings would reflect the combined effects of the generated dislocations and twins. To identify the individual contribution of twins, it is necessary to examine the flow stress in two materials, one with twins and one without, both subjected to the same loading history. It has been established that pre-straining of BCC can inhibit twin formation during subsequent shock loading. Experimental results by Lindley [13] on low carbon steel showed absence of twins when pre-strained the material up to 8% at room temperature and then tested at -196°C. Biggs and Pratt [14] were able to determine yield

242

stress for slip at -183°C in alpha-iron by suppressing twins through pre-straining to 2% at room temperature. Testing single crystal alpha iron at -195°C, Rosenfield et al. [15] and Churchman and Cottrell [16] have shown that pre-straining with 1% or less is sufficient to suppress twins. Visser and Ghonem [17] have shown that twins are suppressed in low carbon steel up to shock loads of 11GPa with as little as 1% pre-strain at room temperature.   This effect of pre-straining on the generation of twins has also been observed in other BCC metals such as molybdenum where 2% pre-strain was sufficient to suppress twin formation during shock loading to 9GPa at room temperature [18]. From the studies mentioned above, it is clear that pre-straining can be utilized as a means of generating microstructures that would not produce twins as a result of shock loading.

As mentioned above, the objective of this work is to account for the role of twin volume fraction in the dynamic stress-strain relationship of shock loaded low carbon steel. For this purpose, the deformation behavior of the steel is described in terms of a thermal activation model which partitions the flow stress into athermal and thermal stress components. Quantifying these components require the knowledge of the model material parameters as defined by the separate contributions of dislocations and twins to the deformation process. To achieve this, steel specimens in both the as-received (hot rolled) and pre-strained (cold rolled) conditions were shock loaded using a single stage light gas gun. These provided two materials with similar loading histories but with differing twin volume fractions. Following this, a modified form of the thermal activation flow stress model was applied to predict the stress-strain behavior due to pre-shock loading. The parameters of the model were obtained through dynamic compression tests using a split Hopkinson pressure bar at various temperatures. The resulting dynamic flow stress has

then been used to identify the thermal and athermal stress components and determine the role of twin volume fraction on the total dynamic flow behavior. The model predictions are then compared with experimental results and explained in terms of dislocation kinetics related to the shock induced microstructure changes.

5.3.   **Material and Post Shock Microstructure**

The material of study is A572 Grade 50 low carbon steel cut from the flange section of a hot rolled I-beam. The microstructure in the as-received condition consists of alpha-ferrite grains with dispersed pearlite colonies. The carbon content of the steel in weight percent is 0.23 with an average grain size of 30 μm. Figure 5-1 shows optical micrographs of the as-received and 3% rolled steel. The latter material, as discussed above, will be used to identify the post shock deformation in the absence of twins.
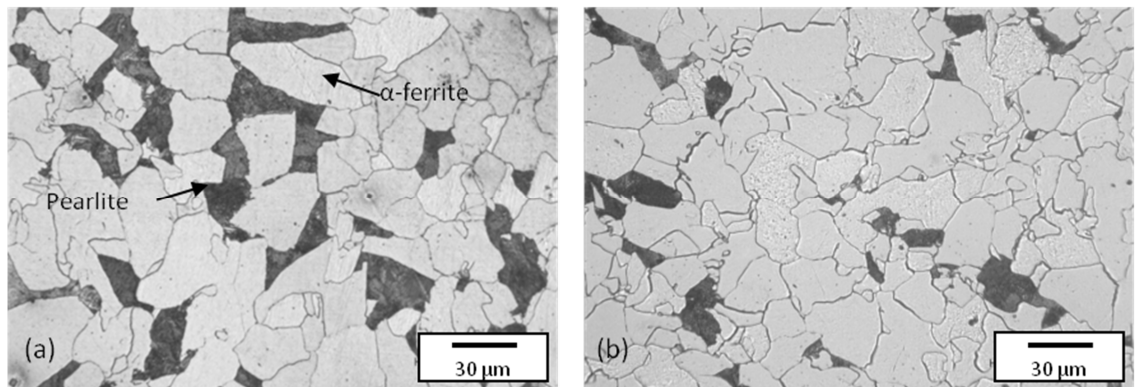
Figure 5-1: Optical micrographs of A572 grade 50 low carbon steel. The lighter color phase is the ferrite and darker phase is the pearlite colonies. a) as-received microstructure and b) 3% cold rolled microstructure (surfaces are polished to a 1μm finish and etched using 5% nital solution for 5-7 seconds).

Steel specimens were shock loaded by plate impact using a single stage light gas gun described in details in Ref. [19]. These specimens were sectioned, polished, and etched to study the post-impact microstructure. In the as-received condition the α-ferrite grains deformed by both slip and twinning when subjected to impact loading. Figure 5-2 shows that the twin volume fraction is exponentially proportional to the impact stress [13]. It must be mentioned here the trend shown in this figure is limited to the applied load of 14GPa. It is expected that at higher load levels the twin volume fraction would tend to saturate as other deformation mechanisms including shear banding and phase transformation would begin to dominate [20,21].
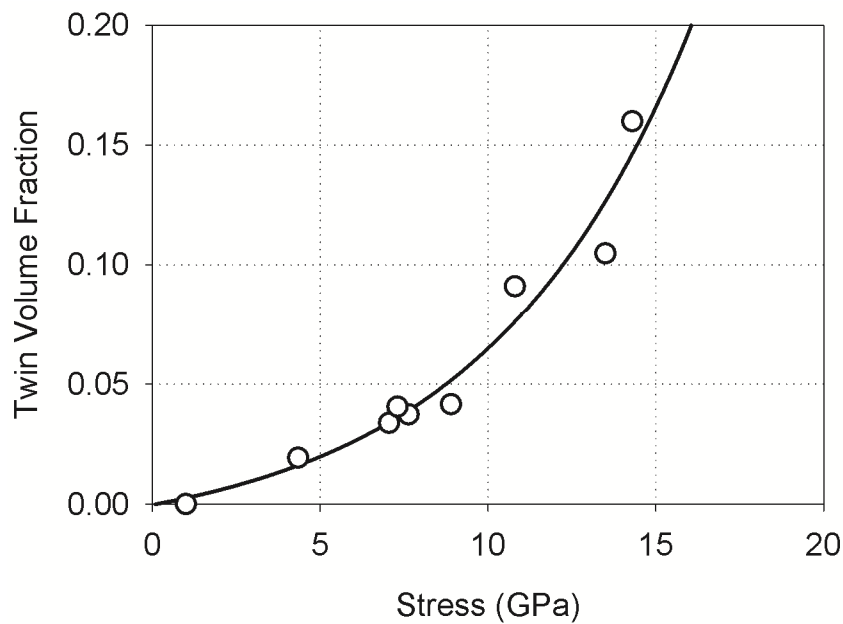
Figure 5-2: Twin volume fraction vs. impact pressure for as-received steel [28]

SEM micrographs shown in Figure 5-3 were taken perpendicular to the impact direction in both the as-received and 3% pre-strained materials. Figure 5.3(b), indicates the absence of twins in the pre-strained material. Furthermore, Figure 5-4 shows target

(1%pre-strain condition) and projectile (as-received condition) materials from the same plate impact test. Since this was a symmetric impact where target and projectile are of the same material and impedance, the pressure generated in both are considered equal. This image shows that as little as 1% pre-strain suppressed twin nucleation at a loading condition that generates profuse twinning in the as-received material.
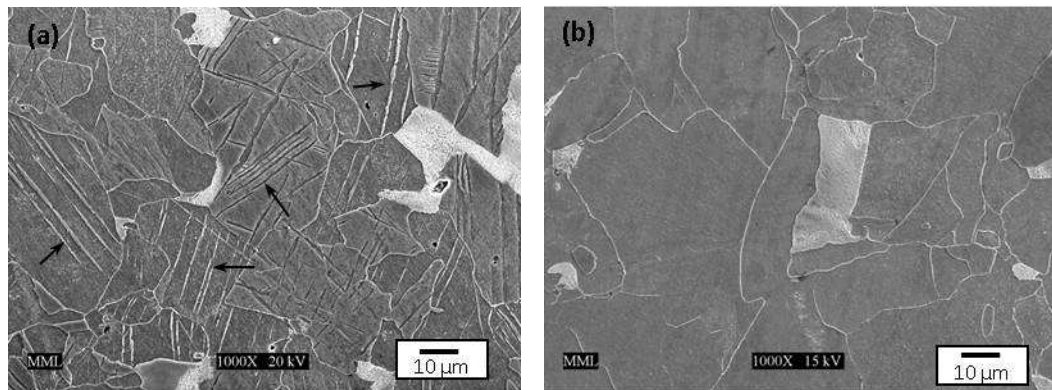
Figure 5-3: SEM micrographs of shock loaded as-received and pre-strained steel samples; white regions are the pearlite phase and dark regions are the ferrite phase; arrows indicating twins (a) as-received steel impacted at 11GPa resulting in 9% twin volume fraction, (b) 3% pre-strain steel impacted at 11GPa with no twins present.
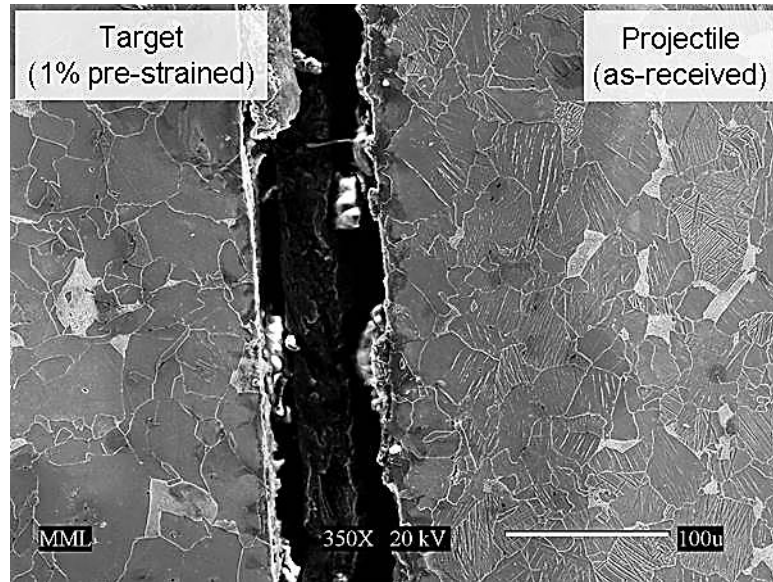
Figure 5-4: Steel target and projectile interface after 11GPa impact. The projectile was in the as-received condition, while the target was pre-strained 1% prior to impact.

5.4.   **Significance of Twins**

Quasi-static tension tests performed on specimens with different twin volume fraction show that the yield strength approaches the ultimate strength of the material as twin volume fraction increases see Figure 5-5. The convergence of these curves indicates that the plastic hardening characteristics are becoming less prominent and the ability of the material to store defects during post-impact plastic deformation has decreased, which is represented by the loss in work hardening [20]. However, although the yield and UTS can be directly related to the twin volume fraction, it is not possible to identify whether the twins are the primary feature for the increase.
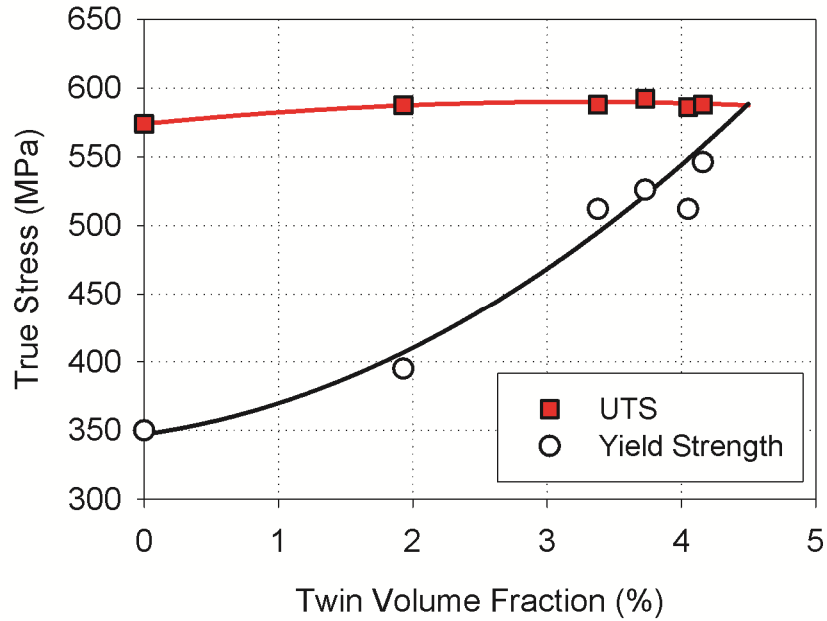
Figure 5-5: Ultimate tensile strength and yield stress of post-impact tensile specimens as a function of twin volume fraction taken from true stress-true strain curves.

It is important to mention here that during shock loading, the contribution of dislocation generation to the strain rate is occurring by the generation of partial dislocations [21], which in turn lead to twin formation, and any strain accommodation due to dislocation slip is occurring with perfect dislocations which are already present in the material. A material with a high density and homogeneous distribution of perfect dislocations will tend to be less prone to twinning since the plastic deformation can be accommodated purely by slip of full dislocations [22]. Therefore, prior mobile dislocation density is inversely proportional to the number of probable twin nucleation sites and altering the initial dislocation density leads to a differing volume fraction of twins for a similar shock load condition. This can be achieved via cold rolling.

Hardness measurements vs. impact stress of two types of specimens, the as-received (with twins) and those which have pre-strained between 1% and 20% (no twins), are shown in Figure 5-6.
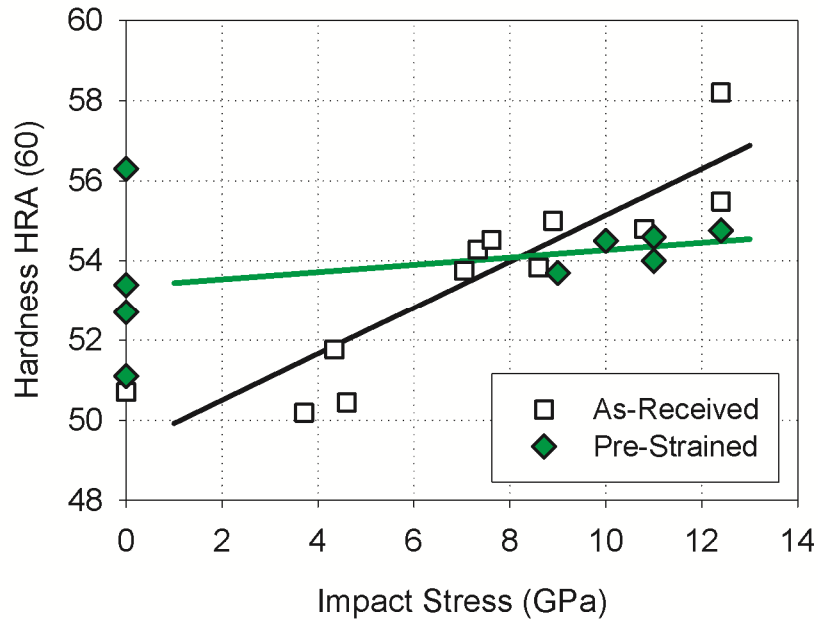
Figure 5-6: Rockwell hardness vs. impact stress for as-received and pre-strained specimens. Pre-strained specimens shown here were strained between 1% and 20% prior to impact.

This figure indicates that the dependence of hardness on the impact stress is higher in the as-received than those which were first pre-strained. Ganin et al. [24] have developed a relation for the change in hardness of shock loaded iron, attributing this change to a decrease in twin spacing as the twin density increases. This indicates that twins are effective barriers to dislocations resulting in an increase in hardness, which is analogous to an increase in yield.

The influence of pre-existing deformation twins can also be examined through the dynamic flow stress curves. A set of dynamic compression tests were carried out using a

split Hopkinson pressure bar (SHPB) at strain rates ranging from 1.3E+3 s^{-1} to 4.7E+3 s^{-1} and at temperatures between 293K and 923K on specimens which were first shock loaded. A total of six different specimens are utilized in this set of tests. The pre strain condition and pre-shock loading levels are listed in Table 5-1 below. Note, that the as-received steel contains profuse twinning while the 3% pre-strain steel is absent of twins.

Table 5-1:   A list of six specimens with different pre-strain and pre-shock loading conditions that are used to examine the significance of twins in relation to the flow stress of the low carbon steel material

Specimen ID	Pre-Strain	Impact Pressure (GPa)
AR-0	0%	0
AR-6	0%	6
AR-11	0%	11
3PS-0	3%	0
3PS-6	3%	6
3PS-11	3%	11

The SHPB specimens were cut from the center of the impact region of each impacted target disc. These specimens were then surface ground to ensure parallel surfaces for planarity during dynamic compression testing and to remove any heat affected zone at the projectile target interface. For each test condition, multiple tests of were carried out and results were averaged and smoothed to eliminate inherent oscillation due to the nature of dynamic testing

Figure 5-7 shows the flow stress of both the as received and the 3% pre strain specimens. The latter was plotted by offsetting the strain to account for the pre-strain history.
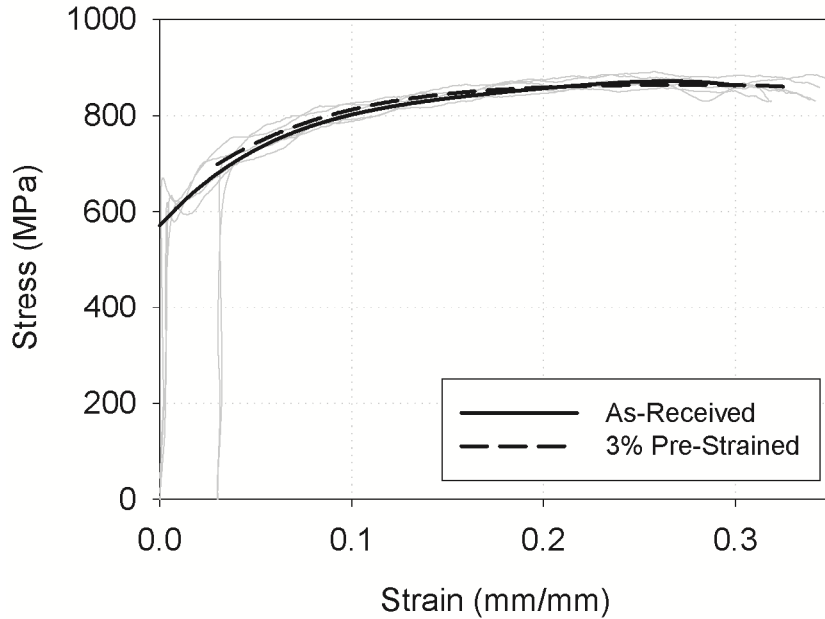
Figure 5-7: Multiple true stress-true strain curves having an average strain rate of 4.7E+3 s^{-1} at room temperature. Bold lines are smoothed fitting of the experimental curves.

As was done with the as-received specimens, a minimum of two tests were completed for each specimen and test condition and averaged into a single curve. The stress-strain curves of shock loaded specimens can be plotted in a similar manner, by adjusting the strain values to account for the strain induced by the prior impact, as shown in Figure 5-8. The strain due to impact loading, as shown in Figure 5-23 of the appendix, was equal to 2.35% and 4.15% for the 6 GPa and 11GPa shock loaded specimens, respectively. Therefore, in Figure 5-8b and Figure 5-8d, the 6GPa and 11GPa specimens which were pre-strained by 3% prior to impact were adjusted by the total of 5.35% and 7.15% strain, respectively. The averaging and smoothing process was completed for strain values ranging between 5% and 25%, as the low strain levels are inaccurate due to a lack of

stress equilibrium and elastic wave dispersion. Therefore, the curves presented are extrapolated back to zero percent strain based on the curve fit of the given strain range.
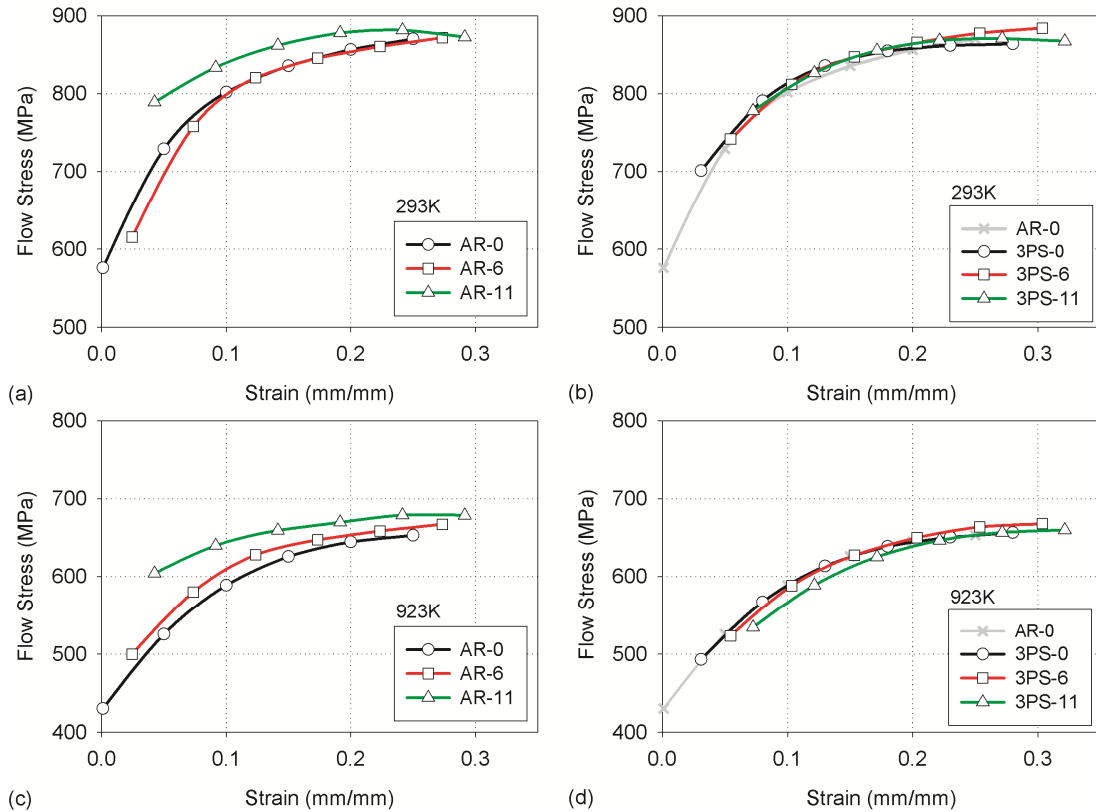
Figure 5-8: Dynamic flow stress at an average strain rate of 4.7 E+3 s^{-1} with the strain shifted to include the strain induced by the pre-straining and the prior impact of the a) as-received (AR) and impacted specimens at 293K b) 3% pre-strained (3PS) and impacted specimens tested at 293K c) as-received (AR) and impacted specimens tested at 923K (includes AR-0 as a reference) d) 3% pre-strained (3PS) and impacted specimens tested at 923K (includes AR-0 as a reference).

From the curves presented in Figure 5-8a, it can be seen that the flow stress of the 11GPa impacted specimen is significantly higher than that of the as-received specimen. The 3% pre-strained specimen impacted at 11GPa, Figure 5-8b, shows no such increase

in flow stress compared to that of the non-impacted specimen. This is also true when testing at high temperature (923K), as shown in Figure 5-8a and Figure 5-8b. This indicates that the twins are acting as barriers to dislocation slip during dynamic testing and because of this, increase the total flow stress of the material.

In conclusion, quasi-static tensile testing showed that the yield strength and ultimate tensile strength are both increased as a function of impact pressure and also show that as the impact pressure is increased the work hardening is diminished, indicated by the reduction in difference between the yield and UTS. The hardness of both as-received and pre-strained specimens indicate that the twins do indeed contribute to the enhanced strength of the material. The hardness of the as-received specimens exhibit a higher dependency to the impact pressure than the pre-strained counterparts, owing to the presence of twins in the microstructure. Dynamic compression tests of the impacted steel specimens have been done at 293K and 923K. Results indicate that the increase in flow stress due to dislocations are due to strain hardening, which can be accounted for by adjusting the flow stress curve to a strain corresponding to the strain induced by the impact. The similarity in flow stress for the pre-strained material suggest that the defect generation and storage mechanisms of the pre-strained steel during shock loading are similar to those created when deforming the material continuously at a lower rate. However, the as-received specimens, which include deformation twins, showed an enhanced flow stress due to the TB acting as dislocation barriers. These results are explained in terms of the interaction between dislocations and twins in detail in the following section.

5.5. Dislocation-Twin Interactions in Shock Loaded Steel

In regards to the presence of deformation twins in impacted microstructure, much of the research related to dislocation-twin boundary interactions has focused on FCC materials. The basic concepts associated with this work, can, however, be applied to the BCC microstructure. Zhang [25] used atomistic simulation to show that twin boundaries act as strong barriers to screw dislocation motion in FCC metals. Simulation of a set of dislocations encountering a TB showed that the leading partial dislocation is immobile in the twin due to constraint of the stacking fault ribbon connecting to the trailing partial remaining in the matrix. The partials must coalesce into a full dislocation before dissociating into partials again within the twin region; stress concentrations due to pile-up of dislocations at the boundary promote this process. Ezaz et al. [26,27] utilized molecular dynamics to simulate tensile deformation in FCC copper. Their results proved that TBs act as barriers to dislocation glide in FCC. Several dislocation mechanisms can occur during dislocation-TB interactions depending upon the stress field and direction of loading in relation to the slip and twin system such as Lomer, stair-rod, and Frank partial dislocation nucleation. These nucleated mechanisms give rise to local stress fields and increased energy barriers for slip in the twin and matrix. Gao and Zhang [28] introduced a constitutive model for high strain rates and consider grain boundaries and twin boundaries acting in a similar manner to impede dislocation motion. The twins are treated as barriers which effectively reduce the grain size and, as such, were considered to be as an athermal stress component. Their work, however, accounted for the role of twins in terms of a constant embedded into a recovery coefficient. Saxl [29] discusses the interaction of slip dislocations with twins and, based on the work of Sleeswyk and

Verbraak [30], notes that a step is formed on the twin boundary when a dislocation propagates over the TB. This step is a result of the impeding dislocations dissociating at the TB which leaves behind a partial dislocation of the twinning type, with the remaining part potentially propagating further into the twinned region. Shen et al. [31] also discuss the interaction occurring during tensile deformation of copper, again relating the TB to a conventional grain boundary owing to the dissociation of the dislocation at the interface due to stress concentrations from pile-ups and evidence of dislocation debris left behind at the TB.

Of the few studies that have been carried out on BCC metals, Sainath and Choudhary [32] provided insight into the interaction of dislocations and twins in iron during both tensile and compressive loading using atomistic simulations of BCC nanopillars. They observed that during compression, the yield stress was highly dependent on TB spacing. This has been shown to be a result of the TBs acting as barriers to full dislocations, preventing nucleation and expansion of dislocation loops and the accumulation of screw dislocations at the interface. Furthermore, it was shown that upon passing through the TB, the dislocation can transmit along the same glide plane, or deviate to a different plane. Mrovec et al. [33] also used simulations to study BCC metals with regards to specific planes and directions of dislocation and boundary systems in tungsten. For the $\Sigma 3 \left(11\bar{2} \right)$ boundary, which is the type of boundary associated with twins in BCC metals, they found that the dislocation immediately dissociates into $1/6 \left[111 \right]$ partial dislocations, two of which glide along the TB in opposite directions with the third partial residing at the interaction site, resulting in formation of a step at the TB, as shown schematically in Figure 5-9.
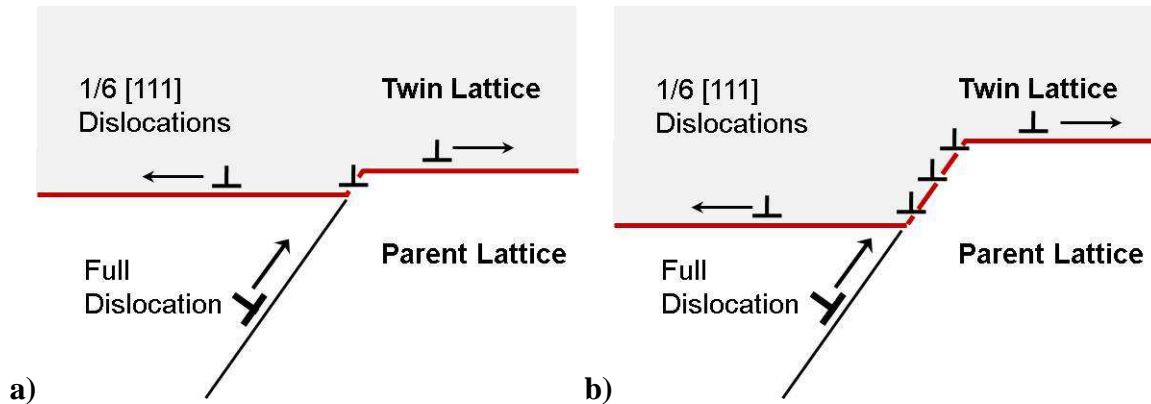
Figure 5-9: Dislocation-twin interaction resulting in dissociation of a full dislocation into three partial dislocations when encountering the TB (bold red line) shown for a) a single full dislocation dissociating and for b) after multiple dissociations, increasing the size of the step along the TB.

Nilles and Olson [34] studied the energy associated with coherent twin boundaries (TB). Through an annealing procedure they were able to determine a ratio between stacking fault energy and twin boundary energy. Shibuta et al. [35] utilized molecular dynamics to calculate the boundary energy in BCC iron and determined that the energy associated with twin boundaries was equal to 0.6 J/m2, whereas in FCC crystals the boundary energy was zero. This difference was attributed to the difference in the atomic packing of the planes for BCC and FCC crystals, where the BCC structure does not have a closed packed plane leading to a higher energy twin boundary.

From the studies outlined, it has been made clear that in both FCC and BCC metals, TB can act as barriers to dislocation slip. Furthermore, the boundary energy in BCC has been shown to possess a higher energy than in FCC metals which can lead to a higher resistance of dislocation motion. In these studies it has also been shown that the yield stress is dependent upon the TB spacing in a similar manner to grain boundaries and the

Hall-Petch grain size effect. This has also been discussed for HCP metals in which twin-twin intersections result in potential locking mechanisms for twinning dislocations, leading to sessile dislocation locks. Overcoming these obstacles would result in a stress which is unaffected by thermal energy or strain rate, as they occur over a large distance [28]. These types of twin-twin intersections are also shown to occur in the BCC steel in this study, occurring more frequently as the twin volume fraction increases, as shown in Figure 5-10. The steps created in the TB by dislocation-twin interaction, as discussed by Mrovec [33], can also be seen in twin-twin interaction, Figure 5-11, where twinning partials making up the incoherent boundary of imposing twins encounter a twin on a different plane.
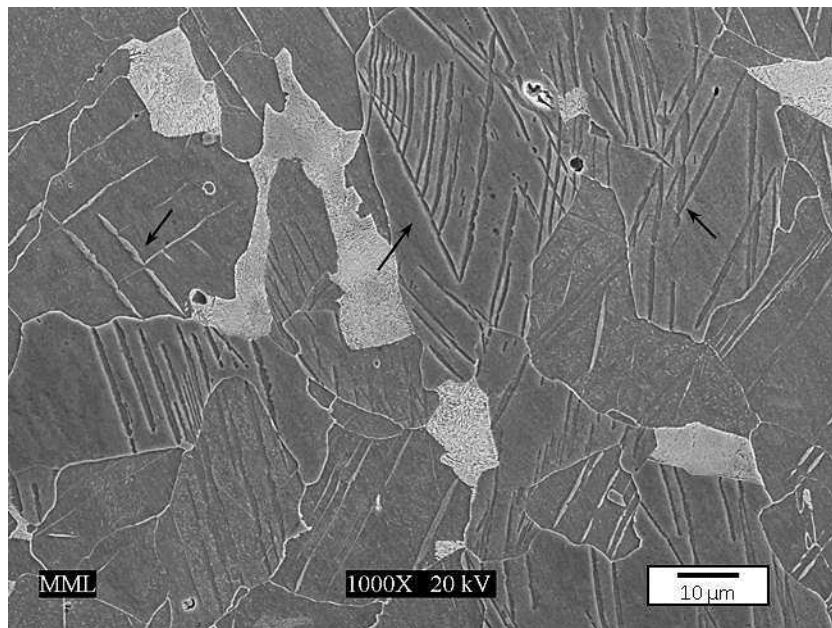
Figure 5-10: Twin-twin interaction in BCC α-iron which was previously impacted at 11GPa.

257
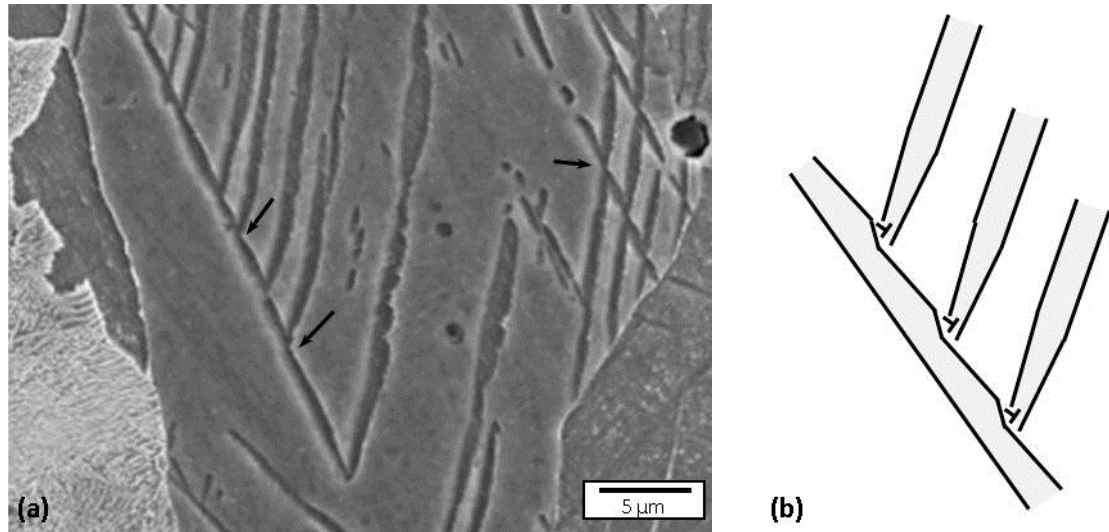
Figure 5-11: a) SEM micrograph of steps created in twin due to twinning dislocations interacting with coherent twin boundary and b) schematic representation of such steps

Based on the studies discussed, it is a reasonable approach to include the effects of deformation twins as an athermal stress component, written in terms of the twin volume fraction. As shown by Mrovec [33], a full dislocation, upon encountering a twin boundary, will result in the glide of two partial dislocations along the boundary, with the third partial remaining at the boundary. It can therefore be inferred that dislocations which interact with twins produce 1/3 less strain accommodation than those which do not, and additional dislocation generation would then be required leading to an increase in flow stress. The formulation of the model and determination of parameters are discussed in the following sections.

5.6.   Modeling Flow Stress in Pre-Shocked Material

Modeling the flow stress as the sum of separate stress components is based on the concept that stresses developed in the material, as a result of dynamic loading, are related to the different mechanisms associated with dislocation/barrier interactions. The flow stress during plastic deformation occurs due to dislocation motion and their resistance to barriers. This stress is split into parts according to the type of barriers; short range, long range, and drag components. In BCC metals, short range barriers, those less than 10 atomic diameters [8], are controlled by the resistance of the actual lattice and point defects within. This stress is controlled by the strain rate and temperature, thus is deemed as thermal stress, σ_{TH}. Long range barriers, those greater than 10 atomic diameters, are controlled by stress fields from forest dislocations and grain boundaries [8], and thermal energy is not sufficient to aid in overcoming these obstacles. The stress required to overcome these long range barriers are not affected by the strain rate, and are only indirectly affected by temperature through the elastic shear modulus, thus is deemed as the athermal stress component, σ_A. As the strain rate is increased, the flow stress becomes more sensitive to strain rate. This has largely been thought to be due to dislocation drag caused by scattered phonons or solute atoms in the lattice [10,11]. However, it has been shown that the increase of stress in the 10^3-10^4 s^{-1} range is not caused by dislocation drag, but rather by an increased dislocation generation rate [41], while others have shown that the shift from thermally-activated to viscous drag mechanism occurs at strain rates on the order of 10^5-10^7 s^{-1} [42,43]. As the strain rates in this study are all within the 10^4 s^{-1} range, this drag component shall be neglected in the following analysis.

The summation of these two stress components results in the total flow stress required to move dislocations, as illustrated in Figure 5-12. The large wavelength hills represent the long range, athermal stress barriers. The peaks and valleys imbedded along these hills represent the stress fields due to short range, thermal stress barriers. It can be seen that the mechanical threshold stress, $\hat{\sigma}$, represents the total flows stress when there is no thermal assistance, occurring at 0K. As the temperature of the material is increased, the additional thermal energy assists in dislocations overcoming thermal obstacles, effectively decreasing the resistance of short range barriers. As the temperature is further increased, approaching a critical temperature, the mechanical stress needed to move dislocations is dependent solely on the resistance of athermal stress barriers, beyond which any increase in temperature will have no effect.
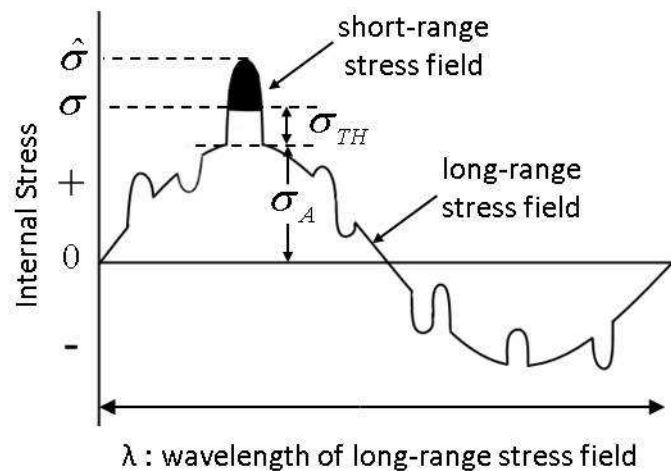
Figure 5-12: Stress required for dislocations to overcome long and short range stress fields. [5]

Thus, the total flow stress can simply be written as a sum of the thermal and athermal components:

$$\sigma = \sigma_A + \sigma_{TH} \tag{5.1}$$

The thermally active thermal stress component, σ_{TH}, as mentioned above, is due to interactions between dislocations and short range barriers. To attain a general relation between temperature, strain rate and the thermal stress component, the energy required for a dislocation to overcome a barrier by thermal activation is written as

$$\Delta G = G_0 \left[1 - \left(\frac{\sigma_{TH}}{\hat{\sigma}} \right)^p \right]^q \tag{5.2}$$

The constants p and q represent the shape of the barrier and vary between $0 < p \leq 1$ and $0 \leq q \leq 2$. $\hat{\sigma}$ is the stress required for a dislocation to overcome a barrier without any thermal assistance, and G_0 is the energy of the Peierl's barrier per atom required to overcome a barrier solely by thermal activation and is given by

$$G_0 = \hat{\sigma} \lambda l b \tag{5.3}$$

where λ and l are the average effective barrier width and spacing respectively. The strain rate is related to the activation energy ΔG by the most general form written as,

$$\dot{\varepsilon} = \dot{\varepsilon}_0 \exp\left(-\frac{\Delta G}{kT} \right) \tag{5.4}$$

where k is the Boltzmann's constant and T is the testing temperature. The reference strain rate $\dot{\varepsilon}_0$ is determined as a function of dislocation density as

$$\dot{\varepsilon}_0 = bl\rho_m\omega_0 \qquad (5.5)$$

where b is the burgers vector, for BCC materials along the <111> direction is $\sqrt{3}a/2$ and l is the average dislocation barrier spacing which is on the same order as b so that $l \approx b$, ρ_m is the mobile dislocation density, and ω_0 is the attempt frequency to jump a barrier.

Solving for σ_{TH} from Equation (5.2) the thermal stress is expressed as:

$$\sigma_{TH} = \hat{\sigma}\left[1 - \left(\frac{kT}{G_0}\ln\frac{\dot{\varepsilon}}{\dot{\varepsilon}_0}\right)^{1/q}\right]^{1/p} \qquad (5.6)$$

where $\hat{\sigma}$ is the mechanical threshold stress at 0K, T is current temperature, G_0 is the energy of the Peierl's barrier per atom, $\dot{\varepsilon}$ is the imposed strain rate, and $\dot{\varepsilon}_0$ is the reference strain rate.

The athermal stress, σ_A, as shown by Taylor et al. [44] is a function of strain and other microstructural parameters and is thus, the athermal stress is written as

$$\sigma_A = \sigma^*\varepsilon^n + \sigma_m \qquad (5.7)$$

where ε is the strain, n is the strain sensitivity , and σ_m is the stress component due to the microstructural characteristics that could include twin volume fraction. The data used for determining the constants in this equation must be at a sufficiently high temperature in order to remove any thermal component of stress. The experimental data used to

determine the athermal component of stress is done at or above the critical temperature where the temperature effects, and thus the thermal stress component, are removed.

The introduction of dislocations and twins in the microstructure due to the shock loading can be included within the model presented. Assuming that the dislocations in BCC material do not impede upon themselves as barriers, it is expected that their increased density due to the impact induced straining can be accounted for purely by adjusting the strain term in Equation (5.7), now written as

$$\varepsilon_{eff} = \varepsilon + \varepsilon_0 \tag{5.8}$$

with ε being the strain during the current compression test, and ε_0 being the prior strain history induced by pre-straining and shock loading.

As discussed in the previous section, the twins introduced from the shock loading will be included within the athermal stress component of the model. They will be accounted for by including a term related to the twin volume fraction.

$$\sigma_m = \sigma_0 + f(\alpha) \tag{5.9}$$

where σ_0 is the microstructural contribution of the initial material condition, which is effectively the yield stress at the critical temperature. The term $f(\alpha)$ is a function of the volume fraction of twins, α, to be determined subsequently from dynamic compression tests. The foundation of the application of twins to the athermal stress component will be discussed in terms of dislocation slip and the barrier that the twin boundaries present in the following section.

Combining Equations (5.7), (5.8), and (5.9) as the athermal stress component, and summing with the thermal stress component, Equation (5.6), the total flow stress is expressed as

$$\sigma_{TH} = \sigma^* \varepsilon_{\textit{eff}} + \sigma_0 + f(\alpha) + \hat{\sigma}\left[1 - \left(\frac{kT}{G_0}\ln\frac{\dot{\varepsilon}}{\dot{\varepsilon}_0}\right)^{1/q}\right]^{1/p} \quad (5.10)$$

The parameters for this model are determined through a set of experimental compression tests. These tests are done on a set of as-received and 3% pre-strained steel specimens which have previously been shock loaded. The experimental work and model parameter determination are described in later sections.

5.7.   Model Parameters

In this section the parameters for the thermal activation model presented in the previous section are determined, including the effects of prior impact, due to residual microstructure variation, on the flow stress components. It has been shown that increasing the impact stress leads to an increase in flow stress; see Figure 5-8. From micrographs of the impacted steel shown in Figure 5-3 and Figure 5-4, the most obvious cause of this is due to the addition of mechanical twins. The second component, which is inherent to any deformation process, is the dislocation substructure. An experimental procedure is carried out using a SHPB to determine parameters for the model presented. Results from these tests are used to determine the influence of impact loading of the dynamic flow stress.

5.7.1. **Thermal Flow Stress**

The flow stress at 923K is subtracted from the total to obtain the thermal flow stress component. As other others have pointed out, the athermal flow stress is proportional to the shear modulus, and the flow stress can be normalized by the ratio μ_0/μ, where μ_0 and μ are the shear modulus at 0K and at the current temperature, respectively. However, just as done in the work of Nemat-Nasser and Guo [11], this is not an important factor in our work and $\mu_0/\mu(T) \approx 1$ was employed. After subtracting the athermal from the total flow stress, Equation (5.6) can be simplified for fitting to experimental data, written as

$$\sigma_{TH} = \hat{\sigma}\left[1 - (AT)^{1/q}\right]^{1/p} \tag{5.14}$$

where

$$A = -\frac{k}{G_0}\ln\frac{\dot{\varepsilon}}{\dot{\varepsilon}_0} \tag{5.15}$$

Equation (5.14) is fit to the experimental thermal flow stress to determine $\hat{\sigma}$. Figure 5-13 shows the thermal flow stress vs. temperature for the as-received and 3% pre-strained specimens. Figure 5-14 and Figure 5-15 respectively show the thermal flow stress vs. temperature for the as-received and 3% pre-strained specimens which were previously impacted at 6GPa and 11GPa.
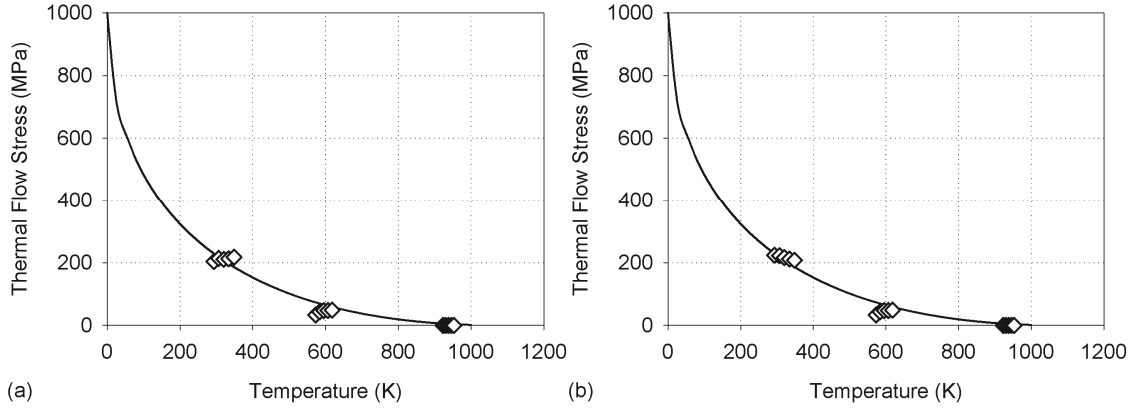
Figure 5-13: Thermal flow stress for the a) as-received and b) 3% pre-strained steel
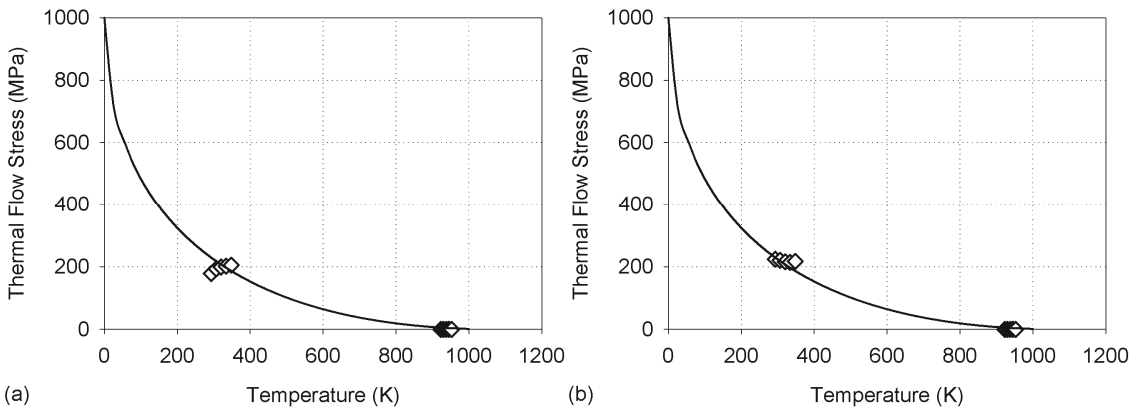
Figure 5-14:   Thermal flow stress for the a) as-received steel previously impacted by 6GPa, and b) 3% pre-strained steel previously impacted by 6GPa
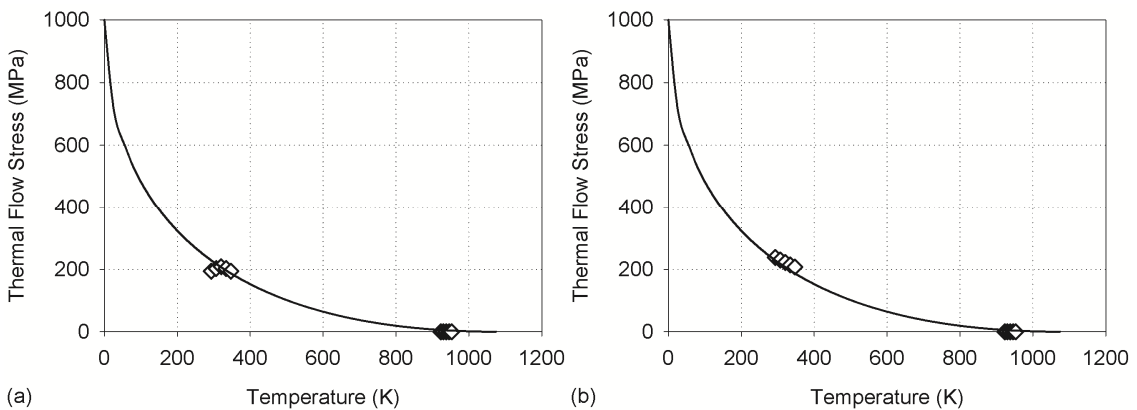
Figure 5-15:   Thermal flow stress for the a) as-received steel previously impacted by 11GPa, and b) 3% pre-strained steel previously impacted by 11GPa

The activation energy for iron [45], $G_0=0.52$ eV, was utilized in this work. The constants $p=1/2$ and $q=2$ are obtained from work by Nemat-Nasser [10] on BCC Vanadium. The dislocation density, ρ_m, is determined using data generated in the work of Conrad and Christ [48] on alpha-iron, as shown in Figure 5-16. The initial dislocation density was determined by fitting a curve to this data and which yields a value of $5E+12$ m^{-2}, which is in good agreement with the initial dislocation density used in the work of Voyiadjis and Abed [47].
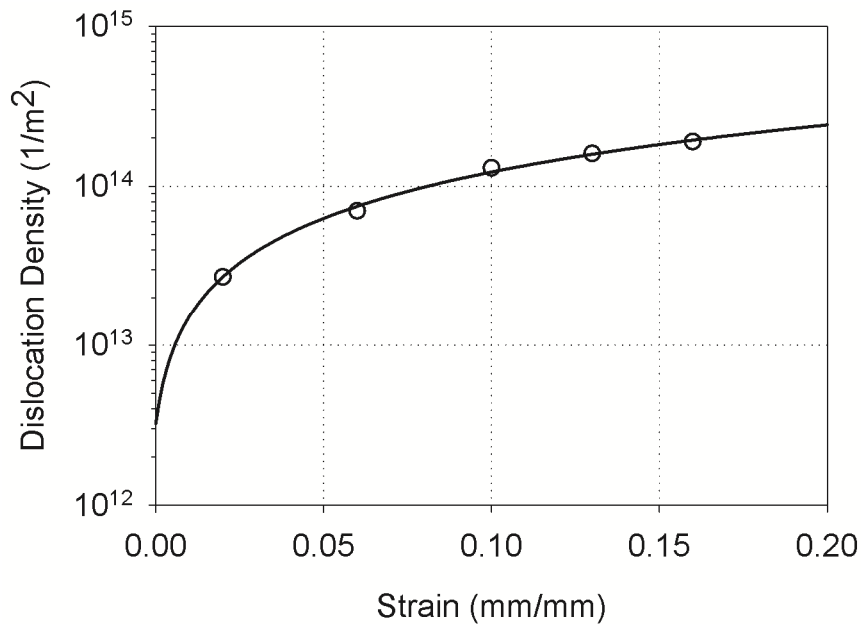
Figure 5-16: Dislocation density vs. strain for polycrystalline iron [24]

Dislocation spacing in the case of BCC metals can be set approximately equal to the burgers vector. It should be noted however, that for FCC materials, this value should be related to the dislocation density, such that $l=1/\sqrt{\rho_m}$. Reasoning for these differences is due to the types of barriers associated with each specific crystal structure. In BCC

267

metals, as described elsewhere [50-52], the thermal stress is due to the lattice itself which acts as the main resistance to dislocation motion, and the spacing should therefore be on the same order as the lattice spacing, therefore $l \approx b$. For FCC metals, the main source of short range barriers are forest dislocations, therefore as the dislocation density is increased, the mean free path decreases which is described through the relation $l = 1/\sqrt{\rho_m}$ by several authors [12,50]. This results in a 3 to 4 order of magnitude difference in values when calculating the reference strain rate. Replacing the attempt frequency, ω_0, and dislocation spacing, l, in Equation (5.5) with the velocity of dislocations, the reference strain rate is rewritten as

$$\dot{\varepsilon}_0 = \rho_m b v \qquad (5.16)$$

The limiting velocity of dislocations described by Gilman [51] can be used here and is calculated as

$$v = (1/\pi)(\mu/\rho)^{1/2} \qquad (5.17)$$

where the shear modulus $\mu = 8.279E + 10\,\text{Pa}$ and the material density is $\rho = 7814\ kg/\text{m}^3$, resulting in a velocity of $v = 1035$ m/s. When setting the dislocation density to $\rho_m = 5.0E + 12\,\text{m}^{-2}$ for the as-received material, the reference strain rate is calculated as $\dot{\varepsilon}_0 = 1.28E6\,\text{s}^{-1}$. This is comparable with values obtained for vanadium [11]. With the increase in dislocation density for the 3% pre-strained material, determined as $\rho_m = 2.8E + 13\,m^{-2}$ from Figure 5-16, a dislocation velocity set to $v = 185$ m/s maintains the same reference strain rate. Taking an average strain rate of all tests within this work to be 4700 s^{-1}, the simplified fitting parameter A from Equation (5.15) is calculated as

$A=9.29\text{E-}4 \text{ K}^{-1}$.   The constants are shown in Table 5-2 and Table 5-3 for the as-received and 3% pre-strained material, respectively.

Table 5-2: Constants for the thermal flow stress equation for the as-received material

	G_0 (eV)	k (eV/K)	q	p	v (m/s)	b (m)	ρ_m (m^{-2})	$\dot{\varepsilon}_0$ (s^{-1})	$\dot{\varepsilon}$ (s^{-1})
$\hat{\sigma}$									
1000	0.52	8.62E-05	2	1/2	1035	2.47E-10	5E+12	1.28E+06	4700

Table 5-3:   Constants for the thermal flow stress equation for the 3% pre-strained material

	G_0 (eV)	k (eV/K)	q	p	v (m/s)	b (m)	ρ_m (m^{-2})	$\dot{\varepsilon}_0$ (s^{-1})	$\dot{\varepsilon}$ (s^{-1})
$\hat{\sigma}$									
1000	0.52	8.62E-05	2	1/2	185	2.47E-10	2.80E+13	1.28E+06	4700

As shown in Figure 5-13 through Figure 5-15, the thermal flow stress is relatively insensitive to the strain. Furthermore, it is shown that the thermal flow stress is also insensitive to the level of impact. Adiabatic heating was accounted for by adjusting the temperature at each level of strain. As the specimen is compressed, the temperature is increased by

$$\Delta T = \frac{\eta}{\rho} \int_0^\varepsilon \frac{\sigma}{C_V} d\varepsilon \tag{5.18}$$

where ρ is the material density, η is the inelastic heat fraction set as an approximate equal to 1, and C_V is the constant volume heat capacity.   At an initial test temperature of 293K, a 55K increase in temperature occurs from the range of 5% to 25% strain and there is an

increase of approximately 30K when initially testing at 923K. This temperature increase will also be included in the modeling efforts.

The critical temperature, that at and above which the thermal flow stress component is zero, can be calculated as

$$T_c = -\frac{G_0}{k}\left(\ln\frac{\dot{\varepsilon}}{\dot{\varepsilon}_o}\right)^{-1} \tag{5.19}$$

Utilizing the values from Table 5-2, the average critical temperature for this material is $T_c = 950\,K$. The experimental testing temperature used in this work, set to be 923K, is a reasonable value for the critical testing temperature, as a curve fit of experimental data shows that the flow stress only decreases by less than 5 MPa between 923 and 950K.

5.7.2. Athermal Flow Stress

The athermal flow stress component presented in Equation (5.2), is that of a classic hardening form such as the Ramberg-Osgood equation [52]

$$\varepsilon = \frac{\sigma}{E} = K\left(\frac{\sigma}{E}\right)^n \tag{5.20}$$

or in the one dimensional form of the Norton-Hoff model where plastic strain rate is related to stress as:

$$\dot{\varepsilon}_{plastic} = \left(\frac{\sigma}{\lambda^*}\right)^{N^*} \tag{5.18}$$

or in the strain dependent portion of the Johnson-Cook model

$$\sigma = \underbrace{\left(A + B\varepsilon^n\right)}_{\text{Strain Hardening}} \underbrace{\left[1 + C\ln\dot{\varepsilon}^*\right]}_{\text{Strain Rate Effect}} \underbrace{\left[1 - T^{*m}\right]}_{\text{Temperature Effect}} \quad (5.21)$$

The two terms, σ^* and n, in Equation (7) control the hardening rate. The term σ_m accounts for microstructural features. Equation (5.2) is modified to include the strain induced by prior impact, and is now written as

$$\sigma_A = \sigma^* \varepsilon_{eff} + \sigma_m \quad (5.22)$$

where $\varepsilon_{eff} = \varepsilon + \varepsilon_0$, with ε being the strain during the current compression test, and ε_0 being the prior strain history induced by pre-straining and shock loading. Equation (5.22) is fit to the experimental data of specimens tested at 923K, shown in Figure 5-8c and Figure 5-8d, to determine the hardening parameters σ^* and n, as shown in Figure 5-17. These values, for the as-received material for the pre-strained material, are presented in Table 5-4 and in Table 5-5, respectively.
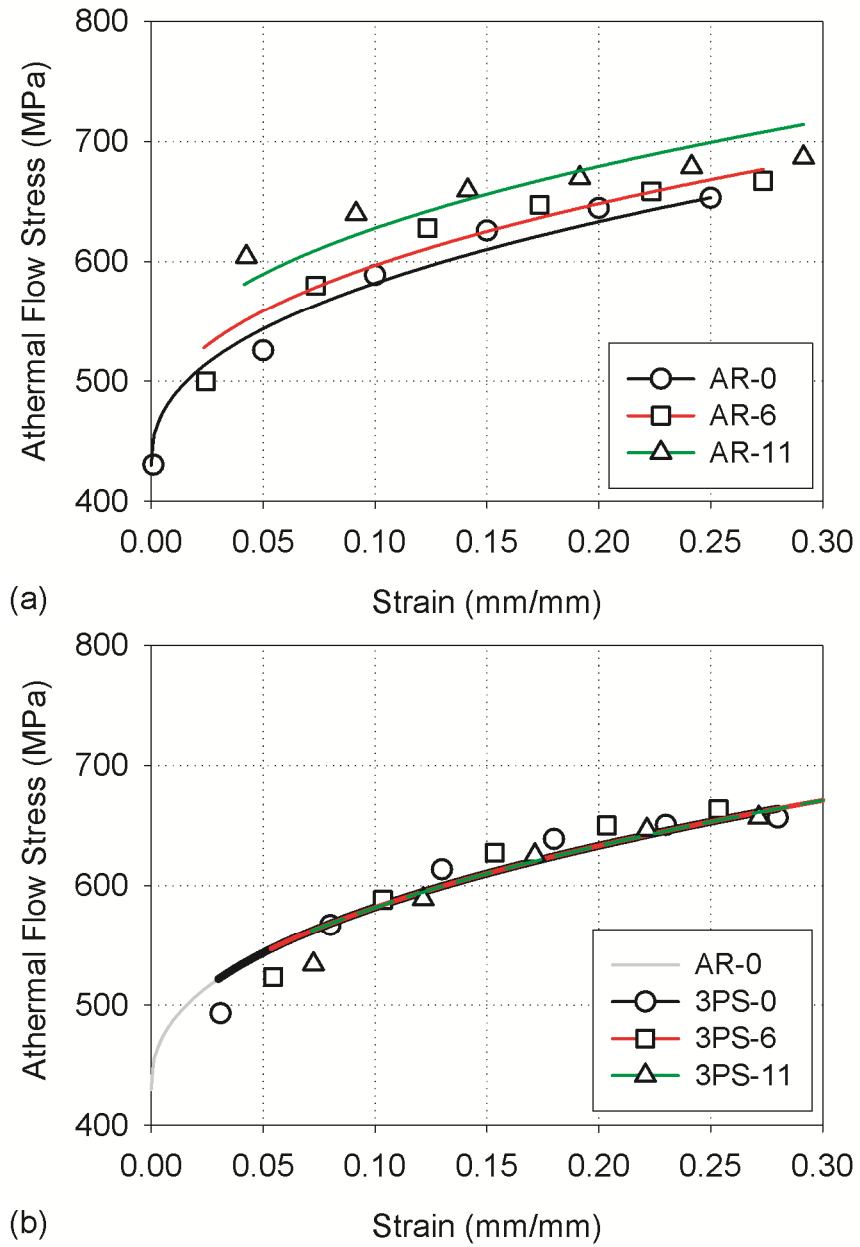
Figure 5-17: Athermal flow stress for the a) as-received and b) 3% pre-strained steels.

Table 5-4: Athermal Flow stress constants for the as-received material

AS-RECEIVED ATHERMAL PARAMETERS			
	σ^* (MPa)	σ_m (MPa)	n
AR-0	400	430	0.42
AR-6	400	445	0.42
AR-11	400	476	0.42

Table 5-5: Athermal Flow stress constants for the 3% pre-strained material

3 % PRE-STRAINED ATHERMAL PARAMETERS			
	σ^* (MPa)	σ_m (MPa)	n
3PS-0	400	430	0.42
3PS-6	400	430	0.42
3PS-11	400	430	0.42

As shown in Figure 5-17 the hardening parameters, σ^* and n, are relatively insensitive to the change in microstructure due to impact, and average values of $\sigma^* = 400$MPa and $n=0.42$ were set for all cases. For the pre-strained steel shown in Figure 5-17b, all of the data is represented by a single set of constants, which are those determined for the as-received steel. However, as shown in Figure 5-17a, there is a jump in the athermal flow stress for the as-received steel which is attributed to an increase in σ_m.

When the stress-strain curves of the 3% pre-strained and impacted steel are adjusted to the effective strain levels, the flow stress level and hardening rates are similar to that of the non-impacted specimens, as shown in Figure 5-8b and Figure 5-8d. This is reflected through the constant values obtained for the athermal parameters shown in Table 5-5. This indicates that the defect generation and storage mechanisms of the pre-strained steel

during shock loading are similar to those created when deforming the material continuously, at a lower rate. This has also been confirmed by TEM in the work of Mahajan [36] who showed that α-iron, pre-strained to 5% strain and shock loaded to 5GPa, exhibits a dislocation network similar to the un-shocked material. The dislocation structure in the ferrite grains is shown in Figure 5-18 for the 3% pre-strained steel impacted at 11GPa, resulting in approximately 7% total strain.
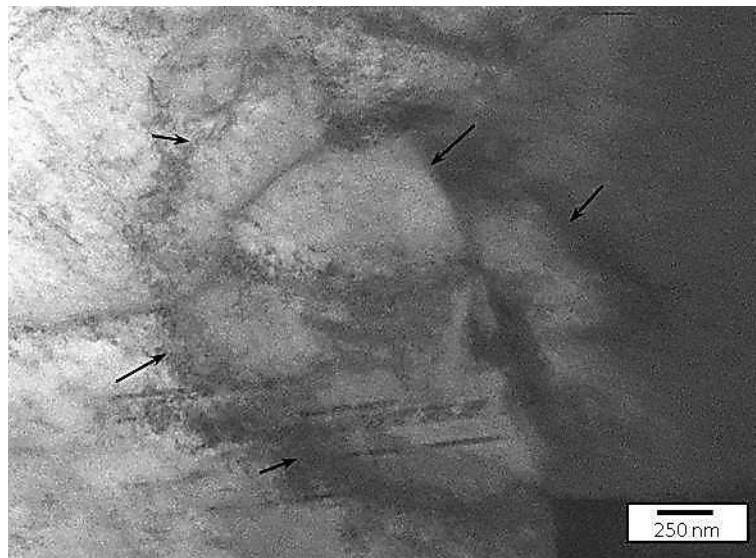
Figure 5-18: Dislocation cell structure in ferrite grains after 3% pre-strain and 11GPa shock loading resulting in approximately 7% total strain.

The cell structure shown in Figure 5-18 exhibits similar features to α-iron strained at low strain rate to a similar strain level, as seen in the work of Lan et al. [37]. The twins in the microstructure are considered to act as barriers to dislocation motion [38,39]. As Gray and Vecchio [40] have pointed out, the lack of hardening in the BCC tantalum can be attributed to the lack of twins present in the shock loaded tantalum, similar to the lack of hardening in the pre-strained specimens.

5.8. **Model Simulation and Results**

As shown in Figure 5-8a and Figure 5-8c, unlike the pre-strained steel, the flow stress of the as-received and impacted specimens is higher than that of the as-received material. This increase in flow stress is accounted for in the microstructural term σ_m of the athermal stress component of Equation (5.7). The twin dependent term in Equation (5.9), $f(\alpha)$, can be written in terms of the twin volume fraction as determined from the of the athermal stress parameter σ_m.

$$f(\alpha) = \beta \alpha^m \qquad (5.23)$$

where α is the twin volume fraction, and $\beta = 260 \text{ MPa}$ and $m = 0.73$ which are constants describing the contribution of twin volume fraction to the athermal stress.

Combining Equations (5.10) and (5.23), the total flow stress is written as

$$\sigma = \sigma^* \varepsilon_{eff} + \sigma_0 + \beta \alpha^m + \hat{\sigma} \left[1 - \left(\frac{kT}{G_0} \ln \frac{\dot{\varepsilon}}{\dot{\varepsilon}_0} \right)^{1/q} \right]^{1/p} \qquad (5.24)$$

This equation is applied to experimental curves to check the validity of parameters determined. Figure 5-19 shows an experimental true stress-true strain curve compared with an isothermal model simulation and a simulation with predicted effects of adiabatic heating included, utilizing Equation (5.15). As this figure shows, including the adiabatic heating effects provides a closer fit to the experimental data.

(a)

(b)
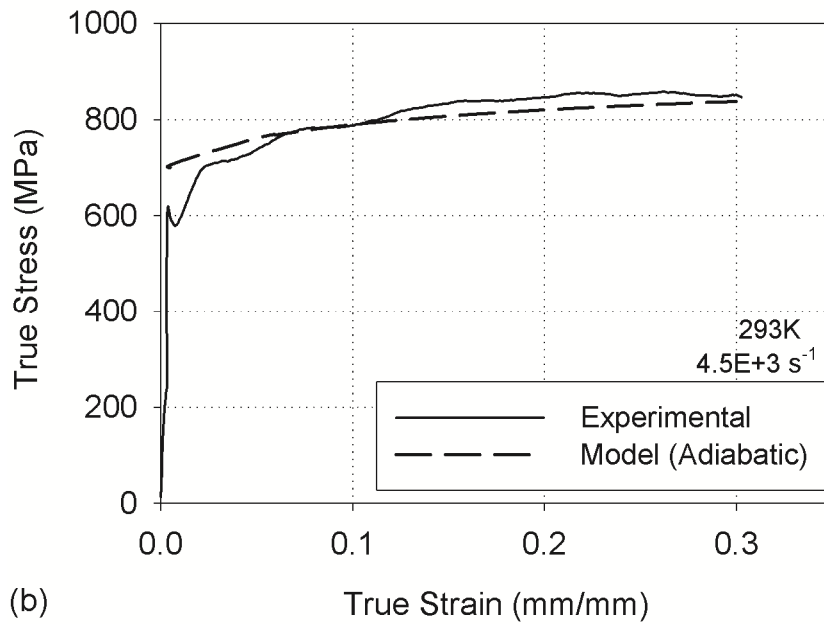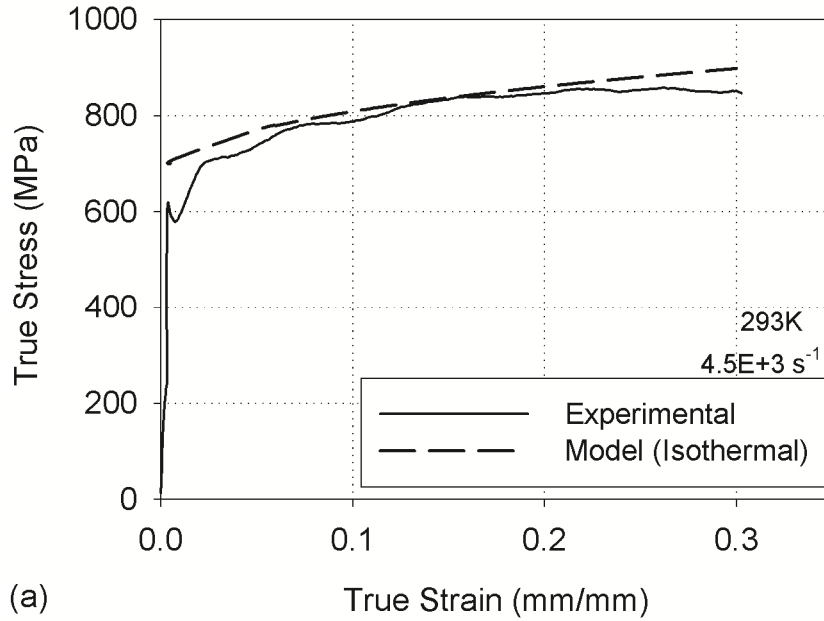
Figure 5-19: Experimental stress-strain curves for as-received material at a strain rate of 4.5E+3 s^{-1} and at room temperature compared with model including adiabatic heating effects.

As shown in Figure 5-20, the model is also accurate in calculating the flow stress for the as-received and pre-strained steels at strain rates of 2.8E+3 s^{-1} and 2.3E+3 s^{-1}, which

are lower than those used in the determining model parameters. This is also shown for materials impacted at 3.7GPa and 13GPa which were then tested at a strain rate of 1.3E+3 s^{-1} in Figure 5-21.

(a)

(b)
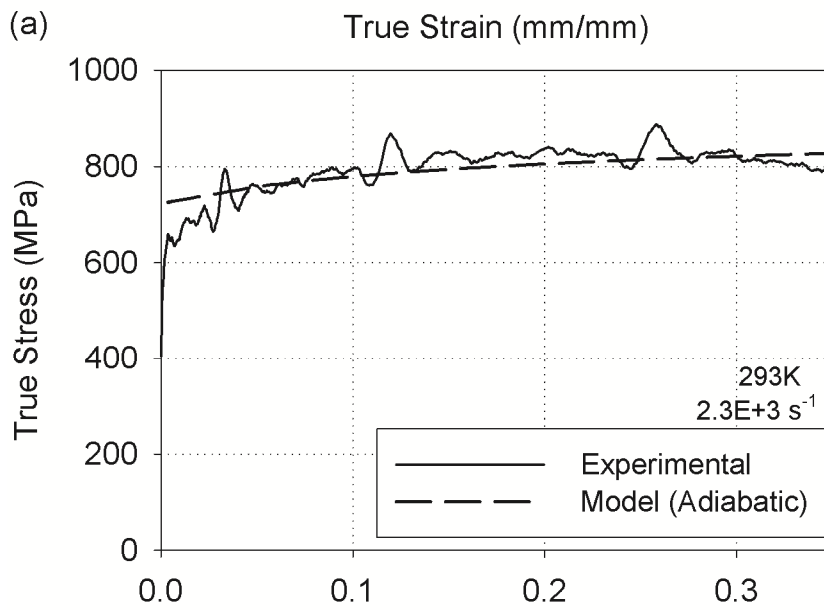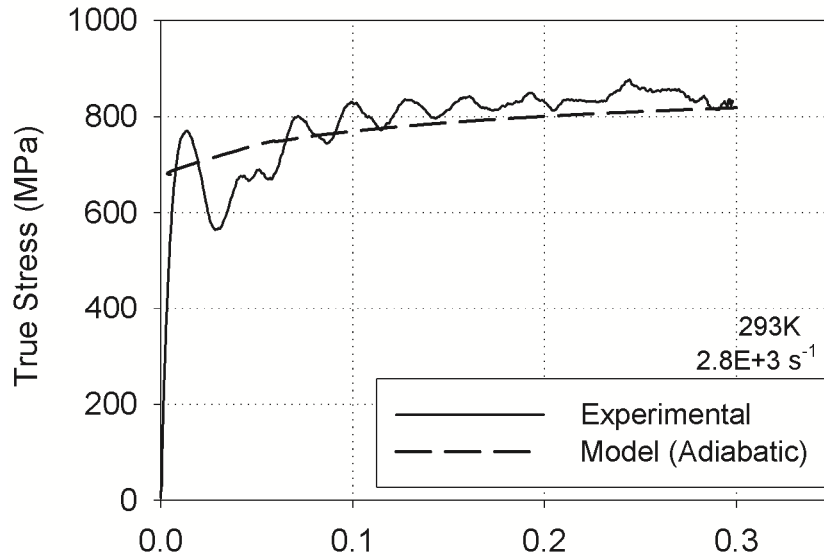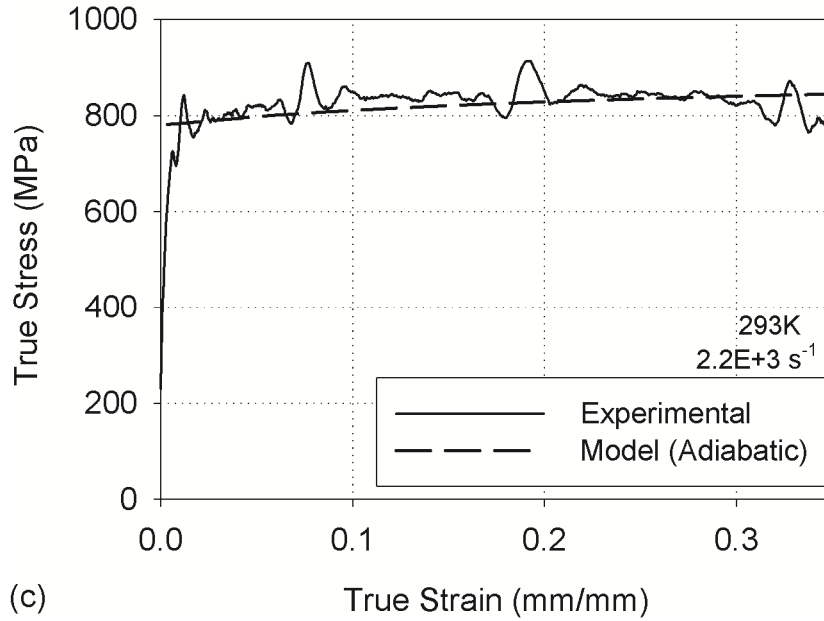
Figure 5-20: Experimental stress-strain curves at room temperature compared with model predictions including adiabatic heating for a) as-received material at a strain rate of 2.8E+3 s^{-1}, b) 3% pre-strained material at a strain rate of 2.3E+3 s^{-1}, and c) 10% pre-strained material tested at a strain rate of 2.2E+3 s^{-1}.
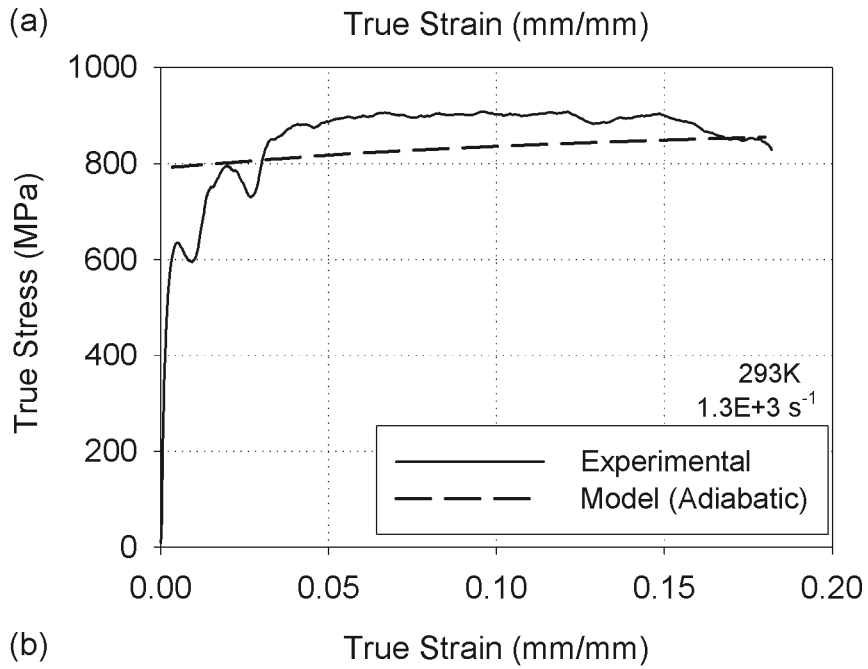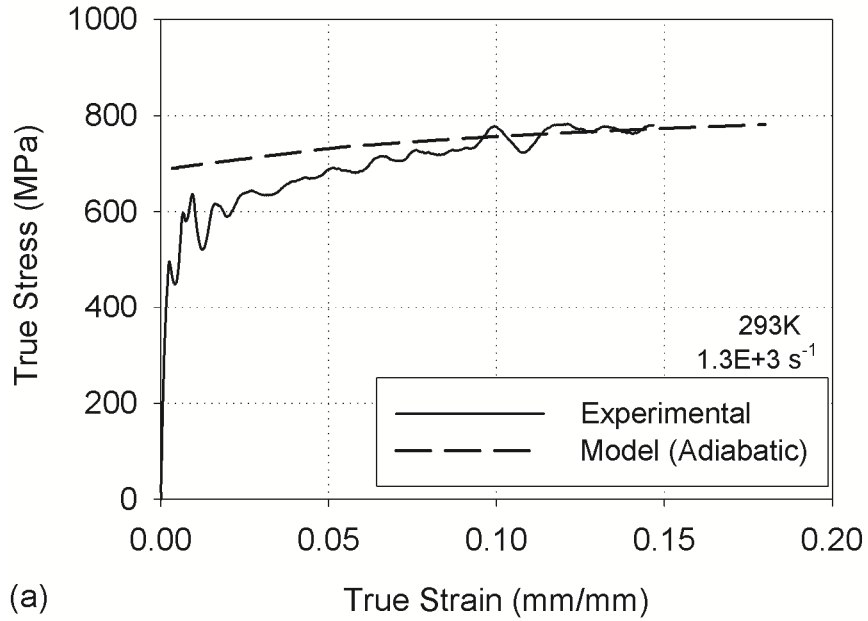
Figure 5-21: Experimental stress-strain curves at room temperature compared with model predictions including adiabatic heating for a) as-received material previously impacted at 3.7GPa and tested at a strain rate of 1.3E+3 s^{-1} and b) as-received material previously impacted at 13GPa and tested at a strain rate of 1.3E+3 s^{-1}

5.9.   **Conclusions**

The goal of the study presented in this paper was aimed at identifying the role of pre-existing deformation twins in the dynamic stress-strain relationship of shock loaded low carbon steel. Major outcomes and results of this work can be summarized as follows:

- A set of as-received and 3% pre-strained steel specimens were subjected to shock loads of 6GPa, and 11GPa. The as-received microstructure has shown development of deformation twins, the volume fraction of which increases with the shock load magnitude. The shocked microstructure, however, indicated that pre-straining to 3% is effective in inhibiting twin formation and therefore the strain during impact loading is accommodated purely by dislocation motion.

- The effects of shock loading and significance of twins on the mechanical properties of the steel have been examined in several ways. Quasi-static tensile tests, hardness tests, and dynamic compression tests all showed that the twins do indeed contribute to the enhanced flow stress of the material due to the TB acting as dislocation barriers.

- The shock loaded specimens as well as ones with no prior shock loading were subjected to dynamic compression tests at temperatures in the range 293K to 923K at strain rates between $1E+3$ s^{-1} and $5E+3$ s^{-1}. The resulting stress-strain curves were partitioned into thermal and athermal stress components using thermal activation concepts based on dislocations interactions with thermal and athermal stress barriers. Results of this work show that the thermal stress component of both the as-received and pre-strained materials is insensitive to the corresponding impact strain history. The athermal stress component for the as-received shock loaded

specimens is shown to be proportional to the loading pressure while for specimens which have been pre-strained before shock loading, the athermal stress displayed a constant value at all impact loads. This difference in athermal stress between as received and pre-strained materials is explained in terms of the twin volume fraction.

- The developed flow stress formulations which expresses the athermal stress component as an explicit function of the twin volume fraction, have been applied to predict the flow stress in materials that have been independently impacted at 3.7GPa, 7GPa and 13GPa. Results of this application were compared with those generated experimentally indicating validity of concepts and formulations presented in this work.

5.10. **Appendix**

The flow stress curves of shock loaded specimens have been adjusted to account for the strain history due to impact and/or pre-strain. The deviatoric strain resulting in plastic deformation imparted by the shock loading is written as [18]

$$\varepsilon = \frac{2}{3} \ln \frac{V}{V_0} \qquad (5.11)$$

Where V_0 and V are the initial and shock specific volumes, respectively. The specific volume during the shock loading can be determined from the following relation derive from the Rankine-Hugoniot equations relating particle velocity, pressure, and specific volume [53]

$$u_p = [(P - P_0)(V_0 - V)]^{1/2} \tag{5.12}$$

Alternatively, one could replace the specific volume in Equations (5.11) and (5.12) with the material density ρ as

$$V = \frac{1}{\rho} \tag{5.13}$$

A pressure vs. particle velocity curve can be generated by measuring the peak impact pressure and projectile velocity, V, where $u_p = 1/2V$ for symmetric impacts, during several shock load experiments and a relationship can be derived, as shown in Figure 5-22.
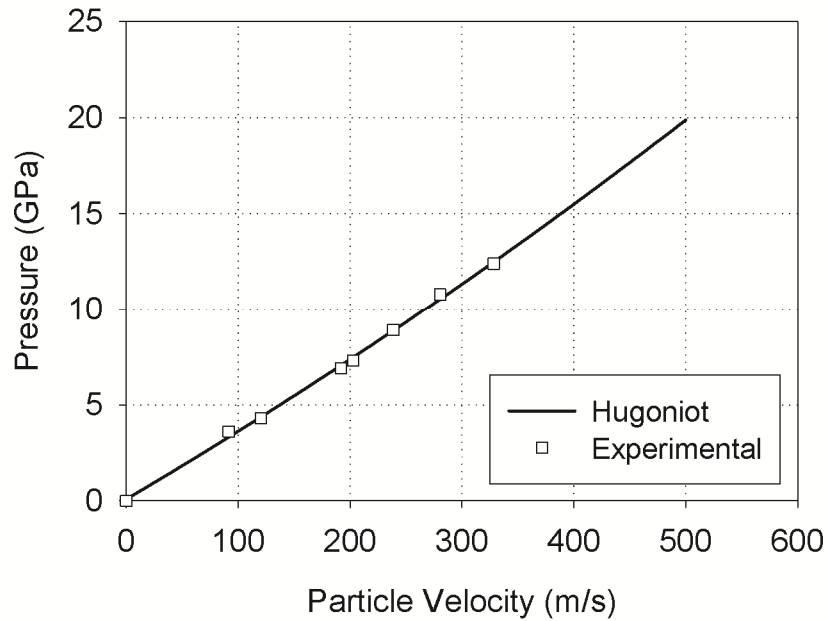
Figure 5-22: Pressure vs. particle velocity during shock loading for A572 grade 50 steel.

With a known relation between the pressure, P, and particle velocity, u_p, the shock specific volume can be determined from Equation (5.12) and subsequently be plugged into Equation (5.11) to solve for the strain as function of impact pressure, as shown in Figure 5-23.
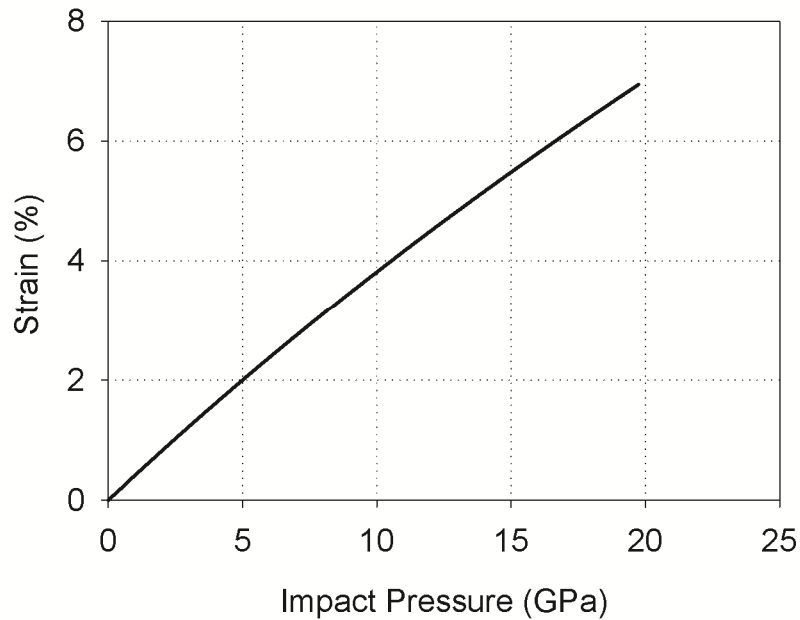
Figure 5-23: Strain generated during shock loading, as calculated by Equations (1), (2), and (3)

The flow stress curves of the 6GPa and 11GPa shocked specimens were adjusted to start at strains of 2.35% and 4.15%, respectively, determined from Figure 5-23, which are shown in Figure 5-8a and Figure 5-8c. Specimens which were pre-strained by 3% prior to impact were adjusted by the total of 5.35% and 7.15% strain for the 6GPa and 11GPa, respectively, and are shown in Figure 5-8b and Figure 5-8d.

5.11. References

[1]   Smida, T., Bošanský, J., Deformation twinning and its possible influence on the ductile brittle transition temperature of ferritic steels, Materials Science and Engineering. A287 (2000) 107–115.

[2]   Jolley, W., Hull, D., Effect of Prestrain and Strain Aging on the Brittle Fracture of 3.25% Silicon Iron, Acta Metallurgica 12 (1964) 1337-1352.

[3]   Biggs, W.D., Pratt, P.L., The Deformation and Fracture of Alpha-Iron at Low Temperatures, Acta Metallurgica 6 (1958) 694-703.

[4]   Visser, W., Sun, Y., Gregory, O., Plume, G., Rousseau, C-E., Ghonem, H., Deformation Characteristics of Low Carbon Steel Subjected to Dynamic Impact Loading, Materials Science and Engineering. A528 (2011) 7857–7866.

[5]   Johnson, Gordon R., and William H. Cook. "A constitutive model and data for metals subjected to large strains, high strain rates and high temperatures." *Proceedings of the 7th International Symposium on Ballistics*. Vol. 21. No. 1983. 1983.

[6]   Zerilli, Frank J., and Ronald W. Armstrong. "Dislocation-mechanics-based constitutive relations for material dynamics calculations." *Journal of Applied Physics* 61.5 (1987): 1816-1825.

[7]   Murr, L.E., Meyers, M.A., Shock-induced deformation twinning in tantalum, Acta Materialia 45 (1) (1997) 157–175.

[8]   Thermally Activated Deformation of Metals. Conrad. *Journal of Metals*. 1964. pg 582-588

[9]   J. Johnson and D. Tonks, "Dynamic Plasticity in Transition from Thermal Activation to Viscous Drag," 1991, APS Topical Conference on the Shock Compression of Condensed Matter.

[10]   Handbook of Materials behavior Models. Section 5. Physically based Rate- and Temperature-Dependent Constitutive Models for Metals, Nemat-Nasser. 2001. pg 387-397.

[11]   High strain-rate response of commercially pure vanadium. Nemat-Nasser, Guo. *Mechanics of Materials*. 32 (2000) pp. 243-260.

[12]   Modelling plastic deformation in BCC metals: dynamic recovery and cell formation effects. E.I. Galindo-Nava, P.E.J. Rivera-Díaz-del-Castillo. *Material Science and Engineering A*. Vo. 558, No. 15. (2012) pp. 641-648.

[13]   Lindley, T.C., The effect of a prestrain on the low temperature mechanical properties of a low carbon steel, Acta Metallurgica. 13 (1965) 681-689.

[14]   Biggs, W.D., Pratt, P.L., The Deformation and Fracture of Alpha-Iron at Low Temperatures, Acta Metallurgica 6 (1958) 694-703.

[15]   Rosenfield, A.R., Averbach, B.L., Cohen, M., Twinning Occurrence in Iron Single Crystals, Acta Metallurgica. 11 (1963) 1100-1101

[16]   Churchman, A.T., Cottrell, A.H., Yield Phenomenon and Twinning in α-Iron, Nature 1951

[17]   Visser, W., and H. Ghonem. "Twin nucleation in cold rolled low carbon steel subjected to plate impacts." *Materials Science and Engineering: A* 687 (2017): 28-38.

[18]   Mahajan, S., Bartlett, A.F., Influence of Prior Mechanical and Thermal Treatments on Shock Induced Substructures in Molybdenum, Acta Metallurgica. 19 (1971) 1111-1119.

[19]   Visser, William. *High Strain Rate Deformation Mechanisms of Body Centered Cubic Materials Subject to Impact Loading*. PhD Thesis. University of Rhode Island, 2017.

[20]   D. Firrao, P. Matteis, G. Scavino, G. Ubertalli, M.G. Ienco, G. Pellati, P. Piccardo, M.R. Pinasco, E. Stagno, R. Montanari, M.E. Tata, G. Brandimarte, S. Petralia. "Mechanical twins in 304 stainless steel after small-charge explosions." *Materials Science and Engineering*. A 424 (2006) 23-32.

[21]   L.M. Dougherty, E.K. Cerreta, E.A. Pfeif, C. Trujillo, G.T. Gray. "The impact of peak shock stress on the microstructure and shear behavior of 1018 steel." *Acta Materialia* 55 (2007) 6356-6364.

[22]   Ferreira, P.J., Vander Sande, J.B., Amaral Fortes, M., Kyrolainen, A., Microstructure Deveolopment during High-Velocity Deformation, Metallurgical and Materials Transactions. A 35A (2004) 3091-3101.

[23]   Mahajan, S., Effects of Existing Substructure on Shock-Twinning Behavior of Iron, Physica Status Solidi. Vol 2, Issue 2, (1970) 217-223.

[24]   Ganin, E., Y. Komem, and A. Rosen. "Shock induced hardness in α-iron." *Materials Science and Engineering* 33.1 (1978): 1-4.

[25]   Zhang, Jiayong, et al. "Twin Boundaries merely as Intrinsically Kinematic Barriers for Screw Dislocation Motion in FCC Metals." *Scientific reports* 6 (2016).

[26] Ezaz, Tawhid, Michael D. Sangid, and Huseyin Sehitoglu. "Energy barriers associated with slip–twin interactions." *Philosophical Magazine* 91.10 (2011): 1464-1488.

[27] Ezaz, Tawhid. *An advanced perspective on twin growth in Nickel-Titanium.* University of Illinois at Urbana-Champaign, 2011.

[28] Gao, C. Y., and L. C. Zhang. "Constitutive modelling of plasticity of fcc metals under extremely high strain rates." *International Journal of Plasticity* 32 (2012): 121-133.

[29] Saxl, I. "The incorporation of slip dislocations in twins." *Czechoslovak Journal of Physics* 18.1 (1968): 39-49.

[30] Sleeswyk, A. W., and C. A. Verbraak. "Incorporation of slip dislocations in mechanical twins—I." *Acta metallurgica* 9.10 (1961): 917-927.

[31] Shen, Y. F., et al. "Tensile properties of copper with nano-scale twins." *Scripta Materialia* 52.10 (2005): 989-994.

[32] Sainath, G., and B. K. Choudhary. "Deformation behaviour of body centered cubic iron nanopillars containing coherent twin boundaries." *Philosophical Magazine* 96.32-34 (2016): 3502-3523.

[33] Mrovec, Matous, Christian Elsaesser, and Peter Gumbsch. "Interactions between lattice dislocations and twin boundaries in tungsten: a comparative atomistic simulation study." *Philosophical Magazine* 89.34-36 (2009): 3179-3194.

[34] Nilles, J. L., and D. L. Olson. "Energy of a bcc Iron Deformation Twin Boundary." *Journal of Applied Physics* 41.2 (1970): 531-532.

[35]   Shibuta, Yasushi, Shinya Takamoto, and Toshio Suzuki. "A molecular dynamics study of the energy and structure of the symmetric tilt boundary of iron." *ISIJ international* 48.11 (2008): 1582-1591.

[36]   Mahajan, S. "Shock-Induced Substructural Changes in Prestrained Iron." *physica status solidi (b)* 33.1 (1969): 291-299.

[37]   Lan, Y., H. J. Klaar, and W. Dahl. "Evolution of dislocation structures and deformation behavior of iron at different temperatures: Part I. strain hardening curves and cellular structure." *Metallurgical and Materials Transactions A* 23.2 (1992): 537-544.

[38]   Steinmetz, David R., et al. "Revealing the strain-hardening behavior of twinning-induced plasticity steels: Theory, simulations, experiments." *Acta Materialia* 61.2 (2013): 494-510.

[39]   Mompiou, Frédéric, et al. "In situ TEM study of twin boundary migration in sub-micron Be fibers." *Acta Materialia* 96 (2015): 57-65.

[40]   Gray, George T., and Kenneth S. Vecchio. "Influence of peak pressure and temperature on the structure/property response of shock-loaded Ta and Ta-10W." *Metallurgical and Materials Transactions A* 26.10 (1995): 2555-2563.

[41]   Lee, Woei-Shyan, et al. "Effects of prestrain on high temperature impact properties of 304L stainless steel." *Journal of Materials Research* 25.4 (2010): 754-763.

[42]   Tang, Meijie, and Jaime Marian. "Temperature and high strain rate dependence of tensile deformation behavior in single-crystal iron from dislocation dynamics simulations." *Acta Materialia* 70 (2014): 123-129.

[43]   Park, H., et al. *EXPERIMENTAL TESTS OF VANADIUM STRENGTH MODELS AT HIGH PRESSURES AND STRAIN RATES*. No. LLNL-PROC-431291. Lawrence Livermore National Laboratory (LLNL), Livermore, CA, 2010.

[44]   G. Taylor, "The Mechanism of Plastic Deformation of Crystals. Part I. - Theoretical," *Proceedings of the Royal Society of LondonL Series A,* pp. 362-387, 1934.

[45]   Allen, G. A. "The activation energies of chromium, iron and nickel in gallium arsenide." *Journal of Physics D: Applied Physics* 1.5 (1968): 593.

[46]   Conrad, H., Christ, B., Variation of Dislocation Density and Stored Energy with Grain Size, Commander Space Systems Division, United States Air Force. 1963

[47]   Voyiadjis, George Z., and Farid H. Abed. "Effect of dislocation density evolution on the thermomechanical response of metals with different crystal structures at low and high strain rates and temperatures." *Archives of Mechanics* 57.4 (2005): 299-343.

[48]   Direct measurement of isothermal flow stress of metals at elevated temperatures and high strain rates with application to Ta and Ta-W alloys. S. Nemat-Nasser, J.B. Isaacs. *Acta Metallurgica*. Vol. 45, No. 3. (1997) pp. 907-919.

[49]   Flow stress of FCC polycrystals with application to OFHC Cu. S. Nemat-Nasser, Y. Li. *Acta Mater*. Vol 46, No. 2. (1998) pp. 565-577.

[50]   Shetty, M. N. *Dislocations and mechanical behaviour of materials*. PHI
        Learning Pvt. Ltd., 2013.

[51]   J. Gilman. The Limiting Speeds of Dislocations. Metall. Mater. Trans A. 31.
        (2000) 811.

[52]   Ramberg, Walter, and William R. Osgood. "Description of stress-strain curves
        by three parameters." (1943).

[53]   Morris, Charles E. "Shock-wave equation-of-state studies at Los Alamos."
        Shock Waves 1.3 (1991): 213-222.

CHAPTER 6

MAJOR CONCLUSIONS AND FUTURE RECOMMENDATIONS

6.1.   Major Conclusions

The overall goal of this dissertation is to investigate the deformation response of A572 grade 50 steel when subjected to impact loading. The goal of this work has been achieved by performing experimental, analytical and numerical research in three integrated tasks. These tasks are carried out through experimental, analytical and numerical research in order to achieve the goal of this research. The first is to determine the relationship between the evolution of deformation twins and the impact pressure. Secondly, a stress criterion for twin nucleation during high strain rate loading is developed which can account for the strain history or initial dislocation density. Lastly, a method is applied for separating the effects of dislocations and twins generated by shock loading in order to determine their role in controlling the flow stress of the material. The major conclusions of this dissertation are listed below.

1. A direct and unique relationship between impact stress and volume fraction of twins has been experimentally established.

2. Microscopic observation of impact specimens indicate that slip and mechanical twinning are two competing deformation mechanisms occurring during high rate loading of low carbon steel. The lenticular shape of the twins indicates that the twin formation mechanism is by progressive shear of the parent lattice. As impact

stress increases, another twinning plane becomes active, and results in large amounts of intergranular twin-twin interactions.

3. Based on microscopic observations, an analytical twinning model aiming at predicting twin volume fraction incorporating both slip and twinning mechanisms has been applied and shown to accurately calculate twin volume fraction. This model was coupled with a rate dependent model implemented into numerical procedures and was capable of capturing deformation response and twin formation during impacts for the given stress range.

4. Quantitative analysis of the post-impact stress-strain curves clearly shows an increase in both yield and ultimate strength, which indicates an increase in stored dislocations in the microstructure as a result of impact loading. However, while the yield and UTS both benefit from shock loading, the available strain energy is drastically reduced; up to 87%. If this trend is extrapolated further, it will show that the yield and ultimate tensile strength converge, thus eliminating available energy.

5. It is apparent that as the shock loading is increased, new twinning planes are activated. Qualitative analysis provides insight into the dislocation-twinning interaction during plastic deformation. Low impacted specimens reveal small fluctuations in stress-strain response representing that of type-B serrations. At higher impact levels, the presence of multiple twinning planes and twin-twin interactions results in the transition of type-B serrations to type-C load drops during plastic deformation. This suggests that twin-twin interactions play a

significant role in controlling plastic deformation, which is responsible for instability within the microstructure.

6. The twins play an important role in the direction of cracking during failure. They provide new interfaces at which cracks may initiate and propagate, and also control the direction of crack propagation.

7. Using a single stage light gas gun, deformation mechanisms in low carbon steel specimens subjected to plate impacts have been examined in as-received, hot rolled steel. It is observed that under this type of loading, twins are a contributing deformation mechanism and twin volume fraction exponentially increases with the impact pressure. The twin volume fraction was measured using standard point count method, the maximum of which was 16% occurring with an impact pressure of approximately 14 GPa.

8. High strain rate deformation mechanisms were examined in the same steel in pre-strained conditions. Pre-straining was completed using low strain rate, cold rolling procedures to strains of 1%, 3% and 20%. Impact loading was performed on specimens in the same direction as the pre-straining. It has been shown that the twin nucleation stress is proportional to the level of pre-strain. This has been explained in terms the dislocation network, density and configuration within the steel as modified by cold rolling prior to impact loading. A 1% pre-straining, has raised the threshold pressure for the onset of twin nucleation to 11 GPa.

9. Twin formation during high strain rate loading and/or low temperature loading was described based on a progressive shear of atoms rather than a local shuffle concept. This occurs by a shift of atoms on the {112} planes in the $\langle 111 \rangle$ direction by a

displacement 1/3 burgers vector for BCC metals. A minimum of 3 {112} layers is required to form a stable twin for compatibility across the twin habit plane. It is assumed that at these loading conditions, the strain rate of the material is controlled by the velocity of preexisting perfect dislocations and by the generation of partial dislocations. The nucleation of partial dislocations is preferential at high applied stresses due to a lower free energy of nucleation at high strain rates and low temperatures. Furthermore, the partial dislocations are more operative at these conditions due to their higher jump frequency. These partial dislocations, if formed on successive planes, are responsible for the formation of the deformation twins.

10. An explicit form of the critical twin nucleation stress has been developed based on strain rate accommodation by perfect dislocations and partial dislocations. The form of the equation considers the velocity of perfect dislocations and the generation rate of partial dislocations utilizing Gilman's limiting dislocation velocity equation and the Orowan strain rate relation.

11. Parameters for the critical twin nucleation stress in as-received steel and 1% pre-strained steel have been determined through plate impact tests and low temperature SHPB compression tests. The SHPB compression tests were carried out at liquid nitrogen temperatures. Under this type of loading, the thermal activation of dislocations is lowered, thereby increasing the threshold stress for perfect dislocation slip to a level higher than that for twin nucleation. At this low temperature condition, deformation twins are present at strain rates lower than that

encountered in room temperature plate impact tests. As such, SHPB compression tests can be used to correlate strain rate and twin nucleation stress.

12. Observation of nonparallel and intersecting twins in grains led to a modification of a model originally presented by Johnson and Rohde. By assuming that deformation twinning is occurring primarily on {112} <111> systems, the applied stress was resolved on multiple planes. These stress components were then applied to separate twin growth equations to account for the multiple twin systems.

13. The shock loaded specimens as well as ones with no prior shock loading were subjected to dynamic compression tests at temperatures in the range 293K to 923K at strain rates between $1E+3$ s^{-1} and $5E+3$ s^{-1}. The resulting stress-strain curves were partitioned into thermal and athermal stress components using thermal activation concepts based on dislocations interactions with thermal and athermal stress barriers

14. The stress-strain curves of the pre-strained and impacted steel adjusted to the effective strain, the flow stress exhibit similarity to that of the non-impacted specimens. This indicates that the defect generation and storage mechanisms of the pre-strained steel during shock loading are similar to those created when deforming the material continuously at a lower rate. However, the microstructure of the as-received and shock loaded material which included deformation twins showed flow stress higher than that of the as-received material.

15. A constitutive model based on thermally activated dislocation interaction with barriers is applied to partition the dynamic flow stress into thermal and athermal components. Results of this work show that the thermal stress component of both

the as-received and pre-strained materials is insensitive to the corresponding impact strain history. The athermal stress component for the as-received specimens which have been previously shock loaded is shown to be proportional to the loading pressure while for specimens which have been pre-strained before shock loading, the athermal stress displayed a constant value at all impact loads. This difference in athermal stress between as received and pre-strained materials is explained in terms of the deformation twin volume fraction existed in the microstructure.

16. The developed flow stress formulations which expresses the athermal stress component as an explicit function of the twin volume fraction, have been applied to predict the flow stress in materials that have been independently impacted at 3.7GPa, 7GPa and 13GPa. Results of this application were compared with those generated experimentally indicating validity of concepts and formulations presented in this work.

6.2. **Future Recommendations**

The selection of the material for this research was dictated by the broader scope of a funded research program to study shock loading of civil structures. Structural steel is used extensively as the reinforcing phase of these structures. For this purpose the material used in this study was selected as A572 grade 50 low carbon steel, which has a primarily α-ferrite BCC structure, with dispersed grains of pearlite. The particular steel specimens used in this study were taken from the web section of a single, hot rolled I-

Beam. Shock loading and dynamic compression tests of the material in the as-received and pre-strained conditions were completed as an integral part of this study. For carrying out this research, a light gas gun, described in Chapters 3-5, and an SHPB, described in Chapters 4 and 5 were used to generate basic knowledge of the role of planar impacts on, i) the deformation mechanism as a function of impact pressure (Chapter 3), ii) the critical twin nucleation stress as a function of impact and strain history (Chapter 4), and iii) the shock induced microstructure features effect on the dynamic flow stress (Chapter 5). Results of these studies allude to a set of recommendations for future research. These are divided into recommendations pertaining to the test material and those relating to the experimental procedures.

6.2.1.   **Material Recommendations**

Results of the current study focusing on the impact related deformation mechanisms showed that twinning is an important factor in controlling deformation at high strain rates. A limitation, however, was clear in the relatively low number of twins generated in this material for the tested shock loading range. Increasing the twin volume fraction would enhance and thus notably differentiate the material response under different impact loads. This limitation, as discussed in Chapter 1, is due to the nature of stacking faults in the BBC structure, where a material with a lower stacking fault energy would have a higher tendency to twin due to the difficulty of cross slip and climb and the formation of partial dislocations. In order to further explore the outcome of the study in relation to the separate contributions of twin volume fraction and dislocation density, it is recommended

to select a material in which mechanical twinning dominates the deformation process and as such, would result in either a higher volume fraction of deformation twins, such as in the FCC structures of silver or copper, or would have a more pronounced influence on accompanying dislocations, such as in HCP crystals which have limited slip systems. Furthermore, the low carbon steel used in this study has a ferritic-pearlitic microstructure with the pearlite colonies occupying a 9% volume fraction, acting as a strengthening phase. The post impact stress-strain response therefore reflects the relative contribution of these two phases; pearlite and ferrite. No attempt was made in this work to assign an impact resistance role for each of the phases. Focusing on the structural steel, it is recommended to first use a material with a dominant α-ferrite phase, such as pure iron. Following this, an impact study could be conducted as a function of pearlite volume fraction. For structural steel this can be achieved by altering the carbon content, thereby changing the amount of pearlite formed. The work of Spirdione [1] and Maciejewski [2] showed that different heat treatment procedures can alter the pearlite volume fraction if the original chemical composition must be retained.

A third observation relating to the material used in this study deals with the initial microstructure. As mentioned above, the material was used in the as-received, hot rolled condition which results in a structure with residual stresses due to retained dislocations. This condition was used intentionally to study the shock loading effects on the commercially available steel. The preexisting dislocation network would contribute to the impact deformation response. An important recommendation in this regard is to set a consistent initial material condition that can be described as structures free of dislocation. This condition can be achieved by one of two routes. The first is a full annealing process

that requires heating the material above approximately 673°C, which corresponds to the eutectoid temperature, followed by a controlled cooling rate to allow the carbon to migrate and form pearlite colonies. In this process, recrystallization and grain growth take place, thus resulting in a stress free structure free of any extrinsic dislocations. The second approach to obtain a structure relatively free of dislocations by a stress relief annealing process at or below 640°C. In this approach dislocations are able to move resulting in dislocation annihilation or rearrangement into lower energy configurations, as discussed in Chapter 5.

6.2.2. **Experimental Recommendation**

As discussed in the previous chapters of the dissertation, experimental work has utilized a light gas gun to impact test specimens with shock loads up to 16 GPa at strain rates above 10^4 s⁻1. The outcome of these tests in the form of pressure versus particle velocity yields the Hugoniot curve for defining the locus of shock states. Results of the impact experiments using the gas gun point out to a set of recommendations described below.

With the design and operation of the single stage gas gun in the MMRL, there have been several design modifications throughout trial experiments in an effort to continually improve upon the operating procedures and experimental measurements. During plate impact experiments the projectile is held true and carried down the length of the barrel with by a disposable carrier called the sabot. This component, while sacrificial in nature, required several iterations before achieving a robust design that could withstand all

pressure levels while at the same time attempting to minimize weight, as discussed in Chapter 2. Aside from the weight, the main feature controlling consistency of velocity in this design is the tolerance between the barrel and the sabot body. During the machining process, the heat generated can affect the final diameter of the sabot, and result in a loose or tight fit, causing lower and unpredictable velocities. Others have utilized O-rings to create a seal in the barrel [3] however this still relies on holding tight tolerances within the O-ring grooves. In this regard a recommendation can be made to utilize plastic piston rings which would eliminate the diameter as being the critical factor in determining the fit in the barrel. This ring acts as a spring seal which can expand or contract against the barrel wall with a constant pressure fit. The sealing against the barrel occurs on the edge of the piston ring, and seals against the sabot between the face of the piston ring and the edge of the groove machined into the sabot as shown in Figure 6-1.
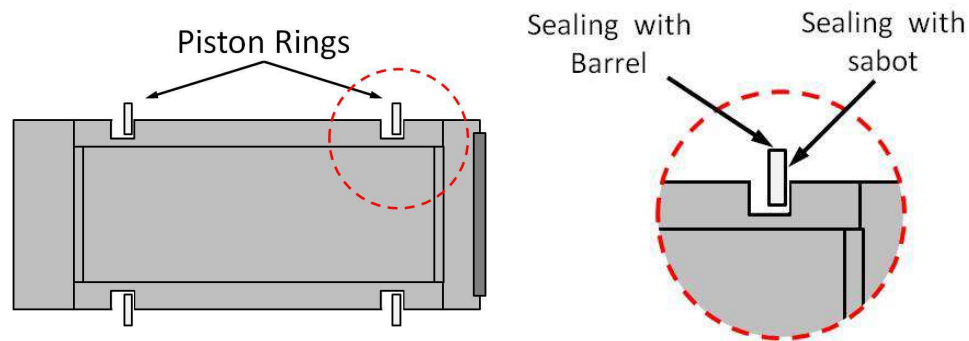
Figure 6-1: Recommended sabot design configuration with piston rings for better pressure seal.

The second future recommendation for plate impact testing is in regards to target configuration. Wave propagation occurring during a planar plate impact test can cause complex wave reflections from free surfaces, edges, and corners that may affect the area

300

of the material to be investigated. Following the work by Bourne [4], Gray [5], and
Lassila [6], the use of radial momentum ring to trap the radial waves and prevent
reflection back into the center of the specimen should be employed. Also, as described
by Gray [7] and Lassila [6], a cover plate can be utilized to retain a good surface finish of
the specimen in order to minimize material loss due to localized surface heating effects.
A detailed configuration of the suggested setup is shown in the work of Vignjevic et al.
[8] which includes the cover plate, radial momentum rings, and backing plates and is
shown here in Figure 6-2.
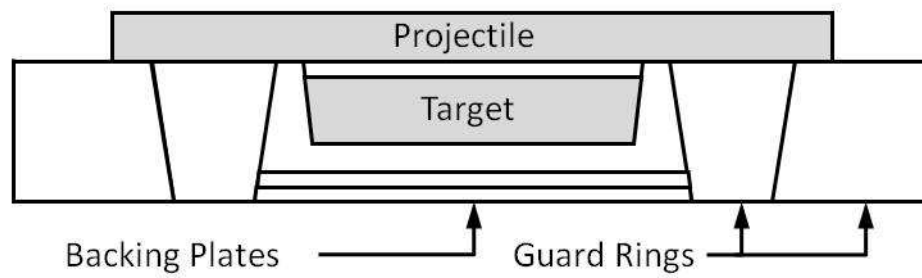
Figure 6-2 :Recommendation for a target configuration as suggested by Vignjevic et al.
[6] for eliminating radial reflections and ensuring a 1D state of strain.

The third future recommendation regarding plate impact testing is in regards to the
velocity measurement system. The current system utilizes a set of culminated lasers
aimed perpendicular to the barrel just prior to the target. The light from the lasers are
captured in a set of high speed photo detectors via fiber optic cables and voltages are
recorded using the oscilloscope. This system is also used to trigger the oscilloscope and
stress gauge power supply. Since the lasers are mounted directly to the barrel/target
fixture to ensure a perpendicular mounting configuration, every experiment requires
realignment due to the vibrations caused by the rupture discs bursting and impact of the

target specimen. A better isolation system of the lasers should be looked into or another velocity measurement method could be used. One such method could include high speed pressure transducers mounted at specified distances down the length of the barrel, measuring the pressure behind the projectile as it passes the transducer. This type of system would eliminate alignment procedures and would not be affected by vibrations and could also be used to measure projectile acceleration.

6.3. **References**

[1] Spirdione, Justin. "Microstructure-dependent dynamic flow stress in metallic alloys." (2015).

[2] Maciejewski, Kimberly. "The role of microstructure on deformation and damage mechanisms in a Ni-based superalloy at elevated temperatures." (2013).

[3] Plume, Gifford. "Response of materials to various shock loading conditions generated by plate impact experiments." (2013).

[4] Bourne, N. K., W. H. Green, and D. P. Dandekar. "On the one-dimensional recovery and microstructural evaluation of shocked alumina." *Proceedings of the Royal Society of London A: Mathematical, Physical and Engineering Sciences*. Vol. 462. No. 2074. The Royal Society, 2006.

[5] Gray III, George T. "Shock recovery experiments: an assessment." *Shock compression of condensed matter* (1989): 407-414.

[6] Lassila, D. H., and G. T. GRAY III. "Effects of shock prestrain on the dynamic mechanical behavior of tantalum." *Le Journal de Physique IV* 1.C3 (1991): C3-19.

[7] Gray, George T., and Kenneth S. Vecchio. "Influence of peak pressure and temperature on the structure/property response of shock-loaded Ta and Ta-10W." *Metallurgical and Materials Transactions A* 26.10 (1995): 2555-2563.

[8] Vignjevic, Rade, et al. "Lagrangian analysis led design of a shock recovery plate impact experiment." *International Journal of Impact Engineering* 77 (2015): 16-29.

APPENDIX A

SINGLE STAGE LIGHT GAS GUN

A.1. **Testing Procedure**

The single stage light gas gun designed and built in the MMRL is a fairly simple machine to operate, however requires several preparation steps and delicate alignment procedures which are essential in order to achieve accurate results. The steps required to conduct a plate impact experiment using the single stage gas gun are outlined here.

1. Install rupture discs. As described in Chapter 2, the gas gun utilizes two sets of rupture discs to hold the pressure in the main chamber and secondary chamber and are used to launch the projectile. The pressure differential created by bleeding pressure from the secondary chamber is what causes the sequential breakage of the discs, allowing pressure to be applied behind the projectile and ultimately launching it down the length of the barrel. Several materials were considered for the rupture disc material, include premade aluminum rupture discs, including those made by BS&B systems, however the cost per disc outweighed the benefits of having prefabbed discs, and the discs are not stackable, meaning that the chamber pressures would be bound to specific increments set by the rupture discs available. The material used for the rupture discs in this gas gun are made of thin sheets of polyester material, commonly used as overhead projector transparencies. Each disc is approximately 0.004 in. thick and can be stacked together to achieve higher rupture pressures. Initial testing on the discs led to a rupture pressure per

sheet of approximately 100 psi, however at higher input pressures, bulging of the discs occurs and decreases the breaking pressure considerably. This led to a range of breaking pressure per disc of 70-100 psi, which accounts for the bulging or any imperfections in thickness or quality. Several trial runs have also led to the use of an additional rupture disc between the secondary and barrel section so that there is no premature firing using only the secondary chamber gas. When filling the system to the secondary chamber pressure, fill below the actual secondary chamber pressure desired (approximately 15 psi less). The bulge in the main disc caused by the increase in pressure of the main chamber will slightly increase the secondary chamber pressure.

For example, if the main chamber pressure is to be filled to 1700 psi, the secondary chamber should be filled to 850 psi for a difference in pressure of 850 psi, and a total of 14 discs are to be used between the main and secondary chambers (labeled Main Disc in Figure 2-14), and 15 discs between the secondary chamber and barrel section (labeled Secondary Disc in Figure 2-14). The minimum and maximum breaking pressures of the two sets of discs are shown in Table A- 1

Table A- 1: Break pressures for gas gun experiment using 14 and 15 rupture discs in the main and secondary chambers.

Chamber	Break Pressure per disc		# of Discs	Total Break Pressure	
Main	Min	70	14	Min	980
	Max	100		Max	1400
Secondary	Min	70	15	Min	1050
	Max	100		Max	1500

As shown in Table A- 1, the difference in pressure between the main and secondary chamber of 850 psi is below the minimum breaking pressure of both sets of rupture discs

and the main chamber input pressure of 1700 will be enough to exceed and break the discs once bleeding the secondary chamber pressure for firing the gun.

The polyester rupture discs are prepared using a hole punch to match the dimensions of the bolt hole patter of the secondary chamber as shown in Figure A-7. An example of the rupture discs is shown in Figure A- 1.
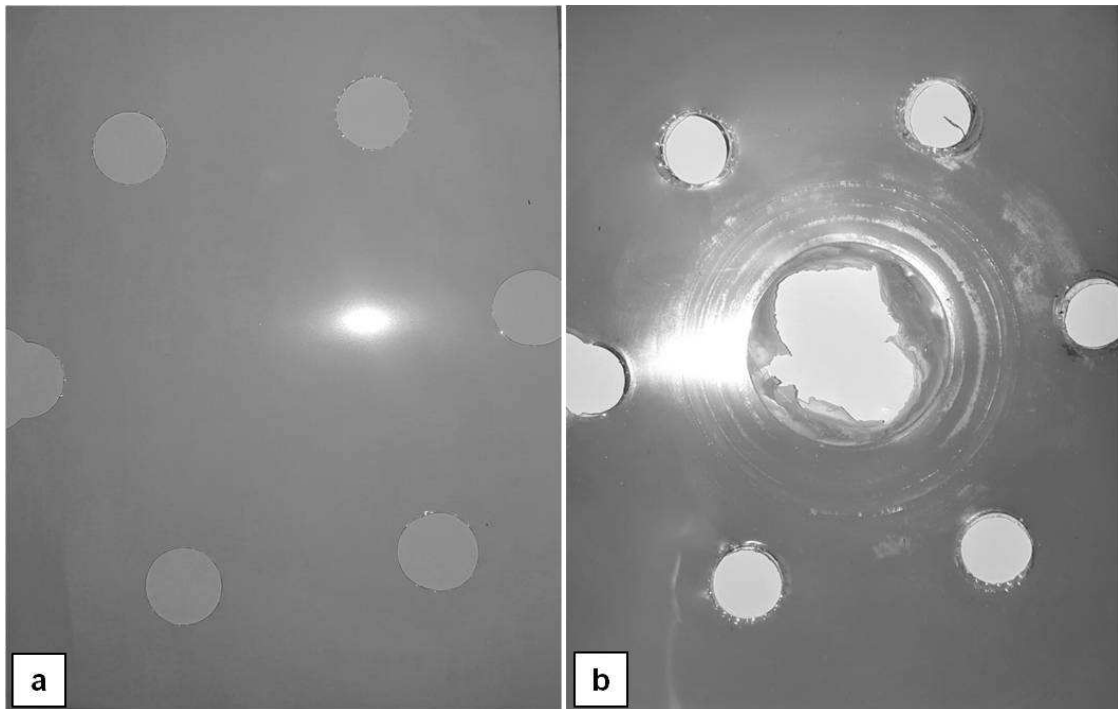
Figure A- 1:   a) Rupture disc with hole pattern punched b) rupture disc after an experiment.

After selecting a desired input pressure, the rupture discs should be placed between the secondary chamber and barrel section, and between the main chamber and secondary chamber, and all six bolts should be torqued to 400 ft-lb, as shown in Figure A- 2.
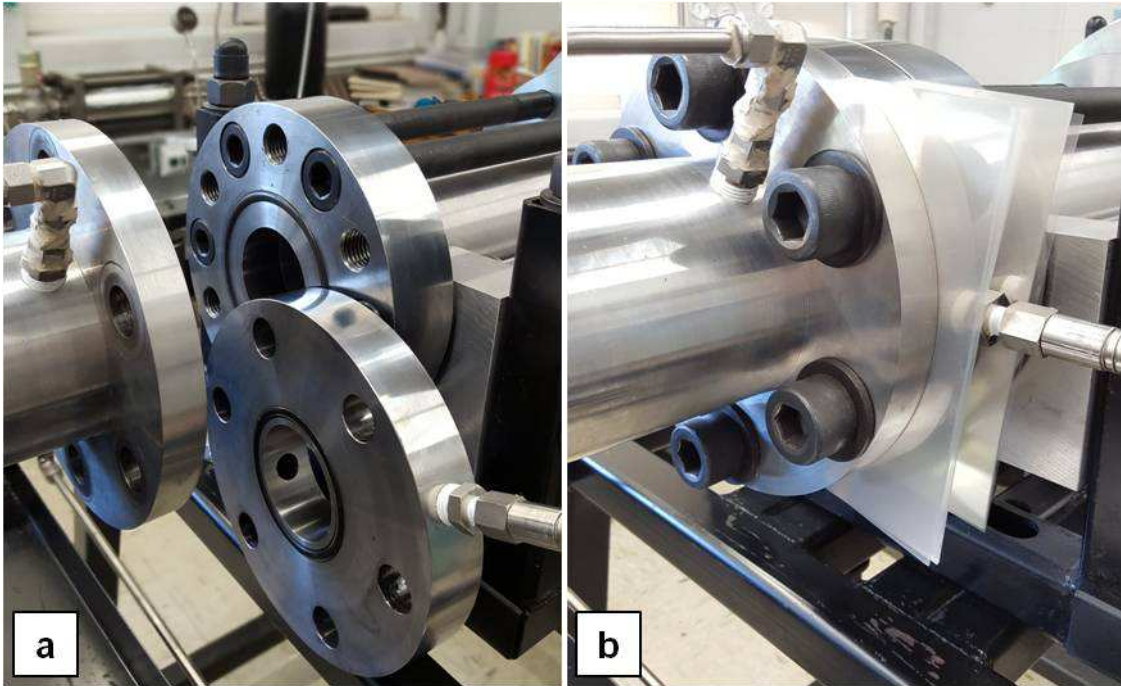
Figure A- 2: a) Barrel connector, secondary chamber, and main chamber separated for installing rupture discs. b) Rupture discs installed and sections bolted back together.

2. Load the projectile (Step 1 of 2). The projectile disc travels down the barrel with the help of a support carrier, called a sabot. The sabot is a sacrificial projectile which supports the actual projectile disc in order to keep the disc from tumbling or tilting as it is launched towards the target. The sabot design and dimensions are shown in Figure 2-32. When running a set of experiments, it is best to machine all sabots required for the test set at the same time in order to achieve consistent dimensions, and therefore predictable and consistent velocities. The projectile/sabot package needs to be loaded down the barrel prior to placing the target specimen in position. To do so, insert the sabot into the end of the barrel. Use a lubricant oil or light grease such as Vaseline to reduce friction and provide a better seal.

3. Mount the specimen. For planar plate impact loading tests, the target specimen is made up of two flat circular discs which have been surface ground to ensure all surfaces are planar. The two discs are used to sandwich the manganin stress gauge. The discs are bonded together using a two part epoxy and allowed to cure for a minimum of 48 hours. Prior to bonding the stress gauge, 6" leads are soldered to the exposed copper stress gauge tabs. These leads will connect to the pulse power supply via a 50Ω coaxial cable.

The specimen is held in place by three 3/8"-16 bolts as shown in Figure 2-33 and Figure 2-34. The impact face of the target creates a vacuum tight seal against the target mount/vacuum chamber using a -231 O-ring. These bolts only need to be finger tight, as using a wrench would break the bolts at the reduced area section.

4. Prior to connecting the stress gauge leads to the terminals, a resistance measurement of the gauge at the leads is needed. After measuring the gauge resistance, utilize an adjustable potentiometer (referred to as the "dummy gauge") to match the gauge resistance. (should be approximately 50Ω).
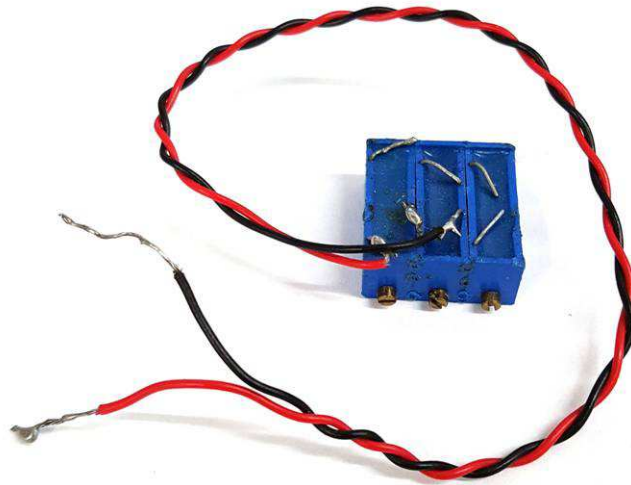
Figure A- 3: Simple in-house made dummy gauge made from three potentiometers wired in series.

Connect this dummy gauge to the terminals and measure the resistance at the BNC connector which directly attaches to the stress gauge power supply. This new resistance (including the gauge, leads, and full length of the BNC cable) will be used as the base gauge resistance in the stress calculation. The dummy gauge can now be excited using the power supply, and the power supply can be balanced. (Refer to Dynasen manual for balancing methods). After balancing the power supply, disconnect the dummy gauge, and connect the actual stress gauge leads. Recheck the gauge resistance at the end of the BNC cable to make sure the leads are not broken.

5. Laser Alignment. The laser alignment must be checked prior to experiments. Previous experiments may have knocked the lasers out of alignment, and adjustments may be required to achieve the best signal from the photo detectors. Lateral adjustments and tilt adjustments can be made using the adjustment screws on the laser blocks shown

in Figure 2-26. The laser blocks also include a culminating lens if the laser beam needs to be focused.

6. Ready the catch chamber. The clay catch box within the catch chamber should be repacked with high density clay. Once repacked, rotate the catch box so that the opening of the box faces the opening of the chamber, pointing towards the gas gun barrel. Ensure that the support rods are fully fixed to the mounts on the catch box. Close the catch chamber door and secure all four latches. Slide the catch chamber towards the gas gun and secure the catch chamber damper system on the gas gun frame using the side toggle clamps. Refer to Figure A- 4 for a visual of this step.
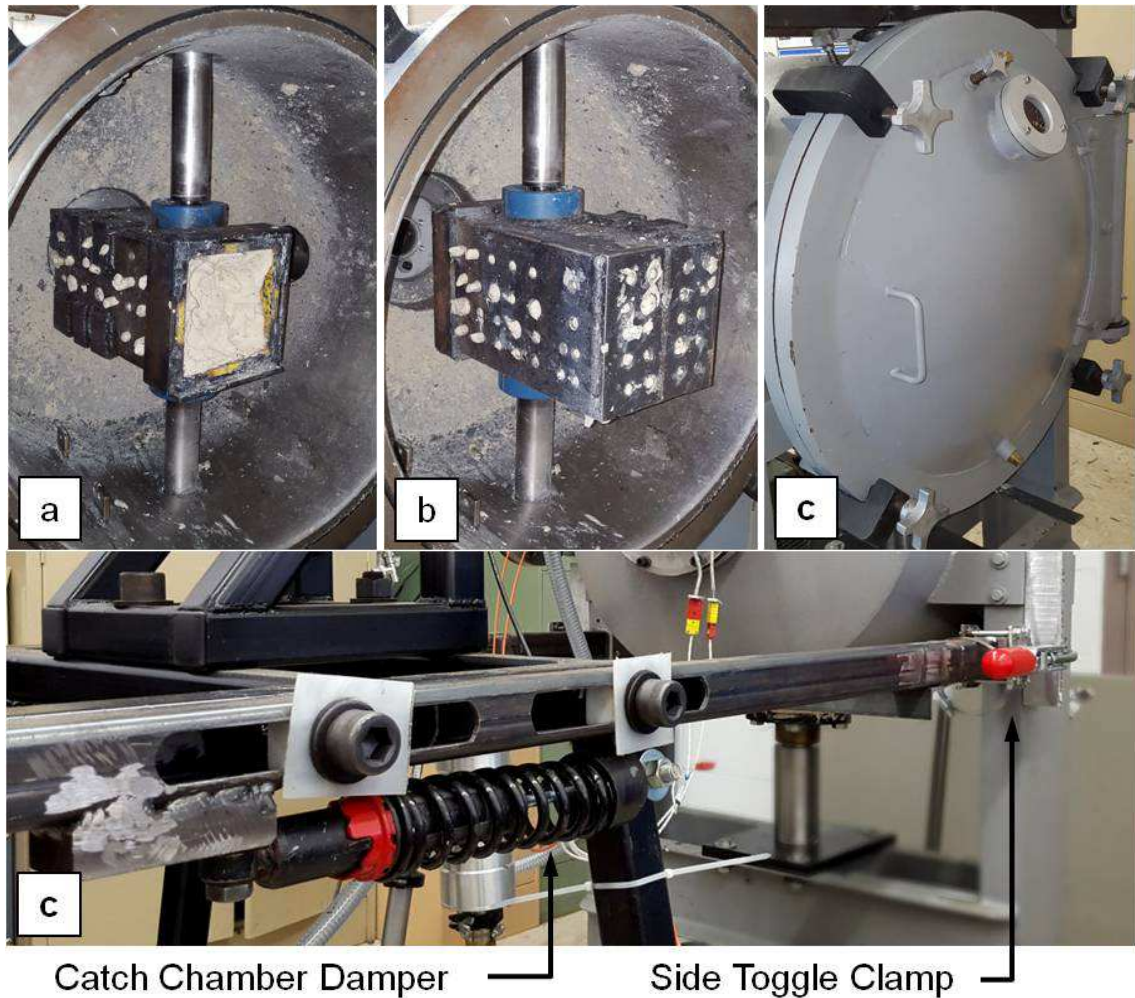
Figure A- 4: Specimen catch chamber

7. Loading the projectile (Step 2 of 2) The gas gun has two valves for controlling the vacuum, labeled "Vacuum Valve 1" and "Vacuum Valve 2" shown in Figure A- 5 and Figure A- 6. Both of these valves should be in the closed position (handle perpendicular to flow direction) prior to starting the vacuum pump. Turn the vacuum pump on. Once the vacuum pump is on, slowly open Vacuum Valve 1. This will create a vacuum behind the projectile, and pull the projectile down the length of the barrel in the ready position. A slight thud will occur which is the back of the projectile bottoming out at the end of the

barrel, and indicates that the projectile is in the correct position. At this point, Vacuum Valve 1 can be fully opened.
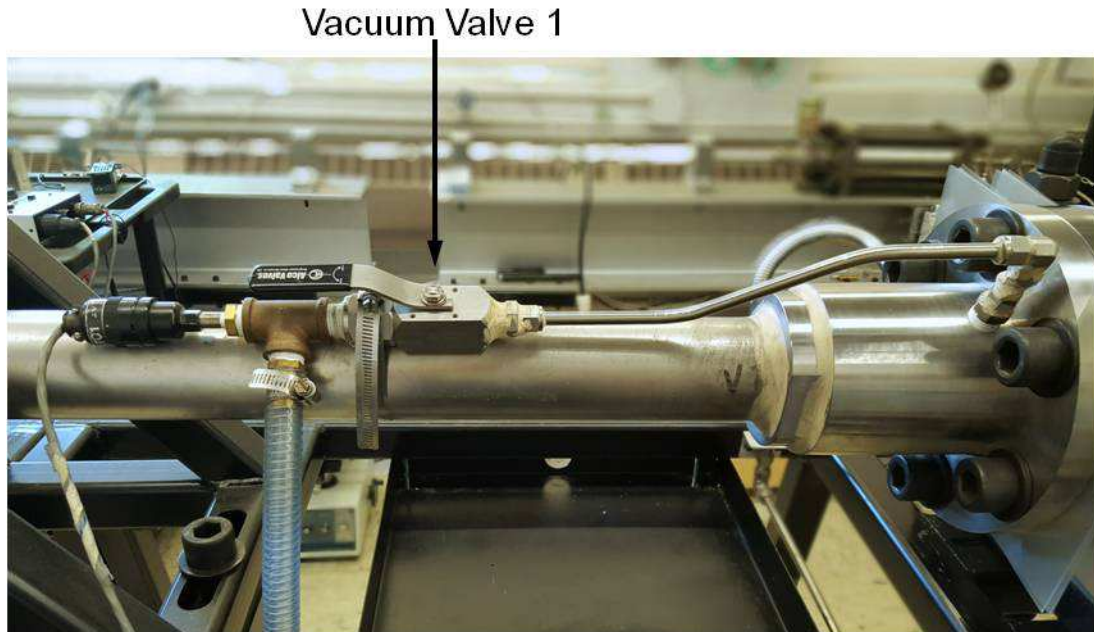
Figure A- 5: Vacuum valve 1 used for step 2 of loading the projectile.

8.   Evacuate target chamber. Once vacuum valve 1 is fully opened, slowly open Vacuum Valve 2. This will evacuate the volume between the projectile and the target. Allow sufficient time for a good vacuum to be drawn. During this time the chamber can be partially filled and the diagnostics can be set.

9. Put on ear and eye protection from this point forward.

Figure A- 6: Vacuum valve 2 used for evacuating the barrel and target fixture.

10. With the vacuum pump still running, the gas gun can be filled to the secondary chamber pressure. To do this, refer to Figure 2-12 and Figure 2-13. All valves should be in the initial position as listed here:

1. Gas cylinder valve- closed

2. Manifold tank valve 1, 2, and 3 - closed

3. Regulator - closed

4. Chamber fill valve - closed

5. Control panel valve 1 - open

6. Control panel valve 2 - closed

7. Control panel valve 3 -closed

8. Vacuum Valve 1 - open

9. Vacuum Valve 2 - open

To start the fill process, first open the valve on top of the gas cylinder. Second, open the Tank 1 valve on the manifold. Third, set the regulator to above the maximum pressure to be used for the current test. Now that the manifold and tank is all set, move over to the control panel. Turn the pressure gauges on to monitor the pressure in the main and secondary chambers. Begin filling the main and secondary chambers simultaneously by gradually opening the Fill valve. You should see the pressure increase equally for the main and secondary chambers. Fill until approximately 10-15 psi below the desired secondary chamber pressure and stop.

11. At this point, the chamber is partially filled. Close Vacuum Valve 2 first, and then Vacuum Valve 1, and turn off the vacuum pump.

12. Set the diagnostics. With the oscilloscope still in the run position, the signal from the lasers/photo detectors should still be at an acceptable level. Set the oscilloscope to "READY". Turn the "Power For Trigger Channel On Dynasen" switch to the "ON" position (refer to Figure 2-23). This will provide a 6V signal sent from the oscilloscope to the Dynasen power supply once the oscilloscope is trigger to record. Hit the "RESET" button on the Dynasen pulse power supply to ready. The instruments are now ready to record.

13. Back at the control panel, "Valve 1" can be closed. With "Valve 1" closed, the "Fill Valve" can be gradually opened again to slowly continue to fill the main chamber to the desired pressure level.

14. At this point all valves should be in the positions as listed here:

      1. Gas cylinder valve- open

      2. Manifold tank valve 1, 2, and 3 - open

3. Regulator - open

4. Chamber fill valve - closed

5. Control panel valve 1 - closed

6. Control panel valve 2 - closed

7. Control panel valve 3 -closed

8. Vacuum Valve 1 - closed

9. Vacuum Valve 2 - closed

15. To fire the gas gun, open "Valve 2" to depressurize the secondary chamber. Doing so will increase the pressure differential above the rupture pressure threshold across the main disc, and subsequently across the secondary disc.

16. After firing the gas gun, and before checking on the specimen and the oscilloscope recording, close the gas cylinder valve and bleed the remaining pressure from the lines by opening "Valve 3" and then opening the "Fill Valve". Once this is done, all pressure is out of the system and it is safe. Close the Tank 1 valve on the manifold, followed by turning off the regulator, then closing the "Fill Valve".

17. Data can be saved from the oscilloscope directly to an external flash drive. Since there is such a large quantity of data points, it is best to use the oscilloscopes "gating" function when saving data. Always check that the data was saved on the flash drive prior to clearing out the data on the oscilloscope.

A.2. Final Checklist for Gas Gun Operation

Insert rupture discs

Check laser alignment and adjust as necessary

Load projectile in end of barrel

Check O-ring at end of vacuum chamber

Mount target on target holder

Measure resistance of stress gauge

Measure resistance of stress gauge with BNC cable

Using the dummy gauge resistor, set equal to stress gauge resistance and balance the pulse power supply

Attach stress gauge leads to connections outside vacuum chamber

Clamp catch chamber to gas gun frame damper system

Make sure clay in catch box is re-packed and aligned with barrel and connecting rods are secure

Close catch chamber door and secure with the 4 clamps

Check that the laser block bolts are tight

Check that the fiber optic cables are tight

Double check the laser signals

Begin pumping vacuum behind projectile only to pull projectile fully into barrel

Begin pumping vacuum in vacuum chamber

Triple check laser signals

While still pumping vacuum, begin to fill both main and secondary chamber up to

secondary chamber pressure

Close vacuum valve in vacuum chamber

Close vacuum valve behind projectile

Turn off vacuum pump

Set oscilloscope to "single"

Turn power supply trigger switch "on"

Push power supply "reset" button

Ensure that the power supply "ready" light is on

Close equalization valve on pressure control panel

Continue to fill the main chamber only up to desired pressure

Open the fire valve on the pressure control panel

A.3. **Gas Gun Mechanical Drawings**

This appendix section contains all detailed drawings for the design of the single stage light gas gun in the MMRL facilities.

12.00 ±0.015

∅6.81 ±0.010

∅8.63 ±0.010

UNLESS OTHERWISE SPECIFIED:

DIMENSIONS ARE IN INCHES
TOLERANCES:
FRACTIONAL±
ANGULAR: MACH±   BEND ±
TWO PLACE DECIMAL ±
THREE PLACE DECIMAL ±

INTERPRET GEOMETRIC
TOLERANCING PER:

MATERIAL

FINISH

DO NOT SCALE DRAWING

NAME   DATE

DRAWN
CHECKED
ENG APPR.
MFG APPR.
Q.A.
COMMENTS:

TITLE:

NPS8_SCH160_12inch_july26

SIZE DWG. NO.   REV
A

SCALE: 1:8 WEIGHT: SHEET 1 OF 1

5   4   3   2   1

NEXT ASSY   USED ON

APPLICATION

PROPRIETARY AND CONFIDENTIAL

THE INFORMATION CONTAINED IN THIS
DRAWING IS THE SOLE PROPERTY OF
<INSERT COMPANY NAME HERE>. ANY
REPRODUCTION IN PART OR AS A WHOLE
WITHOUT THE WRITTEN PERMISSION OF
<INSERT COMPANY NAME HERE> IS
PROHIBITED.

Figure A- 7:   NPS8-SCH160, 17-4 stainless steel pipe used for the main pressure chamber body.
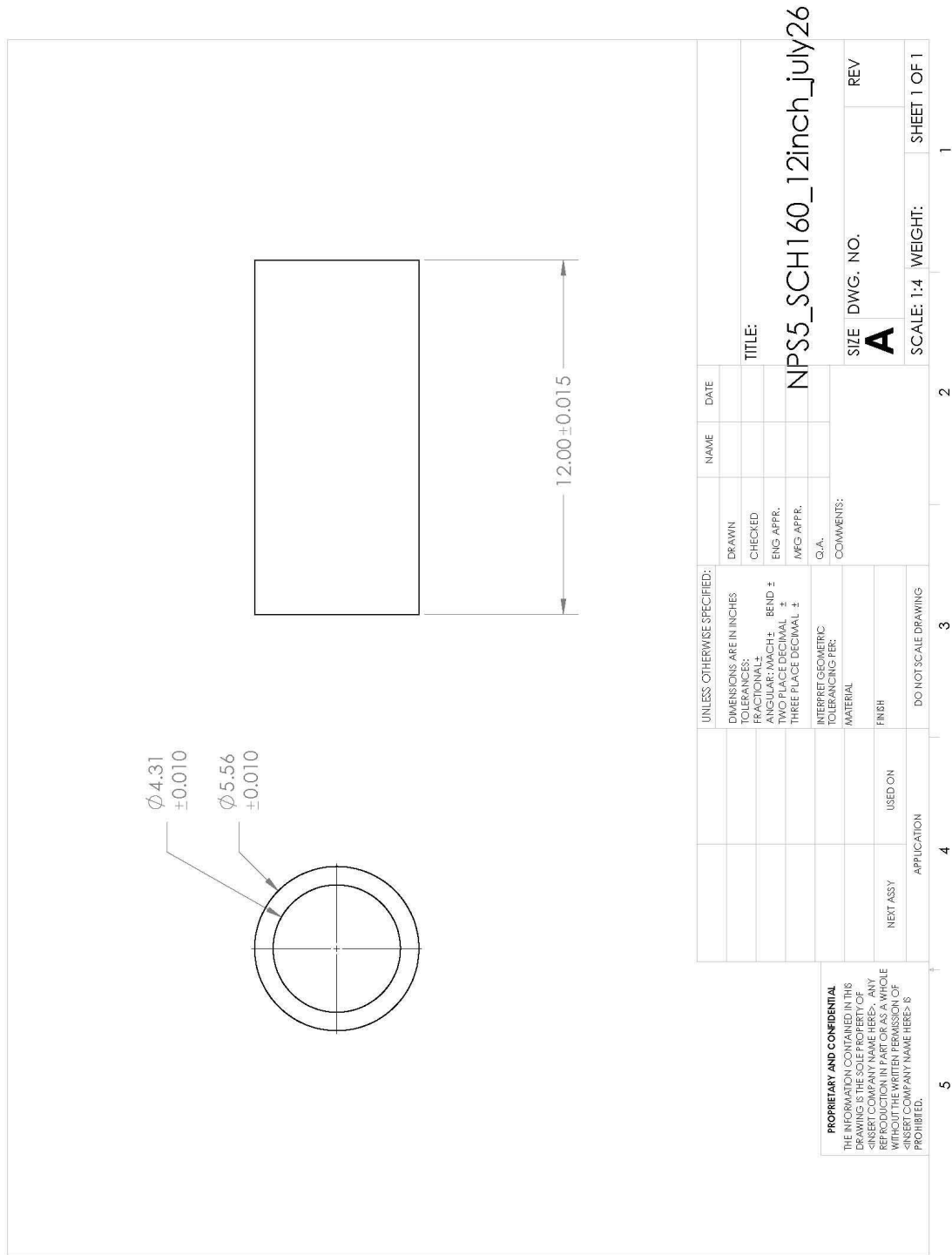
Figure A- 8: NPS5-SCH160, 17-4 stainless steel pipe used for the main pressure chamber body.
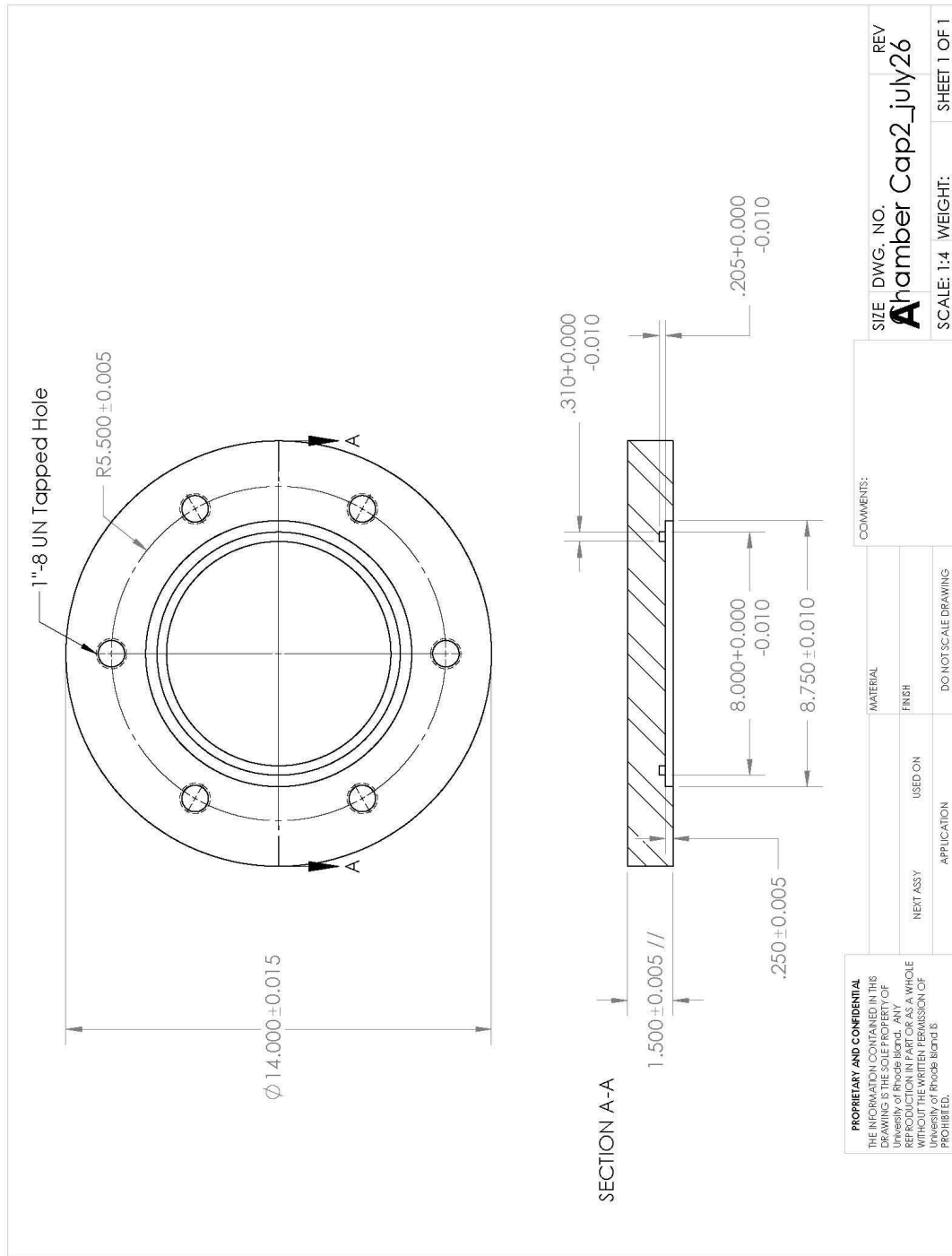
Figure A- 9: End cap of main pressure chamber to be bolted to the back of the NPS8 pipe. A taped hole at the center was added for filling the main chamber.

R5.500±0.005

1.032±0.005

Ø14.000±0.015

1.500±0.005 //

SECTION A-A

A

A

COMMENTS:

MATERIAL

FINISH

DO NOT SCALE DRAWING

USED ON

NEXT ASSY

APPLICATION

SIZE DWG. NO. REV

A hamber Cap july26

SCALE: 1:4 WEIGHT: SHEET 1 OF 1
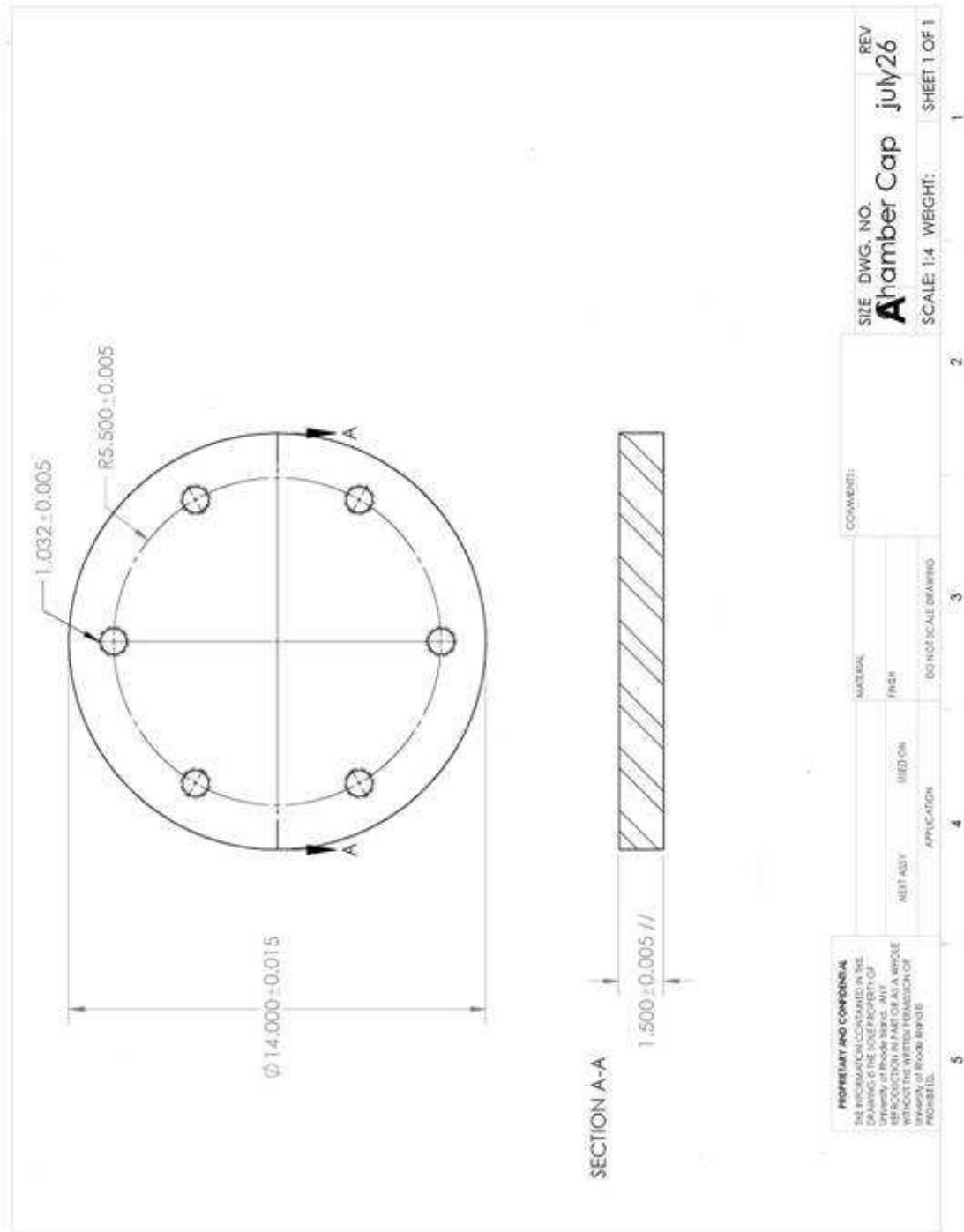
Figure A- 10: Additional end cap made of heat treated D2 tool steel. This additional end plate is held on with 1"-8 nuts on the same bolts used to attach the threaded back plate shown in Figure A- 9. This end cap reduces the deflection of the end plate which was resulting in gas leakage from the NPT tapped pressure fill line for the main chamber.

Figure A- 11: Tapered connector between the NPS8 pipe and the NPS5 pipe making up the main chamber.

Figure A- 12: Tapered connector between the main chamber (NPS5 pipe) and the first secondary chamber. Also serves as the interface for the first set of rupture discs.
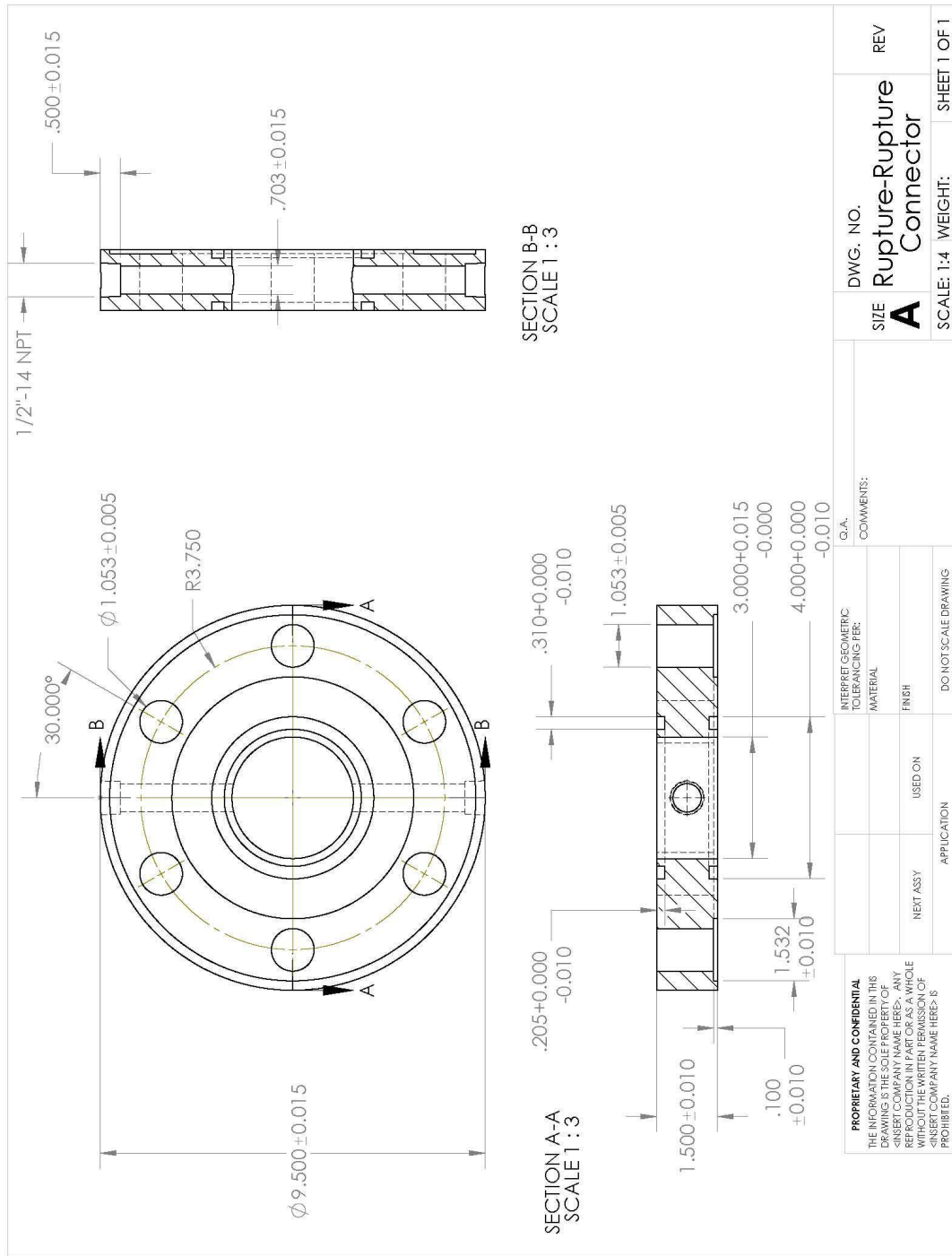
Figure A- 13: The secondary pressure chamber which is encapsulated by rupture discs on either side. This chamber also includes a fitting for the gas fill and a pressure dump valve.

Figure A- 14: Connector between the secondary chamber and the barrel section. Also serves as the interface for the second set of rupture discs. A tapped hole was added for drawing vacuum in the barrel section behind the projectile in order to load the projectile down the barrel.

3"-8 UN 2B

R2.250±0.050

4.000±0.015

1.000±0.050

COMMENTS:

MATERIAL

FINISH

DO NOT SCALE DRAWING

NEXT ASSY   USED ON

APPLICATION

SIZE DWG. NO.   REV
B   Barrel Nut1_july26

SCALE: 1:2   WEIGHT: SHEET 1 OF 1

Figure A- 15: Jam nut for barrel threads mounted in the Rupture-Barrel connector shown in Figure A- 14.

327

Figure A- 16:   Barrel section of gas gun mad of 316 stainless steel.   Both ends are threaded for mounting to the pressure chamber and to mount target and vacuum chamber. Inner barrel is 2" diameter and honed to a surface finish of 8Ra. Overall length is 10ft.
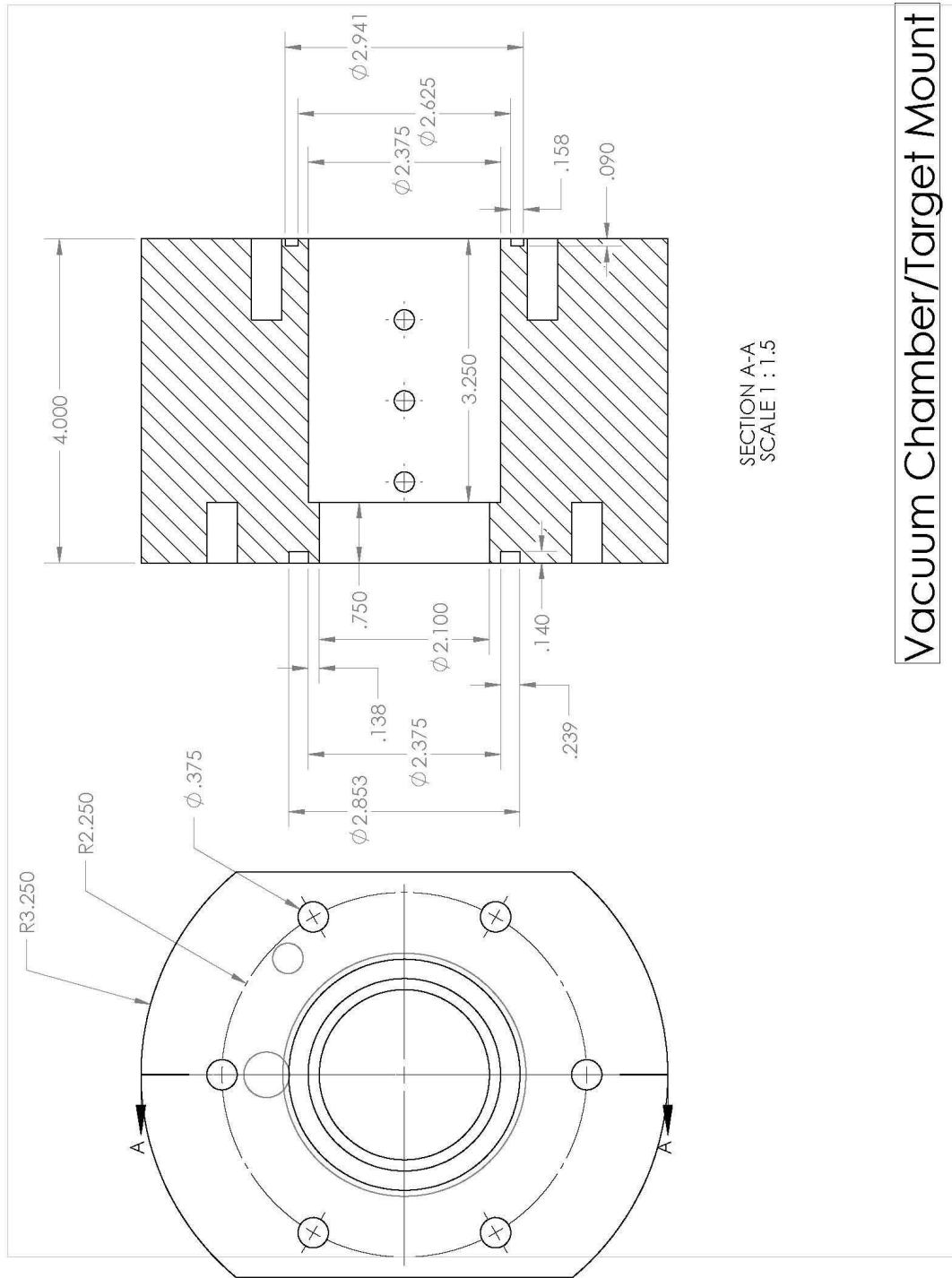
Figure A- 17: Vacuum chamber / Target fixture. This mounts to the end of the barrel and holds the target assembly. There are through ports for the laser and fiber optics to be mounted on each side.
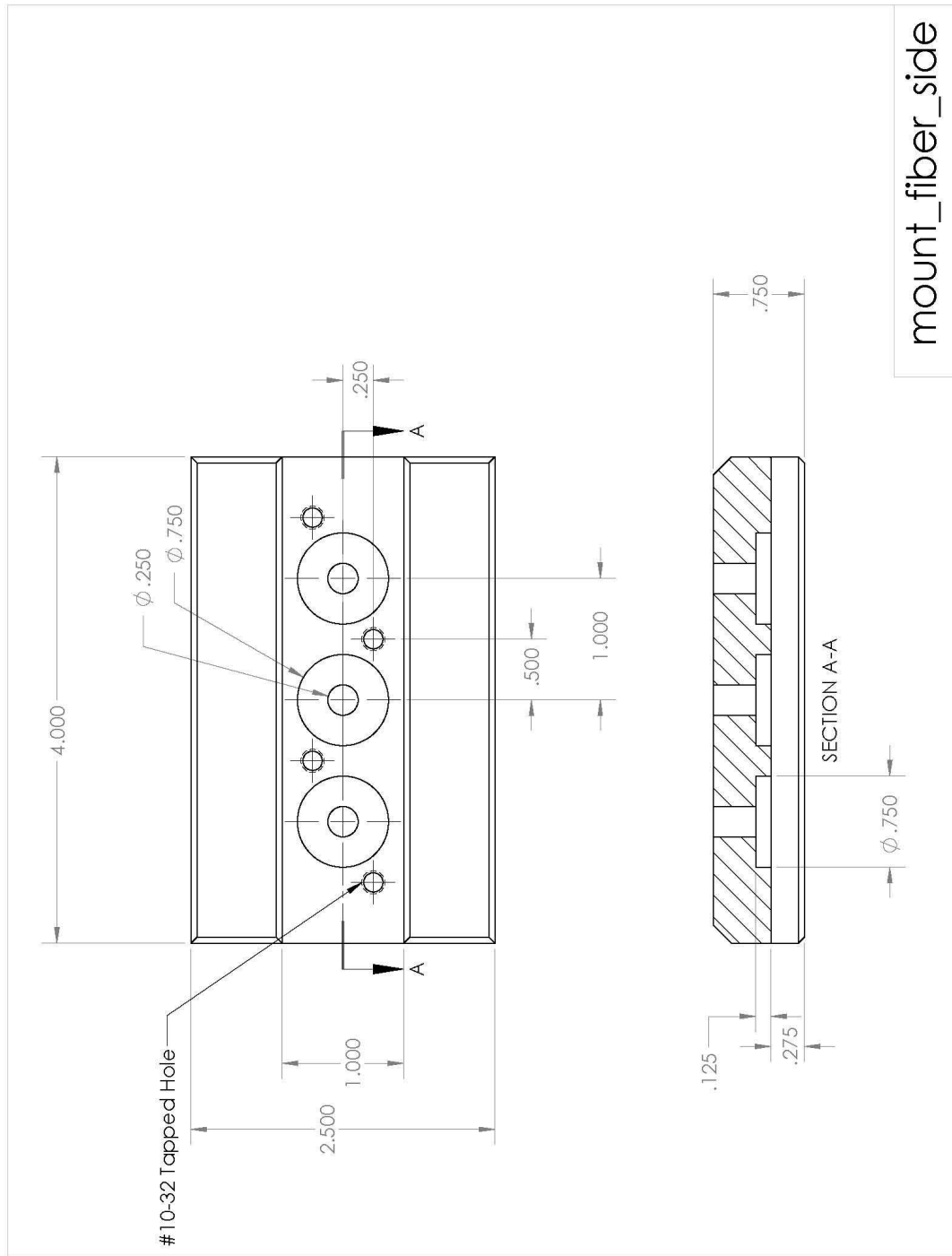
mount_fiber_side

Figure A- 18: Mount for vacuum tight optical through ports. This mount is bolted to the flat side of the vacuum chamber and contains polycarbonate windows.
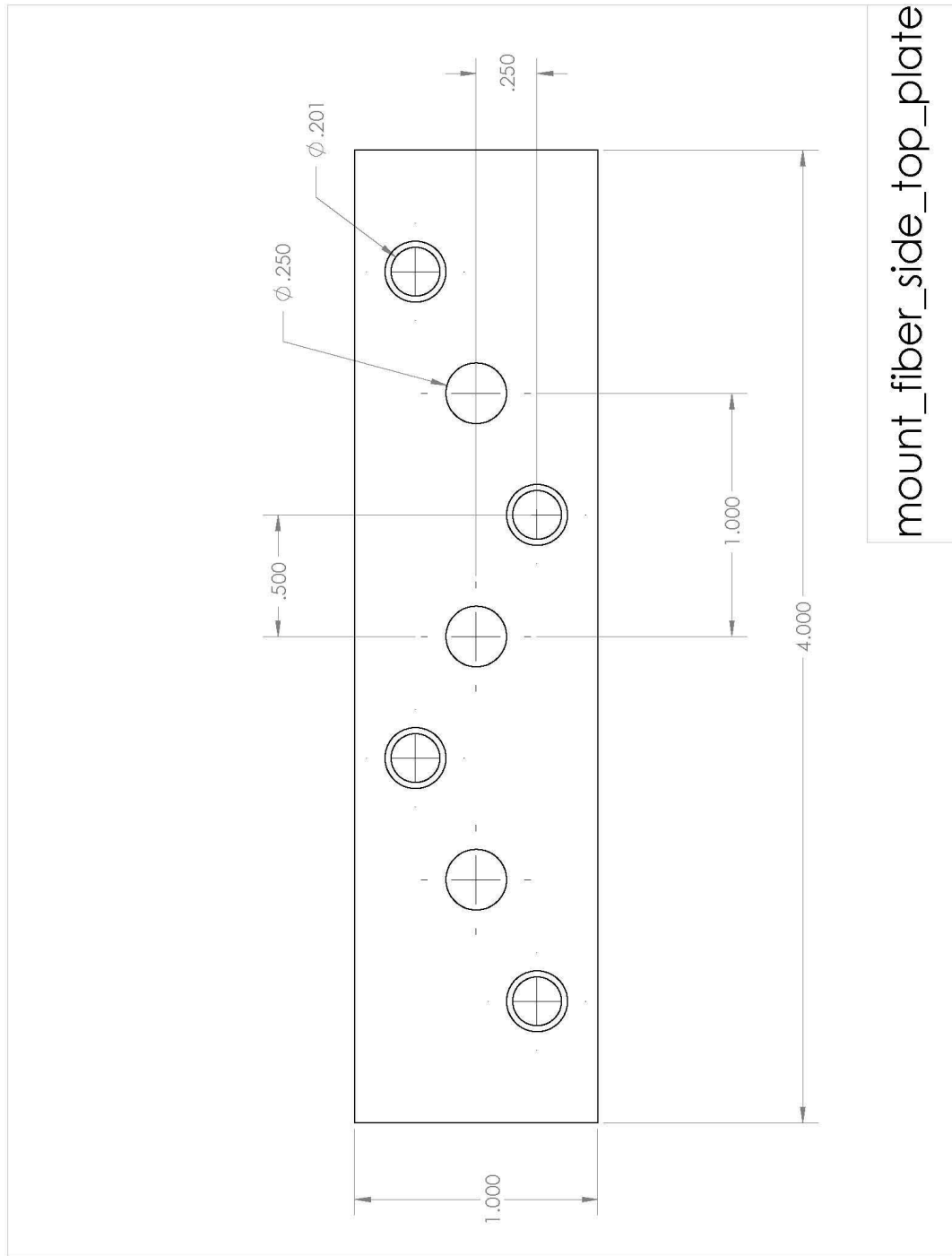
Figure A- 19: Plate for mounting polycarbonate windows in the mount (Figure A- 18).
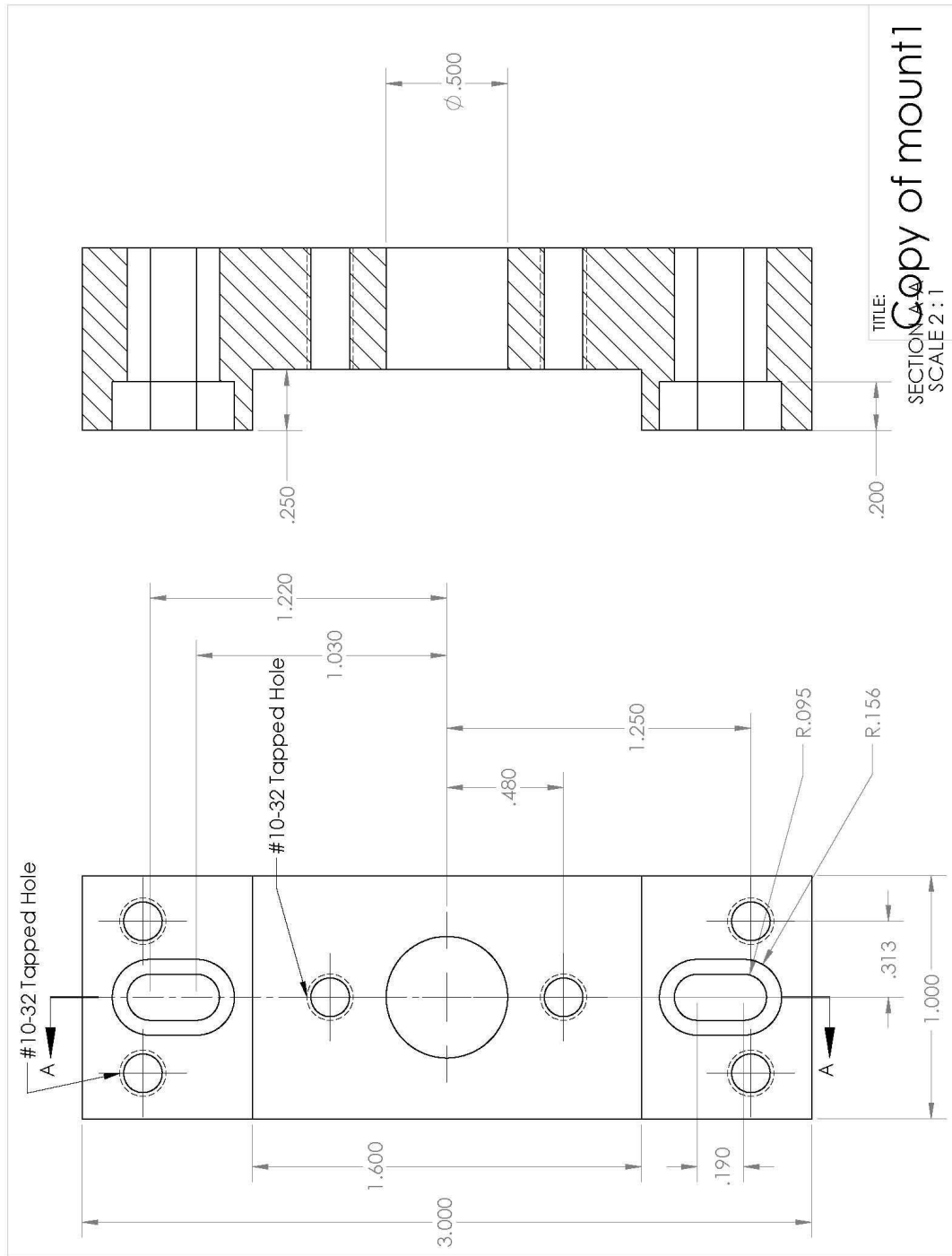
Figure A- 20: Base mount for lasers. This mount provides vertical positioning and tilt adjustments
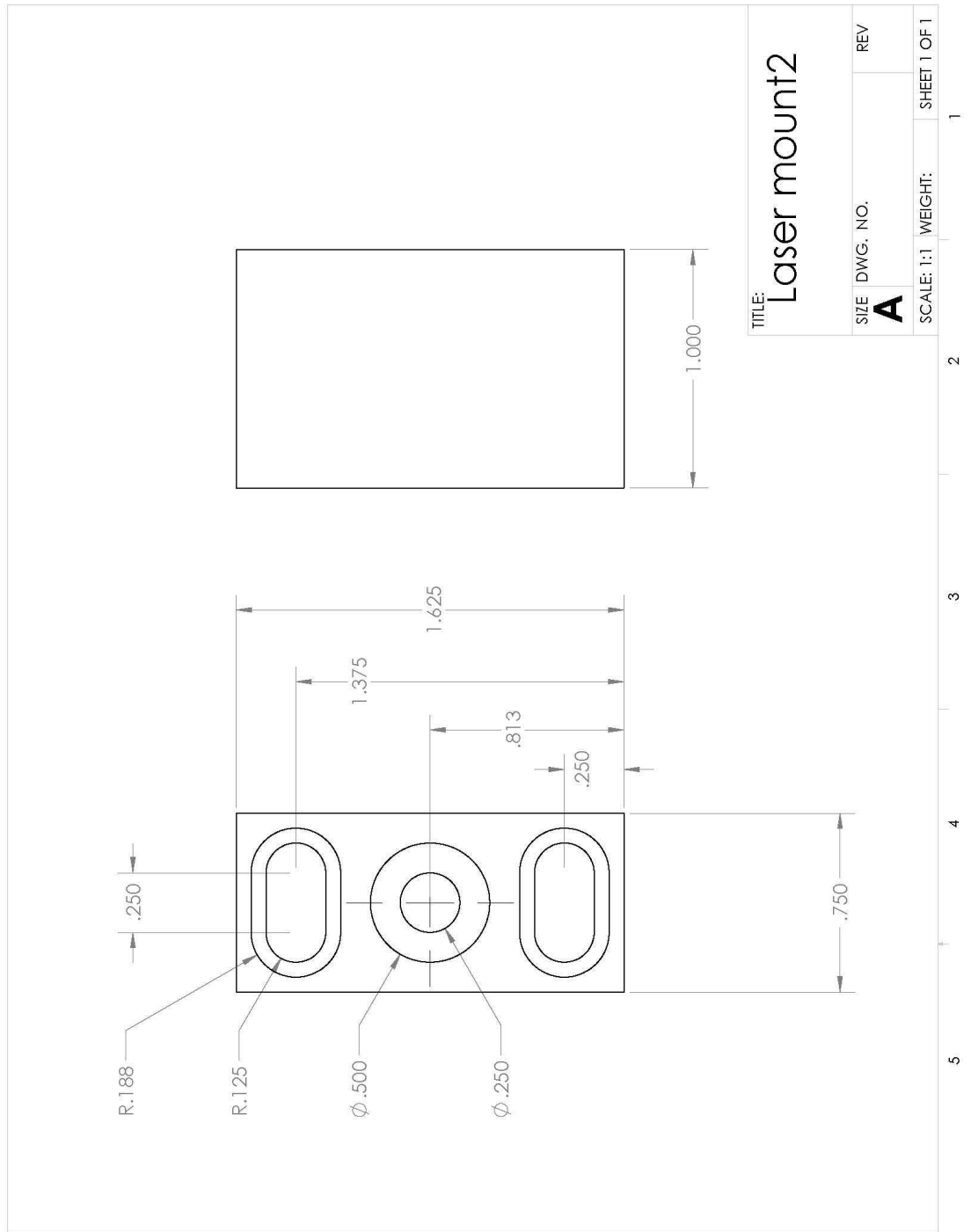
Figure A- 21: Top mount for lasers. The laser diode is press fit into the center hole. This mount allows for horizontal positioning and is mounted on top of the mount shown in Figure A- 20.

A.4. **Frame Mechanical Drawings**

This appendix section contains all detailed drawings for the design of the supporting frame for the single stage light gas gun in the MMRL facilities.

The frame supporting the gas gun is made of 2"x2" steel square tube welded in sections. The main frames shown in Figure A- 22 and Figure A- 28 are bolted together, with a total length of 12 feet and incorporate slotted mounts for the sub frames which allow horizontal alignment of the entire gas gun apparatus. Each sub frame incorporates vertical slotted mounts to allow vertical adjustments. Adjustable feet were incorporated at the corners of the chamber and barrel main frames to provide stability. All of the frame components are bolted together using 1"-8 bolts to support the weight of the gas gun apparatus and provide rigidity to the connections during firing.
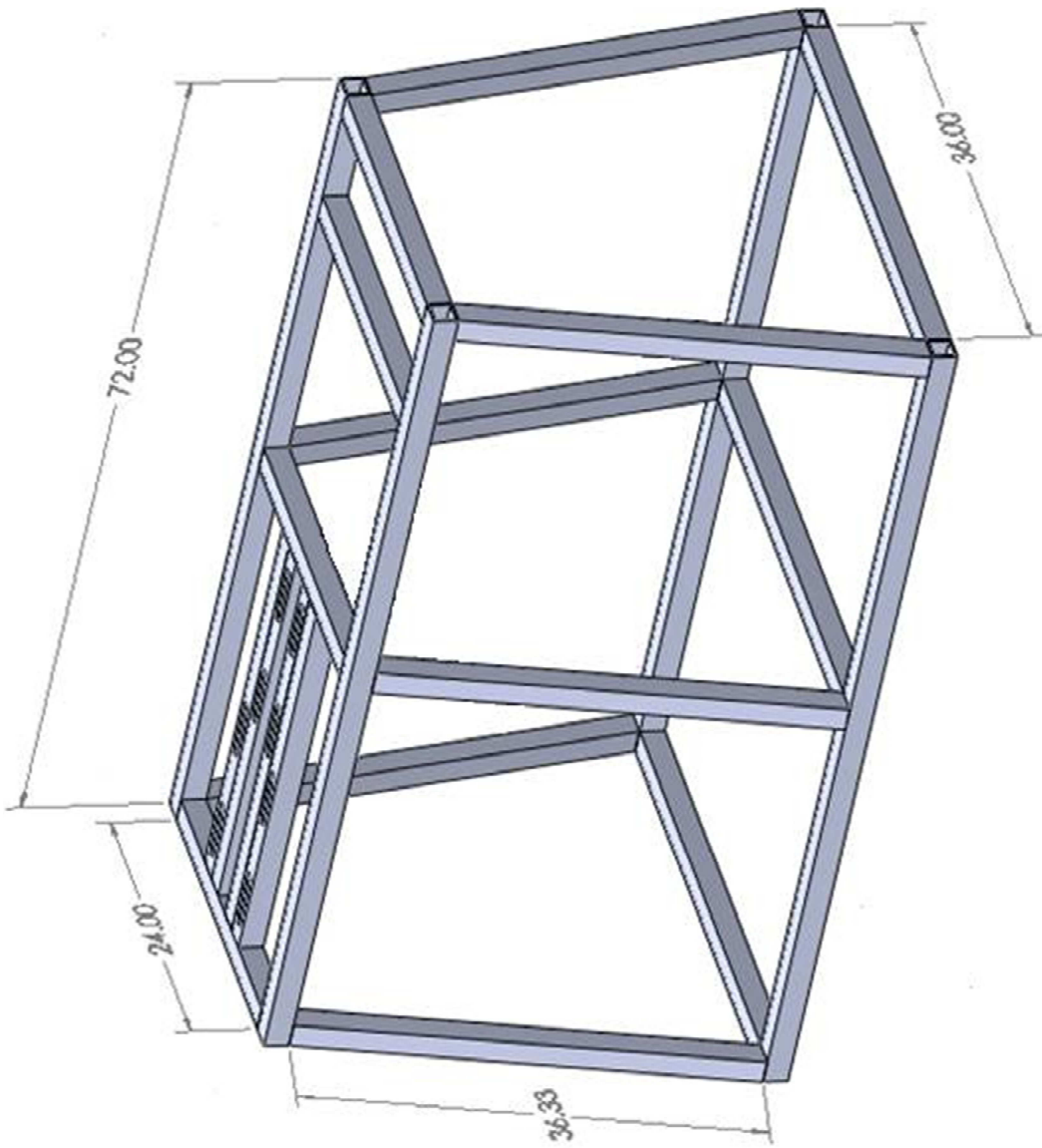
Figure A- 22: Isometric view of main chamber frame section.
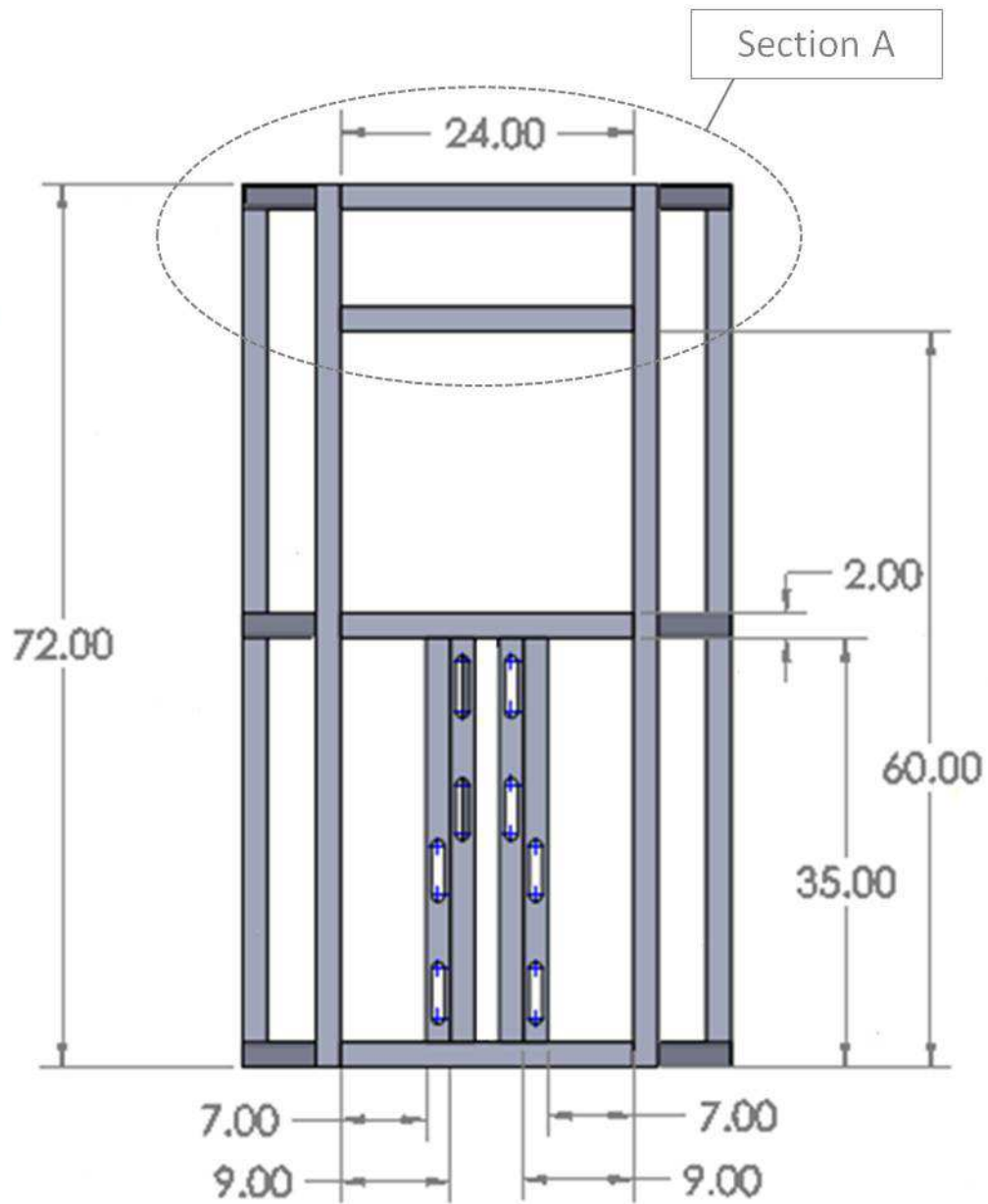
Figure A- 23: Top view of pressure chamber main frame section
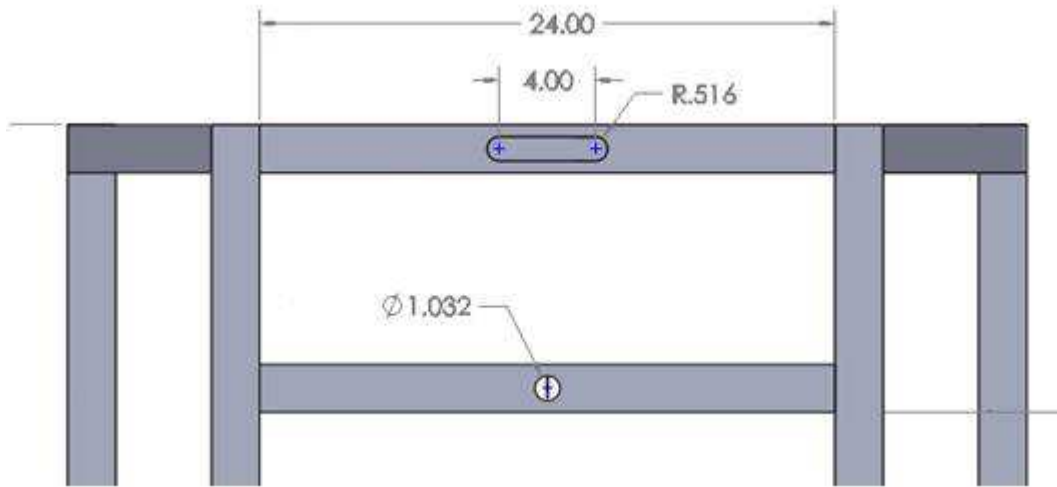
Figure A- 24: Section A detailed view from Figure A- 23.
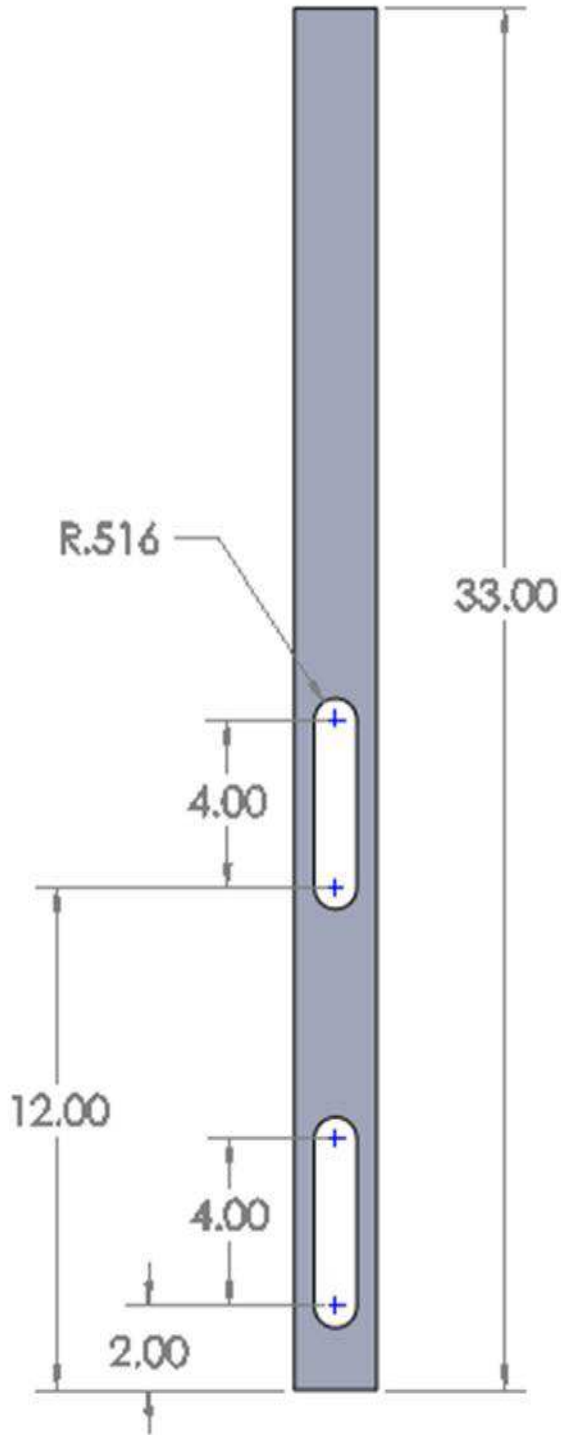
Figure A- 25: Detailed view of four slotted members on top of pressure chamber main frame section shown in Figure A- 22.
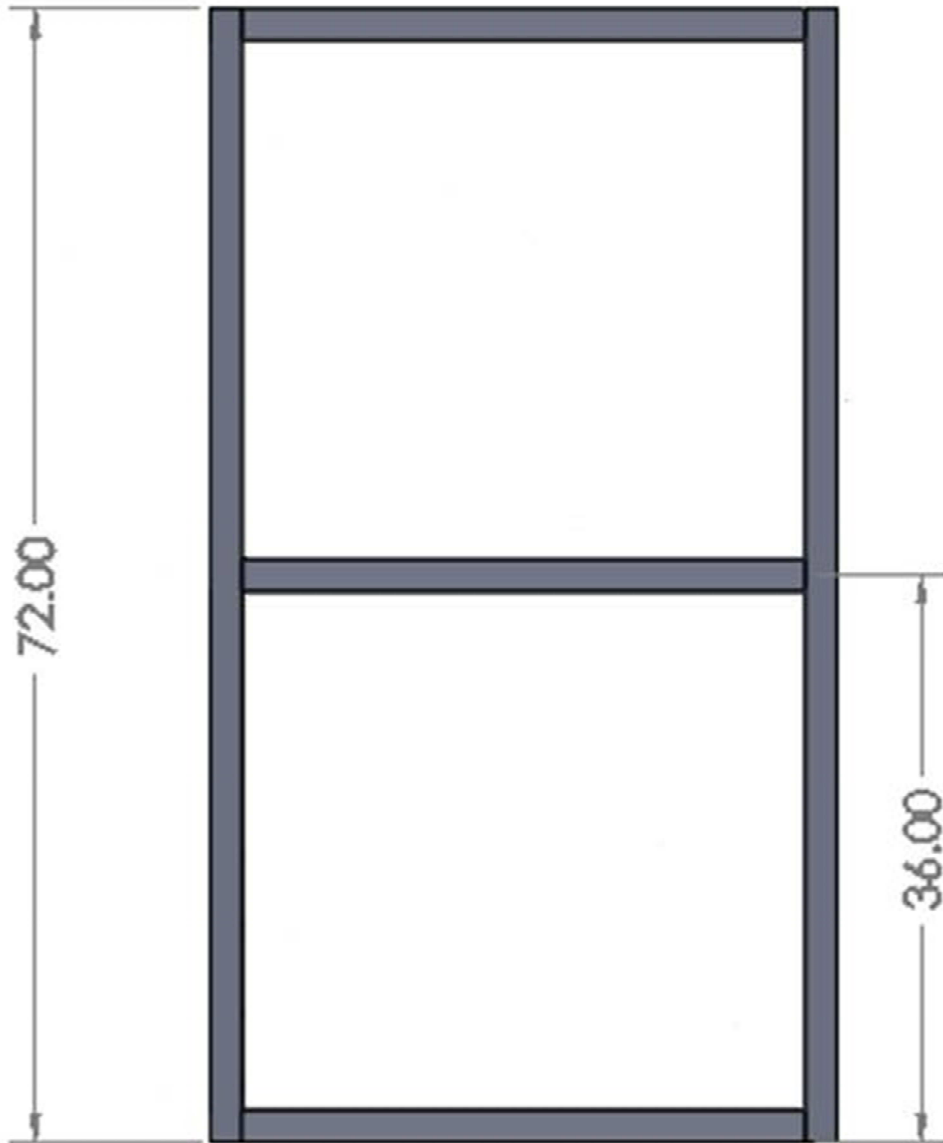
Figure A- 26: Side View of pressure chamber main frame section
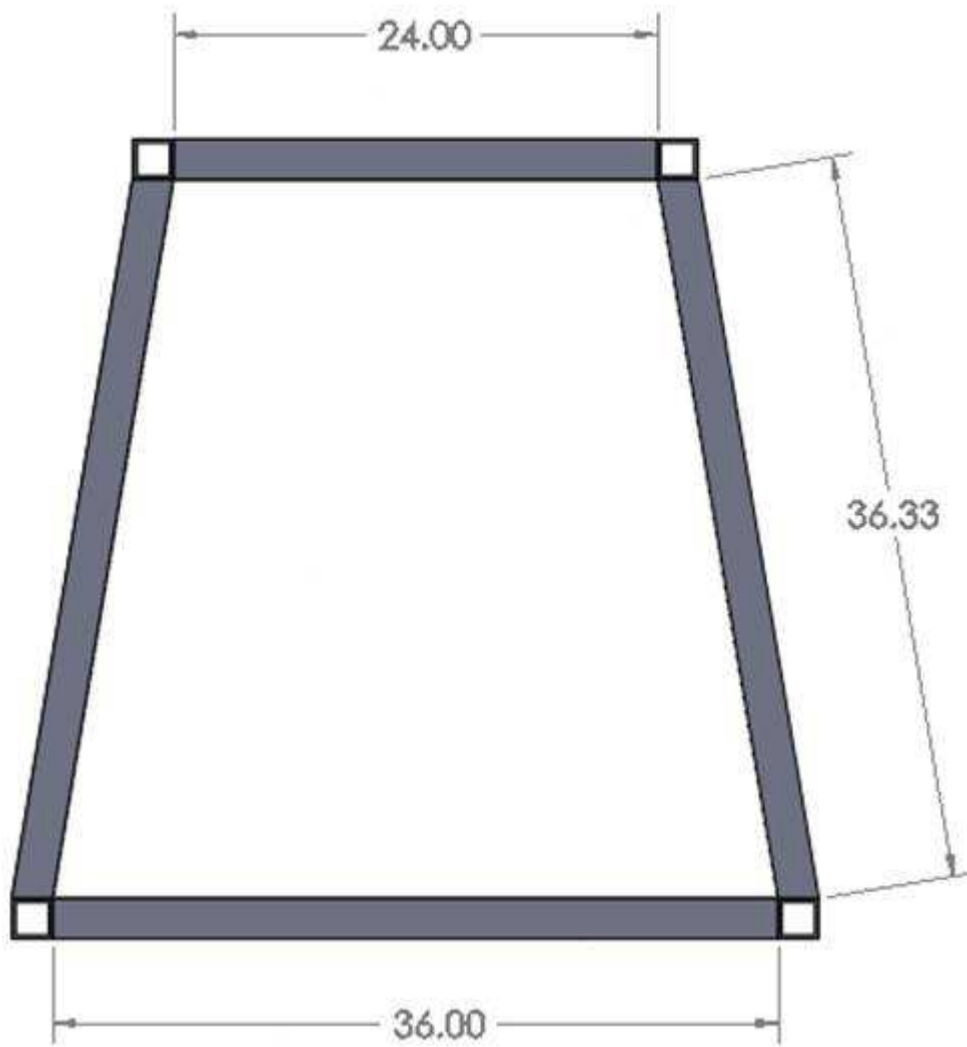
Figure A- 27: Front view of pressure chamber main frame.

340
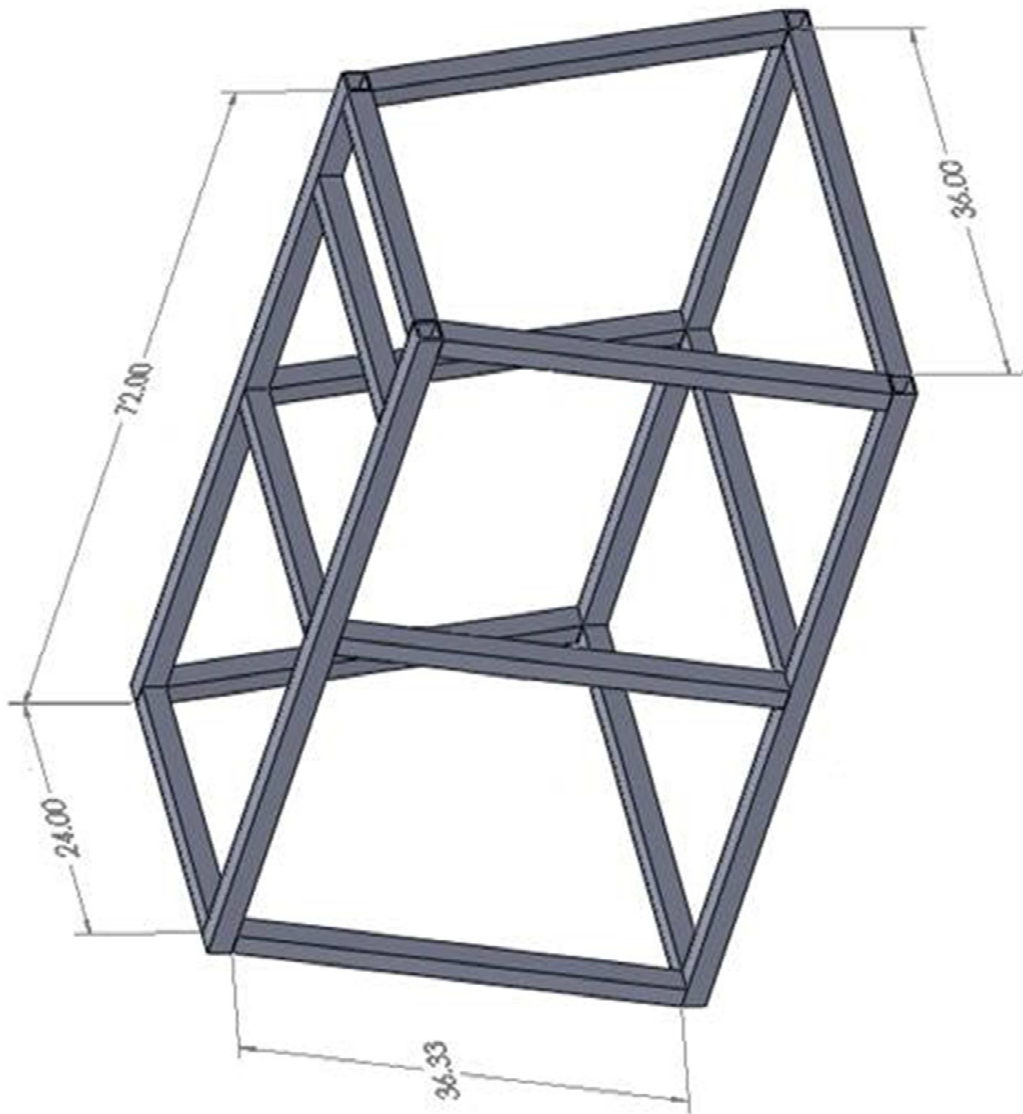
Figure A- 28: Isometric view of barrel main frame.

341
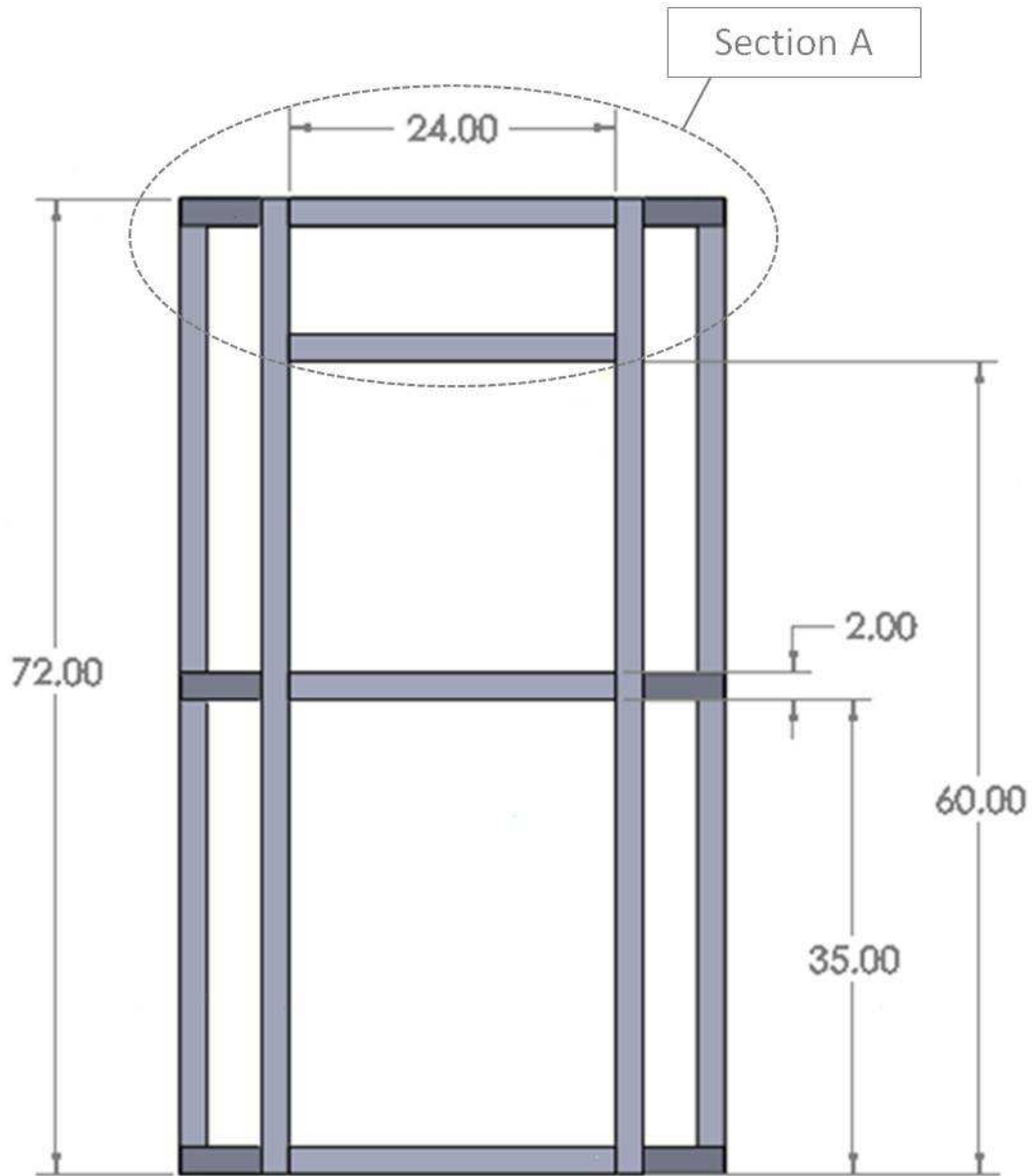
Figure A- 29: Top view of barrel main frame. Section A is shown in Figure A- 24. Side view and front view are the same as shown in Figure A- 26 and Figure A- 27.
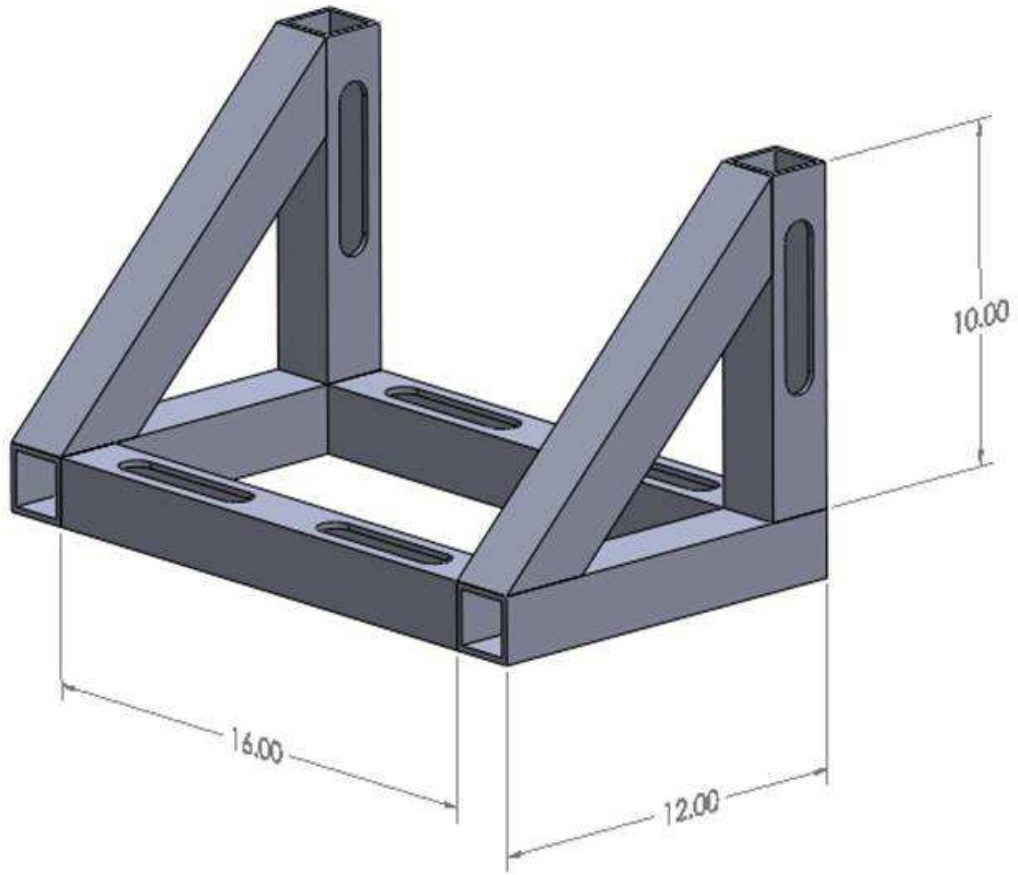
Figure A- 30: Isometric view of NPS 8 sub frame. Mount for main chamber portion of pressure chamber.
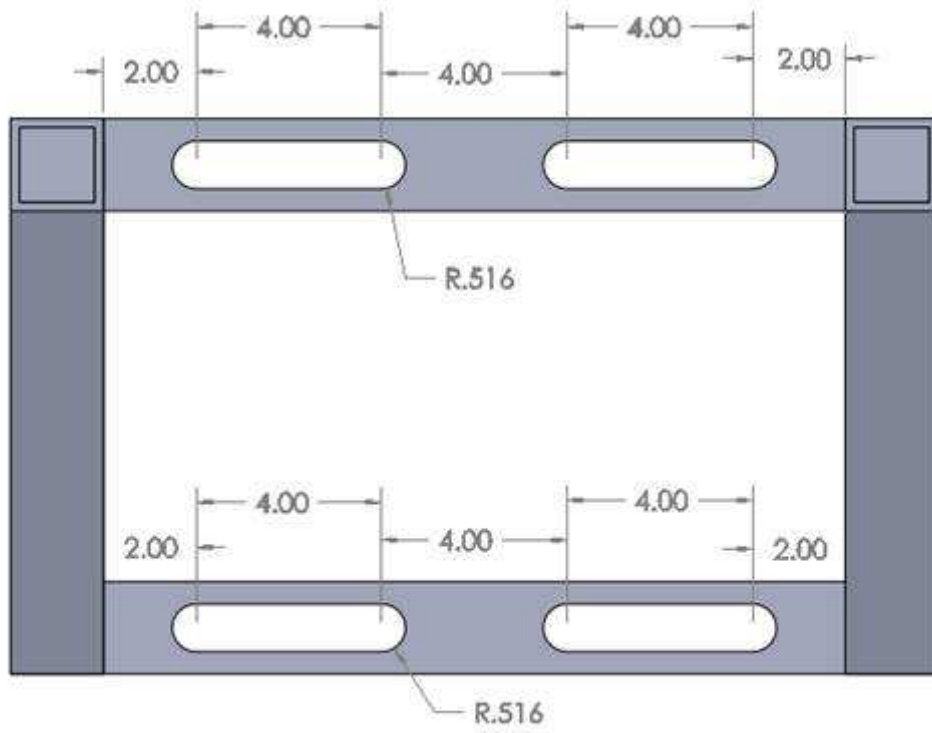
Figure A- 31: Top view of NPS 8 sub frame. Mount for main chamber portion of pressure chamber.
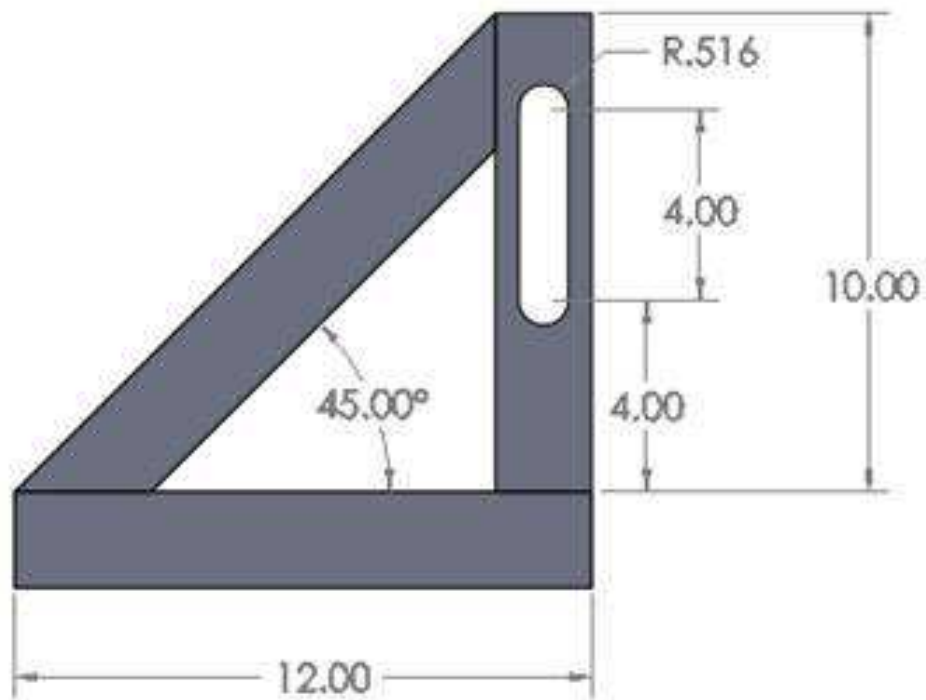
Figure A- 32: Side view of NPS 8 sub frame. Mount for main chamber portion of pressure chamber.
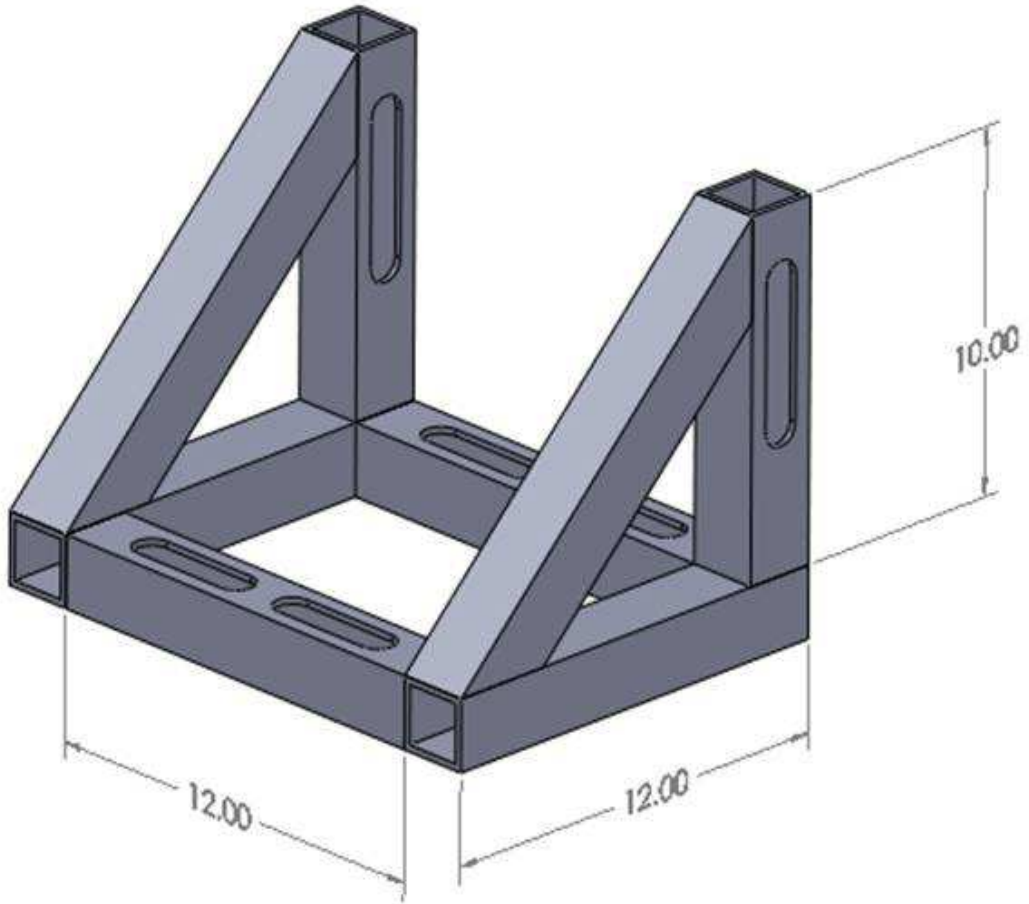
Figure A- 33: Isometric view of NPS 5 sub frame. Mount for secondary chamber portion of pressure chamber.
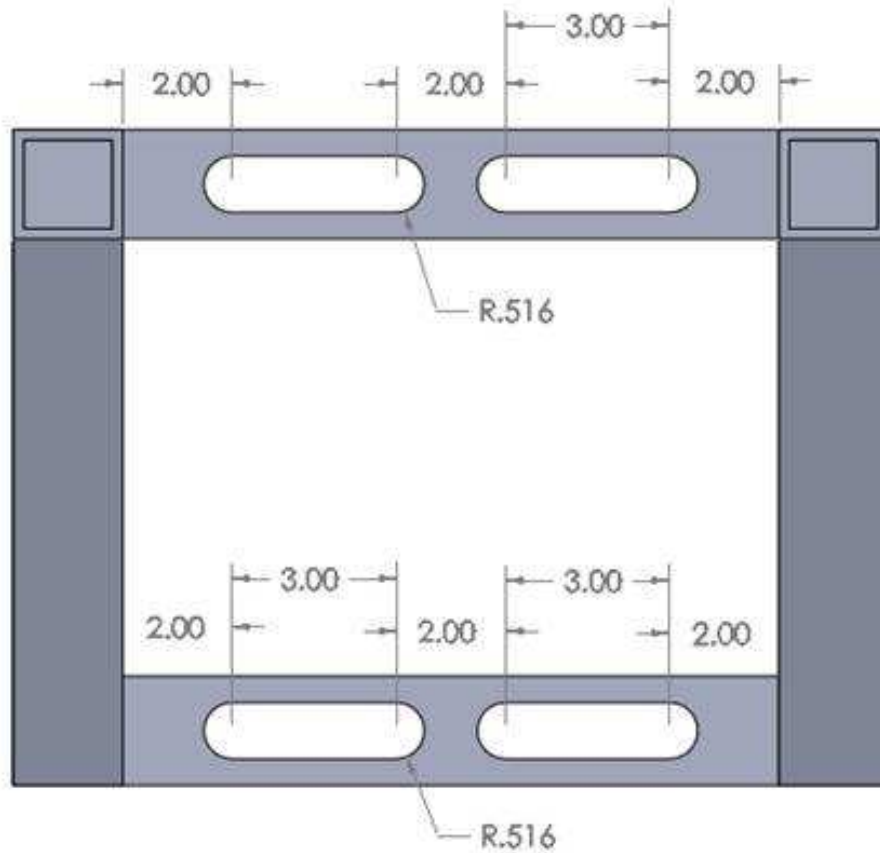
Figure A- 34: Top view of NPS 5 sub frame. Mount for secondary chamber portion of pressure chamber.
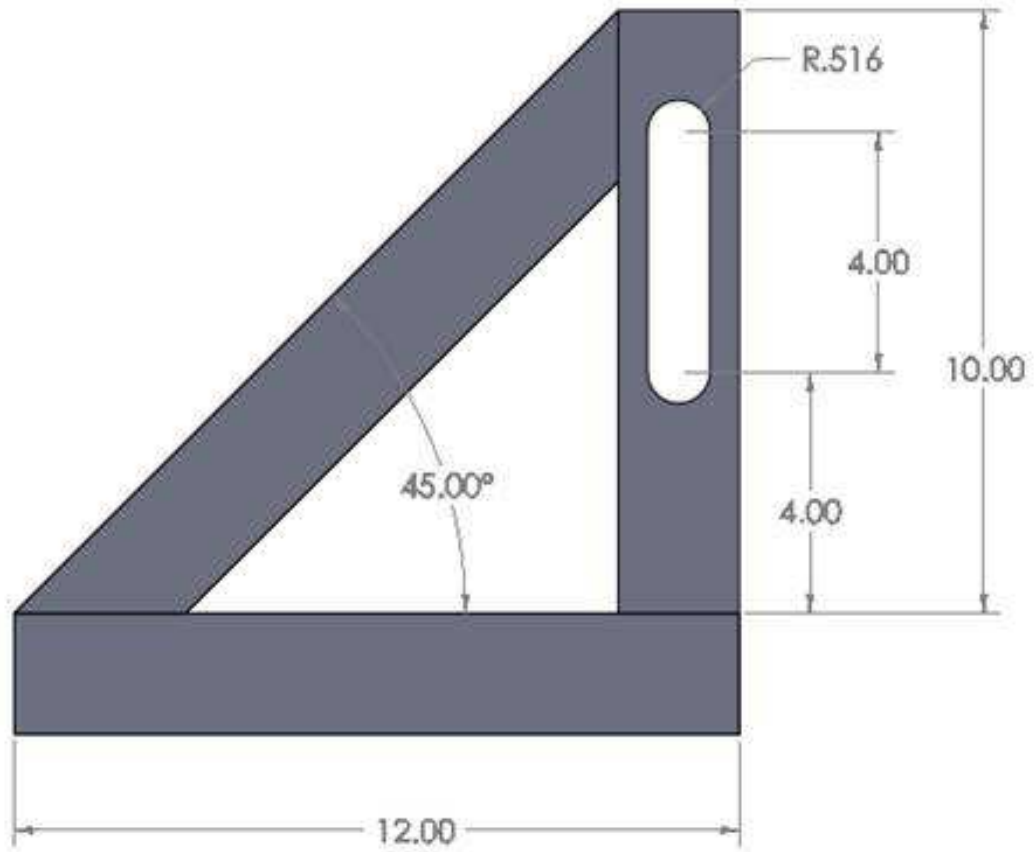
Figure A- 35: Side view of NPS 5 sub frame. Mount for secondary chamber portion of pressure chamber.
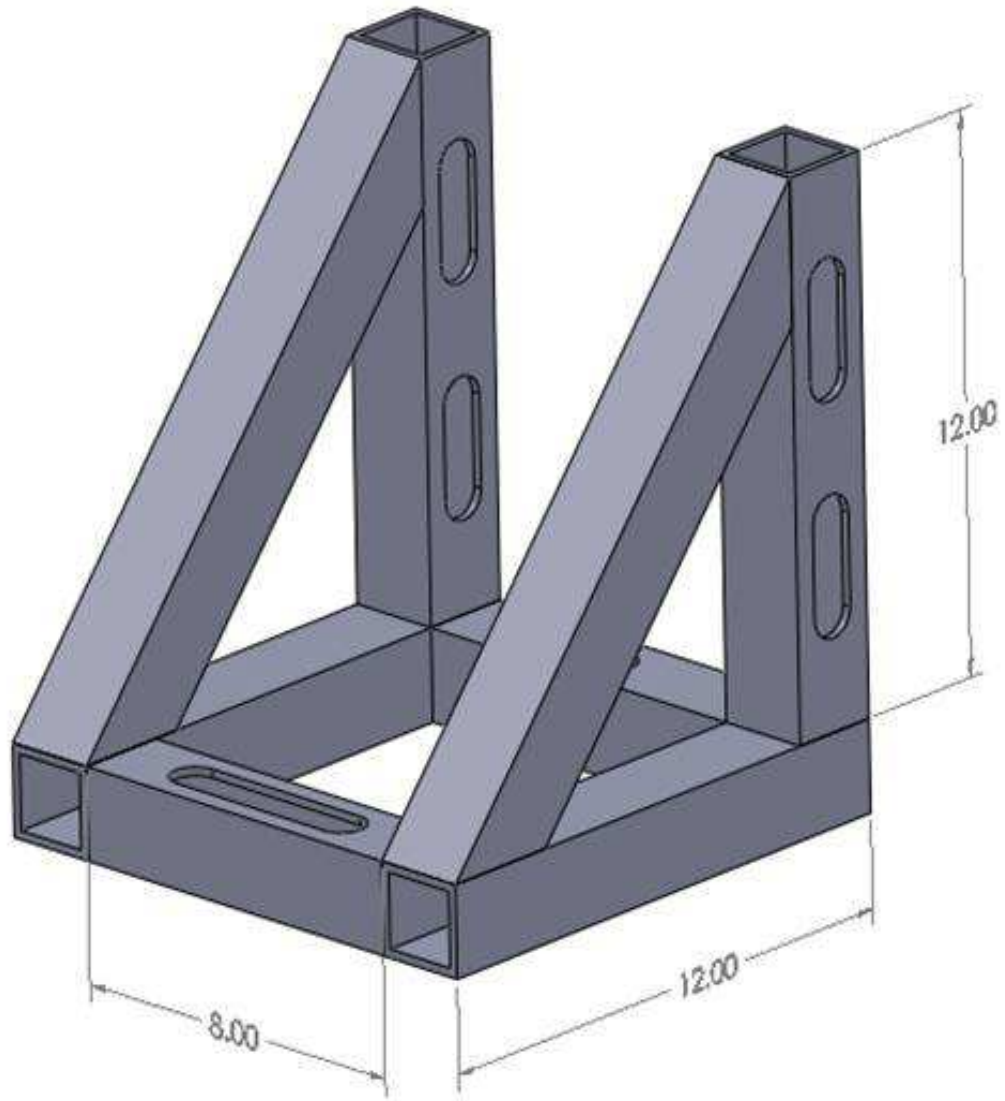
Figure A- 36: Isometric view of barrel sub frame, two required.
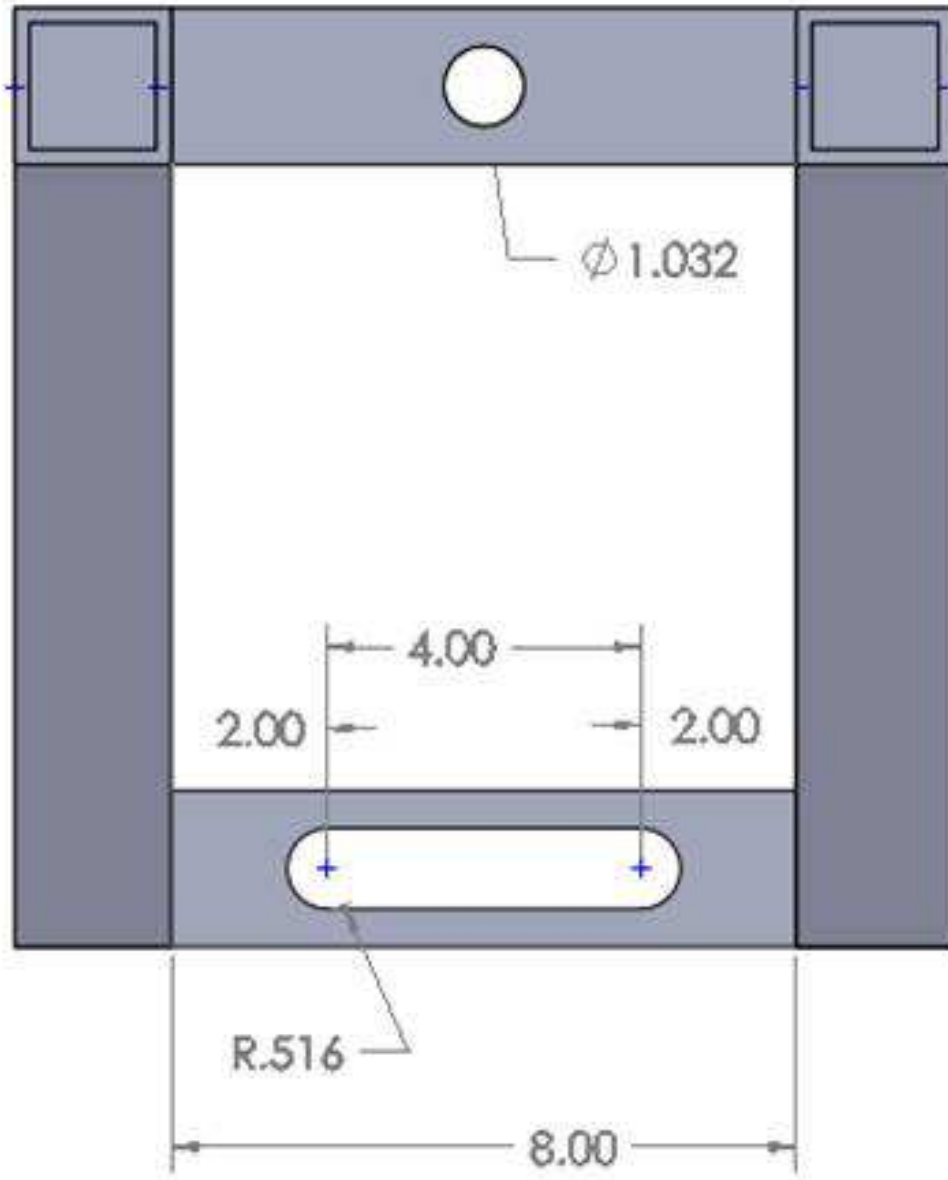
Figure A- 37: Top view of barrel sub frame.
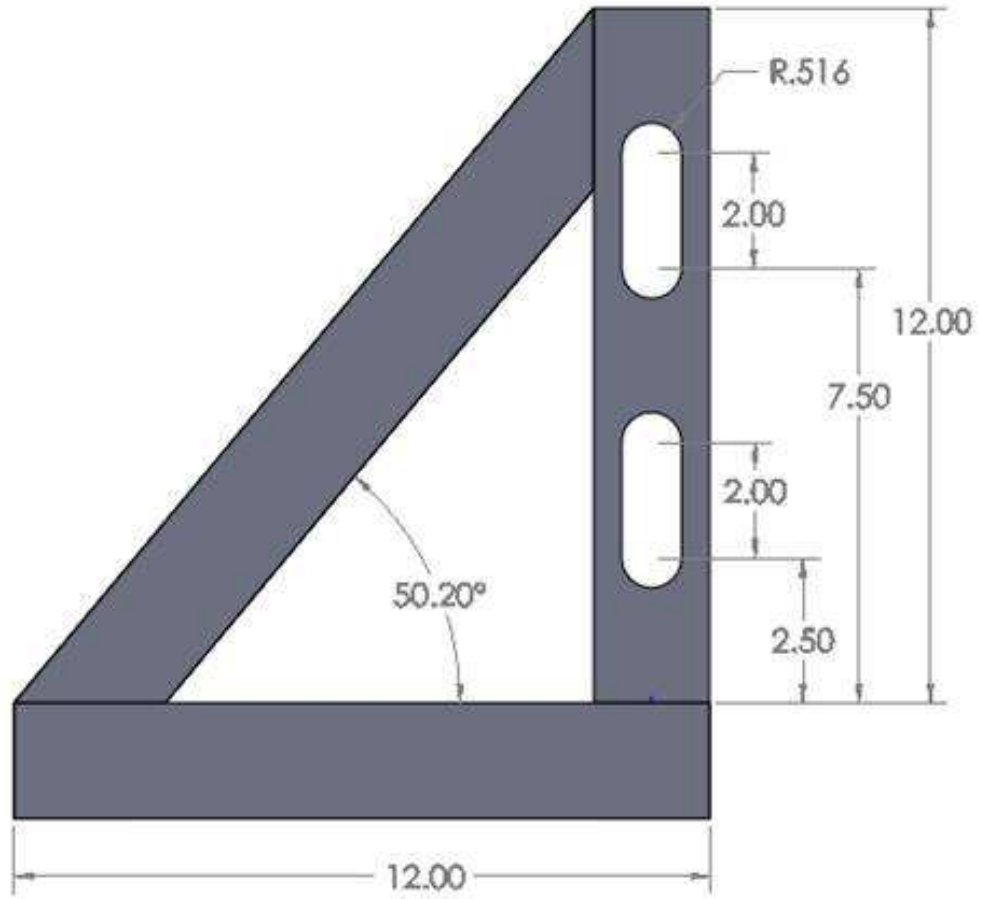
Figure A- 38: Side view of barrel sub frame.

BIBLIOGRAPHY

"*DET10A(/M) Si Biased Detector User Guide*" .ThorLabs. Revision E, 2015.

"*Piezoresistive Pulse Power Supply Model CK2-50/0.050-300 Instruction Manual*," Dynasen Inc., (1996).

A. T. Owens, "Development of a Split Hopkinson Tesnsion Bar for Testing Stress-Strain Response of Particulate Composites Under High Strain Rates of Loading," Aubrun Univerisity, Auburn, Alabama, 2007.

A.W. Sleeswyk. "Twinning and the Origin of Cleavage Nuclei in α-Iron." *Acta Metallurgica.* 10 (1962) 803-812.

AK Steel. Product Bulletin 17-4 PH-B-08-01-07

Allen, G. A. "The activation energies of chromium, iron and nickel in gallium arsenide." *Journal of Physics D: Applied Physics* 1.5 (1968): 593.

Antoun, Tarabay. *Spall fracture*. Springer Science & Business Media, 2003.

Armstrong, R. W. and Worthington, P. J., in Metallurgical Effects at High Strain Rates. p. 401, (edited by R. W. Rohde, B. M. Butcher. J. R. Holland and C. H. Karnes), Plenum. New York (1973).

Asay, J. R., and Mohsen Shahinpoor. *High-pressure Shock Compression of Solids*. New York: Springer-Verlag, 1993. Print.

Asay, J., Clint A. Hall, and Marcus Knudson. "Recent advances in high-pressure equation-of-state capabilities." *Sandia National Report, SAND2000-0849C* (2000).

B. Hopkinson, "A Method of Measuring the Pressure Produced in the Detonation of High Explosives or by the Impact of Bullets," *Philosophical Transactions of the Royal Society A,* vol. 213, pp. 437-457, 1914.

Biggs, W.D., Pratt, P.L., The Deformation and Fracture of Alpha-Iron at Low Temperatures, Acta Metallurgica 6 (1958) 694-703.

Boresi, Arthur P., and Omar M. Sidebottom. *Advanced Mechanics of Materials*. 4th ed. New York: Wiley, 1985. Print.

Bourne, N. K., W. H. Green, and D. P. Dandekar. "On the one-dimensional recovery and microstructural evaluation of shocked alumina." *Proceedings of the Royal Society of London A: Mathematical, Physical and Engineering Sciences*. Vol. 462. No. 2074. The Royal Society, 2006.

Bullens, Denison Kingsley. *Steel and its heat treatment*. John Wiley & sons, inc., 1918.

Chen, Weinong W., and Bo Song. "Dynamic characterization of soft materials." *Dynamic Failure of Materials and Structures*. Springer US, 2009. 1-28.

Chhabildas, Lalit C., Lee Davison, and Yasuyuki Horie. *High-pressure shock compression of solids VIII: The science and technology of high-velocity impact*. Vol. 8. Springer Science & Business Media, 2005.

Christian, J.W., Mahajan, S., Deformation Twinning, Progress in Materials Science. 39 (1995) 1-157.

Christian, John Wyrill, and Subhash Mahajan. "Deformation twinning." *Progress in materials science* 39.1 (1995): 1-157.

Churchman, A.T., Cottrell, A.H., Yield Phenomenon and Twinning in α-Iron, Nature 1951.

Conrad, H. "Thermally activated deformation of metals." *JOM* 16.7 (1964): 582-588.

Conrad, H., Christ, B., Variation of Dislocation Density and Stored Energy with Grain Size, Commander Space Systems Division, United States Air Force. 1963

D. Fahr. "Analysis of stress-strain behavior of type 316 stainless steel." ORNL/TM-4292 (1973), Oak Ridge National Laboratory report.

D. Firrao, P. Matteis, G. Scavino, G. Ubertalli, M.G. Ienco, G. Pellati, P. Piccardo, M.R. Pinasco, E. Stagno, R. Montanari, M.E. Tata, G. Brandimarte, S. Petralia. "Mechanical twins in 304 stainless steel after small-charge explosions." *Materials Science and Engineering*. A 424 (2006) 23-32.

D. Hull, and D. J. Bacon. *Introduction to Dislocations*. Oxford: Butterworth-Heinemann, 2001. Print.

Davison, L., D.E. Grady, M. Shahinpoor, "*High-pressure Shock Compression of Solids II*," Springer, New York. (1996).

De Resseguier, T., Hallouin, M., Stress relaxation and precursor decay in laser shock-loaded iron, Journal of Applied Physics 84 (4) (1998) 1932–1938.

Dieter, George Ellwood, *Mechanical metallurgy*. New York: McGraw-Hill, 1961.

Diggs, T., Rosenberg, S., Geil, G., Heat Treatment and Properties of Iron and Steel (1966)

Direct measurement of isothermal flow stress of metals at elevated temperatures and high strain rates with application to Ta and Ta-W alloys. S. Nemat-Nasser, J.B. Isaacs. *Acta Metallurgica*. Vol. 45, No. 3. (1997) pp. 907-919.

E. Pink, S. Kumar. "Patterns of serrated flow in low-carbon steel." *Materials Science and Engineering*. A201 (1995) 58-64.

E. Zaretsky. Dislocation multiplication behind the shock front. J. Appl. Phys. 78 (6) (1995). 3740-47.

Ferreira, P.J., Vander Sande, J.B., Amaral Fortes, M., Kyrolainen, A., Microstructure Deveolopment during High-Velocity Deformation, Metallurgical and Materials Transactions. A 35A (2004) 3091-3101.

Firrao, D., Matteis, P., Scavino, G., Ubertalli, G., Ienco, M.G., Pellati, G., Piccardo, P., Pinasco, M.R., Stagno, E., Montanari, R., Tata, M.E., Brandimarte, G., Petralia, S., Mechanical twins in 304 stainless steel after small-charge explosions, Materials Science and Engineering. A424 (2006) 23–32.

Flow stress of FCC polycrystals with application to OFHC Cu. S. Nemat-Nasser, Y. Li. *Acta Mater*. Vol 46, No. 2. (1998) pp. 565-577.

Frew, D. J., MICHAEL J. Forrestal, and W. Chen. "Pulse shaping techniques for testing brittle materials with a split Hopkinson pressure bar." *Experimental mechanics* 42.1 (2002): 93-106.

G.R. Johnson, W.H. Cook. "A constitutive model and data for metals subjected to large strains, high strain rates and high temperatures." In*: Proceedings of the Seventh International Symposium on Ballistic*, La Hague, Netherlands. (1983) 541–547.

Galindo-Nava, E. I., and P. E. J. Rivera-Díaz-del-Castillo. "Modelling plastic deformation in BCC metals: Dynamic recovery and cell formation effects." *Materials Science and Engineering: A* 558 (2012): 641-648.

Gama, Bazle A., Sergey L. Lopatnikov, and John W. Gillespie. "Hopkinson bar experimental technique: a critical review." *Applied Mechanics Reviews* 57.4 (2004): 223-250.

Ganin, E., Y. Komem, and A. Rosen. "Shock induced hardness in α-iron." *Materials Science and Engineering* 33.1 (1978): 1-4.

Goni, Miguel, and Carl-Ernst Rousseau. "On the Use of Ultrasonic Pulse-Echo Immersion Technique for Measuring Real Attenuation." *Experimental Mechanics of Composite, Hybrid, and Multifunctional Materials, Volume 6*. Springer International Publishing, 2014. 255-257.

Gordon, P. A., et al. "Screw dislocation mobility in BCC metals: the role of the compact core on double-kink nucleation." *Modelling and Simulation in Materials Science and Engineering* 18.8 (2010): 085008.

Graham, R. A. "Shock-induced electrical switching in polymeric films." *Megagauss Physics and Technology*. Springer US, 1980. 147-150.

Gray III, G.T., Levescu, V., Cerreta, E.K., Mason, T.A., Maudlin, P.J., Bingert, J.F., Influence of shockwave obliquity on deformation twin formation in Ta, DYMAT (2009) 963-969

: an assessment." *Shock compression of condensed matter* (1989): 407-414.

Gray III, George T. "Shock recovery experiments: an assessment." *Shock compression of condensed matter* (1989): 407-414.

Gray, George T., and Kenneth S. Vecchio. "Influence of peak pressure and temperature on the structure/property response of shock-loaded Ta and Ta-10W." *Metallurgical and Materials Transactions A* 26.10 (1995): 2555-2563.

H. Kolsky, "An Investigation of the Mechanical Proprties of Materials at very High Rates of Loading," *Proc. Phys. Soc. B,* vol. 62, pp. 676-700, 1949.

Hirth, John P., and Jens Lothe. *Theory of dislocations*. John Wiley, New York, 1982.

Hull, D., Orientation and temperature dependence of plastic deformation processes in 3.25% silicon iron, Proc. R. Soc. A (1963) 274: 5-20.

Hull, Derek, and David J. Bacon. *Introduction to dislocations*. Butterworth-Heinemann, 2001.

Isbell, William M. *Measuring the Dynamic Response of Materials*. London: Imperial College Press, 2005.

J. Gilman. The Limiting Speeds of Dislocations. Metall. Mater. Trans A. 31. (2000) 811.

J. Krafft, A. Sullivan and C. Tipper, "The Effect of Static and Dynamic Loading and Temperature on the Yield Stress of Iron and Mild Steel in Compression," *Proceedings of the Royal Society of London A,* vol. 221, no. 1144, pp. 114-127, 1954.

J. P. Hirth and L. Kubin. Dislocations in Solids. Vol 15. The Netherlands: North-Holland, Ch 89. Dislocations in Shock Compression and Release. 2009, pp. 91–197.

J.E. Field, S.M. Walley, W.G. Proud, H.T. Goldrein, C.R. Siviour. "Review of experimental techniques for high rate deformation and shock studies." *International Journal of Impact Engineering*. 30 (2004) 725-775.

J.N. Johnson, R.W. Rohde. "Dynamic deformation twinning in shock-loaded iron." *J. Appl. Phys.* 42.11 (1971): 4171-82.

J.W. Christian, S. Mahajan. "Deformation twinning." *Progress in Materials Science* 39 (1995): 1-157.

J.W. Taylor. "Dislocation Dynamics and Dynamic Yielding." J. Appl.Phys. 36.10 (1965): 3146-50

J.Y. Richard Liew. "Survivability of steel frame structures subject to blast and fire." *Journal of Constructional Steel Research*. 64 (2008) 854-866.

Jeelani, S., et al. *Two-Stage Light-Gas Gun Installation for Hypervelocity Impact Studies*. No. TR-73-3. NORTH CAROLINA STATE UNIV AT RALEIGH, 1973.

Johnson, J.N., Rohde, R.W., Dynamic deformation twinning in shock-loaded iron, Journal of Applied Physics. 42 (11) (1971) 4171–4182.

Johnston, W.G., Gilman, J.J., Dislocation Velocities, Dislocation Densities, and Plastic Flow in Lithium Fluoride Crystals, Journal of Applied Physics. 30 (2) (1959) 129-144

Jolley, W., Hull, D., Effect of Prestrain and Strain Aging on the Brittle Fracture of 3.25% Silicon Iron, Acta Metallurgica 12 (1964) 1337-1352.

Jones, A_H_, W. M. Isbell, and C. J. Maiden. "Measurement of the Very-High-Pressure Properties of Materials using a Light-Gas Gun." *Journal of Applied Physics* 37.9 (1966): 3493-3499.

K. D. Robertson, S.-C. Chou and J. H. Rainey, "Design and Operating Characteristics of A Split Hopkinson Pressure Bar Apparatus," Army Materials and Mechanis Reserach Center, Watertown, Massachusetts, 1971.

K. Maciejewski, Y. Sun, O. Gregory, H. Ghonem. "Time-Dependent Deformation of Low Carbon Steel at Elevated Temperature." (Submitted for Publication)

K. Renard, S. Ryelandt, P.J. Jacques. "Characterisation of Portevin-Le Chatelier effect affecting an austenitic TWIP steel based on digital image correlation." *Materials Science and Engineering.* A527 (2010) 2969-2977.

Kanel, G.I., S.V. Razorenov, V.E. Fortov, "*Shock-wave Phenomena and the Properties of Condensed Matter,*" Springer, New Yorrk. (2004).

Karaman, Sehitoglu, Gall, Chumlyakov, Maier. Deformation of single crystal Hadfield steel by twinning and slip, Acta Mater. 48 (2000) 1345-1359.

Kibey, S., Liu, J.B., Johnson, D.D., Sehitoglu, H., Predicting twinning stress in fcc metals: Linking twin-energy pathways to twin nucleation, Acta Mater. 55 (2007) 6843-6851.

Klassen-Neklyudova, M.V., Mechanical Twinning of Crystals. Consultants Bureau. Ney York (1964)

Klepaczko, J. "Application of the split Hopkinson pressure bar to fracture dynamics." *Proc. 2 nd Conf. Mechanical Properties of Materials at High Rates of Strain, Oxford, England, Mar. 1979,*. 1980.

Krauss, George. *Steels: processing, structure, and performance*. Asm International, 2015.

L. Jiang, J. Jonas, R. Mishra, A. Luo, A. Sachdev, S. Godet. "Twinning and texture development in two Mg alloys subjected to loading along three different strain paths." *Acta Materialia*. 55 (2007) 3899-3910.

L.E. Murr, M.A. Meyers. "Shock-induced deformation twinning in tantalum." *Acta Materialia* 45.1 (1997): 157-75.

L.-L. Wang, Fondations of Stress Waves, New York, New York: Elsevier, 2007.

L.M. Dougherty, E.K. Cerreta, E.A. Pfeif, C. Trujillo, G.T. Gray. "The impact of peak shock stress on the microstructure and shear behavior of 1018 steel." *Acta Materialia* 55 (2007) 6356-6364.

Lassila, D. H., and G. T. GRAY III. "Effects of shock prestrain on the dynamic mechanical behavior of tantalum." *Le Journal de Physique IV* 1.C3 (1991): C3-19.

Lee, Woei-Shyan, et al. "Effects of prestrain on high temperature impact properties of 304L stainless steel." *Journal of Materials Research* 25.4 (2010): 754-763.

Lewis, Jack L., and Werner Goldsmith. "A biaxial split Hopkinson bar for simultaneous torsion and compression." *Review of scientific instruments* 44.7 (1973): 811-813.

Lindholm, U. S., and L. M. Yeakley. "High strain-rate testing: tension and compression." *Experimental Mechanics* 8.1 (1968): 1-9.

Lindley, T.C., The effect of a prestrain on the low temperature mechanical properties of a low carbon steel, Acta Metallurgica. 13 (1965) 681-689.

M. A. Kaiser, "Advancements in the Split Hopkinson Bar Test," Virginia Polytechnic Institute and State University, Blacksburg, Virginia, 1998

M. Meyers. A Mechanism For Dislocation Generation In Shock-Wave Deformation. Scripta Metallurgica. 12. (1978) 21-26

Machcha, Ashok R., and Sia Nemat-Nasser. "Effects of geometry in pressure–shear and normal plate impact recovery experiments: Three-dimensional finite-element simulation and experimental observation." *Journal of applied physics* 80.6 (1996): 3267-3274.

Maciejewski, Kimberly. "The role of microstructure on deformation and damage mechanisms in a Ni-based superalloy at elevated temperatures." (2013).

Mahajan, S. "Shock-Induced Substructural Changes in Prestrained Iron." *physica status solidi (b)* 33.1 (1969): 291-299.

Mahajan, S., Accommodation at deformation twins in bcc crystals, Metallurgical Transactions. A 12A (1981) 379–386.

Mahajan, S., Bartlett, A.F., Influence of Prior Mechanical and Thermal Treatments on Shock Induced Substructures in Molybdenum, Acta Metallurgica. 19 (1971) 1111-1119.

Mahajan, S., Effects of Existing Substructure on Shock-Twinning Behavior of Iron, Physica Status Solidi. Vol 2, Issue 2, (1970) 217-223.

Marsh, S. P., editor, "*LASL Shock Hugoniot Data*," University of California Press, CA, (1980).

Mason, T.A., Bingert, J.F., Kaschner, G.C., Wright, S.I., Larson, R.J., Advances in Deformation Twin Characterization Using Electron Backscattered Diffraction Data, Metallurgical and Materials Transactions. A 33A (2002) 949-954

Messerschmidt, Ulrich. *Dislocation dynamics during plastic deformation*. Vol. 129. Springer Science & Business Media, 2010.

Meyers, M., et al. "Dynamic response of single crystalline copper subjected to quasi-isentropic laser and gas-gun driven loading." *Journal de Physique IV (Proceedings)*. Vol. 134. EDP sciences, 2006.

Meyers, M.A., "*Dynamic Behavior of Materials*," John Wiley & Sons Inc., New York. (1994).

Meyers, M.A., Benson, D.J., Vöhringer, O., Kad, B.K., Xue, Q., Fu, H.-H., Constitutive description of dynamic deformation: physically-based mechanisms, Materials Science and Engineering. A322 (2002) 194–216.

Meyers, M.A., Vöhringer, O., Lubarda, V.A., The onset of twinning in metals: A constitutive description, Acta Materialia 49 (2001) 4025–4039.

Mitchell, A. C., and W. J. Nellis. "Diagnostic system of the Lawrence Livermore National Laboratory two-stage light-gas gun." *Review of scientific instruments* 52.3 (1981): 347-359.

Mompiou, Frédéric, et al. "In situ TEM study of twin boundary migration in sub-micron Be fibers." *Acta Materialia* 96 (2015): 57-65.

Morris, Charles E. "Shock-wave equation-of-state studies at Los Alamos." *Shock Waves* 1.3 (1991): 213-222.

Murr, L.E., Meyers, M.A., Shock-induced deformation twinning in tantalum, Acta Materialia 45 (1) (1997) 157–175.

N. Narasaiah, K.K. Ray. "Small crack formation in a low carbon steel with banded ferrite-pearlite structure." *Materials Science and Engineering.* A392 (2005) 269-277.

Nemat-Nasser, S. "Physically based rate-and temperaturedependent constitutive models for metals." *Handbook of Materials Behaviour Models, Academic Press, San Diego, CA* (2001): 387-397.

Nemat-Nasser, Sia, and J. B. Isaacs. "Direct measurement of isothermal flow stress of metals at elevated temperatures and high strain rates with application to Ta and TaW alloys." *Acta Materialia* 45.3 (1997): 907-919.

Nemat-Nasser, Sia, and Weiguo Guo. "High strain-rate response of commercially pure vanadium." *Mechanics of Materials* 32.4 (2000): 243-260.

Nemat-Nasser, Sia, and Yulong Li. "Flow stress of fcc polycrystals with application to OFHC Cu." *Acta Materialia* 46.2 (1998): 565-577.

Ngo, T., et al. "Blast loading and blast effects on structures–an overview." *Electronic Journal of Structural Engineering* 7 (2007): 76-91.

Niewczas, Marek. "Dislocations and twinning in face centred cubic crystals." *Dislocations in solids* 13 (2007): 263-364.

O. Gregory, J. Oxley, J. Smith, M. Platek, H. Ghonem, E. Bernier, M. Downey, C. Cumminskey. " Microstructure characterization of pipe bomb fragments." *Materials Characterization.* 61.3(2010) 347-354.

Ogawa, K. "Edge dislocations dissociated in {112} planes and twinning mechanism of bcc metals." *Philosophical Magazine* 11.110 (1965): 217-233.

P. Gumbsch, H. Gao. Dislocations faster than the speed of sound. Science. 283 (1999) 965-968.

P. Rodriguez. "Serrated Plastic Flow." *Bulletin of Material Science*. Vol. 6, No. 4, (1984) 653-663.

Park, H., et al. *EXPERIMENTAL TESTS OF VANADIUM STRENGTH MODELS AT HIGH PRESSURES AND STRAIN RATES*. No. LLNL-PROC-431291. Lawrence Livermore National Laboratory (LLNL), Livermore, CA, 2010.

Piekutowski, A. J., and K. L. Poormon. "Development of a three-stage, light-gas gun at the University of Dayton Research Institute." *International journal of impact engineering* 33.1 (2006): 615-624.

Plume, Gifford. "Response of materials to various shock loading conditions generated by plate impact experiments." (2013).

Priestner, R., and W. C. Leslie. "Nucleation of deformation twins at slip plane intersections in BCC metals." *Philosophical Magazine* 11.113 (1965): 895-916.

R. Davies, "A Critical Study of the Hopkinson Pressure Bar," *Philosophical Transactions of the Royal Society of London A,* vol. 240, no. 821, pp. 375-457, 1948

R. Hull, C. Jagadish, R.M. Osgood, Jr., J. Parisi, Z.Wang, H.Warlimont. Dislocation Dynamics During Plastic Deformation. 2010

R.J. Wasilewski. "Mechanism of bcc twinning: Shear or shuffle?" Metallurgical Transactions. 1 (1970) 2641-2643.

R.W. Armstrong, W. Arnold, F. Zerilli. Dislocation mechanics of copper and iron in high rate deformation tests. Journal Of Applied Physics. 105, (2009) 23511

Raiser, G., R. J. Clifton, and M. Ortiz. "A soft-recovery plate impact experiment for studying microcracking in ceramics." *Mechanics of Materials* 10.1 (1990): 43-58.

Ramberg, Walter, and William R. Osgood. "Description of stress-strain curves by three parameters." (1943).

Ramesh, K.T. "High Strain Rate and Impact Experiments" Part D.33. Springer Handbook of Experimental Solid Mechanics. 2008

Rand, James. An analysis of the split Hopkinson pressure bar. NOLTR 67-156 (1967)

Reed-Hill, Robert E. *Physical Metallurgy Principles.* 2nd ed. New York: Nostran, 1973. 611-660.

Rosenberg, Z., A. Ginzberg, and E. Dekel. "High shock pressure measurements using commercial manganin gauges." *International Journal of Impact Engineering* 36.12 (2009): 1365-1370.

Rosenberg, Z., and Y. Partom. "Longitudinal dynamic stress measurements with in-material piezoresistive gauges." *Journal of applied physics* 58.5 (1985): 1814-1818.

Rosenberg, Z., D. Yaziv, and Y. Partom. "Calibration of foil-like manganin gauges in planar shock wave experiments." *Journal of Applied Physics* 51.7 (1980): 3702-3705.

Rosenfield, A.R., Averbach, B.L., Cohen, M., Twinning Occurrence in Iron Single Crystals, Acta Metallurgica. 11 (1963) 1100-1101

S. Mahajan. "Accommodation at deformation twins in bcc crystals." Metallurgical Transactions A. 12A (1981) 379-386.

S. Mahajan. "Interrelationship between slip and twinning in B.C.C. crystals." *Acta Metallurgica*. 23 (1975) 671-684.

S.A. Atroshenko, N.S. Naumova, S.A. Novikov. "Influence of high-velocity impact on metals." *International Journal of Impact Engineering*. 33 (2006) 62-67.

Saada, Georges, and Patrick Veyssière. "Work hardening of face centred cubic crystals. Dislocations intersection and cross slip." *Dislocations in Solids* 11 (2002): 413-458.

Samanta, S. K. "Dynamic deformation of aluminium and copper at elevated temperatures." *Journal of the Mechanics and Physics of Solids* 19.3 (1971): 117in1123-122in4135.

Satish C. Gupta, R.G. Agarwal, J.S. Gyanchandani, S. Roy, N. Suresh, S.K. Sikka, A. Kakodkar And R. Chidambaram, A Single Stage Gas Gun For Shock Wave Studies, In Shock Compression of Condensed Matter–1991, edited by S.C. Schmidt, R.D. Dick, J.W. Forbes and D.G. Tasker, Elsevier, Amsterdam, 1992, Pages 839-842

Scapin, Martina. *Shock-wave and high strain-rate phenomena in matter: modeling and applications*. Diss. Politecnico di Torino, 2013.

Shetty, M. N. *Dislocations and mechanical behaviour of materials*. PHI Learning Pvt. Ltd., 2013.

Sikka, S. K. "Behaviour of materials under shock loading conditions." *Bulletin of Materials Science* 15.1 (1992): 35-46.

Sleeswyk, A. W. "½< 111> screw dislocations and the nucleation of {112}< 111> twins in the bcc lattice." *Philosophical Magazine* 8.93 (1963): 1467-1486.

Smallman, Raymond E., and Ray J. Bishop. *Modern physical metallurgy and materials engineering*. Butterworth-Heinemann, 1999.

Smida, T., Bošanský, J., Deformation twinning and its possible influence on the ductile brittle transition temperature of ferritic steels, Materials Science and Engineering. A287 (2000) 107–115.

Smida, T., Bošanský, J., Deformation twinning and its possible influence on the ductile brittle transition temperature of ferritic steels, Materials Science and Engineering. A287 (2000) 107–115.

Spirdione, J., et al. "Role of pearlite colonies on the dynamic flow stress of low carbon steel." *Materials Science and Engineering: A* 679 (2017): 446-454.

Spirdione, Justin. "Microstructure-dependent dynamic flow stress in metallic alloys." (2015).

Steinmetz, David R., et al. "Revealing the strain-hardening behavior of twinning-induced plasticity steels: Theory, simulations, experiments." *Acta Materialia* 61.2 (2013): 494-510.

Swinburne, T. D., et al. "Theory and simulation of the diffusion of kinks on dislocations in bcc metals." *Physical Review B* 87.6 (2013): 064108.

T. De Resseguier, M. Hallouin. "Stress relaxation and precursor decay in laser shock-loaded iron." *J. Appl. Phys.* 84.4 (1998): 1932-38.

T. Smida, J. Bošanský. "Deformation twinning and its possible influence on the ductile brittle transition temperature of ferritic steels." *Materials Science and Engineering*. A287 (2000) 107-115.

Tang, Meijie, and Jaime Marian. "Temperature and high strain rate dependence of tensile deformation behavior in single-crystal iron from dislocation dynamics simulations." *Acta Materialia* 70 (2014): 123-129.

Taylor, J.W., Dislocation Dynamics and Dynamic Yielding, Journal of Applied Physics. 36 (10) (1965) 3146–3150.

Timoshenko, Stephen P., and Sergius Woinowsky-Krieger. *Theory of plates and shells*. McGraw-hill, 1959.

Totten, George E., ed. *Handbook of residual stress and deformation of steel*. ASM international, 2002.

V. Panov. "Modeling of Behavior of Metals at High Strain Rates" PhD Thesis. Cranfield University. (2005)

Vignjevic, Rade, et al. "Lagrangian analysis led design of a shock recovery plate impact experiment." *International Journal of Impact Engineering* 77 (2015): 16-29.

Visser, W., and H. Ghonem. "Twin nucleation in cold rolled low carbon steel subjected to plate impacts." *Materials Science and Engineering: A* 687 (2017): 28-38.

Visser, W., Sun, Y., Gregory, O., Plume, G., Rousseau, C-E., Ghonem, H., Deformation Characteristics of Low Carbon Steel Subjected to Dynamic Impact Loading, Materials Science and Engineering. A528 (2011) 7857–7866.

Voyiadjis, George Z., and Farid H. Abed. "Effect of dislocation density evolution on the thermomechanical response of metals with different crystal structures at low and high strain rates and temperatures." *Archives of Mechanics* 57.4 (2005): 299-343.

W. Chen and B. Song, Spilt Hopkinson (Kolsky) Bar - Design, Testing and Applications, New York, New York: Springer, 2011.

Walker, Harold Leroy. *Grain sizes produced by recrystallization and coalescence in cold-rolled cartridge brass*. University of Illinois at Urbana Champaign, College of Engineering. Engineering Experiment Station., 1945.

Wasilewski, R.J., Mechanism of bcc twinning: Shear or shuffle?, Metallurgical Transactions. 1 (1970) 2641–2643.

Yiannakopoulos, G. *A review of manganin gauge technology for measurements in the gigapascal range*. No. MRL-TR-90-5. Materials Research Labs Ascot Vale (Australia), 1990.

Zeng, Z., Deformation Behaviour, Microstructure and Texture Evolution of CP Ti Deformed at Elevated Temperatures, PhD Thesis. Royal Institute of Technology. 2009

Zhao, Y. H., et al. "Influence of specimen dimensions and strain measurement methods on tensile stress–strain curves." *Materials Science and Engineering: A* 525.1 (2009): 68-77.

Zhernokletov, M.V., B.L. Glushak, "*Material Properties under Intensive Dynamic Loading*," Springer, New York. (2006).